Structural and Magnetic Studies of Strongly Correlated Electronic Systems

Gareth S. Oakley

A thesis presented for the degree of

Doctor of Philosophy

University of Edinburgh

2000

Declaration

This thesis is entirely of my own composition. The work presented within it was performed by me, unless otherwise stated, and was conducted during the period of October 1996 to October 1999. None of the work outlined in this thesis has been previously submitted for the award of any qualification.

Gareth S. Oakley

Structural and magnetic studies of strongly correlated electronic systems

Abstract

Understanding of strongly correlated systems is of great importance in our understanding of fundamental solid-state science, and in the design and improvement of many technologically useful magnetic systems. In this thesis studies of two such systems are presented. The first system is the jarosite mineral family $AM_3(SO_4)_2(OH)_6$ (where A = H_3O, K; M = Fe, Cr) which is an experimental manifestation of a kagome lattice antiferromagnet. Such a lattice displays unusual magnetic behaviour which may be of direct relevance to high temperature superconducting materials. A variety of neutron experiments have been performed to investigate the nature of the spin dynamics in the case of the hydronium iron salt, which is unique to the iron series in not exhibiting long range magnetic order. Single crystal studies have been used to probe the nature of the ground state of the potassium salt, and the first unambiguous determination of the magnetic structure is presented. Neutron diffraction studies and muon measurements have been performed on the hydronium chromium salt, the behaviour of which appears to contrast with that of the iron analogue.

The second system of study is the series of compounds $La_{1-x}M_xMnO_3$ (where M = Ca,Pb). which are of interest due to their potential application in read-write head devices. A combination of both dc susceptibility measurements and neutron diffraction studies have been used to investigate the magnetic behaviour of both these systems in key areas of the temperature-composition phase diagrams. The electronic fluctuations in the calcium system have been studied using muon spin relaxation techniques.

Acknowledgements

I'd like to begin by expressing my sincere thanks to Andrew for all the help, guidance and support I have received over the past three (and a bit) years. Your boundless energy and enthusiasm is certainly infectious (witness the single crystal experiments!) and I hope it survives the test of the endless 'administration' which it will, no doubt, be subjected to in the future.

A great debt of thanks also goes to Dick Visser for all the help on my various experiments at central facilities. Your expertise has proved invaluable and your company perennially entertaining.

None of the neutron and muon work would have been possible without the aid of the local contacts in each case, so my thanks and admiration are extended to Ken Anderson, Chris Baines, Dierk Herlach, Kevin Knight, Jiri Kulda, Kim Lefmann, Eddy Lelièvre-Berna, James Lord, Garry McIntyre, Amir Murani, Stephanie Pouget, Clemens Ritter, Ross Stewart and Waldemar Waeber respectively.

Thanks also go to Gavin for help with the chemical analysis presented in this work (and repair of the machinery), Anthony Powell for help with the HRPD data and to Simon Carling for various pieces of computing help.

On the occasions when I actually spent some extended periods of time in Edinburgh, life has always been enlivened by the various occupants of the Harrison group office, and I wish to express my gratitude for the company provided by Andrew, Gavin, Gui-Hua, Clare, Carolyn, Binbing, Debbie, Douglas, Keith, Graham and Vinesh, and various summer visitors and project students too numerous to mention here!

I'd also like to thank all those who have helped store my belongings, and in particular, myself since the end of October, since without their help writing up would have been even more stressful. My thanks therefore go to Scott, Bronagh and Angus, Helen, Ally and Kathy, David, Rachel and Steve. I promise I'll leave you all in peace now!

Finally I'd like to extend a special thank you to all my friends and family for the support and company they have provided me with over the past three years. It really is very much appreciated. I'd also like to thank Helen for her company and patience, particularly in the past few months. It *is* truly finished now!!!

Conferences attended

19/9/96 - 20/9/96	Neutron and Muon Beam Users Meeting, Rutherford Appleton Laboratory, Oxfordshire
16/12/96 - 17/12/96	Polar Solids Discussion Group, Annual Christmas Meeting, University of Sussex, Brighton
4/6/97	British Crystallographic Association (Industrial Group), Workshop on diffraction at elevated temperatures, Pilkington Technology Centre, Lathom
9/6/97 - 11/6/97	Departmental Physical Section Meeting at Firbush Point Field Centre
21/7/97 - 25/7/97	Royal Society of Chemistry Third International Conference on Materials Chemistry (MC^3), University of Exeter, Exeter
2/9/97 - 5/9/97	Royal Society of Chemistry Autumn Meeting and Pre-Doctoral Symposium, University of Aberdeen, Aberdeen
24/9/97 - 25/9/97	Neutron and Muon Beam Users Meeting, Rutherford Appleton Laboratory, Oxfordshire
1/10-2/10/97	Royal Society Discussion Meeting on Understanding and Utilising Colossal Magnetoresistance Materials, London
21/9/98 - 23/9/98	Polarised Neutrons for Condensed Matter Investigations (PNCMI98) Workshop, Institut Laue-Langevin, Grenoble, France

24/9/98 - 26/9/98 CNRS and Royal Society of Chemistry, First Materials Chemistry Discussion: Novel Syntheses and New Materials, ICMCB, University of Bordeaux, France

24/8/99 - 26/8/99 Departmental Physical Section Meeting at Firbush Point Field Centre

Published Papers

G.S.Oakley, D.Visser, J.Frunzke, K.H.Andersen, A.S.Wills and A.Harrison, *Physica B* **267-268** 142 (1999)

G.S.Oakley, S.Pouget, A.Harrison, J.Frunzke and D.Visser, *Physica B* **267-268** 145 (1999)

Table of contents

List of Abbreviations

1D	One-dimensional
2D	Two-dimensional
3D	Three-dimensional
χ_m	Molar dc magnetic susceptibility
μ_B	Bohr magneton (9.27498×10^{-24} JT^{-1})
μ_{eff}	Effective value of the moment
θ_{CW}	Curie Weiss Theta
CMR	Colossal Magneotresistance
DM	Dzyaloshinsky-Moriya interaction
fc	Field cooled
frac	Fractional occupancy
fwhm	Full width at half maximum
G-L	Ginzberg-Landau theory
GMR	Giant Magnetoresistance
H	Hamiltonian
ILL	Institut Laue-Langevin, Grenoble, France
ISIS	ISIS neutron spallation source, Chilton, Oxfordshire
J	Exchange coupling constant
L	Two dimensional spin-spin correlation length
LMU	Laboratory for Muon-spin spectroscopy, Paul Scherrer Institute, Switzerland
M	Magnetisation

mft	Mean field theory
MR	Magnetoresistance
MuSR	Muon spin relaxation
NN	Nearest neighbour
NNN	Next-nearest neighbour
PSI	Paul Scherrer Institute, Switzerland
S	Spin quantum number
SCGO(x)	$SrCr_xGa_{12-x}O_{19}$
SGF	Strongly geometrically frustrated
SQUID	Superconducting Quantum Interference Device
T	Temperature
t	reduced temperature
T_C	Curie Temperature
T_f	Spin glass freezing transition
T_N	Néel temperature
TAS	Triple axis spectrometer
TGA	Thermogravimetric analysis
XRD	X-ray diffraction
zfc	Zero field cooled

Chapter 1 Introduction

1.1 Strongly correlated systems

The nature and properties of solids have proved of great interest to both chemists and physicists throughout this century. Experimental work has used a combination of diffraction techniques, often using X-rays or neutrons, as well as probes of quantities such as the heat capacity and conductivity, in order to attempt to gain understanding of both the periodic array of atoms within given solids and the properties of such materials. However the link between experimentalist and theorist has proved more difficult to bridge. Whilst experimentally it is trivial to class materials as either insulators or metals, a theoretical understanding of such behaviour has proved greatly more complex. Classical theories for the description of a metal, based on the '*free electron model*' whereby an electron gas surrounds a lattice of positively charge ions (the so called 'ion core'), proved unable to model properties such as the large specific heat and magnetic susceptibility expected for completely free charge carriers reliably [1]. Quantum mechanical models, using Fermi-Dirac statistics in order to apply the Pauli exclusion principle, improved the theoretical description of metals, but were unable to successfully predict whether any particular system would exhibit metallic, semi-conducting or indeed insulating behaviour, in other than a small number of systems [2]. Such work was developed for a single electron, based on the premise that for any given electron an effective potential could be used to describe its interaction with surrounding ions and electrons [3].

In all cases the fundamental stumbling block to improved understanding rested upon the fact that the properties of a given particle (usually momentum and position) are strongly coupled to the other particles within the system. The problem is therefore a many body one, and such systems are termed '*strongly correlated*', to highlight the coupling between particles. A further complication is introduced when degrees of freedom in a given system are coupled together, such as in the case of the magnetoresistance of a material, where electronic motion is coupled with an applied magnetic field.

A huge impetus to the work on strongly correlated systems was provided by the discovery of high temperature superconductivity in the system $YBa_2Cu_3O_{6+\delta}$ in the mid 1980's [4]. Experimentally it proved a spur to improve sample preparation techniques since it soon became clear that differences in the stoichiometry of a given system could make a large difference to its measured properties. This meant re-evaluation of, not only, traditional high temperature synthetic routes to bulk powders, but also single crystal growth techniques and preparation of uniform thin films. From a theoretical standpoint such systems were fascinating, since theory could not reproduce such high superconducting transition temperatures, and work turned to improving upon the BCS theory of superconductivity [5]. Interest was re-ignited in modelling unusual and exotic magnetic ground states, since it became clear that the nature of the ground state, and low lying excitations, in $YBa_2Cu_3O_{6+\delta}$ and related layered systems such as those based on the parent compound La_2CuO_4, were important in determining the nature of the superconducting properties of such systems.

It was in such a climate that a 'rediscovery' of the lanthanum manganite solid solutions was made in the late 1980's and early 1990's [6-10]. Such systems, of generic formula $Ln_{1-x}M_xMnO_3$ (where Ln is a Lanthanide ion and M is a divalent metal ion such as Ba,Ca,Sr or Pb) were first studied in the 1950's [11] but interest was revived due to the remarkable magnetoresistive behaviour they exhibit over a wide range of solution. The complex interplay of structural and magneto transport, in particular the correlation between the peak in magnetoresistance and a ferromagnet transition, and the sensitivity of the properties of such solutions to changes in the concentration of M proved irresistible to theorists and experimentalists alike as a challenging testing ground for the theory of complex electronic systems.

What the work in this thesis attempts to do is to consider both experimental and theoretical models relevant to the general problem of modelling and understanding strongly correlated systems. To this end the work is split into two main sections. The first section is devoted to the Kagome antiferromagnet, as modelled by the jarosite family $AM_3(SO_4)_2(OH)_6$, where A is a monovalent ion such as D_3O^+, K^+, Na^+ and M is a trivalent metal such as Fe^{3+} or Cr^{3+}. Theoretical interest in the Kagome antiferromagnetic lattice relates to its geometry, well separated layers of vertex sharing triangles giving rise to an unusual magnetic ground state. Such ground states may be directly relevant to those of superconducting materials [12]. Interest in jarosites stems from the fact that they appear to provide the most appropriate realisation of this kind of magnetic system, and so provide a direct testing ground for the various theoretical models which have been devised to predict and rationalise the properties of this unusual class of magnet. The chemical flexibility of the jarosite family is also attractive, since it allows exploration of the effect of a variety of

different spins, and to this end both systems with Fe^{3+} (S = 5/2) as the magnetic ion, and also systems containing Cr^{3+} (S = 3/2) have been investigated. Not only is it possible to monitor the nature of the magnetic coupling between moments by changing the nature of the magnetic ion in such systems, but it is also possible to probe the balance between the various exchange forces by substitution of the linking sulfate group. To this end studies on the series of compounds $KFe_3(XO_4)_2(OH)_6$, where X = S, Cr and Se have been performed.

The second half of the work concentrates on the series of compounds $La_{1-x}M_xMnO_3$ (where M = Ca and Pb). In the case of the calcium system work has focussed on concentrations of Ca where the system sits on the point of both a metal–insulator and ferro-antiferromagnetic transition. The work performed has been in two parts. Firstly high resolution neutron powder diffraction measurements have been used in order to study the crystallographic distortions which occur as the parent material $LaMnO_3$ is doped with calcium, and secondly muon spin relaxation measurements have been carried out in order to investigate the nature of spin fluctuations as the magnetic ground state changes on crossing the transition point T_C. Further neutron powder diffraction studies have been carried out in the case of the Pb system in order to monitor the change in crystallographic distortion on progressive doping of the parent compound $LaMnO_3$.

Before describing the background to the two different systems in more detail it will be of benefit to review both the nature of some basic aspects of magnetism, and the techniques available to a magnetochemist in characterising any given samples. The following section therefore outlines some of the basic principles of magnetic theory [13], in advance of the next Chapter which considers the variety of techniques which

can be used to characterise not only the chemical but also the magnetic properties of any experimental systems.

1.2 Magnetic susceptibility and the Curie Law

The magnetic susceptibility χ of a material can be described by the expression

$$\chi = \frac{M}{H} \tag{1.1}$$

where M is the magnetisation, defined as the magnetic moment per unit volume, and H is the applied magnetic field strength. In situations where the susceptibility is negative the sample is said to exhibit *diamagnetism*. Diamagnetism is a property of all materials and arises from the interaction of paired electrons with an applied magnetic field. Upon introduction of an applied field of strength H there is a reduction in the concentration of magnetic flux lines in comparison to that of free space, in other words the sample will be repelled by the applied field. Such a response is both temperature and field independent, and generally small in magnitude.

A positive value of the magnetic susceptibility on the other hand corresponds to a *paramagnetic* response. Paramagnetism is a property of unpaired electrons and thus a paramagnetic material will act so as to concentrate flux lines of any applied field and will therefore be attracted towards regions of high flux density. Whilst the response is independent of field strength it does generally show a considerable temperature dependence. To a first approximation, such paramagnetic behaviour can be described using the Curie Law which states that

$$\chi = C/T \tag{1.2}$$

where C is the Curie constant and T is the temperature in Kelvin. Thus a plot of χ^{-1} *vs.* T will yield a straight line, from which the Curie constant can be calculated. In many cases however, instead of using the Curie constant, an alternative figure is quoted, that of the effective moment μ_{eff}. This gives a measure of the number of unpaired electrons per mole of material under investigation and is given by the equation

$$\mu_{eff} = [(3k/N_A)^2(\chi T)^{1/2}] = [g^2 s(s+1)]^{1/2}\mu_B \qquad (1.3)$$

where k is the Boltzmann constant, N_A the Avogadro number, g the Landé factor and s is the electron spin. Methods of measuring the bulk susceptibility of a sample are outlined in the next Chapter. It should be noted in passing however that confusion may arise as to the units appropriate to these quantities. In SI units the factor μ_0 must be introduced on the right hand side of equation 1.1 and the units of M and H are then Am^{-1} and those of χ $JT^{-2}m^{-3}$. However it is still common to use equation 1.1 as it stands and to quote the magnetic susceptibility in terms of the moles of sample and hence, in cgs units of emu cm^{-3}, where μ_0 is defined as 1 and is dimensionless and 1 emu $\equiv 1cm^3$. The conversion factor between SI and cgs units is therefore given by 1 $JT^{-2}m^{-3} \equiv 10^{-7}$ emu cm^{-3}. It is the molar susceptibility which will be used in this thesis, since it may be converted more rapidly to give the effective moment and so a comparison with the angular momentum of unpaired electrons in the systems under investigation.

1.3 Microscopic origin of magnetic susceptibility

If the case of a simple magnet of isolated atoms is considered, with spin and orbital quantum numbers S and L respectively, then if Russell-Saunders coupling applies, *i.e.*

S and L couple vectorially to give the total angular momentum quantum number J, the moment μ_J associated with J is given by

$$\mu_J = g\mu_B\sqrt{J(J+1)} \tag{1.4}$$

where μ_B is the Bohr magneton as defined by the relation

$$\mu_B = |e|h/2mc \tag{1.5}$$

where e is the electronic charge in C, m the mass of the electron in kg and c the speed of light in ms^{-1}. Since, in this case, Russell-Saunders coupling applies, the value of g is given by

$$g = \frac{3J(J+1)+S(S+1)-L(L+1)}{2J(J+1)} \tag{1.6}$$

It should be noted that this expression will not hold in the case of first row transition metals, since the ligand field will perturb J, and hence contributions from s and l of the individual ligand field split states need to be calculated explicitly.

If a magnetic field H is applied to the magnetic ion discussed above, then the ground state will be Zeeman split into $(2J+1)$ m_j states of energy E_{mj} given by

$$E_{mj} = - m_j g\mu_B H_z \tag{1.7}$$

where z denotes the orientation of the magnetic field. Each state m_j will have a projection of the moment along the field direction as given by

$$\mu_{mj} = m_j g\mu_B \tag{1.8}$$

The net polarisation $<\mu_{mj}>$, given by the Boltzmann average over all states m_j, is

$$<\mu_{mj}> = \frac{\sum_{m_j=-J}^{J}\mu_{mj}\exp(-E_{mj}/kT)}{\sum_{m_j=-J}^{J}\exp(-E_{mj}/kT)} \tag{1.9}$$

If the Zeeman splitting is small relative to kT then this expression simplifies to

$$< \mu_{mj} >= \frac{g^2 \mu_B{}^2 J(J+1)}{3kT} \tag{1.10}$$

Thus, for one mole of ions, the molar magnetisation is given by $M = N_A<\mu_{mj}>$, where N_A is the Avogadro number, and the molar susceptibility χ_m, by

$$\chi_m = M/H = C/T \tag{1.11}$$

where $C = \frac{N_A g^2 \mu_B{}^2 J(J+1)}{3k}$ and the result is the Curie Law as introduced above.

1.4 Curie-Weiss Law

Those class of magnets which rigorously obey the Curie Law have no thermally accessible m_j states in higher energy J states, whose population will change with varying temperature, and no appreciable magnetic coupling between ions. However in the case where there *are* such thermally accessible states, or when exchange interactions between ions become significant, the behaviour of such systems can be described by a modification of the Curie Law as given by

$$\chi = C/(T-\theta) \tag{1.12}$$

where C is defined as for the Curie Law and θ is termed the Curie-Weiss constant and parameterises the sign and strength of coupling within any given system. It can be determined from experimental data in a similar fashion to the Curie constant, by plotting χ^{-1} against T and measuring the intercept with the T axis. The case where $\theta <$ 0 describes an antiferromagnet, whilst that of $\theta > 0$ describes the case of a ferromagnet.

A description of this term was first proposed by Weiss [14], in a description of ferromagnetic materials. He assumed that as a material approached the ferromagnetic transition temperature T_C, the atomic spins became aligned by interaction *via* a molecular field. The effect of such interaction was such that each individual spin S_i could be replaced by an average value $<S>$ and so the formalism was termed *mean field theory*. Each moment thus experiences an additional internal field $\boldsymbol{H_m}$ which is directly proportional to the magnetisation of the sample. Thus

$$H_m = \lambda M \tag{1.13}$$

where λ is termed the Weiss field constant. Insertion of this term into the Curie Law then gives the susceptibility in the form

$$\chi_m = M/H = C/(T - \lambda C) \tag{1.14}$$

Thus in the limit when H = 0, M $\neq$ 0 and T = T_C it can be seen that $\lambda C = T_C$.

A similar treatment can be applied to the case of an antiferromagnet, defining the material to consist of two sublattices, one with all spins polarised in a positive direction ('spin up'), the other with all spins of negative polarisation ('spin down'). In this case derivation of the Curie-Weiss Law gives a Curie Weiss constant $\theta = \lambda C/2$.

Whilst mean field theory can describe the behaviour of magnets well above any ordering transition, it will break down on cooling as short-range correlations become significant. Such critical behaviour of magnetic systems in the region $T \sim T_C$ (T_N in the case of an antiferromagnet) will be considered in more detail in Chapter 3.

1.5 Magnetic exchange

The preceding sections 1.2 – 1.4 have considered the microscopic origin of magnetism and the response of an assembly of isolated magnetic ions to an applied magnetic field. Whilst it is possible to assess the magnetic behaviour of a given sample through consideration of its magnetic susceptibility, it is also important to consider what mechanisms allow interaction, or *exchange*, between assemblies of ions. On a simple level *direct exchange* may take place between localised electrons on adjacent ions. Overlap of charge density gives rise to a correlation between spins which is proportional to their scalar product $S_1.S_2$. Applying this to the three dimensional case of a 'real' solid gives rise to the Hamiltonian

$$H = -2J\sum_{i,j} S_i.S_j \qquad (1.15)$$

where J is the exchange integral between adjacent atoms and the summation extends over all neighbouring pairs of atoms. A positive value of J leads to ferromagnetism, a negative value to antiferromagnetism. However in the majority of magnetic systems exchange is somewhat more complex, since the interacting magnetic ions are further apart. In the case of insulators the mechanism of *superexchange* was first proposed by Kramers [15], who suggested that magnetic cations interacted *via* an intervening anion. This can be illustrated in the case of the antiferromagnet MnO, which has a rock salt structure. Overlap between the *d*-orbitals of the Mn(II) ions and the *p*-orbitals of the O anions, in obeyance with the Pauli exclusion principle, leads to an antiferromagnetic array of Mn(II) moments, as depicted below.

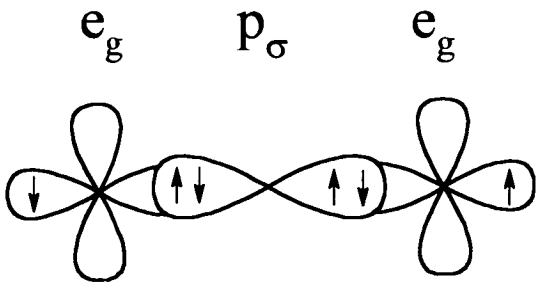

Figure 1.1 Schematic diagram showing electron distribution between manganese ions in MnO. Superexchange between these ions via the intervening oxygen p-orbitals leads to antiferromagnetic spin ordering

In metals there is a long range interaction between conduction electrons and nuclear moments which is proportional to $(1/R^3)$ at relatively large distances R between ions, this being known as the RKKY (Ruderman-Kittel-Kasuya-Yosida) interaction.

Having examined the origins of magnetic behaviour, the next Chapter outlines the various techniques used to characterise the systems studied in this thesis, both in terms of their chemical composition and magnetic behaviour.

References

[1] See for example *'The Theory of electrons'*, H.A.Lorentz (Dover, 1952); *'Theory of the Properties of Metals and Alloys'*, N.F.Mott and H.Jones (Dover, 1958); *'Solid State Physics'*, J.S.Blakemore (Cambridge University Press,1985)

[2] See for example *'Quantum Field Theory of Solids'*, H.Haken, (North-Holland, 1976); *'Principles of the Theory of Solids'*, J.M.Ziman (Cambridge University Press,1972)

[3] See for example *'Energy Band Theory'*, J.Callaway (Academic Press, 1964); Electronic Structure and the Properties of Solids, W.A.Harrison (Freeman, 1980)

[4] K.A.Muller and J.G.Bednorz, *Science* **237**(4819) 1133 (1987); K.A.Muller, J.G.Bednorz and M.Takashige, *Science* **236**(4797) 73 (1987)

[5] J.Bardeen, L.N.Cooper and J.R.Schreiffer, *Phys. Rev.* **108** 1175 (1957)

[6] R.M. Kusters, J. Singleton, D.A. Keen, R. McGreevy, W. Hayes, *Phys. Rev. B* **155** 362 (1989)

[7] R. Von Helmholt, J. Wecker, B. Holzapfel, L. Schultz, K. Samwer, *Phys. Rev. Lett.* **71** 2331 (1993)

[8] K. Chahara, T. Ohno, M. Kasai, Y. Kozono, *Appl. Phys. Lett.* **63**(14) 1990 (1993)

[9] S. Jin, T.H. Tiefel, R. Ramesh, *J. Appl. Phys.* **76** (10) 6929 (1994); S.Jin, T.H. Tiefel, M. McCormack, R.A. Fastnacht, R. Ramesh, L.H. Chen, *Science* **264** 413 (1994)

[10] S. Jin, T.H. Tiefel, M. McCormack, H.M. O'Bryan, L.H. Chen, R. Ramesh, D. Schurig, *Appl. Phys. Lett.* **67**(4) 557 (1995)

[11] G.H. Jonker and J.H. Van Santen, *Physica* **16** 337 (1950); J.H. Van Santen and G.H. Jonker, *Physica* **16** 599 (1950); J.B.Goodenough, *Phys Rev.* **100**(2) 564 (1955); E.O.Wollan and W.C.Koehler, *Phys. Rev.* **100**(2) 545 (1955)

[12] P.W.Anderson, *Science* **235**(4793) 1196 (1987)

[13] For more details see for example *'Introduction to Magnetochemistry'*, R.L.Carlin (Springer-Verlag, 1986), *'Introduction to Solid State Physics'*, C.Kittel (Wiley and Sons, 5th Edition, 1976), *'Solid State Magnetism'*, J.Crangle (Edward Arnold,1991)

[14] P.Weiss *J.Phys.Radium* **4** 661 (1907)

[15] H.A. Kramers, *Physica* **I** 191 (1934)

Chapter 2 Sample Characterisation Techniques

To effectively probe the nature of the systems described in this thesis, a broad range of characterisation techniques needs to be used. Not only is the elemental composition of any given sample of importance, but also its structure, as well as its magnetic properties. This chapter therefore considers each of these problems in turn, concluding with a brief overview of some of the fundamental principles of neutron diffraction which will be of use in interpreting the experimental data presented in subsequent Chapters.

2.1 Chemical characterisation

2.1.1 ICP Atomic emission spectroscopy

Atomic emission spectroscopy (AES) affords the ability to determine the concentration of cations in solution with a sensitivity of the order of parts per million. The sample of interest is dissolved in a suitable solvent and then introduced into a nebulizer through a capillary tube, where argon gas is then introduced in such a way as to create an aerosol gas jet. This jet enters a spray chamber where large droplets of sample are trapped out, leaving the smaller particles to enter the plasma torch, whose temperature is greater than 10^4K; here the droplets are desolvated and atomised, these atoms then being excited with subsequent emission of light [1].

2.1.2 Thermogravimetric analysis

Thermogravimetric analysis (TGA) allows us to monitor the chemical breakdown of given materials on heating, through the measurement of small changes in sample mass as a function of temperature. A TGA machine consists of a delicate electronic microbalance hanging in an oven, capable of heating to, typically, 1500°C. A gas flow of ca. $5Lmin^{-1}$ across the sample crucible is often used. In the specific case of metal oxides, it is possible to use the mass changes seen in the TGA data in order to determine the oxygen content of a given sample, through heating of the sample in a reductive atmosphere such as hydrogen. The change in mass of the sample on heating is recorded, and such changes seen as a function of temperature can be related to the chemical breakdown of the sample. A schematic diagram of the apparatus involved is shown in figure 2.1.

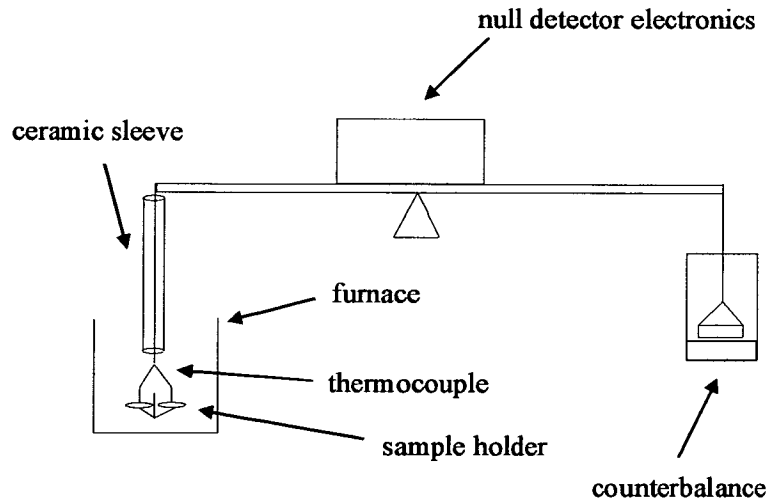

Figure 2.1 Schematic diagram showing arrangement of apparatus for TGA measurements

The shape of the TGA trace is dependent upon the heating rate used (typically 2-10°C min^{-1}), the atmosphere surrounding the sample and the particle size.

It is possible to combine TGA analysis with differential thermal analysis (DTA). In the case of DTA a reference crucible, containing a thermally inert material such as alumina (Al_2O_3) is introduced alongside the sample crucible, both being held symmetrically in the furnace so that the thermal flux experienced by both crucibles is identical. As the furnace warms up the difference, ΔT, between the temperatures of the reference and sample crucibles is recorded. Using such temperature differences it is possible to measure the enthalpy of any phase changes which occur on heating [2].

2.2 Structural characterisation

2.2.1 Powder diffraction

Both X-ray and neutron diffraction provides the solid state chemist with a powerful means of determining the structure of any given crystalline material. In a given diffraction pattern the position of reflections is determined by the geometry of the unit cell, whilst the intensity of such reflections is determined by the so called *structure factor* F_{hkl}^2 which is dependent upon the position and nature of the atoms in the unit cell. A fuller description of the diffraction process is given in the specific case of neutron diffraction in section 2.3.6. However, it is pertinent to consider at this stage how information is extracted from the diffraction data obtained. Whilst single crystal studies are capable of extracting the maximum amount of information about the structure of a material, it is not always possible to grow a crystal of material suitable for such studies. Instead powder diffraction measurements may be performed. In this case determination of the structure factor is made more difficult by the fact that the measured intensity is acquired only with respect to lattice *d*-spacings. Thus no information is gathered as to the orientation of scattering and so reflections which are

close in *d*-spacing will overlap. A breakthrough in the treatment of such data was provided by the *Rietveld* method [3] which is a step by step means of analysing a given powder diffraction pattern, and recognises the fact that a given diffraction pattern will yield information from intensity at each step in the pattern. Thus a least-squares refinement is used to generate a best-fit between the observed diffraction pattern as a whole, and the calculated model, with refinement of a series of factors relating to various specimen parameters (in particular the size of the unit cell and positions of atoms within it), as well as those associated with the instrument involved. Whilst individual reflection profiles will overlap, the Rietveld method does not attempt to allocate observed intensity to any particular Bragg reflections, but rather treats the profile as a whole. The quantity minimised (S_y) in the least squares refinement is given by the equation

$$S_y = \sum_i w_i (y_i - y_{ci})^2 \qquad (2.1)$$

where $w_i = (y_i)^{-1}$, y_i is the observed intensity at the ith step and y_{ci} the calculated intensity at the ith step. The sum is performed over all data points.

The least squares minimisation leads to a set of normal equations containing the derivatives of all the calculated intensities, y_{ci}, with respect to each of the adjustable parameters , which is then soluble by an inversion of the *normal* matrix. This solution is performed iteratively, whereby shifts are applied to the initial parameters in order to improve the model. Since the adjustable parameters and intensities are related non-linearly the starting model must be close to the correct model, otherwise the refinement will not reach a global minimum. Thus it is important to note that the Rietveld method is one of structure *refinement* rather than structure *solution*. The

criterion of fit used in such refinements is similar to those used in single crystal diffraction pattern analysis. The term used is designated the 'R - weighted pattern' or R_{wp} value, which is given by the equation

$$R_{wp} = \left\{ \frac{\sum_i w_i [y_i(obs) - y_i(calc)]^2}{\sum_i w_i [y_i(obs)]^2} \right\}^{1/2} \tag{2.2}$$

where w_i is defined as above, and $y_i(obs)$ and $y_i(calc)$ are the observed and calculated intensity at the ith step respectively.

Whilst a variety of software packages exist to perform such analysis, one of the most commonly used is GSAS (General Structure Analysis System) [4], and it is this package which will be used in the analysis presented in this work. It should be noted in passing that a further statistic calculated during a refinement is the 'goodness of fit', designated χ^2, which is given by the expression

$$\chi^2 = \frac{\left\{ \sum_i w_i [y_i(obs) - y_i(calc)]^2 \right\}}{(N_{obs} - N_{var})} \tag{2.3}$$

where N_{obs} is the number of data points and N_{var} the number of variables in the fit. Thus a perfect fit between observed and calculated data will give a value of χ^2 equal to 1.

2.3 Magnetic properties

2.3.1 Magnetic susceptibility

There are several ways in which the bulk magnetic susceptibility of a sample may be measured, which can be split into two broad categories. Firstly there are 'force' methods, where the force of the interaction between sample and applied field is measured. One example is the Faraday (or Gouy) balance, where the force exerted on a sample placed in a strong magnetic field is measured by consideration of the change in mass of the sample. Alternatively the susceptibility of a sample may be measured 'inductively' by monitoring the current induced in a pick-up coil moved relative to the (magnetically polarised) sample. This is the basis of Superconducting QUantum Interference Device (SQUID) magnetometers. A further possibility is to measure the complex magnetic inductance of the sample under investigation, a method used in the case of A.C. inductance bridges. Each will be considered in turn.

2.3.2 DC Susceptibility

All the measurements performed within this thesis were conducted using a MPMS-2 SQUID magnetometer, supplied by *Quantum Design,* San Diego. The principle of operation is illustrated in figure 2.2.

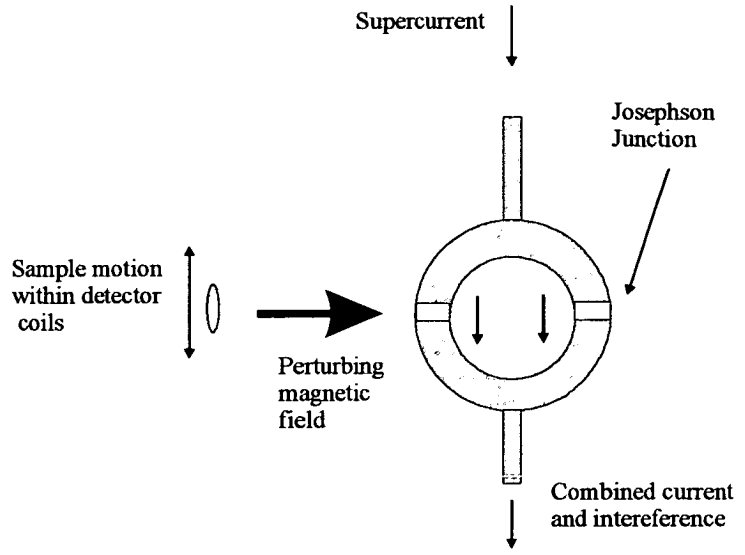

Figure 2.2 Schematic diagram outlining the operation of a SQUID magnetometer. Changes in the magnetisation of the sample are manifested by changes in the tunnelling current

The SQUID itself consists of a loop of superconducting material divided in half by two thin sections of insulating material, these barriers being known as *Josephson junctions*. Such links allow the passage of a supercurrent, *via* quantum mechanical tunnelling; a magnetic field at one junction results in an interference pattern at the point where the two loops combine, this being very sensitive to the magnitude of such a magnetic field. Such a tunnelling current is then amplified by the SQUID and converted into a voltage reading directly proportional to the applied magnetic field. It is thus possible to determine the magnetisation of a sample by moving the sample through detector coils attached to one of the Josephson junctions and monitoring the changes in the measured tunnelling current.

2.3.3 AC Susceptibility

Whilst measurements using dc susceptibility rely on the fact that the magnetisation M is directly proportional to the applied field H, ac susceptibility measurements allow direct measurement of the rate of change of M with respect to H at a given frequency. The technique involves the application of a modest driving field h, the susceptibility χ being measured by taking the value of $\partial M/\partial h$ at some frequency ω. The signal obtained is composed of two parts, the real part $\chi'(\omega)$, corresponding to the dispersion, and an imaginary part $\chi''(\omega)$, corresponding to the absorption. Usually these two terms are related, through a relaxation time, by use of the *Casimir-Du Pré* equations

$$\chi' = \chi_S + \frac{\chi_T - \chi_S}{1+\omega^2\tau^2} \tag{2.4}$$

$$\chi'' = \omega\tau\left(\frac{\chi_T - \chi_S}{1+\omega^2\tau^2}\right) \tag{2.5}$$

where τ is a single relaxation time, χ_T is the isothermal susceptibility in the limit $\omega \rightarrow 0$, and χ_S the adiabatic susceptibility in the limit $\omega \rightarrow \infty$. When $\chi'' = 0$ and $\omega \rightarrow 0$ it is possible to measure the value of χ_T, whilst as $\omega \rightarrow \infty$ $\chi' = \chi_S$. At the point where $\omega = 1/\tau$ there is a point of inflection in $\chi'(\omega)$, whilst $\chi''(\omega)$ has a maximum, allowing determination of an average relaxation time τ_{av} for any given temperature. This technique therefore allows probing of dynamic processes of frequencies up to 10kHz. In order to investigate faster processes the technique of muon spin relaxation may be used as outlined in the next section.

2.3.4 Muon Spin Polarisation Measurements

Muons are short lived particles with a mean lifetime of ~2μs. Whilst both positive (μ^+) and negative (μ^-) muons can be produced, only the case of μ^+ will be considered here. Such muons are resultant from the decay of pions, which in turn are produced *via* the elementary reactions

$$p + p \rightarrow \pi^+ + p + n \tag{2.6}$$

$$p + n \rightarrow \pi^+ + n + n \tag{2.7}$$

where p is a proton, n a neutron and π^+ a pion.

Thus to generate a beam of muons a proton beam (of energy 500-800 MeV) is directed onto a production target, such as elemental carbon or beryllium, the threshold energy for pion production being of the order of 180 MeV. To ensure isotropic polarisation of the resultant muons, the muon beam is generally emitted from pions at rest within the surface layer of the target, and the beam therefore described as consisting of *surface muons*.

Whilst the acronym MuSR can be used to refer to a variety of techniques, muon spin *resonance*, spin *relaxation* or spin *rotation* [5], all of these utilise the three basic properties of the muon particle.

- Muons produced from pion decay are polarised
- Muon decay occurs following the pathway

$$\mu^+ \quad \rightarrow \quad e^+ + \quad \nu_e \quad + \quad \overline{\nu}_\mu \tag{2.8}$$

such that the positrons, e^+, resultant from this decay emerge with sufficient energy to travel substantial distances before annihilation.

- The distribution of decayed positrons is dependent upon the muon polarisation.

In the case of muon relaxation experiments, incident muons are implanted in the sample, generally at an interstitial site, since each muon will behave in a similar fashion to a proton and so implant close to an electronegative ion. If any local magnetic field is present, not parallel to their polarisation, then the muons will precess around it, with a *Larmor frequency* ω_μ given by

$$\omega_\mu = \gamma_\mu B_\mu \tag{2.9}$$

where γ_μ is the muon gyromagnetic ratio ($\gamma_\mu/2\pi$ = 13.554 kHzG^{-1}) and B_μ is the local field.

If all the muons experience a unique magnetic field at their implantation site then the spin polarisation $G_Z(t)$ along the z direction is given by

$$G_Z(t) = \mathrm{Re}(\cos^2\theta + \sin^2\theta \exp(i\omega[t - t_0]) \tag{2.10}$$

where θ is the angle between the initial muon spin and the local field direction, $\omega = \gamma_m \boldsymbol{B}$ and t_0 the muon arrival time

The average taken over a powder sample is then given by

$$G_Z(t) = \frac{1}{3} + \frac{2}{3}\cos(\omega t) \tag{2.11}$$

if t_0 is defined as being equal to zero.

However in real systems the local field may vary over different sites as a result of factors such as nuclear moments, impurities or non-homogeneous freezing of ionic moments. Relaxation of the 2/3 component will result from both dynamical fluctuations and spatial inhomogeneities, but if the former are ignored for the moment and it is assumed that there is a distribution of muon oscillations defined by $\rho(\omega - \omega_0)$ where ω_0 is the mean oscillation frequency, then the polarisation is given by

$$G_Z(t) = \frac{1}{3} + \frac{2}{3}\int d\omega \rho(\omega - \omega_0)\cos(\omega t) \qquad (2.12)$$

and so, depending upon whether ρ is Gaussian or Lorentzian in nature, the component will relax with either a Gaussian or exponential line shape. Thus dynamical fluctuations can only provide additional sources of relaxation. Similarly spatial inhomogeneity in the local field cannot cause relaxation of the 1/3 component since this proportion of the incident muons will always have spin polarisation along the direction of this field. The polarisation of these muons is constant unless the nature of the field changes with time. Thus relaxation of the 1/3 component can result *only* from dynamical fluctuations. The resultant analytical expression is given by

$$G_Z(t) = \frac{1}{3}\exp(-t/T_1) + \frac{2}{3}\exp(-[t/T_G]^2 - [t/T_1])\cos(2\pi ft) \qquad (2.13)$$

The second exponential term tries to account for both static and dynamical relaxation sources. The choice of relaxation function affects the values of T_1 and T_G but will only slightly affect the value of ω which is the primary parameter of interest.

Thus the muons act as probes of local magnetic fields, on a time scale such that static fields ranging from a fraction of a Gauss to several thousand Gauss can be detected, as well as fluctuating fields on a time scale of $10^{-3} - 10^{-9}$s.

In a typical experiment the rate of loss of polarisation in the sample is measured as a function of time and the muon polarisation is then reconstructed from the positron decay distribution. It is possible to apply external fields either along, or perpendicular to, the direction of muon polarisation. In the former case the set up is termed longitudinal field (LF) geometry, where the rate of loss of polarisation in the sample

as a function of applied field along the initial muon spin direction (H_L) is measured. The experimental set up for this is shown schematically in figure 2.3 below.

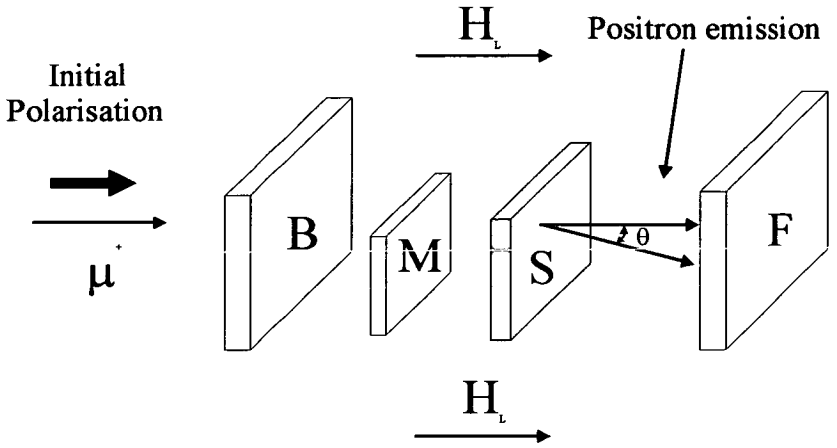

Figure 2.3 Schematic diagram illustrating the set-up in a typical longitudinal (or zero field) muon spin relaxation measurement. Incident muons (μ^+) trigger the start counter (M) before passing through the sample (S) and positron emission occurs (on a trajectory at angle θ to the muon spin) into the backward (B) and forward (F) detectors. The applied magnetic field is designated H_L.

At $t = 0$ positrons are preferentially emitted in the forward direction, whilst as $t \rightarrow \infty$ the muons lose their polarisation and there is no difference between the signal observed in the forward and backward detectors. Hence if the difference between the forward and back detectors, defined as the asymmetry A_0, is calculated then a raw plot of asymmetry against time can be determined.

The transverse field (TF) geometry set-up is shown in figure 2.4 below. This configuration is used to measure not only the frequency of muon precession but also the rate at which it loses phase coherence when the applied field H_T is applied. It

should be noted that it is possible to use an alternative configuration in which H_T is applied in the same direction as the muon spin, and positron emission is then monitored using detectors placed above and below the sample.

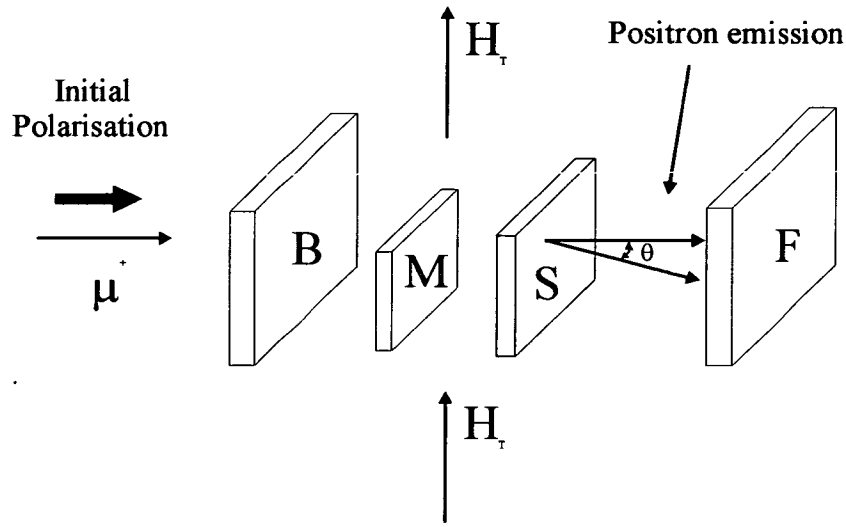

Figure 2.4 Schematic illustration of the transverse field arrangement. The set-up is similar to the longitudinal field arrangement, though in this case the applied field (H_T) is perpendicular to the muon spin direction

Modelling of the data acquired involves the use of analytical functions, which give information as to the static/dynamic components to any magnetic behaviour seen. The number of detected positrons for example in the backward detector (B) is given by

$$N_B(t) = N_0{}^B[B_B + \exp(-t/\tau_\mu)(1 + A_0 P(t))] \qquad (2.14)$$

where B_B is the time independent background, $P(t)$ the muon polarisation function and A_0 the calculated asymmetry. The number of counts in the forward detector (F) can be described in a similar manner.

The constant background terms are measured at a point when there are no muons in the sample and so the expressions can be reduced to

$$B(t) = N_0(t) - N_0{}^B B_B \tag{2.15}$$

$$F(t) = N_F(t) - N_0{}^F F_F \tag{2.16}$$

The *experimental asymmetry* $A_r(t)$ is then given by

$$A_r(t) = \frac{B(t) - F(t)}{B(t) + F(t)} = \frac{(1-\alpha) + (1+\alpha)A_0{}^B P(t)}{(1+\alpha) + (1-\alpha)A_0{}^B P(t)} \tag{2.17}$$

where α is the ratio of raw count rates $\frac{N_0^F}{N_0^B}$

And the *corrected asymmetry* $A(t)$ is then given by

$$A(t) = A_0^B P(t) = \frac{(\alpha-1) + (\alpha+1)A_r(t)}{(\alpha+1) + (\alpha-1)A_r(t)} \tag{2.18}$$

The term α reflects the ratio of effective solid angles of the different counters and is independent of magnetic interaction of the muon with the target. In the TF configuration the value of α is selected so that in the limit as $t \to 0$, $P(t) = 0$ in the most strongly relaxing spectrum for a given sample. The value of α is extremely sensitive to factors such as the magnitude of an applied field, slight changes in the sample position and by the position of the proton beam on the production target.

Muons implanted in a sample depolarise as an equilibrium ratio of spin up and spin down is approached. Thus if there is a field distribution $\rho(B)$ as given by

$$\rho(B) = \frac{\gamma_m^3}{\sqrt{2\pi\Delta^2}} \exp\left(\frac{-\gamma_\mu^2[B - B^s]^2}{2\Delta^2}\right) \tag{2.19}$$

where B^s is some average field (either external or induced by magnetic ordering) and Δ/γ_m the rms of the field distribution, then the static relaxation function $g_0(t)$, (assuming that $B^s = 0$) is given by

$$g_0(t) = \int d^3B\rho(B)G_z(t) \qquad (2.20)$$

$$= \frac{1}{3} + \frac{2}{3}(1-\Delta^2t^2)\exp(-\frac{1}{2}\Delta^2t^2)$$

which is termed the *Static Kubo-Toyabe Function*

2.3.4.1 Generation of muons: pulsed vs. direct current beams

The ISIS facility at the Rutherford Appleton Laboratory and the LMU facility at the Paul Scherrer Institute (PSI) in Switzerland, directly complement each other, allowing the experimentalist to probe a large range of relaxation times. In the case of ISIS pulses of muons are generated by the focussing of a proton beam onto a graphite target, set at 45° to the direction of the beam. A single pulse muon beam is generated with a full width at half height maximum (fwhm) of 80ns, an energy of 3.2meV and intensity of $4x10^5$ muons s^{-1}. Such a burst of muons starts the multistop 'clock' when it is detected in front of the sample; positrons subsequently emitted are then detected by an array of scintillation counters in the forward and backward banks. In the case of the MuSR instrument there are 2 sets of 16 scintillators giving 32 detectors in all. A constant background is achieved amounting to something of the order of 10^{-5} of the counts in the first bins of the polarisation rate *versus* time histogram, obtained using a multiple channel analyser. Time resolution is limited by the pulse width, Δ, since this uncertainty is manifested in the timing which starts each time the first muons are incident upon the detector. In practice this means that any time dependence of the

μSR signal which is on a scale comparable with, or faster than, the pulse width will be averaged out.

In the case of the PSI facility the proton beam is continuous. In order to determine a muon decay event, detection of a positron/electron is required within a time period specified as the *data gate*, typically of 10μs duration. Thus a 'good' decay event sees a coincidence of a positron/electron signal with this data gate. If a muon is stopped by the sample then there will be a coincident signal from the detectors in front of the sample, but no signal in the detectors behind the sample, this being termed the μ_{stop} *signal*. In order to determine the number of events, as a function of the time the muons spend in the target before decay, a clock is started by the μ_{stop} signal and stopped by the 'good' decay event signal. Allowance is also made for second muon events, such as a stopped muon which follows a previously stopped muon within the time interval of the data gate, and such events are removed from the detected muon signal. However the rate *versus* time histogram generated in such experiments, will still contain a time independent background, brought about by accidental start-stop events, such as background radiation simulating μ_{stop} and positron/electron signals.

The limits to experimental work performed at the LMU facility are two fold. In order to determine a frequency of precession to any great precision there should be at least one complete oscillation within the data gate. In practice, for a 10μs data gate, the lowest accessible frequency is 100kHz equivalent to a field of around 7G. The highest accessible frequencies are dependent upon the intrinsic time resolution of the detection electronics, relating to the time taken for light incident upon the scintillators

to pass to the photo-tubes, and the transit time within the photo-tubes to the processing electronics.

2.3.5 Mössbauer Spectroscopy

Mössbauer spectroscopy uses gamma ray emission resulting from radioactive decay to determine the microscopic environment around a given magnetic ion [6]. If the simple case of a gaseous atom/molecule emitting a quanta of energy E_v is considered, then the emission has a momentum associated with it equal to E_v/c. Conservation of momentum thus dictates that the emitter will recoil with momentum P_A such that

$$P_A = Mv_R = -E_v/c \tag{2.21}$$

where M is the mass of the emitter and v_R the recoil velocity.

The recoil energy E_R of the emitter is then given by

$$E_R = Mv_R^2/2 = P_A^2/2M = E_v^2/2Me^2 \tag{2.22}$$

In the case of gamma emission the energy of the emitted rays is high and so the recoil velocity of a normal atom or molecule is significant. The energy of the emitted gamma rays, E_γ, comes only from nuclear decay from an excited to a ground state and must therefore also provide the recoil energy. Thus the relationship

$$E_\gamma = E_t - E_R \tag{2.23}$$

holds, where E_t is the nuclear transition energy. Thermal motion of the emitter leads to Doppler broadening of the emitted radiation.

It is clear that for Mössbauer to be feasible the following conditions must be met.

- The energy of the nuclear transition involved is large enough to give useful gamma radiation of energies in the range 10-150 kV.

- The dominant decay process must be that of excited to ground state with gamma emission.
- The lifetime of the excited state must be sufficiently long to avoid a large uncertainty in the value of the nuclear transition energy, lifetimes in the range 1-100ns are suitable.
- The excited state emitter must have a precursor which is long lived and easy to handle.
- The ground state of the isotope used as source must be stable, either as a high natural abundance isotope or capable of easy enrichment.
- The source should also have a high absorption cross section.

2.3.5.1 Experimental set up

A typical set-up for such experiments is shown schematically below.

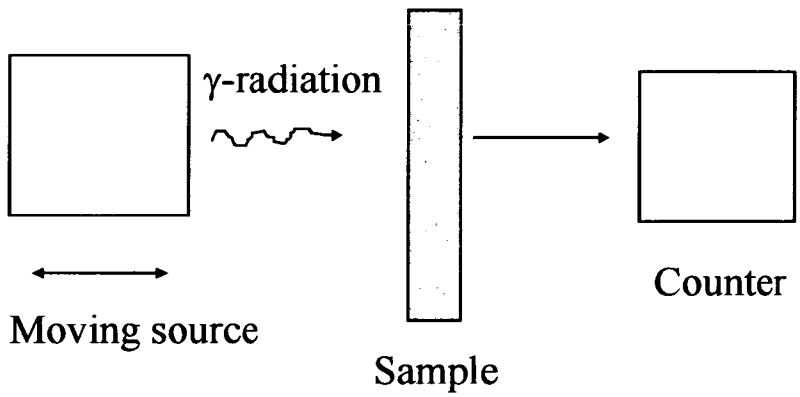

Figure 2.5 Schematic diagram showing the arrangement in a typical Mössbauer experiment

Such a set-up utilises the Doppler effect. The source and absorber are moved relative to each other with a controlled (measured) relative velocity, absorption occurring

when the energy of the modulated photons is equal to E_t for the absorber. What is recorded during an experiment is thus a plot of the intensity of the radiation absorbed as a function of relative velocity.

A significant amount of information regarding the nature of the ground and excited states in a given sample can be extracted from such experiments. Notably there will be a change in the radius of the excited state relative to the ground state (denoted ΔR), which is related to the radius of the ground state R, by the expression

$$\delta = (\varepsilon_0 / 5)(Ze^2R^2)(\Delta R / R)[|\psi_s(abs)|^2 - |\psi_s(source)|^2] \qquad (2.24)$$

where δ is termed the *isomer shift* and is the change in electrostatic energy on decay of the nuclei, Z is the atomic number, e the electronic charge, ε_0 the permittivity of free space and $|\psi_s|$ is the s-electron wavefunctions at nuclei in the source and absorber respectively.

The value of δ is dependent upon the electron density at the nucleus and so is most sensitive to changes in the s-electron orbital occupancy, though changes in p and d orbitals will also influence the s-electron density through screening. It should be noted that the value of $\Delta R/R$ is entirely nucleus dependent and so can take a value which is either positive or negative.

Nuclei with $S > 1/2$ have a quadrupole moment and so their energy is affected by any electric field gradient (efg) at the nucleus. In Mössbauer transitions there is a quadrupole moment associated with either, or both, the upper and lower states of the nucleus under study and hence there is a splitting of the emission/absorption, unless the efg at the nucleus is zero.

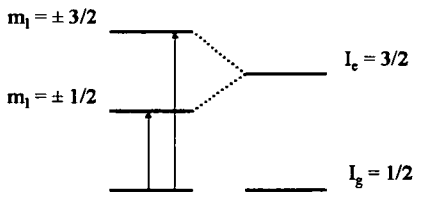

Figure 2.6 Quadrupolar splitting as illustrated for the ^{57}Fe nucleus

The above figure illustrates the quadrupolar splitting which occurs in the case of the ^{57}Fe nucleus. Whilst the ground state (designated *g*) is unaffected since it does not possess a quadrupole moment, the excited state (designated *e*) is split into a doublet. Selection rules are such that $\Delta m_I = 0, \pm 1$. The splitting between the two energy levels is designated the *quadrupole splitting*, and is related, not only to the nuclear quadrupole moment Q, but also the principal value of the efg tensor and a quantity η, a measure of the departure of the efg from axial symmetry.

Any applied field, of strength B, will affect the energy levels E_m of any nucleus with $S > 0$. Such energy levels are given by the expression

$$E_m = -\mu B / I \cdot m_I = -g\mu_N B m_I \qquad (2.25)$$

where $g = \mu/I\mu_N$ and μ_N a nuclear magneton, whilst m_I is the projection along z of the magnetic quantum number of the nucleus with values I, $(I-1)$, $(I-2)$,.....$-(I-1)$, $-I$. Thus the nuclear energy levels are split into $(2I+1)$ levels separated in energy by $\mu B/I$.

2.3.6 Neutron Diffraction

Investigations of the structure of condensed matter are aided by the fundamental properties of neutrons, most notably that their wavelength is comparable to the separation of nuclei in a crystal and that their change in energy due to inelastic processes is frequently of the same order of magnitude as their initial energy. This combined with charge neutrality and a spin magnetic moment of $S = 1/2$ make neutrons powerful probes of both crystallographic and magnetic unit cells [7].

In the case of X-ray diffraction, scattering of incident X-ray radiation occurs from electron density at an atomic site, and so is not particularly sensitive to lighter elements, in the presence of heavier ones. Neutron diffraction however, involves the scattering of neutrons from the nuclei of particular elements, and so is more sensitive to lighter elements since each element, and indeed each isotope, has a different characteristic scattering length, which does not increase steeply with atomic number.

In a neutron scattering experiment what is measured are quantities known as *scattering cross-sections*. An illustration of the idea of such a cross-section is shown below.

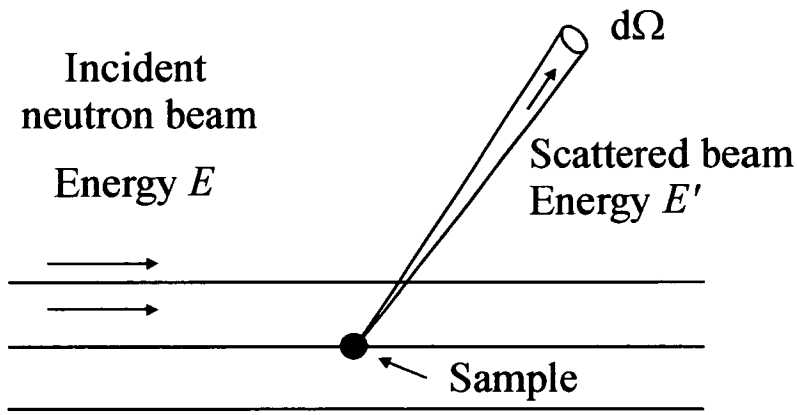

Figure 2.7 A neutron beam is scattered by a small sample into solid angle dΩ

The incoming neutron beam is incident upon the sample, with energy E, and is then scattered into an angle $d\Omega$ with energy E'. If the incident flux is I_0 neutrons(area)$^{-1}$s^{-1} then the number of neutrons per second scattered, σ_s, into such a solid angle $d\Omega$ is given by

$$I_0 d\Omega \int_0^\infty \frac{d^2\sigma_s}{d\Omega E'} dE' = I_0 \frac{d\sigma_s}{d\Omega} d\Omega \tag{2.26}$$

where $\frac{d\sigma_s}{d\Omega}$ = the *partial differential cross section*. If an integration over solid angle is then performed the following result is obtained

$$I_0 \int \frac{d\sigma_s}{d\Omega} d\Omega = I_0 \sigma_s \tag{2.27}$$

The total cross section σ_t is therefore composed of the scattering cross section σ_s and the absorption cross section σ_a (the number of neutrons absorbed by the target per second) as defined by the simple relation

$$\sigma_t = \sigma_a + \sigma_s \tag{2.28}$$

The scattering cross section from a single fixed nucleus is given by $4\pi b^2$ where b is the scattering length, typically of the order of 10fm, this quantity being dependent upon both the chemical nature of the atom and relative orientation of the spins of the nucleus and neutron respectively. The value of b can be real or complex depending upon the nucleus in question. In the case of those nuclei where b is complex, scattering is a resonance phenomenon associated with the formation of a compound nucleus consisting of the original nucleus and neutron, which is close in energy to an excited state. Such nuclei (e.g. ^{157}Gd, ^{113}Cd) strongly absorb neutrons. In the majority of cases however, such a compound nucleus is not formed close to an excited state

and resonance is insignificant with respect to the energy of the incident neutrons. If the spin state I of the nucleus is non-zero, then the neutron-nucleus system will have a spin of $I \pm 1/2$ and there will be two values of the scattering length, whilst in the case where $I = 0$ there will be simply be a single scattering length. The values of such scattering lengths cannot be calculated exactly, and so are determined experimentally. The table below illustrates the large differences in scattering lengths between different isotopes, in this case hydrogen and deuterium.

Nucleus	Combined spin	b/fm
^{1}H	1	10.85
	0	-47.50
^{2}H	3/2	9.53
	1/2	0.98

Table 2.1 Values of scattering lengths for the nuclides hydrogen and deuterium

Hence different isotopes have different scattering lengths, and the scattering length can vary from site to site even for sites entirely occupied by atoms of the same element.

In the case of purely nuclear scattering, summation over all nuclear spin states gives a scattering cross section as

$$\frac{d^2\sigma_s}{d\Omega dE'} = \frac{k'}{k}\left|\left\langle \lambda' \left| \sum_j b_j \exp(i\vec{\kappa}.\vec{R}_j) \right| \lambda \right\rangle\right|^2 \delta(E_\lambda - E_{\lambda'} + E - E') \qquad (2.29)$$

where $\vec{\kappa}$ is the *scattering vector* defined by $\vec{\kappa} = \vec{k} - \vec{k}'$ (the incident and final momenta of the neutron being given by $\hbar\vec{k}$ and $\hbar\vec{k}'$ respectively), $\vec{R}_j$ is the position of atom *j*, b_j the scattering length of the atoms, λ the initial spin state of the scatterer, E_λ and $E_{\lambda'}$ the initial and final energies of the target respectively, and E and E′ the initial and final energies of the neutrons respectively.

The matrix element squared term can be written as

$$\left|<\lambda'|\sum_j b_j \exp(i\kappa.R_j)|\lambda>\right|^2 = \sum_{jl} b_j b_l F_j F_l^* \tag{2.30}$$

(since b_j is independent of the quantum state λ of the scattering system). It is assumed that the value of *b* is real and $F_j = \langle\lambda'|\exp(i\vec{\kappa}.\vec{R}_j)|\lambda\rangle$

Thus if nuclear spins are assumed to have random orientations then the terms b_j and b_l can be replaced with an average value $\bar{b}$, ($\overline{b^2}$ in the special case where $j = l$ and hence $b_j b_l = b_j^2$) and

$$\sum_{jl} b_j b_l F_j F_l^* = \left(\bar{b}\right)^2 \sum_{jl} F_j F_l^* + \left(\overline{b^2} - \left(\bar{b}\right)^2\right) \sum_j F_j F_l \tag{2.31}$$

where the first term on the right hand side represents coherent events and the second incoherent events. These also have associated cross sections and so the scattering cross section (σ_s) can be separated into coherent (σ_c) and incoherent (σ_i) parts as given by

$$\sigma_s = \sigma_c + \sigma_i \tag{2.32}$$

These scattering cross sections can then be used to construct a nuclear correlation function. If a scattering system is composed of N nuclei of scattering length b then the scattering from the set of states $|\lambda\rangle$ to $|\lambda'\rangle$ is described by the expression

$$\frac{d^2\sigma}{d\Omega dE'} = \frac{k}{k'} Nb^2 S(\vec{\kappa},\omega) \tag{2.33}$$

where

$$S(\vec{\kappa},\omega) = N^{-1}\sum_{\lambda} p_\lambda \sum_{\lambda'} \left|\langle\lambda'|\sum_j \exp(i\vec{\kappa}.\vec{R}_j)|\lambda\rangle\right|^2 \delta(E_\lambda - E_{\lambda'} + \hbar\omega) \tag{2.34}$$

$S(\vec{\kappa},\omega)$ is the *scattering function*, p_λ is the probability of the scatterer being in an initial state λ and the energy transfer from neutron to scatterer is given by $\hbar\omega = E - E'$. The time dependence of the scattering function can be written as

$$S(\vec{\kappa},\omega) = (\hbar N)^{-1}\sum_{jl}\int_{-\infty}^{\infty} \exp(i\omega\tau)d\tau \times \left\langle \exp(-i\vec{\kappa}.R_l(0))\exp(i\vec{\kappa}.\vec{R}_j(\tau))\right\rangle \tag{2.35}$$

This expression describes the scattering cross section as the temporal Fourier transform of the correlation function between the position vector of the l^{th} atom at time zero and the j^{th} atom at time τ.

2.3.6.1 Magnetic scattering

Neutrons can also give information as to the magnetic ordering within particular materials since incident neutrons are scattered by the magnetic moments associated with the electronic distribution on each atom. The magnetic spin of an atom is a result of the distribution of electronic moments, and so the actual number of neutrons which will pass through to the detector depends on the quantity

$$\vec{q}\left(\frac{e^2\gamma}{mc^2}\right)Sf$$

where $\vec{q}$ is the magnetic interaction vector, e is the electronic charge, γ the magnetic moment of the neutron, m the mass of the electron, c is the velocity of light, S the spin quantum number and f the atomic form factor. The atomic form factor, f, reflects the fact that as θ becomes non-zero, the net amplitude of scattering falls away, since neutrons will follow different paths depending on which area of the atoms they are scattered from.

In this case it is the interaction of the neutron magnetic moment μ_n with a local magnetic field B which is of interest. If an electron at position $\vec{R}$ has a momentum $\vec{p}$ and a magnetic moment of $\overrightarrow{\mu_e}$, the interaction potential V with the neutron is given by the expression $V = -\overrightarrow{\mu_n}.\vec{B}$ where

$$\vec{B} = \frac{\mu_0}{4\pi}\left[(curl\frac{\overrightarrow{\mu_e}\times\vec{R}}{\left|\vec{R}\right|^3}) - \frac{2\mu_B}{\hbar}\frac{\vec{p}\times\vec{R}}{\left|\vec{R}\right|^3}\right] \tag{2.36}$$

the first term describes the field resulting from the electronic spin and the latter term describes the field due to orbital motion.

The resulting expression for the magnetic scattering cross section is then given by

$$\frac{d^2\sigma_s}{d\Omega dE'} = (\gamma r_0)^2\frac{k'}{k}\left|\langle\sigma'\lambda'|\sigma.\vec{Q}_p|\sigma\lambda\rangle\right|^2\delta(E_\lambda - E_{\lambda'} + E - E') \tag{2.37}$$

where r_0 is defined by the relation $r_0 = \frac{\mu_e}{4\pi}.\frac{e^2}{4\pi m_e}$,

$\vec{Q}_p$ by the relation $\vec{Q}_p = \sum_l |\kappa|^{-2}\exp(i\vec{\kappa}.\vec{r}_l)\left[\vec{\kappa}\times(\vec{s}_l\times\vec{\kappa}) + \frac{i}{\hbar}(\vec{p}_l\times\vec{\kappa})\right]$,

$\vec{\mu}_e$ by the relation $\vec{\mu}_e = -2\mu_B\vec{s}$

and μ_B is the Bohr magneton, $\vec{s}$ the Pauli spin operator for an electron, m_e the mass of an electron, l the number of scattering electrons in the system and $\vec{Q}_p$ the projection of $\vec{Q}$ onto the plane perpendicular to the scattering vector. It should also be noted that $\vec{Q}$ is related to the Fourier transform of the magnetisation density $\vec{M}(r)$ at position r by the relation $2\mu_B\vec{Q} - \vec{M}(\kappa)$ where $\vec{M}(\kappa) = \int\vec{M}(r)\exp(i\vec{\kappa}.\vec{r})dr$. This magnetisation arises from both electronic spin and orbital motion, whilst the component of magnetisation perpendicular to the scattering vector $\vec{\kappa}$ gives the neutron scattering through its Fourier transform.

In the case of spin-only scattering of unpolarised neutrons, the cross section for scattering from initial state $|\lambda\rangle$ to final state $|\lambda'\rangle$ is given by

$$\frac{d^2\sigma_s}{d\Omega dE'} = (\gamma r_0^2)\frac{k'}{k}\sum_{\alpha\beta}(\delta_{\alpha\beta} - \hat{\kappa}_\alpha\hat{\kappa}_\beta)\langle\lambda|\vec{Q}_\alpha^{\perp}|\lambda'\rangle\times\langle\lambda'|\vec{Q}_B|\lambda\rangle\delta(E_\lambda - E_{\lambda'} + E - E') \qquad (2.38)$$

where $\hat{\kappa}_\alpha$ is the direction cosine of $\vec{\kappa}$ along the α axis.

Assuming that the magnetic density has distinct parts corresponding to each atomic site j at position R_j then the magnetisation can be written as

$$\vec{M}(R) = \sum_j M(R_i + r_j) \qquad (2.39)$$

where r_j is the vector within the atomic position centred upon R_j. This can then be combined with equation (2.34) to relate the scattering directly to the magnetisation density as given by

$$2\mu_B\vec{Q} = \int\sum_j \vec{M}(\vec{R}_j + \vec{r}_j)\exp(i\vec{\kappa}.\vec{R}_j)\exp(i\vec{\kappa}.\vec{r}_j)d\vec{r} \qquad (2.40)$$

Thus each volume element $d\vec{r}$, where M(r) ≠ 0, has vector $\vec{r}_j$, and hence an integration over all atomic sites can be performed. A simple case is where the magnetisation vector is in the same direction throughout the atomic site, a likely occurrence if the atom has no orbital angular momentum, in which case the spin only magnetisation is

$$\vec{M}_j = 2\mu_B\vec{S}_j = \int\vec{M}(\vec{R}_j + \vec{r}_j)d\vec{r}_j \qquad (2.41)$$

where $\vec{M}_j$ is the net magnetic moment and $\vec{S}_j$ the spin at site *j* centred at R_j

This in turn leads to an expression for the Fourier transform $f_i(\kappa)$ of the atomic magnetisation density

$$f_i(\kappa) = \frac{\int\vec{M}(\vec{R}_j + \vec{r}_j)\exp(i\vec{\kappa}.\vec{r}_j)d\vec{r}_j}{\int\vec{M}(\vec{R}_j + \vec{r}_j)d\vec{r}_j} \qquad (2.42)$$

This is analogous to the atomic form factor used in describing X-ray scattering, and is termed the *magnetic form factor*.

Thus the magnetic cross section is small for large scattering vectors and the spin only magnetisation is given by

$$\vec{Q} = \sum_j \vec{S}_j f_j(\vec{\kappa})\exp(i\vec{k}.\vec{R}_j) \qquad (2.43)$$

and the cross section for spin only scattering by

$$\frac{d^2\sigma_s}{d\Omega dE'} = (\gamma r_0)^2\frac{k'}{k}\sum_{\alpha\beta}[(\delta_{\alpha\beta} - \hat{\kappa}_\alpha\hat{\kappa}_\beta)\sum_{jl}\exp(ik.(R_j - R_l)) \times \langle\lambda|S_{l\alpha}f_l(\vec{\kappa})|\lambda'\rangle\langle\lambda'|S_{j\beta}f_j(\vec{\kappa})|\lambda\rangle]$$
$$\times\delta(E_\lambda - E_{\lambda'} + E - E') \qquad (2.44)$$

Since $S_{l\alpha}$ is observable then there must be a Hermitian operator with $S^\dagger_{l\alpha} = S_{l\alpha}$

As with nuclear scattering it is possible to define a magnetic scattering correlation function. If an assembly of N identical atoms with form factor $f(\vec{\kappa})$ is considered then

$$\frac{d^2\sigma}{d\Omega dE'} = \frac{k}{k'}\frac{N}{\hbar}(\gamma r_0)^2 \left|f(\vec{\kappa})\right|^2 \sum_{\alpha\beta}(\delta_{\alpha\beta} - \hat{\kappa}_\alpha \hat{\kappa}_\beta) S^{\alpha\beta}(\vec{\kappa},\omega) \tag{2.45}$$

where

$$S^{\alpha\beta}(\vec{\kappa},\omega) = (2\pi N)^{-1} \sum_{jl} \exp(i\vec{\kappa}.(\vec{R}_j - \vec{R}_l)) \times \langle \lambda | S_{l\alpha} | \lambda' \rangle \langle \lambda' | S_{j\beta} | \lambda \rangle \delta(E_\lambda - E_{\lambda'} + \hbar\omega)$$

If the atomic positions are assumed to be fixed, $S^{\alpha\beta}(\vec{\kappa},\omega)$ may be expressed in terms of the time dependent spin correlation $\langle S_{l\alpha}(0) S_{j\beta}(\tau) \rangle$ as

$$S^{\alpha\beta}(\vec{\kappa},\omega) = (2\pi N)^{-1} \sum_{jl} \exp(i\vec{\kappa}.(\vec{R}_j - \vec{R}_l)) \times \int_{-\infty}^{\infty} \exp(i\omega\tau) \langle S_{l\alpha}(0) S_{j\beta}(\tau) \rangle d\tau \tag{2.46}$$

This can be expressed using the function $\hat{C}^{\alpha\beta}$ with all atoms equivalent, atom j having position vector $\vec{O}$ and atom l position vector $\vec{R}$, thus

$$S^{\alpha\beta}(\vec{\kappa},\omega) = \hat{C}^{\alpha\beta}(\vec{\kappa},t,\omega) = (2\pi)^{-1} \sum_{\vec{R}} \exp(i\vec{\kappa}.\vec{R}) \int_{-\infty}^{\infty} \exp(i\omega\tau) \langle S_{\vec{O}\alpha}(0) S_{\vec{R}\beta}(\tau) \rangle d\tau \tag{2.47}$$

Neutron scattering can thus provide an experimental probe of dynamic scaling as discussed in a later section.

2.3.6.2 Elastic scattering

In the case of the magnetic scattering function then in the paramagnetic state all spin correlations will tend to zero at long times *i.e.*

$$\lim_{\tau \to \infty} \langle S_{\vec{O}\alpha}(0) S_{\vec{R}\beta}(\tau) \rangle = 0 \tag{2.48}$$

However in the ordered magnetic state the opposite is true, and spin correlations will remain finite at long times *i.e.*

$$\lim_{\tau\to\infty}\left\langle S_{\vec{0}\alpha}(0)S_{\vec{R}\beta}(\tau)\right\rangle \neq 0 \tag{2.49}$$

If the correlation function is then split into a term corresponding to $\tau = \infty$ and a remainder, then

$$\left\langle S_{\vec{0}\alpha}(0)S_{\vec{R}\beta}(\tau)\right\rangle = \left\langle S_{\vec{0}\alpha}(0)S_{\vec{R}\beta}(\infty)\right\rangle + \left\langle S_{\vec{0}\alpha}(0)S'_{\vec{R}\beta}(\tau)\right\rangle \tag{2.50}$$

where the prime indicates the difference function $S_{\vec{R}\beta}(\tau) - S_{\vec{R}\beta}(\infty)$. The equation can then be expressed as

$$\int_{-\infty}^{\infty}\exp(i\omega\tau)\left\langle S_{\vec{0}\alpha}(0)S_{\vec{R}\beta}(\infty)\right\rangle d\tau = 2\pi\delta(\omega)\left\langle S_{\vec{0}\alpha}(0)S_{\vec{R}\beta}(\infty)\right\rangle \tag{2.51}$$

Within this scattering is the zero energy transfer scattering termed *elastic scattering*, which can be expressed as

$$S_{el}^{\alpha\beta}(\vec{\kappa},\omega) = \delta(\omega)\sum_{\vec{R}}\exp(i\vec{\kappa}.\vec{R})\left\langle S_{\vec{0}\alpha}(0)S_{\vec{R}\beta}(\infty)\right\rangle \tag{2.52}$$

Since such magnetic ordering is effectively infinite in spatial extent then, in a crystalline lattice, the sum over $\vec{R}$ will give delta functions at magnetic reciprocal lattice points, this being termed *Bragg scattering*. It is important to note that in the static approximation the differential scattering gives the spin correlations at $\tau = 0$ whilst elastic scattering gives spin correlations over infinite times. Such differential scattering gives both delta function Bragg scattering from long range order at magnetic reciprocal lattice points and diffuse scattering from short range order, whilst elastic scattering is simply the Bragg scattering part of the differential scattering.

2.3.6.3 Measurement of static correlation functions

If an integration over all ω of the magnetic correlation function is performed, with the scattering vector κ fixed, then the only variable is the δ function and

$$\int_{-\infty}^{\infty}\delta(E_\lambda - E_{\lambda'} + \hbar\omega)d\omega = \hbar^{-1} \tag{2.53}$$

Thus

$$\int_{-\infty}^{\infty}S^{\alpha\beta}(\kappa,\omega)d\omega = N^{-1}\sum_{jl}\exp(i\kappa.(R_j - R_l))\langle S_{l\alpha}S_{j\beta}\rangle = \sum_{R}\exp(i\kappa.R)\langle S_{0\alpha}S_{R\beta}\rangle \tag{2.54}$$

Excepting the cases where κ is a reciprocal lattice point, the latter function then gives the static correlation function $C^{\alpha\beta}(\kappa,t,h)$ as

$$C^{\alpha\beta}(\kappa,t,h) = \int_{-\infty}^{\infty}S^{\alpha\beta}(\kappa,\omega)d\omega \tag{2.55}$$

Hence there are two methods to measure the static correlation function, either by derivation of the function by integration over ω of the measured magnetic scattering function, or secondly by measuring *all* neutrons scattered into solid angle $d\omega$ without regard to energy. What is then observed can be written as

$$\frac{d\sigma}{d\Omega} = \frac{N(\gamma r_0)^2}{k\hbar}\int_0^{\infty}dE'k'\left|f(\kappa)^2\right|\sum_{\alpha\beta}(\delta_{\alpha\beta} - \hat{\kappa}_\alpha\hat{\kappa}_\beta)S^{\alpha\beta}(\kappa,\omega) \tag{2.56}$$

The integral involves the variables k', κ, ω which vary with E' as given by

$$E' = \frac{\hbar^2(k')^2}{2m} \qquad E' = E - \hbar\omega \qquad \kappa = k - k' \tag{2.57}$$

with the direction of k' fixed.

In general this is impossible to evaluate exactly, though if the weight of $S^{\alpha\beta}(\kappa,\omega)$ is at low frequency such that $\hbar\omega << E$ then an approximation is achieved by keeping k' and κ constant; thus $|k'| = |k|$ and

$$\frac{d\sigma}{d\Omega} = \frac{N}{\hbar}(\gamma r_0)^2 |f(\kappa)|^2 \sum_{\alpha\beta}(\delta_{\alpha\beta} - \hat{\kappa}_\alpha \hat{\kappa}_\beta)\hat{C}^{\alpha\beta}(\kappa,t,h) \qquad (2.58)$$

which enables the spin correlation function $\hat{C}$ to be measured in the static approximation.

The latter method is advantageous since it is easier to measure the differential cross section. However the disadvantage is in being unable to determine how good the approximation truly is.

2.3.6.4 Nuclear elastic scattering

In section 2.3.6.2 it was shown how the magnetic scattering of neutrons from an ordered state included an elastic scattering term arising from correlations which were infinite over time and distance. However in the paramagnetic state such correlations are zero, and there is no elastic scattering term in the cross section. An analogous situation occurs in the case of nuclear scattering, crystalline order giving rise to atomic position correlations over infinite times and distances. As was noted previously *Bragg scattering* is the term used to describe scattering from correlations over both infinite times and distances. It involves a partial differential cross section containing the term

$$\delta(\omega) = \sum_{\vec{g}} \delta(\vec{\kappa} - \vec{g}) \qquad (2.59)$$

Thus scattering is zero unless both $\omega = 0$ and $\vec{\kappa} = \vec{g}$, where ω is defined as per equation (2.53). Since $\omega = 0$ equation (2.53) shows that

$$E = E' \text{ and hence } |\vec{k}| = |\vec{k}'|$$

and for the occurrence of Bragg scattering $\vec{k}$, $\vec{k}'$ and $\vec{g}$ must form a triangle in reciprocal space as shown in figure 2.8 below.

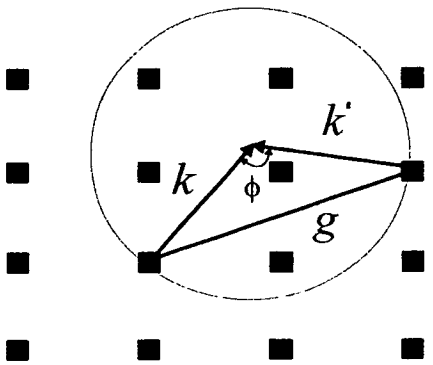

Figure 2.8 The geometry of Bragg scattering. Bragg scattering will occur for a fixed incident wavevector $\vec{k}$ only when a reciprocal lattice point lies on the circle as shown

As can be seen from this diagram, if ϕ is the angle through which the neutron is scattered, then

$$g = 2k\sin(\phi/2) \tag{2.60}$$

which is Bragg's Law. In real space the neutron wavelength, λ, and the spacing of planes in the crystal, d, are related to k and g by the equations $k = \frac{2\pi}{\lambda}$ and $g = \frac{2\pi}{d}$ whilst the *Bragg angle* is defined as $\theta = \phi/2$ hence equation (2.60) becomes

$$\lambda = 2d\sin\theta \tag{2.61}$$

which is the more recognisable form of Bragg's Law.

Whilst Bragg's Law determines the condition for scattering, the scattering *intensity* is governed by the nature of the differential cross section. In the case of magnetic elastic scattering for spin only magnetism this quantity is defined as

$$\frac{d\sigma}{d\Omega} = (\gamma r_0)^2 \frac{N(2\pi)^3}{\upsilon_0} \sum_{\vec{g}} \delta(\vec{\kappa} - \vec{g}) \times \sum_{\alpha\beta} (1 - \hat{\vec{\kappa}}_\alpha \hat{\vec{\kappa}}_\beta) F_\alpha^*(\vec{\kappa}) F_\beta(\vec{\kappa}) \qquad (2.62)$$

where $F_\alpha(\vec{\kappa})$ is termed the *magnetic structure factor* as given by

$$F_\alpha(\vec{\kappa}) = \sum_j S_{j\alpha} f_j(\vec{\kappa}) \exp(i\vec{\kappa}.\vec{r}_j) \exp(-W_j) \qquad (2.63)$$

All quantities have been defined previously excepting the term exp(-W_j) which is the Debye-Waller factor, a term which allows for the fact that any given atom will vibrate about its lattice site. The sum over j is performed over all magnetic atoms within the magnetic unit cell.

Similarly in the case of *nuclear* Bragg scattering

$$\frac{d\sigma}{d\Omega} = \frac{N(2\pi)^3}{\upsilon_0} \sum_{\vec{g}} \delta(\vec{\kappa} - \vec{g}) \left| F(\vec{\kappa}) \right|^2 \qquad (2.64)$$

where $F(\vec{\kappa})$ is termed the nuclear structure factor as given by the equation

$$F(\vec{\kappa}) = \sum_j \overline{b}_j \exp(i\vec{\kappa}.\vec{r}_j) \exp(-W_j) \qquad (2.65)$$

where in this case the sum over j is taken over all the atoms (at positions $\vec{r}_j$)within the unit cell.

Measurement of such structure factors allows the determination of both nuclear and magnetic structures.

2.3.6.5 Inelastic neutron scattering

The work presented in the previous section considered the case of elastic scattering and hence did not concern itself with the energy of the incident or exiting neutrons. Inelastic scattering is important in determining the nature of elementary excitations, both phonons (lattice vibrations) and magnons (magnetic excitations also known as spin waves). In the case of such scattering it is the energy imparted to, or received from, the atoms in the crystal which is of interest, in determining the dispersion relation of the phonons or magnons. The energy distribution of coherently scattered neutrons in a given direction, with either emission or absorption of a quantum of atomic/magnetic excitation contains maxima corresponding to simultaneous satisfaction of the quantum conditions of momentum and energy transfer. Analysis of the energy of the scattered neutrons therefore allows determination of such maxima.

The initial and final neutron energies, respectively E_1 and E_2, are linked through the equation

$$E_1 - E_2 = \pm\varepsilon_k \tag{2.66}$$

where ε_k is the energy of the crystal excitation. In terms of momentum

$$\vec{p}_1 - \vec{p}_2 + \vec{G} = \pm\vec{k} \tag{2.67}$$

where p_1 and p_2 are the initial and final neutron momenta, $\vec{G}$ is the reciprocal lattice vector representing Bragg scattering as outlined in section 2.3.6.4 and k the wave vector of crystal excitation. Combination of equations (2.66) and (2.67) gives

$$\frac{\hbar}{2m}(p_1^2 - p_2^2) = \pm\varepsilon_k \tag{2.68}$$

In a typical experiment with a given reciprocal lattice point as origin it is possible to trace out variations in the crystal momentum in chosen directions in reciprocal space.

At any given scattering angle the spectrometer is set so as to receive scattered neutrons in a given direction, and analysis of the energies of such neutrons determines the neutron energy at which the above equations are satisfied.

Such work is performed on a triple axis spectrometer as depicted in the schematic diagram below.

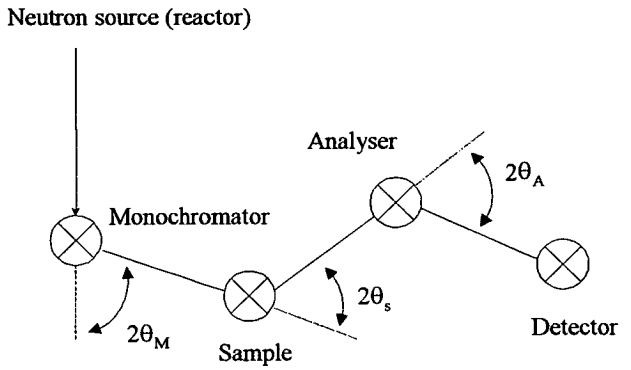

Figure 2.9 Schematic diagram of a triple axis spectrometer. Incoming neutrons from the reactor are scattered through an angle $2\theta_M$ by the monochromator (axis 1) and are then incident upon the sample (axis 2). Neutrons emerging from the sample having been scattered through an angle $2\theta_S$ then pass through an analyser crystal (axis 3) where they are scattered by an angle $2\theta_A$ before finally being analysed by a detector.

It is therefore possible not only to determine the wavelength of the incident neutrons (by adjustment of the position of the monochromator) but also the emergent neutron wavelength and direction (by positioning of the sample) and the energy of the scattered neutrons by positioning of the analyser crystal.

There are two modes of operation which are generally termed '*constant-q*' or '*constant-E*' scanning modes. In 'constant-q' mode the initial and final neutron momenta are fixed (and hence the wave vector ***q***) and the energy varied in order to look for the maximum count at the optimum neutron energy, whilst in 'constant-E' mode the energy of the exiting neutrons is fixed and the wavevector varied.

2.3.6.6 Spin wave dispersion

If the simple case of a collinear ferromagnet is considered, then all the moments are aligned, and will precess in phase about the axis of the internal field. An excitation can consist of the reversal of one spin as illustrated below

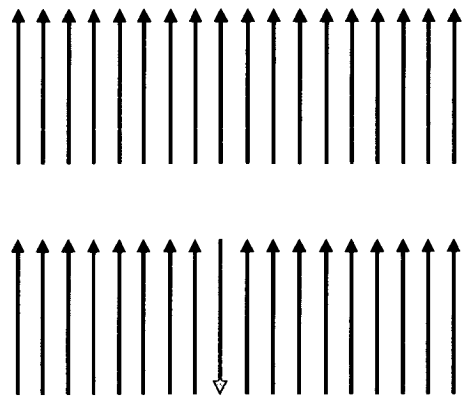

Figure 2.10 Illustration of an excitation in a collinear ferromagnet by reversal of spin direction (blue spin)

However since all the spins are linked to their nearest neighbours by an exchange energy there is an energy penalty in performing such a reversal. To reduce the energy of such an excitation the reversal is shared throughout the spin array as a canting of spins as illustrated below

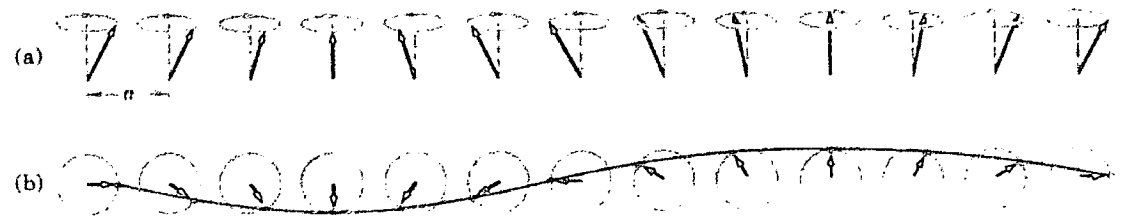

Figure 2.11 Illustration of the creation of a spinwave in a collinear ferromagnet showing the spins (a) in perspective and (b) in plane view displaying one wavelength

Thus the excitation is propagated throughout the lattice as a *spin wave*, the moments having a constant difference in the phase of their precession, ka, where a is the lattice constant, $2\pi/k$ is the wavelength and k is the wave quantum number. Such spin waves are analogous to phonons, and propagate by means of sinusoidal variation in the x or y components of the moments. Classically, a series of N spins of magnitude S with nearest neighbour spins coupled by the Heisenberg interaction can be described by

$$H = -2J\sum_{p=1}^{N}\vec{S}_p.\vec{S}_{p+1} \qquad (2.69)$$

where J is the exchange integral and $\hbar\vec{S}_p$ the angular momentum of the spin at site p. The exchange energy of the ground state is then given by

$$U_0 = -2NJS^2 \qquad (2.70)$$

and the energy of the first excited state, corresponding to reversal of one spin as shown above, by

$$U_1 = U_0 + 8JS^2 \qquad (2.71)$$

However if the spins are allowed to share the reversal, as in figure 2.11 then the energy of the excitation is lowered. The magnetic moment at site p can be written as

$\vec{\mu}_p = -g\mu_B \vec{S}_p$ and the exchange energy is given by

$$-\vec{\mu}_p.[(-2J/g\mu_B)(\vec{S}_{p-1} + \vec{S}_{p+1})] \tag{2.72}$$

The rate of change of angular momentum $\hbar\vec{S}_p$ is equal to the torque which acts on the spin, i.e. $\hbar\frac{d\vec{S}_p}{dt} = \vec{\mu}_p \times \vec{B}_p$ which in terms of cartesian co-ordinates can be written as

$$\frac{dS_p^x}{dt} = (2J/\hbar)[S_p^y(S_{p-1}^z + S_{p+1}^z) - S_p^z(S_{p-1}^y + S_{p+1}^y)] \tag{2.73}$$

and in a similar fashion for $\frac{dS_p^y}{dt}$ and $\frac{dS_p^z}{dt}$. Assuming that $S_p^x, S_p^y << S$ and taking $S_p^z = S$ gives the set of equations

$$\frac{dS_p^x}{dt} = (2JS/\hbar)(2S_p^y - S_{p-1}^y - S_{p+1}^y) \tag{2.74a}$$

$$\frac{dS_p^y}{dt} = (2JS/\hbar)(2S_p^x - S_{p-1}^x - S_{p+1}^x) \tag{2.74b}$$

$$\frac{dS_p^z}{dt} = 0 \tag{2.74c}$$

The desired solutions of these equations are of the form

$$S_p^x = u\exp[i(pka - \omega t)] \quad ; \quad S_p^y = v\exp[i(pka - \omega t)] \tag{2.75}$$

where u and v are constants, p an integer and a the lattice constant. Solution of 2.75 for the case $v = -iu$, which describes circular precession of each spin about the z axis, gives the final result

$$\hbar\omega = 4JS(1 - \cos ka) \tag{2.76}$$

It can be shown [8] that in the case of a ferromagnet the energy of such spin waves, E, in the limit ka << 1, is related to the wave number k by the relation

$$E = \hbar\omega = Dk^2 \tag{2.77}$$

where D is termed the stiffness constant.

A similar derivation can be performed in the case of an antiferromagnet, though in this case two sublattices A and B are defined such that spins with even indices $2p$ lie on sublattice A with spin up ($S_z = S$), and spins with odd indices $2p+1$ lie on sublattice B with spin down ($S_z = -S$). In this case the form of 2.74 for A becomes

$$\frac{dS^x_{2p}}{dt} = (2JS/\hbar)(-2S^y_{2p} - S^y_{2p-1} - S^y_{2p+1}) \tag{2.78a}$$

$$\frac{dS^y_{2p}}{dt} = (2JS/\hbar)(-2S^x_{2p} - S^x_{2p-1} - S^x_{2p+1}) \tag{2.78b}$$

and for the B sublattice

$$\frac{dS^x_{2p+1}}{dt} = (2JS/\hbar)(2S^y_{2p+1} + S^y_{2p} + S^y_{2p+2}) \tag{2.78c}$$

$$\frac{dS^y_{2p+1}}{dt} = -(2JS/\hbar)(2S^x_{2p+1} + S^x_{2p} + S^x_{2p+2}) \tag{2.78d}$$

Forming $S^+ = S_x + iS_y$ then requires solutions of the form

$$S^+_{2p} = u\exp[(ipka - i\omega t)] \quad ; \quad S^+_{2p+1} = v\exp[(ipka - i\omega t)] \tag{2.79}$$

which leads to the result that

$$\omega^2 = \omega^2_{ex}(1 - \cos^2 ka) \tag{2.80}$$

and hence

$$\omega = \omega_{ex}|\sin ka| \tag{2.81}$$

Thus in this case, in the limit ka<<1 the dispersion relation is linear in k

$$E = \hbar\omega = Dk \tag{2.82}$$

Hence a plot of energy *versus* wavenumber can reveal something of the nature of the excitations in a particular system, and allows the strength of the exchange to be determined.

2.3.6.7 Polarised neutrons

As has been illustrated in the preceding sections, the scattering of neutrons from magnetic materials depends upon the relative orientation of the moments of the neutrons and scatterer. The case above considers an unpolarised incident neutron beam, and such experiments have been shown to be capable of providing a large amount of information regarding the nature of magnetic order in systems of study. However it is also possible to perform experiments probing the nature of the orientation of moments within a sample, by use of a polarised incident neutron beam. The use of polarised neutrons relies upon the fact that the spin axis of incident neutrons can be defined by application of a magnetic field such that two components of scattering, parallel (spin up) and anti-parallel (spin down) to the direction of the applied field are defined. If an experimental set-up is then achieved such that the nuclear and spin-up components of one particular Bragg peak of a chosen scatterer cancel each other out, then what is left is a uniquely polarised single spin state beam. This is often achieved through the use of the (111) reflection from a single crystal of the Heusler alloy Cu_2MnAl. Another method used to maintain a single spin state beam is the use of supermirrors. Reflection of neutrons at the surface of a solid magnetised mirror ensures only neutrons of one spin state are transmitted. One other item also used in polarised spectrometers are ^3He spin filters. Such filters act so as to be opaque

to one spin state and transparent to another thus allowing creation of a single spin state beam with no loss of intensity of the outgoing beam. A combination of supermirrors and ^{3}He spin filters are used in combination to great effect on the D7 diffuse scattering spectrometer at the Institut Laue-Langevin (ILL) as will be shown in Chapter 5.

Consideration of the spin state of the scattered neutrons requires the introduction of spin state cross-sections so as to be able to distinguish between the 'spin up' and 'spin down' states. The four possible spin state cross sections are $u \rightarrow u$ $v \rightarrow v$ $u \rightarrow v$ $v \rightarrow u$, where u denotes the spin 'up' state and v the spin 'down' state. The former two processes involve no change in spin state and so are termed *non spin flip* processes, whilst the later two involve a change in spin state and so are termed *spin flip* processes. The scattering cross section as given in equation 2.29 must then be modified so as to read

$$\left(\frac{d^2\sigma}{d\Omega dE'}\right) = \frac{k'}{k}\left|\sum_j \langle \sigma'\lambda'|\hat{b}_j \exp(i\vec{\kappa}.\vec{R}_j)|\sigma\lambda\rangle\right|^2 \delta(E_\lambda - E_{\lambda'} + \hbar\omega) \qquad (2.83)$$

where σ and σ' are the initial and final spin states of the neutron, being either u or v, and the operator $\hat{b}_j$ satisfies the conditions that

$$\hat{b}|+\rangle = b^+|+\rangle \qquad \text{and} \qquad \hat{b}|-\rangle = b^-|-\rangle \qquad (2.84)$$

Equation 2.31 shows that coherent nuclear scattering is proportional to $\overline{b}^2$, whilst incoherent scattering is proportional to $\overline{b^2} - (\overline{b})^2$. From this it can be shown [9] that in the case of coherent scattering there is no change in neutron spin state during the scattering process, whilst in the case of incoherent scattering there are both non spin flip and spin flip processes.

In the case of magnetic scattering the scattering cross section is defined by equation (2.37) and the cross section for non spin flip processes, i.e. $u \rightarrow u$ and $v \rightarrow v$, can then be described using the equation

$$\left(\frac{d^2\sigma}{d\Omega dE'}\right) = (\gamma r_0)^2 \frac{k'}{k} \left|\langle \lambda' | Q_{\perp z} | \lambda \rangle\right|^2 \delta(E_\lambda - E_{\lambda'} + \hbar\omega) \qquad (2.85)$$

Which in turn allows determination of the non spin flip (nsf) scattering cross section as given by

$$\left(\frac{d\sigma}{d\Omega}\right)_{nsf} = \frac{1}{3}(\gamma r_0)^2 N\{\frac{1}{2} gF(\vec{\kappa})\}^2 \exp(-2W) S(S+1)(1-\hat{\kappa}_z^2) \qquad (2.86)$$

Similarly, in the case of spin flip scattering the scattering cross section is described by

$$\left(\frac{d\sigma}{d\Omega}\right)_{sf} = \frac{1}{3}(\gamma r_0)^2 N\{\frac{1}{2} gF(\vec{\kappa})\}^2 \exp(-2W) S(S+1)(1+\hat{\kappa}_z^2) \qquad (2.87)$$

In both cases the z axis is defined as the direction of $\vec{P}$, the polarisation of the incident neutrons. In the case of $\vec{P} \,||\, \vec{\kappa}$ then the value of $\hat{\kappa}_z = 1$, and the scattering is entirely spin flip. If $\vec{P} \perp \vec{\kappa}$ then $\hat{\kappa}_z = 0$ and the scattering cross sections for spin flip and non spin flip are equal. Use of these cross sections in polarisation measurements allow the separation of paramagnetic scattering from other sources of diffuse scattering (such as multiple Bragg scattering or incoherent scattering due to isotope disorder), since only paramagnetic and nuclear spin scattering give rise to spin flip processes. They are distinguishable by measurement of the spin-flip scattering cross section with $\vec{P}$ parallel and then perpendicular to $\vec{\kappa}$. Whilst the nuclear spin scattering is unchanged in both settings, the paramagnetic scattering changes according to the equations given above.

To summarise both coherent nuclear scattering and isotope-disorder scattering are non-spin-flip scattering processes. Nuclear spin-disorder scattering parallel to the polarisation direction will also give rise to non-spin-flip scattering, whilst that perpendicular to the polarisation direction will give rise to spin-flip scattering. If the neutron polarisation lies along the scattering vector then all the magnetic scattering is spin-flip scattering.

Summary

This Chapter has outlined the means by which both the chemical composition and magnetic properties of a given sample may be determined. Of great importance are the various probes of magnetic behaviour and a summary of the timescales accessible through these techniques is shown below.

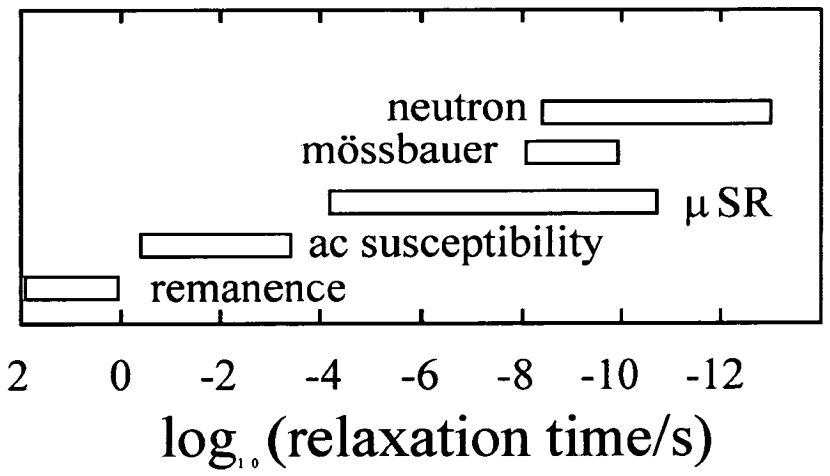

Figure 2.12 Illustration of the accessible timescales available through the use of the various techniques outlined above

An overview of the theory regarding both elastic and inelastic neutron scattering measurements has been given, and this provides a framework from which the experimental work described in subsequent chapters will be described. The next Chapter introduces the nature of critical phenomena and how this applies in the specific case of the kagome lattice antiferromagnet.

References

[1] *ICP-AES Hardware Guide*, Thermo Jarrel-Ash, (1994)

[2] For more details see for example *'An Introduction to Thermogravimetry'*, C.J.Keattch and D.Dollimore (Heyden & Sons Ltd., 1975)

[3] *'The Rietveld Method'*, R.A. Young, (Oxford University Press, 1995)

[4] *'General Structure Analysis System'*, (GSAS), A.C.Larson and R.B. Von Dreele (University of California, 1985)

[5] See for example *'Muon Spin Rotation Spectroscopy, Principles and Applications in Solid State Physics'*, A.Schenck (Adam Hilger Ltd., 1985); *'Muons and pions in materials research'*, ed. J.Chappert and R.I.Grynszpan (Elsevier, 1984); S.F.J.Cox, *J.Phys.C* **20** 3187 (1987)

[6] For more details see for example *'Mössbauer Spectroscopy'*, N.N.Greenwood and T.C.Gibb (Chapman and Hall, 1971)

[7] For more rigorous treatment see for example *'Neutron Diffraction'*, G.E.Bacon (Clarendon Press, 1975); *'Theory of Thermal Neutron Scattering'*, W.Marshall and S.W.Lovesey (Clarendon Press, 1971); *'Magnetic critical scattering'*, M.F.Collins (Oxford University Press, 1989)

[8] F.Keffer, *'Encyclopaedia of Physics'* **18** 1 (1966)

[9] Further details can be found in *'Introduction to the theory of thermal neutron scattering'*, G.L.Squires (Cambridge University Press, 1978)

Chapter 3 Critical Phenomena and the Kagome Lattice Heisenberg Antiferromagnet

3.1 Introduction

Many of the phenomena considered in this thesis involve physical transitions between different states, and it is in light of this that a brief overview of the nature of phase transitions, and in particular critical phase transitions, is given here. More extensive reviews are given elsewhere [1]. If a general system with three phases (gas, liquid and solid) is considered then a typical pressure-temperature phase diagram is shown below.

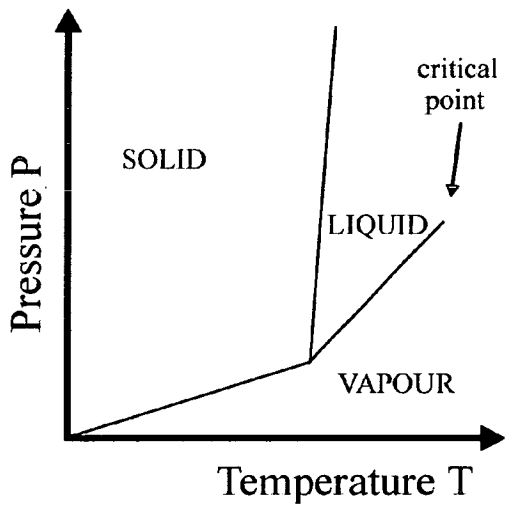

Figure 3.1 Pressure-temperature diagram for a typical gas-liquid-solid system. At the critical point the gas and liquid phases become indistinguishable

The lines mark boundaries between the different phases, with coexistence of two phases *e.g.* liquid and gas possible along such boundary lines. What is of greater interest however is the fact that the phase boundary between liquid and gas dies out at

a point termed the *critical point*, this being the point at which liquid and gas become indistinguishable. Thus it is possible to 'round' the critical point, and so pass from liquid to gas without experiencing any discontinuous change in properties.

To describe this behaviour in terms of the energy of the system it is appropriate to consider the Gibbs Free Energy function $G(P,T)$. On crossing the phase boundary, the free energies of the two phases need not be equivalent, *i.e.* there is no constraint upon the values of $\frac{\partial G}{\partial P}$ and $\frac{\partial G}{\partial T}$, and any differences in these partial derivatives will result in a discontinuity in the first derivative of G, this therefore being termed a *first order transition*. Since by definition

$$C_P = -T\frac{\partial^2 G}{\partial T^2}\bigg|_P \qquad \text{and} \qquad C_P = \frac{\partial H}{\partial T}\bigg|_P \tag{3.1}$$

then H must be discontinuous at the phase transition point and latent heat is involved in the transition.

A *critical phase transition* is considered as any phase transition which passes through a critical point. In such transitions short-lived microregions of one phase in another are found, and as the critical point is approached the size of these regions tends to infinity. This can be illustrated by use of the following example. Consider a macroscopic volume V, split into a number of microscopic cells of volume v, the latter being of the order of the constituent molecules. Each cell also possesses a magnetic moment, which points upward if it is at the centre of a molecule, and downward in all other cases. At temperatures such that $T \gg T_C$ there is rapid and random 'flipping' of magnetic moments from one orientation to the other. As the system is cooled towards T_C 'droplets' of correlated spins appear, which grow in size as the critical temperature

is approached. A point is reached where these correlated regions are of a size which allows the observation of so called *critical scattering*. Such correlations are illustrated below in figure 3.2.

It should be borne in mind that the system does not become fully ordered at T_C in the sense that all the moments are aligned parallel to one another – this may only occur at $T = 0$. Rather, at T_C the net order is zero, and so the cartoon illustrates a small region of the whole system.

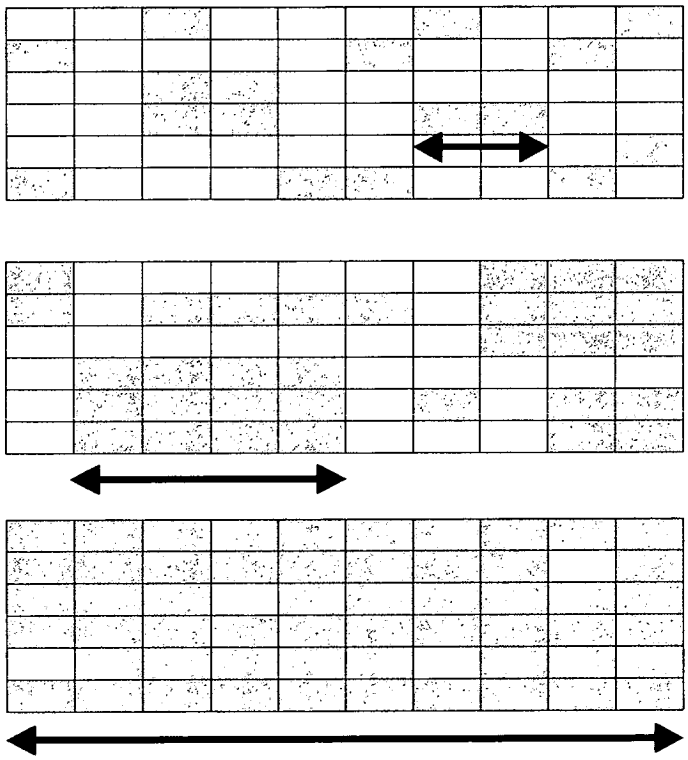

Figure 3.2 Cartoon of system approaching critical point with spins denoted as up (grey) or down (white). At $T>>T_C$ there are few correlations between spins (top diagram). As T approaches T_C from above the correlations between spins grows (middle diagram) before at $T = T_C$ the correlations become large

To summarise, there are three properties common to all critical phase transitions.

- Symmetry is broken at the critical point as represented by an order parameter η which is zero for $T > T_C$ and positive non-zero below this temperature. In the case of ferromagnetism the order parameter follows the degree of magnetisation. Such a critical point also has a dimensionality D (equivalent to the degrees of freedom) which has a large bearing on the properties of phase transitions.
- Close to the critical point there are fluctuating microregions of *both* phases involved. The linear extent of these regions is described using the correlation length ξ which tends to infinity as the critical point is approached.
- The response time of the system tends to infinity as T_C is approached, manifested as a critical slowing down.

3.2 Ginzberg – Landau Theory (Mean field theory)

The most widespread method of treating and describing critical properties is Ginzberg-Landau (G-L) theory. The underlying assumption within this theory is that thermodynamic energy functions can be expanded as a Taylor series near the critical point. This holds for interactions of infinitely long range, and for systems with four or more dimensions. However this will break down as the critical point is reached since in this region all interactions are short range. Nonetheless the theory is useful as a simple treatment of continuous phase transitions.

In considering the phase transition from a ferromagnetic to paramagnetic state, an appropriate order parameter (η) is that of magnetisation(M) and the pertinent energy function is the Helmholtz free energy, $F(T, \eta)$, as given by the expression

$$F(T, \eta) = F_0(T) + \alpha_2(T)\,\eta^2 + \alpha_4(T)\,\eta^4 + \ldots\ldots \qquad (3.2)$$

Then at any given temperature equilibrium is achieved at a point where:

$$\left.\frac{\partial F}{\partial \eta}\right|_T = 0 \qquad \text{and} \qquad \left.\frac{\partial^2 F}{\partial \eta^2}\right|_T > 0 \qquad (3.3)$$

Applying this to the Taylor expansion, and allowing for the change of sign in $\alpha_2(T)$ at the critical temperature, gives the result that, for T > T_C, the free energy has a minimum at $\eta = 0$, whilst below T_C it has minima at $\eta = \pm[\alpha_0(T_C - T)/ 2\alpha_4(T)]^{1/2}$. The calculated magnetic specific heat C_H (*i.e.* at constant field), is then given by

$$C_H = -T\left.\frac{\partial^2 G}{\partial T^2}\right|_H \qquad (3.4)$$

where $G(T,H)$ is the Gibbs Free Energy and $G = F - HM$.

For small applied fields of magnitude H, substitution for M and F yields

$$C_H = -T\frac{d^2 F_0}{dT^2} \qquad (T > T_C) \qquad (3.5a)$$

$$C_H = -T\frac{d^2 F_0}{dT^2} - \frac{\alpha_0^2}{2\alpha_4} \qquad (T < T_C) \qquad (3.5b)$$

Thus, neglecting any temperature dependence in the $\alpha_4(T)$ term, the specific heat will have a downward discontinuity of $\alpha_0^2 / 2\alpha_4$ at T_C (where $\alpha_2(T) = [T-T_C]\,\alpha_0$).

Calculation of the magnetic susceptibility using G-L theory yields

$$\chi_T^{-1} = \left.\frac{\partial^2 F}{\partial M^2}\right|_T = 2\alpha_2(T) + 12\eta^2\alpha_4(T) \qquad (3.6)$$

For T > T_C $\eta = 0$ and $$\chi_T = \frac{1}{2\alpha_0}\frac{1}{(T - T_C)} \qquad (3.7)$$

which is of course the Curie-Weiss Law with the Curie constant C given by $(2\alpha_0)^{-1}$

3.3 Critical Exponents

Whilst G-L theory is able to predict the nature of continuous phase transitions in ferroelectrics and type I superconductors, it fails to accurately predict the nature of transitions in other materials where short-ranged interactions predominate. In an attempt to describe such interactions, and the behaviour of such systems in the vicinity of the critical point, so called '*critical exponents*' are defined, often in conjunction with so called '*reduced variables*'. For example in the region $T \sim T_C$ the temperature dependence of the magnetic susceptibility, χ_T, (in small fields) is given by the expression

$$\chi_T = at^{-\gamma} (T > T_C) \tag{3.8}$$

where the reduced temperature t can be defined as $t = \frac{T - T_C}{T_C}$, and the indices a and γ are termed *critical exponents*. The relationship between such critical exponents can also prove a useful tool in the description of phase transitions. For example, in using magnetic susceptibility as an order parameter, from thermodynamic arguments it can be shown that

$$\chi_T (c_H - c_M) = T\left(\left.\frac{\partial M}{\partial T}\right|_H\right)^2 \tag{3.9}$$

In zero field and just below T_C it is to be expected that

$$\chi_T \sim (-t)^{-\gamma'} \qquad c_H \sim (-t)^{-\alpha'} \qquad \left.\frac{\partial M}{\partial T}\right|_H \sim (-t)^{\beta-1}$$

$$\Rightarrow \qquad A(-t)^{-(\alpha'+\gamma')} \geq B(-t)^{2(\beta-1)} \tag{3.10}$$

where A and B are positive constants. Sufficiently close to T_C then

$$\ln A - (\alpha' + \gamma')\ln(-t) \geq \ln B + 2(\beta - 1)\ln(-t) \tag{3.11}$$

In the limit as the critical temperature is approached from below, ln(-t) $\rightarrow$ -∞. Hence the ln$A$ and ln$B$ terms can be dropped and the expression becomes

$$-(\alpha'+\gamma') \leq 2(\beta-1) \qquad \alpha+2\beta+\gamma' \geq 2 \tag{3.12}$$

The latter expression is known as the *Rushbrooke Inequality*

In the case of G-L theory $\alpha' = 0$ $\beta = 0.5$ and $\gamma' = 1$ hence the inequality becomes an equality.

In the few experimental cases where critical exponents may be calculated with any great accuracy, similar features are observed. This leads to a hypothesis that there are universal parameters governing the nature of such critical phase transitions, *i.e.* for continuous phase transitions the critical exponents are predicted to be the same regardless of either the nature of the microscopic interactions present, or indeed the crystal structure. Whilst this is a very wide generalisation, it does appear to be a useful working hypothesis, the nature of which is outlined in a little more detail below.

3.4 Universality

The *hypothesis of universality* states that for a continuous phase transition the static critical exponents depend only on the following factors.

- The dimensionality of the system d.
- The dimensionality of the order parameter D (simple cases are where it is equal to the number of dimensions in which the order parameter is allowed to vary).
- Whether forces are short or long range.

This thus allows the use of a simple theoretical model for any particular *universality class* (*i.e.* given values of D and d combined with a given ranges of forces). If a

solution to the critical properties of that model can be found then it is applicable to all models within the universality class. Since magnetic models afford a wide range of model systems with which to test theories, it is of benefit to define four standard models in addition to Ginzberg-Landau theory as outlined below.

a) **Ising Model**

The Ising model corresponds to the case where the dimensionality of the order parameter $D = 1$. The exchange Hamiltonian is then given by

$$H = -\sum_{n}\sum_{i}{}' J_i S_n^z S_{n+i}^z \tag{3.13}$$

where S_n^z is the z component of the spin on site at n, J_i the exchange parameter coupling spins on sites at n and $n+i$, and i the nearest neighbour vector. The prime on the second sum indicates that it is restricted such that each pair of interacting spins is only summed once. The order parameter for a ferromagnet, where the value of the exchange parameter J > 0 is given by the summation $\sum_n S_n^z$ and so is one dimensional in nature. This model can be applied to Ising magnets, liquid-glass transitions, ordering in alloys and mixing in liquids.

b) **X-Y Model**

The X-Y model applies to the case of $D = 2$; the exchange Hamiltonian is then given by

$$H = -\sum_{n}\sum_{i}{}' J_i (S_n^x S_{n+i}^x + S_n^y S_{n+i}^y) \tag{3.14}$$

In this case the spins have two components (x and y) and the order parameter is the vector sum of these spins and is therefore two dimensional. Such a model can be applied to 'easy plane' magnets and superfluidity in liquid ^{4}He.

c) **Heisenberg Model**

In this case $D = 3$ and the exchange Hamiltonian is given by

$$H = -\sum_{n}\sum_{i}{}' J_i (S_n^x S_{n+i}^x + S_n^y S_{n+i}^y + S_n^z S_{n+i}^z) \qquad (3.15)$$

Thus individual spins are three dimensional vectors and the model applies to isotropic magnetic materials.

d) **Spherical Model**

In this case $D = \infty$ and assumes that any spin S_n has an infinite number of dimensions. Whilst there are no known experimental systems for which this model is valid, it has the attraction of being solvable exactly.

3.5 Static Correlation Functions

As described in section 3.1 in the region close to the critical transition point there is a build up of blocks of correlated spins, due to the influence of short range interactions. The extent of such correlated regions will increase around the transition point and give rise to critical scattering. To describe such scattering so called 'correlation functions' are used, the spin-spin correlation function describing the probability of finding a spin with the same sign within a unit volume at a distance R, having measured from a spin at $R = 0$ .Since the scattering properties of a material depend upon such correlation functions, it is important to consider how critical scattering can be used to measure the correlation function within the critical region.

If there are spins **S** of dimensionality D lying on a lattice with sites $\boldsymbol{R}$ in d dimensions then the spin correlation function $C(\mathbf{R},t,h)$ is given by

$$C(\mathbf{R},t,h) = \langle \mathbf{S}_0 . \mathbf{S}_\mathbf{R} \rangle - \langle \mathbf{S}_0 \rangle . \langle \mathbf{S}_\mathbf{R} \rangle = \langle (\mathbf{S}_0 - \langle \mathbf{S}_0 \rangle) . (\mathbf{S}_\mathbf{R} - \langle \mathbf{S}_\mathbf{R} \rangle) \rangle \qquad (3.16)$$

where t is the reduced temperature as defined previously, $h = g\mu_B H_e / k_B T$ and H_e is the effective field between cells. It should be noted that the function is averaged over all points of origin **O**.

If there are L lattice sites and a is the lattice parameter then if the size of a correlated block of spins is lLa (where l is simply a length scale factor) this gives

$$C(\tilde{\mathbf{R}},\tilde{t},\tilde{h}) = \left\langle (\tilde{\mathbf{S}}_0 - \left\langle \tilde{\mathbf{S}}_0 \right\rangle).(\tilde{\mathbf{S}}_R - \left\langle \tilde{\mathbf{S}}_R \right\rangle) \right\rangle \tag{3.17}$$

where the tilde, ~, refers to such blocks of spins and $\tilde{\mathbf{R}} = l^{-1}\mathbf{R}$

The exceptional nature of critical behaviour can be evidenced by the fact that the Hamiltonian is assumed to be the same, independent of the size of l, hence for N blocks of size L, and Nl^{-d} blocks of size lL then

$$C(\mathbf{R},t,h) = l^{2(x-d)}C(\tilde{\mathbf{R}},\tilde{t},\tilde{h}) = l^{2(x-d)}C(l^{-1}\mathbf{R},l^y t,l^x h) \tag{3.18}$$

where the reduced field h scales as $\tilde{h} = l^x h$ on increasing the size of the blocks of spins from L to lL.

This can be solved in the general case of zero field to give

$$C(\mathbf{R},t,0) = |\mathbf{R}|^{2(x-d)} f(|\mathbf{R}|/\xi) \tag{3.19}$$

where ξ is the correlation length. At the critical point this can be expressed as

$$C(\mathbf{R},0,0) \approx |\mathbf{R}|^{2-d-\eta} \tag{3.20}$$

where η is the pair correlation function critical exponent. Thus

$$2(x-d) = 2 - d - \eta \quad \text{and} \quad (2-\eta)\nu = \gamma \tag{3.21}$$

where d is the dimensionality, γ the zero field isothermal susceptibility critical exponent and ν the correlation length critical exponent. Further details are given elsewhere [2].

3.6 Critical Dynamics

In the proceeding sections the static properties of any particular system were considered, in terms of the spatial correlations between spins. However it is possible to extend the application of universality to dynamic parameters, since close to any critical point dynamic processes slow down, and at the critical point itself response times tend to infinity. Whilst such divergences follow similar power laws to the static case, the dynamic case is considerably more difficult to describe. A fundamental requirement is to adapt the correlation function derived in section 2.5, so as to include the variable τ for time, and in doing so the time dependence of the correlation function is then given by

$$C(\mathbf{q},t,\tau)=\sum_{\mathbf{R}}\exp^{i\mathbf{q}.\mathbf{R}}\left[\left\langle \mathbf{S}_{\mathbf{O}}(0).\mathbf{S}_{\mathbf{R}}(\tau)\right\rangle-\left\langle \mathbf{S}_{\mathbf{O}}\right\rangle\left\langle \mathbf{S}_{\mathbf{R}}\right\rangle\right] \tag{3.22}$$

This is calculated in the case where $h = 0$ and it is assumed that the average value of $\langle \mathbf{S}_{\mathbf{R}} \rangle$ is time independent, whilst $\mathbf{S}_{\mathbf{R}}(\tau)$ gives the value of $\mathbf{S}$ on site $\mathbf{R}$ at time τ.

The Fourier transform of this with respect to time gives the frequency as a variable and the resultant function is split into both a static and dynamic part as defined by

$$\hat{C}(\mathbf{q},t,\omega)=\underbrace{\hat{C}(\mathbf{q},t)}_{static}\underbrace{F(\mathbf{q},t,\omega)}_{dynamic}d(\omega) \tag{3.23}$$

where $F(q,t,\omega)$ is a spectral weight function normalised such that

$$\int_{-\infty}^{\infty}F(q,t,\omega)d\omega=1 \tag{3.24}$$

It thus expresses the frequency dependence of the correlation with the wavevector q at a given temperature t. The final expression in equation (3.18) is written as

$$d(\omega)=\frac{\omega}{1-\exp(-\hbar\omega\beta)} \tag{3.25}$$

and in the critical region $|\hbar\omega\beta| << 1$, hence d(ω) is a constant, $(\hbar\beta)^{-1}$

Thus in the case of a Heisenberg antiferromagnet at small wavevectors q ($T << T_C$) there are spin wave excitations in the x-y plane with frequency given by

$$\hbar\omega_c(\mathbf{q},t) = c(t)q \qquad \Rightarrow \qquad \hbar q^z f(\mathbf{q}t^{-\upsilon}) = c(t)q \tag{3.26}$$

where ω_c is the characteristic frequency of a block of spins, $c(t)$ is the spinwave stiffness term, z a scaling factor and ν the correlation length critical exponent.

It can then be shown that [2]

$$c(t) \sim t^{(z-1)\nu} \qquad (T < T_C) \tag{3.27}$$

and theory predicts a critical slowing down of spin wave energy such that

$$c(t) \sim t^{\upsilon/2} \text{ and hence } z = 1.5 \tag{3.28}$$

3.7 Dilution of magnetic lattice sites

The focus of much of the preceding three sections has been the desire to describe regions of correlated spins close to the critical point. Such correlated regions are also important in the case of dilution which, in this context, describes the situation where magnetic atoms are replaced by non-magnetic ones in a crystal lattice. As the concentration, p, of magnetic sites is increased so long range order should appear at a *percolation threshold* (p_c) where there is an exchange pathway over the infinite lattice. This will correspond to a *percolation concentration* of magnetic atoms. There will however still be a sharp critical phase transition where $p > p_c$ since close to the critical point T_C, there will be large regions of size ξ, and so if ξ is large enough then the randomness will be averaged out. If the critical exponent of the specific heat $\alpha < 0$ for the undiluted system, then the dilute systems will have the same critical exponents.

Near to the percolation point the lattice consists of long chains of interacting spins with occasional nodes from which three or more chains emanate. The existence of such chains suggests that the thermal properties will be similar to those of a 1D system and so the correlation length is then given by

$$\xi(p-p_c,T)=|p-p_c|^{-\upsilon_P} f(\xi_1,(p-p_c)^{\phi}) \tag{3.29}$$

where ξ_1 is the correlation length of a 1D system at temperature T and ν the correlation length critical exponent.

$$\Rightarrow \qquad \upsilon_p = \phi\upsilon_T \qquad\qquad \gamma_p = \phi\gamma_T \qquad\qquad \eta_p = \eta_T \tag{3.30}$$

For Ising and 1D Heisenberg systems $\phi = 1$ but for 2 and 3D Heisenberg systems it is difficult to determine its value.

At $p < p_c$ the correlation length grows as the critical point is approached and the limit to the size of this is equal to the size of a percolation cluster, or indeed the correlation length of a 1D chain and is given by the expression:

$$[\xi(p-p_c,T)]^{-1} = A(p-p_c)^{\upsilon_P} + B\xi^{-\upsilon_T} \tag{3.31}$$

3.8 Introduction to low dimensional magnetism

In previous sections the nature of the description of phase transitions has been reviewed, and the usefulness of magnetism, in providing experimental probes with which to interrogate the fundamental properties of a given system, has been illustrated. Low dimensional magnetic systems are therefore of great use in verifying such theories, since they allow investigation of how co-operative phenomena are affected both by reduced dimensionality, and indeed the symmetry of the interaction Hamiltonian. A working definition of a low dimensional system is provided by de

Jongh: *'In general a system can be described as of restricted dimensionality d if it is infinite only in one or two spatial directions'* [3]. This definition comprises isolated chains or layers, as well as fibres or thin films of finite thickness, and thus incorporates the kagome lattice as a 2D magnetic system, as will be elaborated upon in due course. Whilst it is of interest to follow the critical behaviour of such a lattice, it is complicated by the fact that the geometry of the lattice prevents spin order being conveyed unambiguously as in the case of a conventional Néel state. This leads to the concept of spin *frustration* which is considered in the next section.

3.9 Magnetism and Frustration

The origin of the term 'frustration' in relation to magnetic systems is not entirely clear, though it is often attributed to Anderson [4]. It can be considered as arising from competition between different terms in any given Hamiltonian, resulting in the system being unable to simultaneously minimise each term in such a Hamiltonian, for a given spin configuration. Such 'competition' can arise from either geometrical constraints related to the symmetry of any given lattice, or from direct competition between nearest neighbour (NN), or indeed next nearest neighbour (NNN) interactions. This concept can be illustrated in two cases as shown in Fig 4.2. In case (a) if two spins are placed on the triangular plaquette with antiferromagnetic nearest neighbour coupling, then it is impossible for a third spin to couple antiferromagnetically to the other spins. A compromise is achieved, with a 120° array as shown in (b), so as to minimise the exchange energy. A further illustration is given in (c) for the case of NN coupled spins on a square plaquette. All the spins can be coupled antiferromagnetically, in the case of the 'loop' of four spins. However if a

random ferromagnetic bond is introduced then one of the spins is required to couple both ferro and antiferromagnetically to its nearest neighbours and is unable to do so, thus leading to spin frustration. This is what happens when the cuprate La_2CuO_4 is diluted with dopants such as Sr [5].

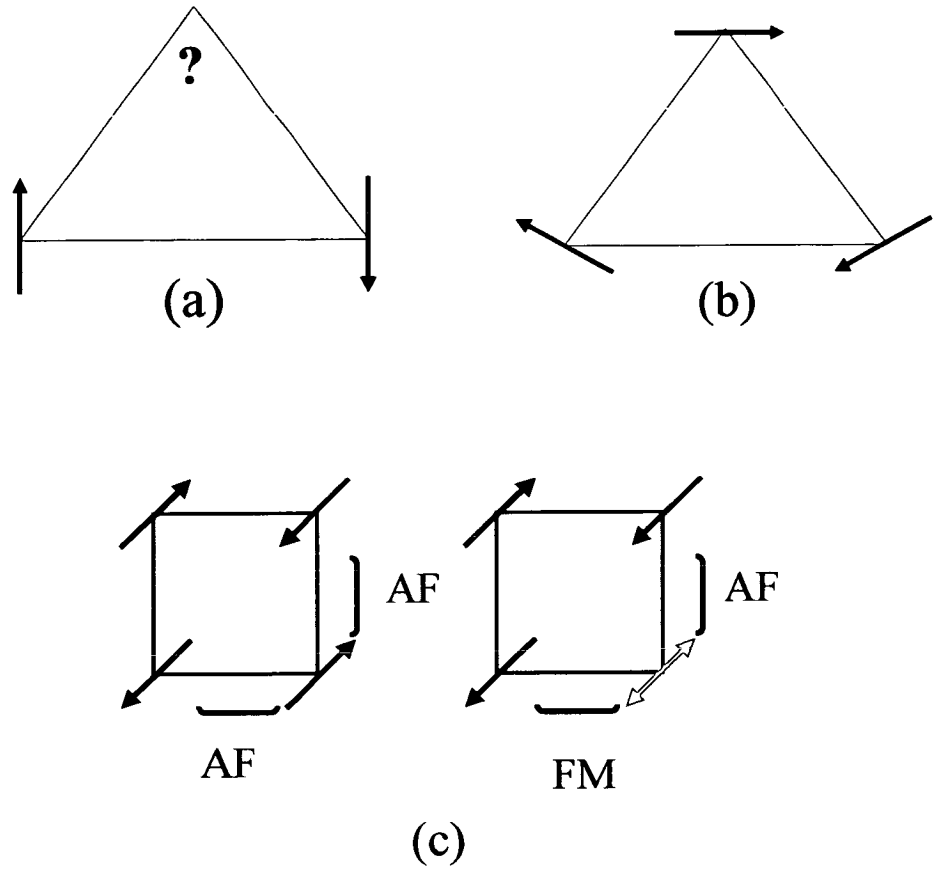

Figure 3.3 (a) Triangular plaquette showing the ambiguity of the third spin in its attempt to couple antiferromagnetically to both of its nearest neighbours; (b) Compensating situation with canted spins; (c) frustration on a square lattice as introduction of a ferromagnetic bond (FM) results in an inability of the fourth spin (green) to couple both ferromagnetically and antiferromagnetically (AF) to its nearest neighbours

Whilst strongly geometrically frustrated systems can be obtained, in principle, through fine tuning antiferromagnetic/ferromagnetic NN interactions, in practice control of such interactions is difficult. A more common approach is to select those systems with NN short ranged antiferromagnetic coupling on lattices composed of triangular plaquettes, which exhibit 'topological' frustration. Since deviation from the Curie-Weiss Law, and hence of $1/\chi_{dc}$ from linearity, occurs at lower temperatures than would be expected for the 'normal' system, determination of the Curie Weiss constant, θ_{CW}, can be carried out accurately and so an empirical measure of frustration can be defined using the ratio

$$f = -\frac{\theta_{CW}}{T_C} \tag{3.32}$$

Since in the case of an unfrustrated 3-D system both quantities, θ_{CW} and T_C, are identical then the condition for frustration must be that the value of $f > 1$[6]. Materials such as MnS and FeO, with face-centred-cubic (fcc) lattices, have a value of $f = 3$ and so are moderately frustrated, whilst materials with $f > 10$ are those which exhibit strong geometric frustration (SGF)[6]. It is important at this point to highlight the difference between those systems which exhibit SGF and those of low dimensionality. For example in 1D, entropy prevents long range order (LRO) regardless of spin dimensionality, whilst in 2D only Ising systems support LRO, and in both cases the critical temperature T_C may be suppressed, being proportional to J', the interaction between chains or planes for 1D and 2D systems respectively. A key difference between low dimensional and SGF systems is the build up of correlations well above the molecular field T_C seen in the former. Furthermore, whilst low

dimensional systems gain entropy by a rarefication of spin density the opposite is true for SGF systems.

Manifestations of such triangular or indeed, more widely speaking, of frustrated lattices, include systems such as the pyrochlore and kagome lattice materials. In the former, tetrahedra of MO_4 fragments are linked together, and frustration arises as spins at the vertices of such tetrahedra interact with each other. In the Kagome lattice triangular plaquettes pack together, with vertex sharing, to produce layers of metal ions which form a 'Star of David' motif. The lattice takes its name from a form of Japanese basket weaving and is illustrated below along with its 3D analogue the pyrochlore lattice.

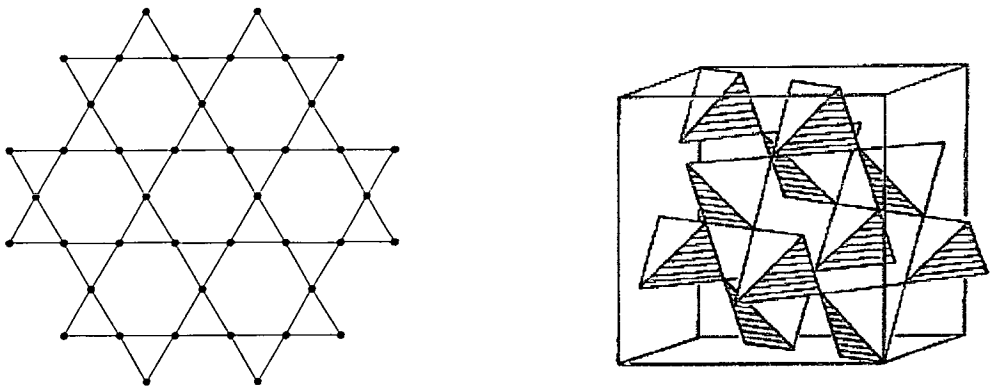

Figure 3.4 Illustration of the Kagome lattice (left) and its 3D analogue the pyrochlore lattice (right)

3.10 Spin Glasses

Having defined the term frustration by the use of a few simple examples it is now pertinent to look at real experimental systems in which spin frustration plays a role in

determining the nature of the magnetism exhibited by such compounds. One large group of systems which exhibit spin frustration are the so called '*spin glasses*' a working definition of which can be given as follows:[7] '*A random mixed interacting magnetic system characterised by a random, yet co-operative freezing of spins at a well defined temperature T_f below which a highly irreversible, metastable frozen state occurs without the usual long range spatial magnetic order*'. It transpires that frustration is a necessary condition for a system to exhibit spin glass behaviour, though there must also be a large degree of randomness, for example in site occupation within the lattice, or in the nature of bond interactions. Experimental examples of such systems include *canonical spin glasses* such as $Cu_{1-x}Mn_x$ and $Au_{1-x}Fe_x$ where a non-magnetic metallic host is doped with magnetic impurities, and $Eu_xSr_{1-x}S$ where dilution of one of the sub-lattices with a magnetic species in place of a non-magnetic ion is performed. In other words to dope an insulator/semi-conductor with a magnetic species.

The properties of such spin glasses can be elucidated using a broad range of techniques.

- Susceptibility – In general the form of dc susceptibility as a function of temperature shows linear Curie-Weiss behaviour over a broad temperature range, until a large deviation at lower temperature at a point T_f. This value of T_f may be smeared out, even in only a modest applied field. A divergence in the zero field cooled / field cooled measurements in the vicinity of T_f is also seen. In the absence of a field and on field warming the behaviour seen is reversible, whereas in the case of zero field cooling and field warming the behaviour seen is irreversible. In the case of canonical spin glasses a deviation temperature is also seen where the

effective moment begins to rise, this being indicative of the onset of ferromagnetic clusters in a paramagnetic background.

In the case of ac susceptibility a cusp is generally seen in the region of T_f, though this is often rounded off if the driving frequency ω is changed, and its position is frequency dependent. This frequency dependence is more pronounced in the case of an insulating spin glass, which is a good distinguishing probe between canonical and spin glass like behaviour.

In spin glasses a sudden onset of the imaginary term $\chi''(T)$ near to T_f is seen, and a peak in $\chi'(\omega)$ corresponds to a maximum in the slope *i.e.*

$$\chi'(T) = (d\chi'/dT)_{max} \tag{3.33}$$

This imaginary component shows that relaxation processes are influencing the measurement and, by decoupling the spins from the lattice, cause absorption. Such effects are not normally seen at magnetic transition points, other than in the case, for example, of a ferromagnet, where hysteresis arises. Such measurements give insight into low frequency/intermediate (10^{-1} – 10^{-5}s) relaxation times.

- Specific Heat – There is very little change in the specific heat, and certainly no distinct sharp maximum, possibly relating to a freezing out of the systematic entropy in short range order at $T > T_f$.
- Resistivity – The critical behaviour of any conventional system is normally reflected in the derivative $d(\Delta\rho)/dT$, where $\Delta\rho$ is the change in resistivity of the material, consequently in the case of metallic spin glasses, negligible change in $d(\Delta\rho)/dT$ is seen at T_f. There is little correlation with T_f, rather a broad maximum

at $T < T_f$. The reason for this is the absence of a periodically ordered state, and hence of any long range spatial correlation function.

- Polarised neutron techniques such as *XYZ* 3-directional analysis [8] allow determination of the extent of diffuse scattering brought about by any short range correlations. This is turn can be modelled to give an idea of the size of correlation lengths in such order. Neutron spin echo measurements can also be used to determine the motion of spins and the distribution of relaxation times, and hence to determine the extent to which moments are frozen as the system is cooled through T_f. Such measurements may be complemented by muon spin relaxation experiments.
- Mössbauer spectroscopy can give an indication of the local nature of the magnetic state. For example if a local field is present then hyperfine field splitting of the ^{57}Fe nuclear spin will be induced leading to a six line pattern, as opposed to a single emission line in the absence of any internal field. The amount of such splitting along with the intensity ratios of the emission lines give valuable information as to the nature of the magnetic state of the sample. Decay processes have an intrinsic lifetime of $\sim 10^{-7}$ s hence if any spin freezing occurs on a longer timescale than this, then hyperfine splitting will occur.

3.11 Spin glass Models

As larger numbers of experimental spin glass systems were discovered, so theorists became increasingly interested in modelling such systems. One immediate problem was the lack of long range order in such systems, and so a difficulty in determining a suitable order parameter with which one could describe the behaviour of the system

close to T_f. Improved theoretical models related an order parameter to temporal correlations and a summary of such models is provided in Appendix A.

3.12 Theory of the Kagome Lattice

The frustration evident in the Kagome lattice has one simple consequence namely an highly degenerate ground state. The absence of long range order in such systems makes it difficult to apply any critical scaling to them using conventional scaling parameters. Instead the chirality of such degeneracy can be used as an order parameter, since the 'handedness' of spins around any individual plaquette cannot be conveyed by a single spin alone. Such a chirality parameter can be described using the expression

$$\kappa = 2/\left(3\sqrt{3}\right)\left[\vec{S}_1 \times \vec{S}_2 + \vec{S}_2 \times \vec{S}_3 + \vec{S}_3 \times \vec{S}_1\right] \tag{3.34}$$

This chirality parameter thus has two possible values, $\kappa = \pm 1$, where the positive value denotes handedness in a clockwise direction. This then defines a fundamental difference between the triangular and kagome lattices, since in the triangular lattice, with edge sharing plaquettes, chirality is unambiguously propagated throughout the lattice, whereas in the case of the kagome lattice chirality information cannot be passed on since only one spin is shared between plaquettes. There are a large number of degenerate states which are contenders for the spin ground state, but two of particular note are the $q = 0$ and $q = \sqrt{3}\times\sqrt{3}$ states, which possess long range spin order and therefore can be described using chirality as an order parameter. These states are labelled as $q = 0$ and $q = \sqrt{3}\times\sqrt{3}$ so as to denote the fact that in the former case the magnetic lattice parameters and structural lattice parameters are identical,

whilst in the latter the magnetic lattice parameters are $\sqrt{3}$ times larger than those of the structural unit cell. In the $q = 0$ state there are three sub-lattices corresponding to a ferromagnetic chirality, whilst in the $q = \sqrt{3}\times\sqrt{3}$ state there are nine sub-lattices and an antiferromagnetic distribution of chirality. These two configurations are depicted below.

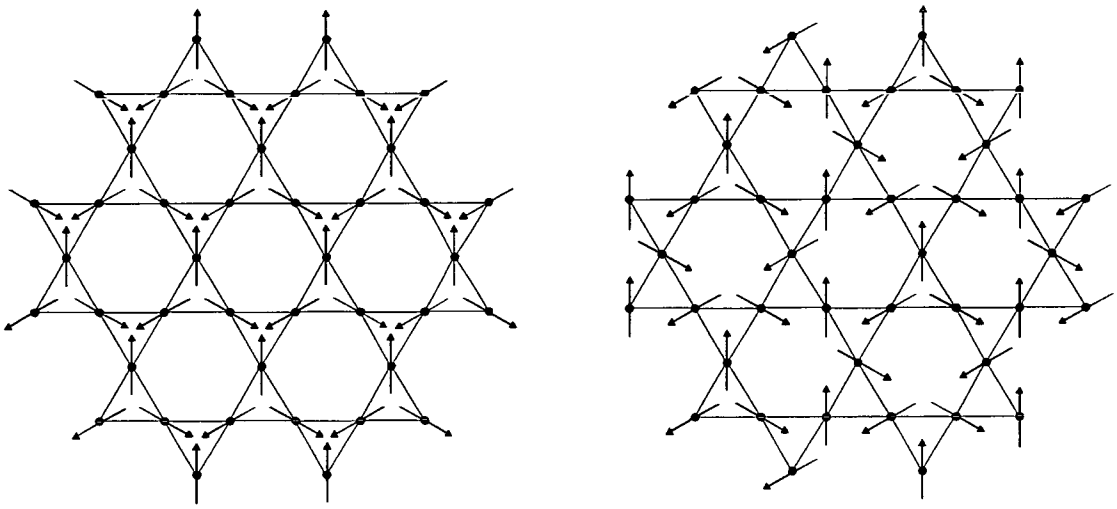

Figure 3.5 Two possible ground state configurations of the Kagome lattice. The diagram on the left represents the $q = 0$ configuration, the diagram on the right the $q = \sqrt{3}\times\sqrt{3}$ configuration

It is widely accepted that the Kagome antiferromagnet with nearest neighbour exchange does not have a Néel ordered ground state at $T = 0$. A considerable amount of work [9] has shown that the system has an unconventional ground state, though its nature is still a matter of debate.

One possible picture is that of a *spin nematic* ground state where there is no ordering of the sub-lattices, though spins are aligned along randomly chosen spin axes. However order is only short-ranged and there is no infinite spin-spin correlation length. Ordering thus occurs, in an analogous way to that found in nematically ordered liquid crystal phases. Within any such nematic phase there may well be

additional weak preferences for states biased along a particular wavevector e.g. that corresponding to the $\sqrt{3}\times\sqrt{3}$ state, but no long range correlations develop. Work by Chalker *et al* [10] suggests that there is a tendency towards $\sqrt{3}\times\sqrt{3}$ *type* nematic order, and calculation of the susceptibility shows a divergence as $T \rightarrow 0$ suggesting that the critical temperature of the system is $T = 0$.

Alternatively the ground state could be considered as some form of *spin fluid* , a quantum ground state where there is no long range order or indeed symmetry breaking. Spin pairs, termed 'singlet' pairs, in a variety of configurations contribute to this ground state, such that the individual $q = 0$ and $q = \sqrt{3}\times\sqrt{3}$ states are inadequate to fully describe the ground state, though they do represent the low lying excitations very well.

Though the exact nature of the ground state is unclear, simulations suggest that coplanar configurations have lower zero-point energies than non-coplanar ones [11]. Whilst non-planar fluctuations cost little or no energy in terms of individual spins, considerable energy barriers to collective non-planar motion are created, which are enhanced by any spin anisotropy present. The degeneracy of such a ground state can be lifted by, for example, thermal or quantum fluctuations, or even by interaction with further neighbours, a process known as '*order by disorder*', which may lead to the onset of long range order . Thermal selection will favour coplanar ground states, since there are a larger number of zero energy modes in comparison with non-coplanar states, thus giving the system access to a wider energy surface in configurational space. Work by Harris and Berlinsky [12] considers the nature of any quantum effects on such systems. Calculations for both the $q = 0$ and $q = \sqrt{3}\times\sqrt{3}$ structures, show that, for nearest neighbour interactions only, the linear spin wave spectra (LSWS) for

the two ordered states are identical and each exhibits a zero energy dispersionless mode, identified as a zero energy local excitation of the spins, with alternating signs around any hexagon. If further interactions J_2 and J_3 are considered then the $q = 0$ structure is stabilised for $J_2 - J_3 > 0$ and the $q = \sqrt{3}\times\sqrt{3}$ structure for $J_2 - J_3 < 0$.

3.13 Experimental frustrated systems

In an attempt to verify a variety of theoretical models much experimental work has focussed on the layered magnetoplumbite isomorph $SrCr_xGa_{12-x}O_{19}$ (SCGO(x)) where S = 3/2 Heisenberg spins sit at the vertices of a kagome lattice coupled by strong antiferromagnetic exchange (Curie-Weiss constant θ_{CW} = -500K). Such materials show spin glass behaviour with a freezing point in the region of 5K depending upon the value of x. Muon spin relaxation measurements [13] show a progressive slowing down of spin fluctuations as SCGO(x) is cooled from well above T_f. Whilst neutron studies show short range correlations of ~7Å (ca. twice the Cr-Cr separation) specific heat measurements reveal an unusual T^2 dependence below T_f, conventionally associated with long range 2D magnetic order. A wealth of experimental evidence has been accumulated on this system [14], however it is not an ideal manifestation of a simple Kagome lattice since some of the Cr^{3+} ions sit in two different triangular lattices between the kagome layers, hence the structure is best described as layers of corner sharing tetrahedra (consisting of two kagome layers with an intervening triangular layer) separated by triangular layers of spins bound in singlets.

Another kagome lattice system is that of $Na_2Mn_3Cl_8$ [15]. In this case layers of d^5 Mn^{2+} ions with an $^6A_{1g}$ ground state sit interleaved with layers of sodium chloride

layers, the manganese ions being separated by a distance of 3.728Å. Such geometry leads to a Kagome lattice of Mn spins with a distance between the Mn layers of spins of around 7Å and an almost complete coverage of magnetic sites on the lattice. The crystal structure is illustrated below with the Kagome layers indicated.

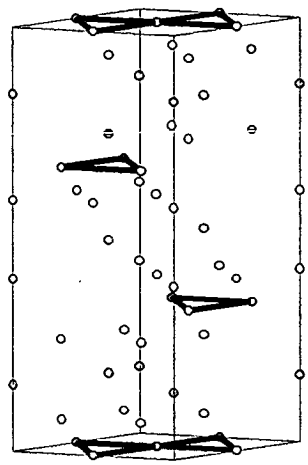

Figure 3.6 Crystal structure of $Na_2Mn_3Cl_8$ with Kagome layers of Mn ions (purple ions) indicated, with interleaved layers of Na ions (grey) and Cl ions (green)

Whilst this would appear to be an attractive system to study there are several problems difficulties associated with it. Firstly it is very difficult to ensure phase purity of the product, since the compound is very hygroscopic and will readily decompose into other sodium and manganese containing phases. Secondly the very low freezing temperature of this system makes it difficult to study since standard cryogenic equipment cannot reliably reach sufficiently low temperatures.

3.14 Jarosite family

A more faithful representation of the simple kagome lattice is provided by the jarosite series of minerals $A\mathrm{Fe_3(SO_4)_2(OH)_6}$ (where A is typically Na, K, Rb, Cs, H_3O, D_3O) and isomorphic families where Fe^{3+} is exchanged for other trivalent metal ions such as Al^{3+}, Cr^{3+}or Ga^{3+}. In such compounds the metal ions form a Kagome lattice with hydroxide and sulphate groups linking such planes of ions together. In all there are four superexchange pathways per magnetic ion. The crystal structure, which indexes with space group $R\ \bar{3}m$, is shown below in figure 3.7.

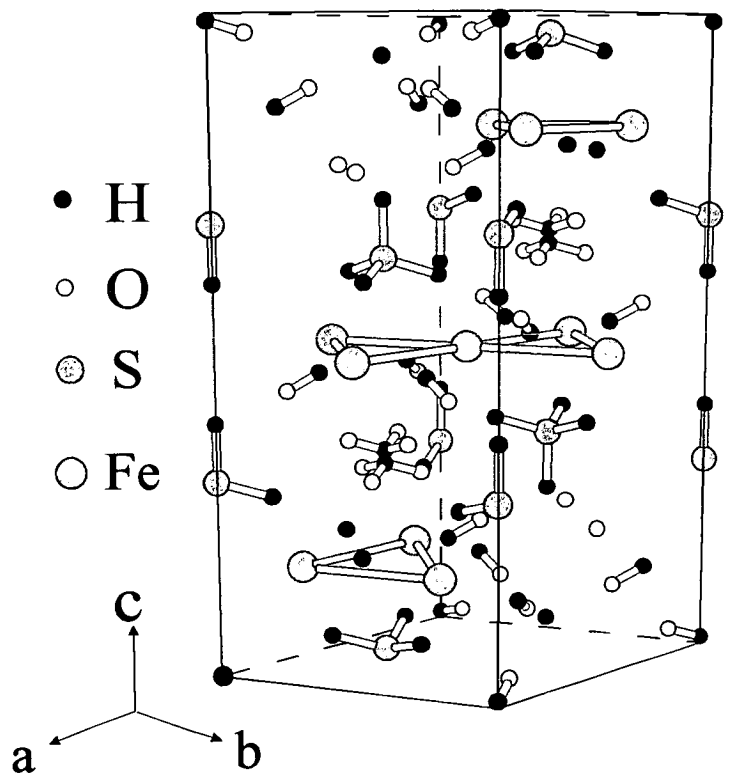

Figure 3.7 Crystal structure of the jarosite family of minerals with Kagome layers indicated by yellow links

All of the magnetic salts, with the exception of the hydronium and deuteronium salts, show some degree of long-range magnetic order with Néel temperatures of the order of 50K, as evidenced by a distinct cusp in the dc susceptibility χ_{dc}. Such measurements reveal no significant divergence in the field-cooled and zero-field-cooled behaviour, whilst the temperature dependence of the inverse susceptibility is seen to be linear in the region 150 - 350K, with values of the Weiss constant θ_{CW}, determined using the Curie-Weiss Law, of the order of –700K. Neutron powder diffraction studies show evidence for additional Bragg peaks below the respective transition temperatures T_f and these have been indexed in all cases on a magnetic cell with an in-plane spin structure corresponding to the q = 0 array depicted in figure 4.6, with a doubling of the *c*-axis relative to the nuclear cell. In addition to the long range order seen, there is also a considerable amount of diffuse scattering attributed to short range two dimensional order within the kagome planes.

The behaviour of the hydronium/deuteronium salt is unique to the family of jarosites [16-21]. In this case powder diffraction measurements show no evidence of long range order down to a temperature of 0.4K. Furthermore dc susceptibility measurements show a cusp at temperatures of the order of 15K and a divergence in the field cooled/zero field cooled measurements indicative of spin freezing and a spin glass transition. The reasons behind this are not immediately apparent since the crystal structure of the hydronium salt is identical to that of the other members of the jarosite family, and there are no obvious differences in the exchange geometry between the Fe^{3+} ions. The only observable difference between the hydronium/deuteronium salts and the other members of the family is in the coverage of the lattice. Whilst jarosites are generally prone to loss of Fe^{3+} during precipitation, the loss is less significant in

the case of the hydronium/deuteronium salts and may be as low as 3%, in comparison to that of the other materials where losses are generally of the order of 5-20% [17]. Thus it would appear that 'dilution' of the lattice, by reduction in the coverage of the Fe^{3+} lattice, leads to the onset of long range order. Such an '*order by dilution*' phenomenon [18] can be illustrated by doping of the pure hydronium salt with a small impurity level of aluminium (ca. 3%). Recent neutron powder diffraction studies of the doped deuteronium salt $(D_3O)Fe_{3-x}Al_x(SO_4)_2(OD)_6$ (with x = 0.03) show evidence for magnetic long range order at 1.4K, whilst dc susceptibility measurements show an enhanced value of T_f , in comparison to that of the undoped sample, of 25K. The lattice coverage in this case was 89±3%. This is a surprising result, since current theoretical models would suggest that dilution of the lattice should lead to a *reduction* in the magnetic transition temperature. Indeed work performed on the analogous hydronium chromium system showed a reduction in the value of T_f on doping of the parent compound. Such results suggest that there is an extremely sensitive balance between exchange forces in the kagome system. Doping of the lattice, either in the form of the introduction of diamagnetic ions, or indeed with simple vacancies, unbalances these forces in a way which favours long range order, suggesting that nearest neighbour and even next nearest neighbour interactions are of importance.

3.14 Summary

This chapter has attempted to give a flavour of the extraordinary nature of the Kagome lattice, and how this might be described theoretically in the context of critical behaviour. In Chapters 4 and 5 experimental work will be presented which has attempted to probe further, both the nature of the magnetic order in the

$KFe_3(SO_4)_2(OH)_6$ system, and the spin fluctuations in the $(H_3O)Fe_3(SO_4)_2(OH)_6$ system.

References

[1] See for example '*The Theory of Critical Phenomena: An Introduction to the Renormalisation Group*' J.J.Binney, N.J.Dowrick, A.J.Fisher and M.E.J.Newman (Clarendon Press, 1992); '*Introduction to Phase Transitions and Critical Phenomena*' H.E.Stanley (Oxford University Press, 1971)

[2] For further details see '*Introduction to Phase Transitions and Critical Phenomena*' H.E.Stanley (Oxford University Press, 1971)

[3] Magnetic Properties of Layered Transition Metal Compounds, *ed.* L.J. de Jongh (Kluwer Academic Publishers, 1990)

[4] P.W.Anderson, *Physics Today* **41**(6) 9 (1988)

[5] P.W.Anderson, *Science* **235** 1196 (1987)

[6] A.P.Ramirez, *Annu. Rev. Mater. Sci.* **24** 453 (1994)

[7] '*Spin Glasses: An Experimental Introduction*' J.A.Mydosh, (Taylor and Francis,1993)

[8] O.Scharpf, H.Capelmann, *Phys. Stat. Sol.(A)* **135** 359 (1993); T.J.Hicks, *Adv. Phys.* **45**(4) 243 (1996)

[9] J.T.Chalker, P.C.W.Holdsworth and E.F.Shender, *Phys. Rev. Lett.* **68** 855(1992); C.L.Henley, *Phys. Rev. Lett.* **62** 2056 (1989); C.L.Henley and E.P.Chan, *J.Mag. Magn. Mat.* **140** 1693 (1995); C.Zeng and V.Elser, *Phys. Rev. B* **42** 8436 (1990)

[10] J.T.Chalker, P.C.W.Holdsworth and E.F.Shender, *Phys. Rev. Lett.* **68** 855 (1992)

[11] A.Chubukov, *Phys. Rev. Lett.* **69** 832 (1992); J.T.Chalker and J.F.G.Eastmond, *Phys. Rev. B* **46** 14201 (1992)

[12] A.B.Harris, C.Kallin and A.J.Berlinsky, *Phys. Rev. B* **45** 2899 (1992)

[13] Y.J.Uemura, A.Keren, L.P.Le, G.M.Luke, B.J. Sternlieb and W.D.Wu, *Hyperfine Interact.* **85** 133 (1994); A.Keren, L.P.Le, G.M.Luke, W.D.Wu, Y.J.Uemura, Y.Ajiro, T.Asano, H.Kuriyama, M.Mekata and H.Kikuchi, *Hyperfine Interact.* **85** 181 (1994); Y.J.Uemura, A.Keren, K.Kojima, L.P.Le, G.M.Luke, W.D.Wu, Y.Ajiro, T.Asano, H.Kuriyama, M.Mekata and H.Kikuchi and K.Kakurai, *Phys. Rev. Lett.* **73** 3306 (1994)

[14] C.Broholm, G.Aeppli, G.P.Espinosa, and A.S.Cooper, *Phys. Rev. Lett.* **65** 3173 (1990); G.Aeppli, S.H.Lee, C.Broholm, T.G.Perring, M.Adams, C.Carlisle, A.D.Taylor, A.P.Ramirez and B.Hessen, *Physica B* **213** 142 (1995); S.H.Lee, C.Broholm, G.Aeppli, A.P.Ramirez, T.G.Perring, C.Carlisle, M.Adams, T.J.L.Jones and B.Hessen, *EuroPhys. Lett.* **35** 127 (1996); P.Schiffer, A.P.Ramirez, K.N.Franklin and S.W.Cheong, *Phys. Rev. Lett.* **77** 2085 (1996);

[15] C.J.J. van Loon and D.J.W.Ijdo, *Acta. Cryst. B* **31** 770 (1975)

[16] A.S.Wills and A.Harrison, *J.Chem.Soc., Faraday Trans.* **92**(12) 2161 (1996)

[17] A.S.Wills, A.Harrison, R.I.Smith and C.Ritter, *Phys. Rev. B* **61**(9) 1 (2000)

[18] A.S.Wills, A.Harrison, S.A.M.Mentink, T.E.Mason and Z.Tun, *EuroPhys. Lett.* **42**(3) 325 (1998)

[19] A.Harrison, K.M.Kojima, A.S.Wills, Y.Fudamato, M.I.Larkin, G.M.Luke, B.Nachumi, Y.J.Uemura, D.Visser and J.S.Lord, *Physica B* (submitted, 1999)

[20] G.S.Oakley, D.Visser, J.Frunzke, K.H.Andersen, A.S.Wills and A.Harrison, *Physica B* **267-268** 142 (1999)

[21] G.S.Oakley, S.Pouget, A.Harrison, J.Frunzke and D.Visser, *Physica B* **267-268** 145 (1999)

Chapter 4 Single crystal studies of $KFe_3(SO_4)_2(OH)_6$

4.1 Single crystal diffraction: D10 instrument ILL

4.1.1 Introduction

As outlined in the previous Chapter there is a large difference in behaviour between the potassium and hydronium jarosite salts. To understand these differences it is necessary to identify the leading terms in the Hamiltonian, and in particular both the strength of exchange J and the nature of the exchange pathways in both systems. Whilst both magnetic susceptibility and neutron scattering measurements have been performed on powdered jarosite samples [1], such data can only provide an indirect probe of the strength of exchange in these materials. Furthermore, in most cases, it is not possible to determine the nature of the magnetic structure unambiguously from powder diffraction measurements, since information is lost regarding the orientation of moments along the crystallographic axes, as outlined in section 2.2.1. Single crystal studies are therefore of great importance since they allow an unambiguous determination of the magnetic structure as well as providing information as to the nature of low lying magnetic excitations and are a more direct probe of the magnitude of J. In addition, the nature of any critical scattering in the region close to T_N can be monitored more effectively, affording the possibility of extracting information regarding critical fluctuations in any given magnetic system with a greater degree of accuracy.

4.1.2 Growth of jarosite single crystals

Preparation of powdered jarosite samples requires careful attention to both temperature and pH in order to maximise the yield of product and, more importantly, to ensure phase purity of product. Excessive temperature (>180°C) or too basic a solution will result in the formation of an amorphous iron hydroxysulfate $Fe_4(OH)_{10}SO_4$ [2]. Studies have been performed to determine the nature of species present in solution [3], suggesting that at low temperature the dominant species are $FeSO_4^+$ and $FeOH^{2+}$. As the temperature of reaction rises so too does the concentration of $Fe(OH)_2^+$, as equilibrium shifts to the hydroxy species, and it is this unit which is believed to form the fundamental chemical building block [2]. Such hydrolysis reactions result in the release of protons, and a corresponding drop in pH which retards further product formation, giving rise to crystallites of product which are typically of the order of 10μm across. Such conditions mitigate against formation of large single crystals, of a suitable size to perform either elastic or inelastic neutron scattering measurements. Whilst formation of large single crystals has not proved possible under laboratory conditions or indeed on laboratory timescales, nature provides rich sources of jarosites in areas such as Greenland, Spain or the United States. A search through a number of mineral collections unearthed a natural single crystal of jarosite measuring 5mm^3 and of mass 15mg, originating from Eureka, Utah. The sample is pictured below, with a matchstick and five pence piece as a point of comparison. A sketch of the crystal showing the relevant faces is also shown below. EDAX (energy dispersive X-ray analysis) measurements showed that the crystal was in fact the potassium salt $KFe_3(SO_4)(OH)_6$, though it was not possible to determine the potassium coverage of the lattice using these results.

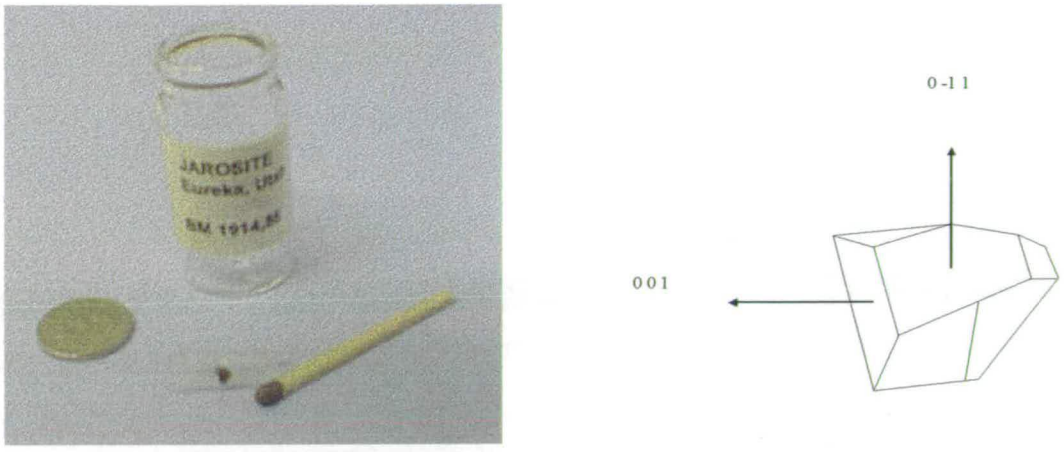

Figure 4.1 Photograph of the single crystal of potassium jarosite with five pence piece as comparison (left). Sketch of the crystal and face orientations (right)

Measurement of the dc susceptibility response of the crystal was performed using a SQUID magnetometer, with a field of 5000G applied both perpendicular and parallel to the *c*-axis. The results are shown below in figure 4.2.

The data show behaviour broadly in keeping with that expected of this sample. A maximum in the first derivative $d\chi/dT$ is seen in both the parallel and perpendicular signals at 65K with a minimum at 61K. The sharp response of the parallel signal close to this maximum is indicative of the onset of critical fluctuations as 3D ordering takes place. Below T_N the parallel signal is greater than that of the perpendicular signal, since small spin fluctuations out of the *a-b* plane continue on cooling.

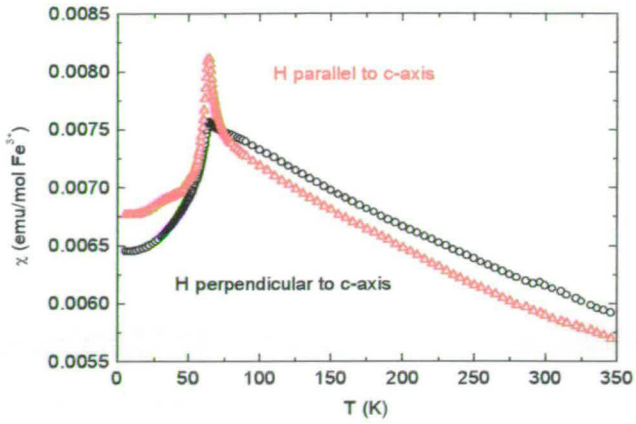

Figure 4.2 Plot of molar susceptibility versus temperature with a field of 5000G applied both parallel(red triangles) and perpendicular(black circles) to the c-axis

4.1.3 Single crystal diffraction

In order to determine the quality of the crystal, along with its crystallographic and magnetic unit cells, measurements were performed using the four circle, triple axis diffractometer D10 at the Institut Laue-Langevin in Grenoble France. The instrument may be used either with or without energy analysis of the beam scattered from the sample, as illustrated below in figure 4.3.

In two axis mode both the monochromator and sample positions may be rotated, whilst the Eulerian cradle allows tilting of the sample in a further two directions. In triple axis mode, whilst the monochromator and sample positions may be rotated as before, the introduction of an analyser, which allows energy resolution of the exiting neutrons, creates a third axis of rotation. Use of the triple axis set-up therefore allows for the possibility of examining excitations within the sample, and the D10 instrument was chosen to perform the experiment since it affords very fine momentum resolution of exiting neutrons. Its suitability in this case was enhanced by the high incident flux

affordable on the instrument, as well as the inherently low background, highly important in the case of such a small crystal containing a large amount of hydrogen.

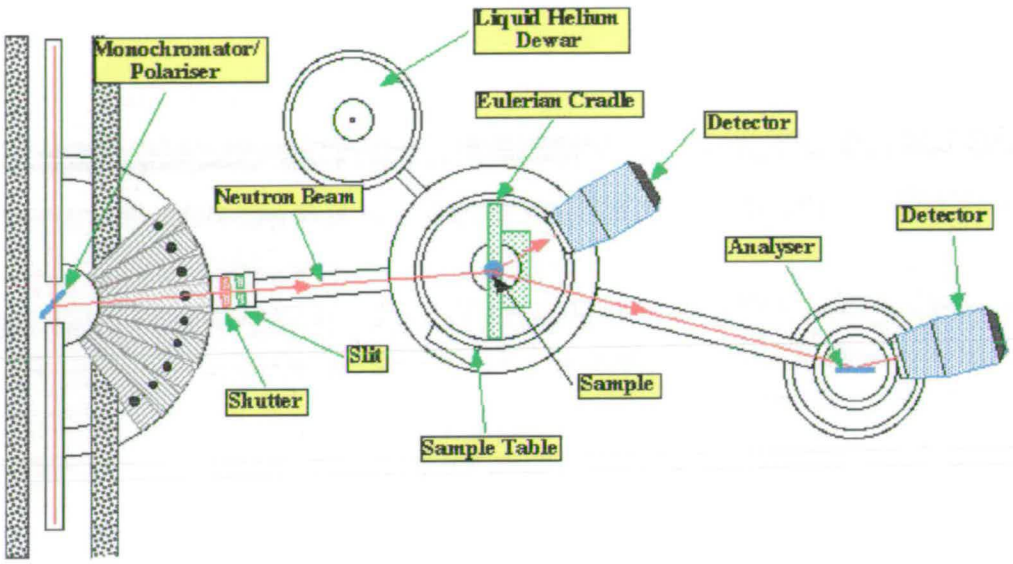

Figure 4.3 Layout of the D10 Single crystal diffractometer showing the two possible modes of operation

Initially the instrument was configured in triple axis mode with an incident wavelength of 2.36Å, and the analyser crystal aligned so as to measure the elastic scattering *i.e.* with the neutron energy change $\Delta E = 0$. Preliminary measurements verified the position of the magnetic reflections (1 0 5/2), (1 1 3/2) and (1 0 11/2), and a series of scans were then performed to follow the intensity of these reflections as a function of temperature on warming from the base temperature of 20K.

The configuration was then changed by removal of the analyser crystal, to two-axis mode and omega-two theta scans performed of the reflections (h,k,l), $(h,k,l+1/2)$, $(h,k,l-1/2)$ and $(-h,k,l) = 3n$ both at 20K and 62.8K. The wavelength settings were

then changed so as to have an incident wavelength of 1.26Å, and further omega-two theta scans performed in two-axis mode, of the reflections (h,k,l) and $(-h,k,l) = 3n$ at 20K. Finally the position of the analyser was fixed and a number of q scans performed to attempt to probe the nature of any diffuse magnetic scattering present.

The 275 nuclear reflections measured at 20K at a wavelength of 1.26 Å, were used in a least squares refinement to determine atomic positions within the unit cell based on the space group $R\bar{3}m$ (Space group No.167, *International Tables for Crystallography:Volume A*). The refined atomic positions are shown below in table 4.1.

Atom type	*x*	*y*	*z*	*uiso/Å²*	*fractional occupancy*
Fe	0.16667	-0.16667	-0.16667	0	0.99431
S	0	0	0.30963	0.3059	1
O1	0	0	0.39436	0	0.91106
O2	0.2228	-0.2228	-0.05346	0.56192	1.00249
O3	0.1273	-0.1273	0.13545	0.74862	1.0649
K	0	0	0	0.14487	0.84518
H4	0.19725	-0.19725	0.11182	1.82172	1
$R_{wp} = 0.053$			$\chi^2 = 7.65$		

Table 4.1 Refined atomic positions derived from nuclear reflections obtained at wavelength of 1.26Å at T = 20K in space group R $\bar{3}$ m

Refinement of the combined reflections from data sets taken with both the 1.26 and 2.36Å wavelengths gives an improvement in the goodness of fit with revised parameters as given in table 4.2 [4].

Atom type	*x*	*y*	*z*	*uiso/Å²*	*fractional occupancy*
Fe	0.16667	-0.16667	-0.16667	0	0.95462
S	0	0	0.31021	0.36610	1
O1	0	0	0.39464	0	1
O2	0.22339	-0.22339	-0.05353	0.67993	1
O3	0.12738	-0.12738	0.13543	0.65420	1
K	0	0	0	0.35200	0.84518
H4	0.19670	-0.19670	0.11178	1.89361	1
$R_{wp} = 0.055$			$\chi^2 = 11.5$		

Table 4.2 Refined atomic positions from combined 344 reflections from both wavelengths of 1.26 and 2.36 Å at 20K in space group R $\bar{3}$ m

To determine the nature of the magnetic unit cell the magnetic reflections measured at 20K and 2.39 Å were used to refine the magnetic unit cell, using the SFLSQ routine within CCSL (Cambridge Crystallography Subroutine Library). With the nuclear structure defined as above with unit cell parameters $a = b = 7.3000$Å and $c = 17.1270$Å and angles $\alpha = \beta = 90°$ $\gamma = 120°$, a magnetic least squares refinement was carried out on the data taken at 20K. Conflicting symmetry operators meant that a satisfactory refinement was only achieved by lowering the nuclear symmetry so as to

have three Fe sites in the unit cell at (1/6 1/2 5/6), (1/2 1/2 1/2) and (5/6 1/6 1/6) with a 120° spin arrangement. Two parameters, a common moment and the angle in the plane of the spins relative to the other two layers in the unit cell, were then refined. This gave a moment of $4.03\mu_B$ at each Fe site and angles ϕ (angle of one spin relative to the a axis) of –60, 90 and 120°.

4.1.4 Critical exponents

In order to determine the magnetisation critical exponent β, the intensity of the magnetic reflections (1 0 5/2), (1 1 3/2) and (1 0 11/2) was measured as a function of temperature in the range 20-64K. At temperatures well below T_N the scattering seen will be purely Bragg scattering and so will have a Gaussian lineshape associated with it, whilst in the region close to T_N, critical scattering will introduce an additional Lorentzian component to the lineshape. Ordinarily therefore, fitting of the individual reflections would involve a combination of Gaussian and Lorentzian functions, with the proportion of the Lorentzian component allowed to increase as $T \rightarrow T_N$. However, in this case, measurement of the individual reflections revealed that the crystal was split, making modelling of the Lorentzian component of scattering very difficult. Therefore all the analysis performed involved the fitting of individual reflections to solely a Gaussian function. An example of the fitting performed is shown for the data sets collected at 20K in the figure below.

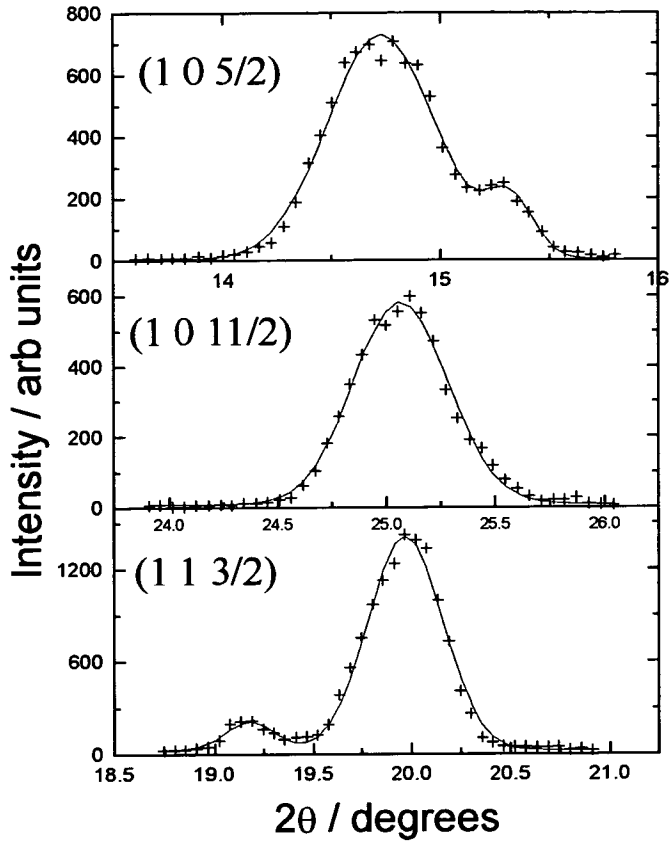

Figure 4.4 Measured reflections at 20K with fit to Gaussian peakshape. The data are denoted by the crosses (+) and the fit by the solid black lines

The temperature dependence of the integrated intensity of the three reflections, normalised to 100,000 monitor counts is shown below.

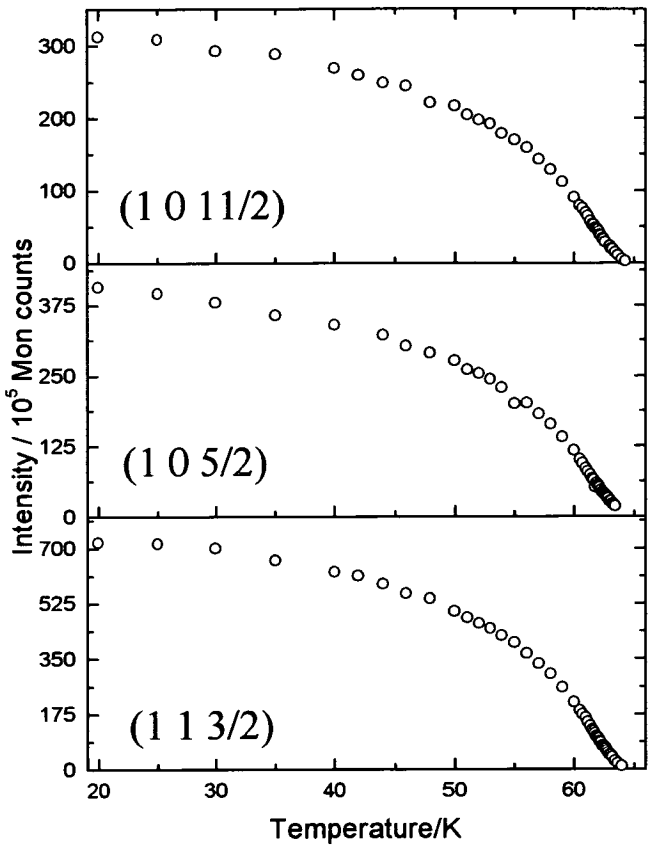

Figure 4.5 Plots of integrated intensity vs. temperature for the magnetic reflections (1 0 11/2) (top), (1 0 5/2) (middle) and (1 1 3/2) (bottom)

A rapidly increasing decline in the integrated intensity is seen as the magnetic transition temperature is approached from below. Whilst an accurate description of the temperature dependence of the integrated intensity, and hence the sublattice magnetisation, requires a polynomial expression of several orders, in practice the first term will dominate the expansion. If the reduced variable t, the *reduced temperature*, is defined using the relation

$$t = \frac{T_N - T}{T_N} \tag{4.1}$$

then the magnetisation, M, is proportional to the exponent β *i.e.*

$$M \propto |t|^{\beta} \tag{4.2}$$

Since the intensity is also related to the square of the magnetisation it can therefore be approximated by the expression

$$I = I_0 (|t|)^{2\beta} \tag{4.3}$$

Hence taking logs of both sides gives the result that

$$\ln I = \ln I_0 + 2\beta \ln(|t|) \tag{4.4}$$

Thus in the region T ~ T_N a plot of ln$I$ against ln($|t|$) gives a straight line of gradient 2β. In practice not only will there be an uncertainty in the value of T_N, but there will also be a background term to subtract from the integrated intensity. The situation is further complicated in this particular case since there are two transition points, T_{N1} and T_{N2}, as shown schematically in the diagram below.

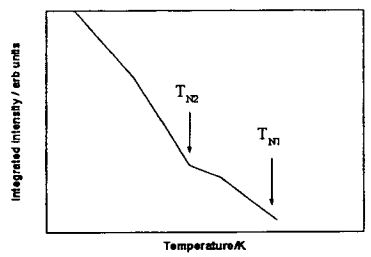

Figure 4.6 Schematic plot of integrated intensity versus temperature in the case of $KFe_3(SO_4)_2(OH)_6$ showing the two transition temperatures T_{N1} and T_{N2}

In the region as T $\rightarrow$ T_{N1} on cooling, there will be a considerable contribution to the integrated intensity from critical scattering, however the quality of the data does not allow a rigorous determination of this contribution. As a consequence, only a single

value of T_N was abstracted from the data. This value, as well as that of the background correction term, were both varied manually in order to determine the value of the exponent β in the region close to T_N. The resulting 'best fits' in the case of each reflection are shown in the figure below.

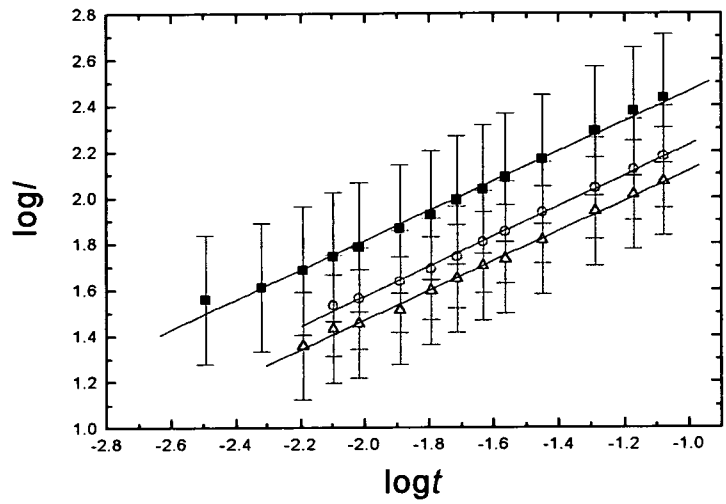

Figure 4.7 Plot of log I vs. log t for the magnetic reflections (1 1 3/2) (filled squares), (1 0 5/2) (open circles) and (1 0 11/2) (open triangles) with least squares linear fits (black lines) and T_N set at 62.2K

The values of the gradients obtained via a least squares linear fitting routine, and the average value for the critical exponent β is shown in the table below. This average value of $\beta = 0.325 \pm 0.010$ is indicative of 3D behaviour and thus reflects the onset of magnetic ordering at T_N. Theoretical predictions [5] suggest that the value of β will take the value 0.31 if the system exhibits 3D Ising behaviour, 0.33 if it exhibits 3D X-Y behaviour and 0.35 in the case of 3D Heisenberg behaviour. The experimentally

determined value of β is therefore consistent with either 3D X-Y or 3D Heisenberg behaviour.

Reflection	Gradient (= 2β)	β
(1 1 3/2)	0.646±0.015	0.323±0.008
(1 0 5/2)	0.657±0.011	0.328±0.006
(1 0 11/2)	0.647±0.012	0.324±0.006
Average	0.650±0.022	0.325±0.010

Table 4.3 Values of the critical exponent β determined from the datasets obtained from the (1 0 5/2), (1 0 11/2) and (1 1 3/2) reflections respectively

At temperatures well below T_N the spin fluctuations in the system will be 2D in character. However as T approaches T_N ($T \sim 5/6T_N$), there will be both 2D and 3D spin fluctuations as interplanar exchange terms begin to influence the Hamiltonian. In cases where the value of β in this 'intermediate' region have been determined for experimental systems, there is close agreement with theoretical work by Bramwell and Holdsworth [6] which suggests that β will take a universal value of $3\pi^2/128 \sim 0.23$. It was therefore of interest to try and determine whether such a crossover region between values of β of 0.23 and 0.33, exists in the present sample. To this end, fitting of the data obtained over the temperature range of 20-56K was performed in a similar manner to that described above. The results obtained are shown in figure 4.8 below.

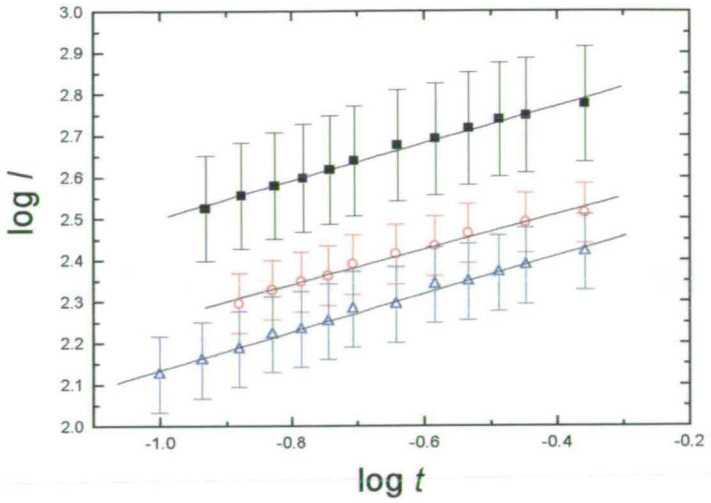

Figure 4.8 Plot of log I vs. log t for the magnetic reflections (1 1 3/2) (filled squares), (1 0 5/2) (open circles) and (1 0 11/2) (open triangles) with least squares linear fits (black lines) and T_N set at 62.2K

The values of the gradients obtained via a least squares linear fitting routine, and the average value for the critical exponent β is shown in table 4.4 below.

Reflection	Gradient (= 2β)	β
(1 1 3/2)	0.449±0.012	0.225±0.006
(1 0 5/2)	0.421±0.017	0.210±0.009
(1 0 11/2)	0.460±0.012	0.230±0.006
Average	0.443±0.024	0.222±0.012

Table 4.4 Values of the critical exponent β determined from the datasets obtained from the (1 0 5/2), (1 0 11/2) and (1 1 3/2) reflections respectively

This result demonstrates a clear crossover region of 56-57K at which the system ceases to behave in a 2D fashion and exhibits 3D behaviour. These values are consistent with the Bramwell-Holdsworth model which proposes the existence of an intermediate region at temperatures just below T_N where both 2D and 3D spin fluctuations exist. The value of $\beta = 0.222$ obtained in this study illustrates that the system is non-Ising and is compatible with both 2D X-Y or 2D planar Heisenberg behaviour. It is also consistent with theoretical work which proposes that a coplanar structure is energetically most favourable at lower temperatures [7], and that thermal fluctuations facilitate the onset of 3D exchange close to T_N. It should be noted that this is the first single crystal experimental determination of critical exponents for a member of the jarosite family.

4.2 CRYOPAD on the IN20 instrument

4.2.1 Introduction

The onset of long range antiferromagnetic order can be seen by the appearance of additional reflections in neutron powder diffraction patterns collected below the Néel temperature of the material in question. However, since the incident beam consists of unpolarised neutrons, that is to say the orientation of neutron moments is completely random, it is not possible to extract any information from the scattered beam regarding the components of spins within the sample, along all three principal axes. However in the case of a polarised neutron instrument, as outlined in Chapter 2, the incident neutrons are polarised such that >95% of the moments are aligned along a particular axis, often that perpendicular to the direction of propagation. Analysis of

the exiting neutron beam thus affords information not only regarding the magnitude of magnetic moments within a sample, but also their direction. In an attempt to unambiguously determine the nature of the magnetic structure in potassium jarosite, work was performed using the CRYOPAD unit on the triple axis spectrometer IN20 at the ILL, Grenoble.

4.2.2 CRYOPAD

In a conventional polarised neutron spectrometer set-up, incident neutrons are polarised along a given direction with the aid of an applied guide field. Whilst this allows for an efficient polarisation of this beam, it also means a loss of information regarding the sample spin array, since such spins will precess and depolarise about any such field. Thus information along the axis perpendicular to that of the applied field is always lost. The difference in the case of the CRYOPAD arrangement [8] is that the sample is shielded from the applied guide field and so the field at the sample is effectively zero, thus allowing full 3-dimensional analysis of the sample spin polarisation, rather than the 3-directional analysis generally performed, measuring simply the ratio of non-spin flip to spin flip as outlined in Chapter 2. The CRYOPAD arrangement is illustrated schematically below in figure 4.9.

If the incident beam is polarised such that all the moments are perpendicular to the direction of propagation, then the transverse guide fields on either side of the sample produce a polarisation vector at an angle θ_{in} (θ_{out}) to the vertical. The superconducting solenoid coils surrounding the sample are calibrated such that they give rise to a precession angle of ϕ_{in} (ϕ_{out}).

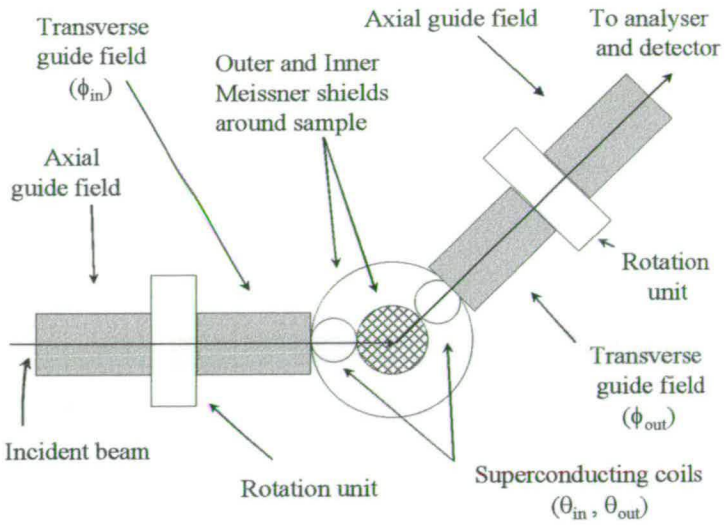

Figure 4.9 Schematic diagram of the CRYOPAD unit

For a given set of values for θ_{in} and ϕ_{in} the corresponding values of θ_{out} and ϕ_{out} can be determined by maximising the flipping ratio measured at the analyser. The transmitted polarisation P_s can be written as

$$P_s = P' + P\cos(\chi - \chi_0) \tag{4.5}$$

where χ is dependent upon either θ_s or ϕ_s (the subscript s referring to the sample) and χ_0, P and P' are constants dependent upon the polarisation direction. If ϕ_s is set to zero and θ_s then varied (where $\chi = \theta_s$) the value of P' is zero, and there are two angles at which $P_s = 0$. These two angles may be determined by measuring the transmitted polarisation for two orthogonal reflections (i.e. with $\theta_{s1} = \theta_{s2} + 90°$); the value of θ_s is then set to position θ_0 to determine the maximum in P_s (perpendicular to the zero point) and the equivalent procedure carried out in order to determine ϕ_s. The amplitude of the scattered polarisation is measured under the conditions that $\theta_s = \theta_0$

and $\phi_s = \phi_0$. Blume's equations [9] may then be used to calculate the scattering polarisation from the incident polarisation, the amplitude of the polarisation either being of the same magnitude of greater than scattering from any pure spin state (though its direction will generally be altered). Any depolarisation of the scattered beam is therefore indicative of the presence of different magnetic domains within the sample.

4.2.3 Experimental

In an attempt to determine the magnetic ground state of $KFe_3(SO_4)_2(OH)_6$ the single crystal sample was mounted in an ILL 'Orange' cryostat along with the CRYOPAD unit on the IN20 polarised neutron triple axis spectrometer at the ILL, Grenoble. The crystal was initially mounted with Kwikfil® on an aluminium pin, with the a^*-b^* plane in the scattering plane, and a sheath of cadmium to protect the sample in the event of the glue failing. A series of scans were then performed measuring pairs of reflections, for example the (0 0 6) and $(0\ 0\ \bar{6})$, and analysis carried out as outlined above. Further measurements were performed with the crystal re-orientated such that the c^* axis lay in the scattering plane.

Analysis of the data [10] collected showed that, at 10K, the magnetic structure adopts a $q = 0$ structure with no component of the moment along the c axis. Such a planar structure concurs with that suggested by previous workers [7], though it is the first time that it has been verified experimentally.

4.3 Spin wave dispersion measurements

4.3.1. IN8 experiment

It is clear from theoretical work by several authors [11] that the nature of the low lying excitations are extremely important in determining both the nature of the groundstate and the behaviour of kagome systems. Such models predict that the spin wave dispersion relation $\varepsilon_\mu(\vec{k})$ for a kagome lattice with nearest-neighbour exchange is given by

$$\varepsilon_\mu(\vec{k}) = JS\sqrt{2[\sin^2 q_1 + \sin^2 q_2 (q_1 - q_2)]} \tag{4.6}$$

where J is the exchange constant, S is the magnitude of the spin and q_1 and q_2 describe the magnitude of the wavevector in the x and y directions respectively, as defined below.

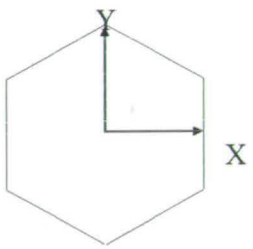

Figure 4.10 Definition of axes as per reference [10]

At the zone boundary this expression yields an energy of $2JS$. Whilst the value of S in the case of the jarosites is 5/2, the value of J can be estimated from the magnetic susceptibility data available. The high temperature susceptibility χ_0 is given by

$$\chi_0 = \frac{1}{(T + 4\widetilde{J}/3)} \tag{4.7}$$

where $\widetilde{J} = JS(S+1)$, and comparison with the Curie-Weiss Law shows that $\frac{4}{3}\widetilde{J} = |\theta_{CW}|$. Thus in the case of S = 5/2

$$|\theta_{CW}| = \frac{4}{3} JS(S+1) \qquad (4.8)$$

$$\sim 12J$$

The value of $|\theta_{CW}|$ is estimated to be 600K from dc susceptibility measurements [12] which gives a value for J of ~ 50K. Conversion of this value into energy units and substitution into (4.8) gives a value for the zone boundary energy of ~ 20meV, suggesting that the dispersion curve seen will rise steeply from the zone centre.

In an attempt to probe the dispersion relation for excitations in the system $KFe_3(SO_4)_2(OH)_6$ the single crystal sample was mounted on the triple axis IN8 spectrometer at the ILL in Grenoble. The instrument is located on the hot source and so affords a large range of energies and momentum transfers, as well as high flux at the sample. The wide range of momentum transfers (3-25meV) was important since it afforded the widest energy range with which to probe the predicted steep dispersion curve. Measurements were performed with the crystal orientated so that the a^*b^* plane lay in the scattering plane, and a series of scans performed at both constant q, with the sample orientation fixed and the analyser crystal rotating, and constant E, with the analyser crystal fixed and the sample rotating. A typical q scan is shown below in figure 4.11. An example of a constant E scan is shown below in figure 4.12.

As both plots indicate, the data collected are very noisy with a large inherent background, making the determination of the nature of any dispersion present very difficult. Scans performed at room temperature showed a large rising background, making it impossible to perform a subtraction from the lower temperature data, in order to determine the magnetic origin or otherwise of the data obtained.

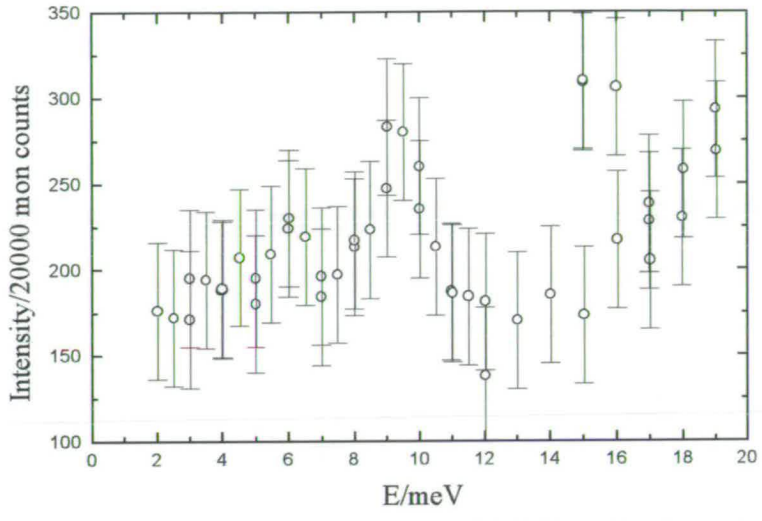

Figure 4.11 Plot of intensity vs. energy for a constant q scan performed at (1.4,1.4,1.5) at 5K

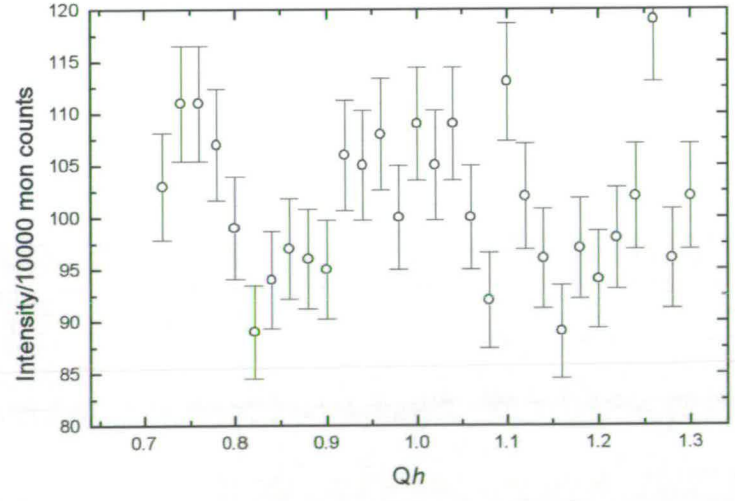

Figure 4.12 Plot of intensity/10000 mon counts vs. Qh (Qk,Ql) at E_i = 3meV and 5K

4.3.2 TAS-6 spectrometer Risø National Laboratory, Denmark

As highlighted in the previous section the nature of the background on the IN8 instrument made it very difficult to assess the nature of any dispersion present. In an attempt to reduce this background further the crystal was mounted on the triple axis TAS-6 instrument at the Risø National Laboratory in Denmark. Whilst the energy transfer range of the TAS-6 instrument is smaller than that of IN8, of the order of 2 – 18meV (reflecting the fact that the instrument sits on a cold source), the background is significantly lower than that of IN8. This is a result of two factors, relating to the nature of the monochromator and analyser, both recently upgraded on the instrument [13]. The use of a sapphire filter at the end of the beam guide, gives a transmission of >80% for first order neutrons, whilst reducing that of higher order neutrons to the order of 10^{-4}, resulting in a large reduction in the number of fast neutrons reaching the monochromator. Furthermore the compact monochromator, in combination with improved shielding material, reduces the amount of radiation scattered from the monochromator in the direction of the scattered neutron beam. A redesigned analyser has seven pyrolytic graphite vanes, rather than the conventional single flat plate, allowing focussing of each individual vane onto the micro-strip area detector. Such horizontal focussing, allows monochromatic focussing without the need for the sample-analyser and analyser-detector distances to be equal, leading to a factor five increase in detected intensity. The ability to horizontally focus the detected neutrons gives an improved E resolution, in comparison to conventional triple axis machines.

Initially the sample was mounted on a M4 aluminium pin in an orientation such that the a^*-b^* plane lay in the scattering plane. A series of constant energy scans, as described above for the case of the IN8 work, were then performed at energy

transfers of 3,4.5 and 6 meV, close to the zone centre. The scan performed at a constant energy of 3meV is shown below.

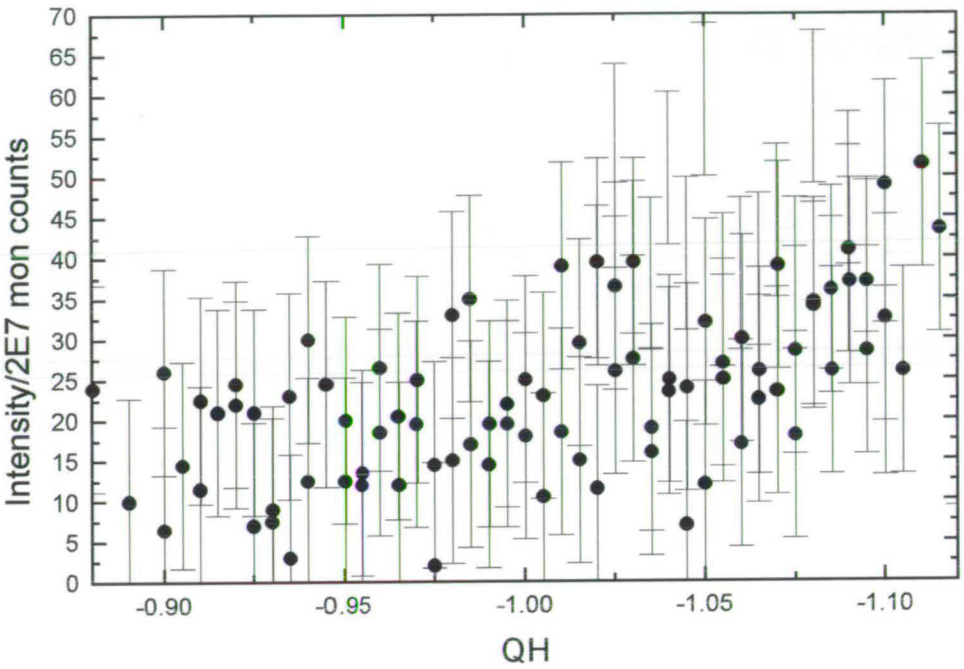

Figure 4.13 Plot of intensity vs. QH at an energy transfer of 3meV (scan taken at 10K)

Despite the large reduction in background counts, as can be seen by the large error bars, it remains difficult to discern the nature of any dispersion present. Further scans were performed, this time in constant q mode, scanning both at the zone centre and close to it. A scan performed at q = (-1,-1,-1.5) is shown below.

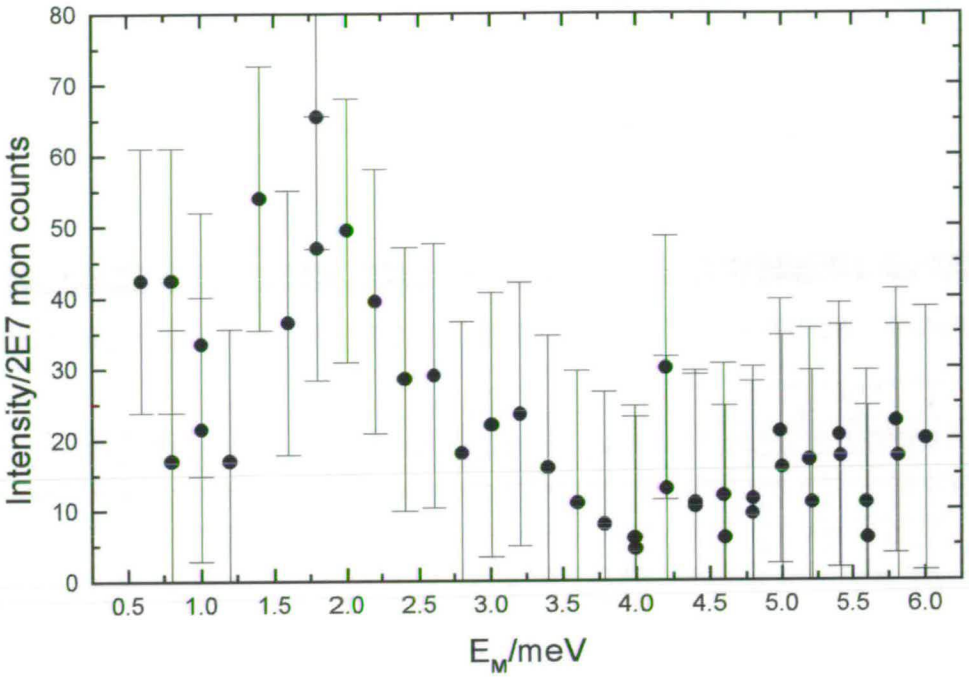

Figure 4.14 Constant q scan performed at the zone centre(-1,-1,-1.5) at 10K

Whilst the error bars are again significant in this case the presence of an excitation at around 2meV is certainly possible. Such a feature is of much lower energy than that predicted for the zone boundary energy and so may well be phononic in character, or indeed a magnetic mode of the main acoustic branch, reflected about the zone boundary. However cryogenic problems meant that it was not possible to perform further scans at higher temperature to determine whether such an excitation was phononic in character, within the time allocated for the experiment.

4.4 Summary

Despite the size of the crystal of potassium jarosite available, a large amount of information has been gleaned regarding the nature of the magnetic ground state in this system. The work performed using the D10 instrument has allowed determination, not only of the crystallographic and magnetic unit cells, but insight into the behaviour of the system as it approaches the transition temperature. Whilst it would be expected to show a crossover from 2D to 3D behaviour as the transition temperature is approached it would appear, from the sub-lattice magnetisation scans performed, that this is not the case. Instead the system remains rigorously 2D in nature, with the dominant exchange pathways in the kagome planes, even close to the Néel temperature. This may also reflect the fact that, as evidenced in the dc susceptibility, there are in fact two transition points and, despite the greatly reduced intensity of reflections above 60K, the limit of the scans performed may well be in the intermediate region between the two transition points. It was to be hoped that CRYOPAD could be used to determine the intermediate structure, however this proved impossible.

The result from the CRYOPAD experiment is the first conclusive demonstration of the coplanar nature of the magnetic ground state, which is of great significance in light of previous theoretical predictions regarding the nature of the magnetic ground state. It is consistent with the determined value of the critical exponent of magnetisation, β, which is indicative of 2D X-Y or 2D planar Heisenberg behaviour.

As far as the excitations are concerned neither of the triple axis experiments produced any significant results regarding the nature of any spin wave dispersion. The combination of the size of the crystal, considerable hydrogen content and background

from the glue used to secure the crystal on the pin, meant that the errors associated with each measurement made them indeterminate. Impractical scan times would be required to try and boost the signal to noise ratio sufficiently to make the scans meaningful. The constant q scan shown in figure 4.12 gives the suggestion of an excitation present at an energy transfer of 2meV, though further investigation of the nature of this excitation, in particular by warming to see whether it is of magnetic origin was not possible.

Future experiments require larger crystals of jarosite samples, either natural or laboratory grown, in order to learn more about the nature of the excitations present in such materials.

References

[1] M.G.Townshend, G.Longworth and E.Roudaut, *Phys. Rev. B* **33** 4919 (1986); T.Inami, S.Maegawa and M.Takano, *J.Mag.Magn.Mat.* **177-181** 752 (1998); A.S.Wills, A.Harrison, S.A.M. Mentink, T.E.Mason and Z.Tun, *Europhys. Lett.* **42**(3) 325 (1998); G.S.Oakley, D.Visser, J. Frunske, K.H.Andersen, A.S.Wills and A.Harrison, *Physica B* **267-268** 142 (1999)

[2] C.Hartig, P.Brand, K.Bohmhammel, *Neue Hutte* **35** 205 (1990); A.Martin and A.Feltz, *Z.Anorg.Allg.Chem.* **575** 115 (1989)

[3] R.S.Sapieszko, R.C.Patel and E.Matijevic, *J.Phys.Chem.* **81** 1061 (1977)

[4] Both refinements were carried out by Dr. G.J.McIntyre of the ILL

[5] See *'Magnetic Properties of Layered Transition Metal Compounds' ed.* L.J. de Jongh (Kluwer Academic, 1990)

[6] S.T.Bramwell and P.C.W.Holdsworth, *J.Phys.:Conden. Matter* **5** L53 (1993); S.T.Bramwell and P.C.W.Holdsworth, *J.Appl. Phys.* **73**(10) 6096 (1993)

[7] J.T.Chalker, P.C.W.Holdsworth and E.F.Shender, *Phys. Rev. Lett.* **68** 855 (1992)

[8] F.Tasset, *Physica B* **156-157** 627 (1989); P.J.Brown, J.B.Forsyth and F.Tasset, *Proc. R. Soc. London A* **442** 147 (1993); F.Tasset, P.J.Brown, E.Leliévre-Berna, T.Roberts, S.Pujol, J.Allibon and E.Bourgeat-Lami, *Physica B* **267-268** 69 (1999)

[9] M.Blume, Phys. Rev. **130**(5) 1670 (1963)

[10] Analysis of the data was performed by Dr. E.Lelièvre-Berna

[11] A.B.Harris, C.Kallin and A.J.Berlinsky, *Phys. Rev. B* **45** 2899 (1992); A.Chubukov, *Phys. Rev. Lett.* **69** 832 (1992)

[12] A.S.Wills, *PhD. Thesis*, University of Edinburgh (1996)

[13] T.E.Mason, K.N.Clausen, G.Aeppli, D.F.McMorrow and J.K.Kjems, *Can. J. Phys.* **73** 697 (1995)

Chapter 5 Deuteronium Iron Jarosite:S=5/2

5.1 Introduction

In the previous Chapter, a number of experiments were described, with the aim of investigating the nature of a single crystal sample of $KFe_3(SO_4)_2(OH)_6$, both in terms of its crystallography and magnetism. Whilst the hydronium salt $(H_3O)Fe_3(SO_4)_2(OH)_6$ possesses similar crystallographic properties, the nature of the magnetism seen in this compound is in complete contrast to that of the potassium salt. Neutron powder diffraction measurements show no evidence of long range order at all temperatures down to 2K. Instead a spin glass freezing transition is seen, as evidenced by a cusp in the dc susceptibility at around 13K, and also through a T^2 dependence in the specific heat [1]. Such a system, whilst displaying no three dimensional long range order, will however exhibit short-range two dimensional order with correlated regions of co-operative spins. Previous experimental work on hydronium samples [1-2] has shown the existence of such short range order, as evidenced by diffuse scattering, the shape of which can be modelled using a Warren function [3]. This function allows a determination of the length scale of the correlated regions, the breadth of the peak being proportional to the size of such regions. The observed diffuse scattering is a very weak feature, in relation to nuclear Bragg scattering, and so is difficult to assess with any precision from conventional powder diffraction data. What was proposed therefore was to look at the nature of this diffuse scattering in more detail, using polarisation analysis as available on the D7 spectrometer at the ILL in Grenoble [4]. This instrument allows determination of the

various components of scattering, by monitoring the effect of moments within the sample on the polarised incident neutrons. The ratio of spin-flipped to non-spin flipped neutrons emerging from the sample along all three directions (*xyz*) is measured, which in turn allows a determination of the magnetic contribution to scattering over a wide Q range ($0.25 \leq Q \leq 4\text{Å}^{-1}$).

Whilst the size of the correlated regions is important in determining the nature of dynamic scattering on the approach to T_f, it is also of interest to determine the degree of spin fluctuations as the system is cooled towards T = 0. A conventional picture of a spin glass involves blocks of correlated spins gradually freezing out, as the sample is cooled, with continued fluctuations within such blocks of spins down to very low temperatures. Muon spin relaxation studies [1,5] suggest that the hydronium system is still dynamic down to temperatures of 2K, though the timescale of such measurements is such that very fast fluctuations will not be seen by the implanted muon before it decays. Neutron spin echo measurements, as described in detail later in this Chapter, provide a complementary technique to muon studies, as well as affording the chance to look at faster fluctuations on a timescale down to the order of nanoseconds. Previous measurements on the strongly frustrated antiferromagnet SCGO(x), suggested that the system was frozen, at least on the instrumental timescale, below a temperature of 2K [6]. It was therefore proposed to look at a sample of deuteronium iron jarosite on the neutron spin-echo spectrometer IN11 at the ILL, in order to assess the nature of spin freezing in this system.

5.2. XYZ 3-directional polarisation analysis

In order to probe the spatial extent of correlated spins in the hydronium iron jarosite system, experimental work was performed on the D7 spectrometer at the ILL. The D7 instrument uses a polarised incident neutron beam, that is to say that a guide field is applied to the incident beam in order to orientate the direction of polarisation of the neutrons along the axis of the applied field, usually in the *z* direction (perpendicular to the beam propagation direction). A beam polarisation of better than 90% is achieved through the use of supermirrors. Any scattering of the neutrons by magnetic moments in the sample will result in a 'spin-flip' or change in the polarisation direction of the neutron beam and such changes can be monitored by the use of further supermirrors aligned in front of the detector banks. The instrumental set-up is shown below.

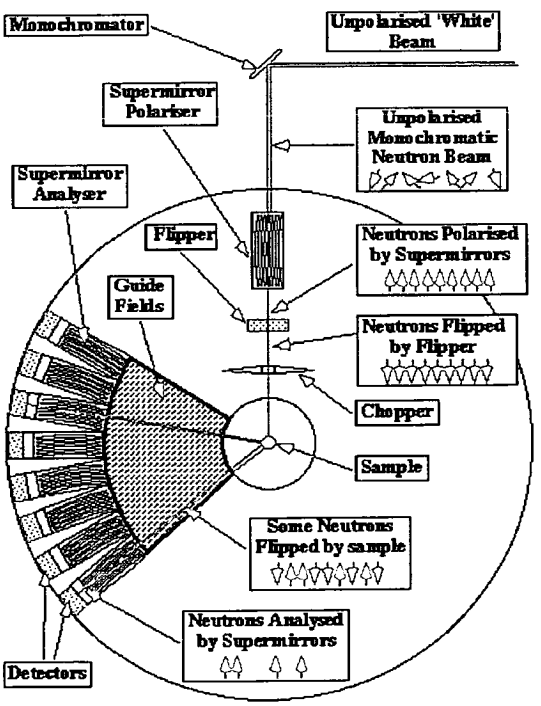

Figure 5.1 Schematic lay out of the D7 spectrometer. For the case of XYZ 3-directional polarisation the chopper is removed

Mezei π flippers in the vicinity of the sample flip the incident polarised neutron beam by $\pi/2$ and, following scattering from the sample, by a further $-\pi/2$; this allows a determination of the nature of spin-flip and non-spin flip scattering. Since spin-flip scattering can only occur as a result of interaction with magnetic moments the ratio of incident (non-spin flip) to detected (spin-flip) neutrons determines the magnitude of any magnetic scattering which takes place. Calibrations using both vanadium (a coherent scatterer) and quartz (a non-magnetic scatterer) samples allows further separation of the detected signal into coherent and incoherent, non-magnetic and magnetic scattering. A deuterated rather than protonated sample was used in the experiment since the large incoherent component to scattering from protonated samples would mask the weak diffuse scattering from the sample.

5.3 D7 Measurements

5.3.1 Sample preparation

Batches of $(D_3O)Fe_3(SO_4)_2(OD)_6$ were prepared by dissolving stoichiometric amounts of $Fe_2(SO_4)_3.xH_2O$ (Putratronic, 99.999%) in D_2O with gentle heating, the solvent then being removed by rotary evaporation. The resulting paste was then redissolved in D_2O and heated in a PTFE lined Parr bomb at 120°C in a precision oven for 48 hours. The precipitate obtained was scraped off the walls of the bomb and filtered under suction in a glove bag filled with dry nitrogen, so as to avoid deuterium-hydrogen exchange. The product was then dried overnight in a vacuum oven at 120°C.

To determine the phase purity of the sample, each batch was loaded into an airtight sample holder and X-ray diffraction patterns taken over a range of 10-120° in two theta. Rietveld refinement of the data using GSAS confirmed the samples were single

phase with space group $R\ \bar{3}\ m$. Samples were also loaded into gelatine capsules and dc-susceptibility measurements performed. Each sample revealed a sharp cusp at 13.8K and a divergence in the zero field cooled and field cooled behaviour in line with previous measurements [1,2]. A sample of $KFe_3(SO_4)_2(OD)_6$ was also prepared. In this case K_2SO_4 (2.88g) and $Fe_2(SO_4)_3.5H_2O$ (23.68g) were dissolved in 100ml of D_2O. The solvent was then removed by rotary evaporation and the remaining solid redissolved in 100ml of D_2O, with addition of 0.49g of D_2SO_4.This solution was then transferred to a stainless steel bomb with PTFE lining and the bomb placed into a precision furnace at 140±0.5°C for 24 hours. The resultant dark yellow precipitate was filtered off under nitrogen, washed with D_2O and dried thoroughly in a vacuum oven. Sample characterisation was carried out as described for the case of the deuteronium sample, results being in line with that seen previously.

5.3.2 D7 Experimental

The sample of $(D_3O)Fe_3(SO_4)_2(OD)_6$ (10.8g) in an annular vanadium can was loaded into an ILL 'Orange' cryostat and cooled to a base temperature of 2K. Scans were then performed at a series of temperatures below and above the freezing transition. The sample of $KFe_3(SO_4)_2(OD)_6$ (10.5g) was then loaded into a similar cylindrical vanadium can and a series of scans performed both below and above the magnetic transition temperature of *ca.* 65K.

The calculated magnetic component of scattering at each temperature is plotted as a function of Q (where $Q = 2\pi/d$ in $Å^{-1}$) in the figure below.

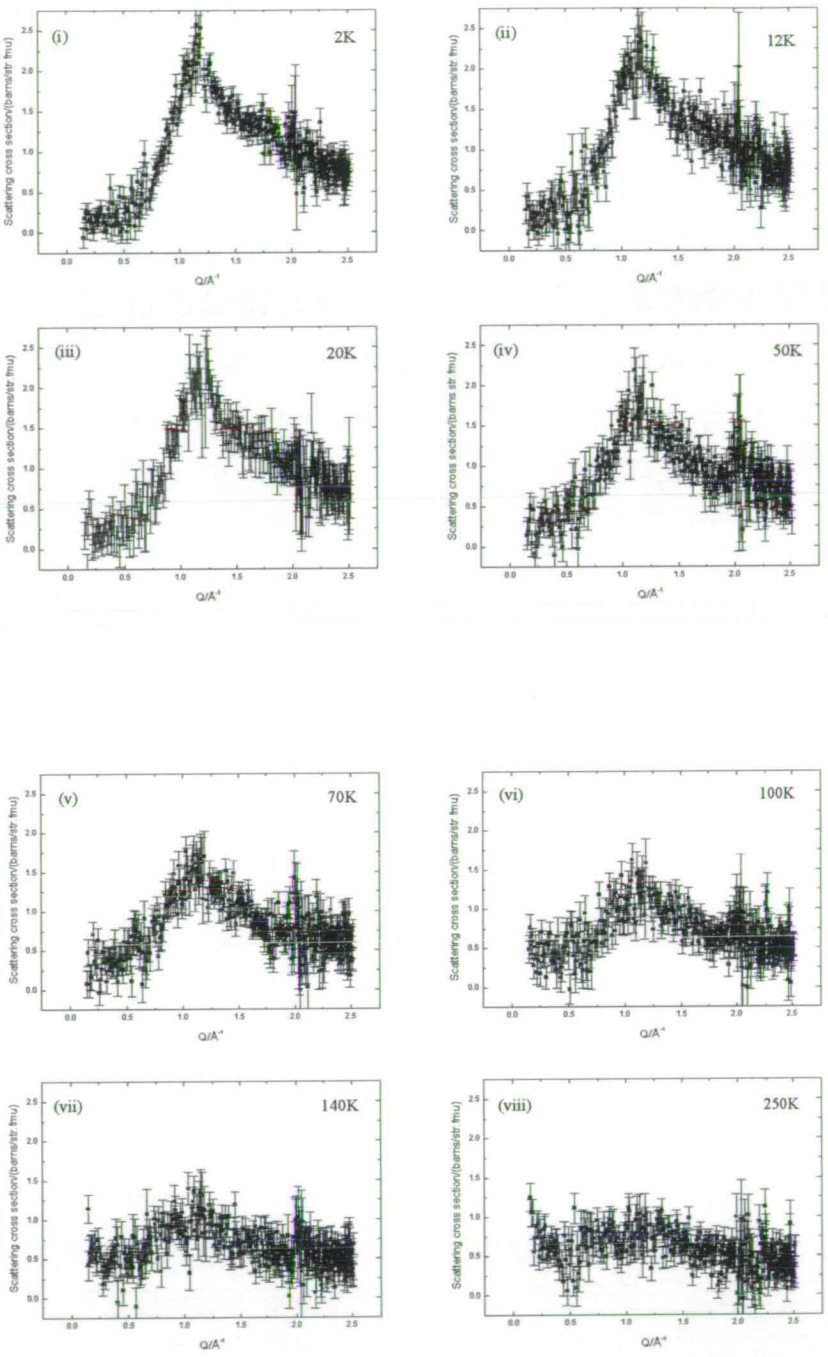

Figure 5.2 Plots of magnetic scattering cross section vs. Q as measured for the sample $(D_3O)Fe_3(SO_4)_2(OD)_6$ at (i)2K, (ii)12K, (iii)20K, (iv)50K, (v)70K, (vi)100K, (vii)140K and (viii)250K respectively

As can be seen at 2K the magnetic scattering is diffuse, with a 'Warren-like' function centred about *ca.* 1.1Å. As the sample is warmed through T_f (= 13.8K) so the diffuse scattering broadens considerably, and the Warren function is progressively lost, though the amount of diffuse scattering is significant up to a temperature of 100K. Whilst the major feature in the data is seen at around 1.1Å, there would also appear to be a smaller feature at around 2Å. However it is of very much lower intensity than the scattering seen at 1.1Å and may well be an artefact of the vanadium calibration performed, and so will not be considered in this study. Data collected at higher Q, in the range 2.5 - 4Å^{-1} were not of a comparable quality to allow the two datasets to be combined and so attention was focussed solely on the lower Q data as shown above.

In an effort to determine the spatial extent of the spin correlations, fitting of the data to a Warren function [3] was performed, as defined by

$$P_{2\theta} = Km\frac{F_{hk}^2(1+\cos^2 2\theta)}{2(\sin\theta)^{3/2}}\left(\frac{L}{\lambda\sqrt{\pi}}\right)^{1/2} F(a).[J(2\theta)]^2 \qquad (5.1)$$

where

$$a = \left(\frac{2\sqrt{\pi}L}{\lambda}\right)(\sin\theta - \sin\theta_0) \qquad (5.2)$$

and

$$F(a) = \int_0^{10} \exp[-(x^2 - a)^2]dx \qquad (5.3)$$

where L is the spin correlation length, λ the wavelength, K a scaling constant, m the multiplicity of the reflection, F_{hk} the two-dimensional structure factor for the spin array, $[J(2\theta)]^2$ the magnetic form factor and θ_0 the peak centre.

In each case the data were edited so as to consider only the region below 2Å, to avoid a spurious weighting to the data, and fitting performed *via* a least squares method, with five iterations, with a fixed peak centre of 1.17Å and varying background, peak intensity and peak width. The position of the peak centre was determined from fitting to the 2K dataset, with manual iteration to find the best fit. The fitted parameters and associated errors are listed in the table below.

T/K	Background/ barns(str.fmu)$^{-1}$	Intensity/ barns(str.fmu)$^{-1}$	Correlation length ξ/Å	Reduced χ^2
2	0.29± 0.04	1.50± 0.06	11.47± 0.28	1.55
12	0.25± 0.05	1.57± 0.07	10.84± 0.31	1.31
20	0.37± 0.04	1.44± 0.05	10.70± 0.30	1.64
50	0.34± 0.03	1.20± 0.05	9.82± 0.30	1.13
70	0.35± 0.04	1.03± 0.05	9.46± 0.33	0.99
100	0.42± 0.03	0.67± 0.05	9.51± 0.49	1.14
140	0.35± 0.05	0.63± 0.07	7.54± 0.34	1.09
250	0.37± 0.07	0.46± 0.09	7.13± 0.43	1.14

Table 5.1 Results of fitting Warren function to data taken from $(D_3O)Fe_3(SO_4)_2(OD)_6$ as a function of temperature in the range 2 – 250K

The temperature dependence of the spin correlation length ξ is shown in figure 5.3 below. The relation between the size of the correlation length (ξ) and temperature (T) of the sample is seen to be of the form $\xi \propto T^{-x}$, but it is not possible from this data to determine the value of x with any degree of accuracy. Recent work [7] suggests that the correlation length will diverge as $T^{-1/2}$ but much more extended studies would be required to verify whether this relationship holds in this case. As can be seen, spin correlations of the order of 7Å at 250K rise to a value of the order of 11Å at 2K. The former is of the order of the distance between opposing ions within an individual hexagon of Fe spins, whilst the latter coincides with the furthest distance between

points on an individual kagome 'star'. These two distances are shown in figure 5.4 below.

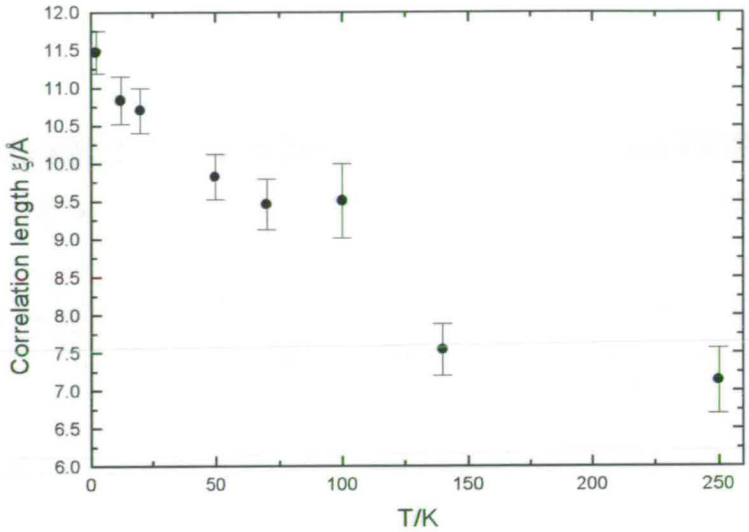

Figure 5.3 Plot of correlation length ξ versus temperature obtained for the sample $(D_3O)Fe_3(SO_4)_2(OD)_6$

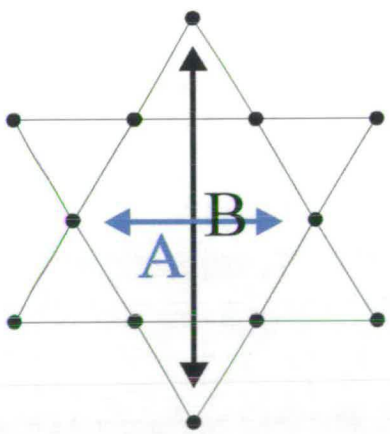

Figure 5.4 Illustration of the distances within a kagome star. Distance A(blue) is of the order of 7Å, whilst distance B(black) is of the order of 11Å

Thus the data suggests that as the system is cooled towards T_f there is a build up of spin correlations such that collective motion of spins extends from individual

hexagons of spins to complete kagome 'stars'. This is consistent with the idea of blocks of 'islands' of spins where a degree of order is frozen in as the sample is cooled, such islands existing within a matrix where there are still considerable spin fluctuations even at low temperatures. Such fluctuations will persist since there is no energy cost in facile motion of blocks of spins within the framework of the lattice. It is also in agreement with the predicted behaviour of 2D layered magnetic systems where the in-plane spin-spin correlation length is expected to fall away on warming through T_f.

In the case of the potassium salt, the observed magnetic scattering cross-sections are shown below.

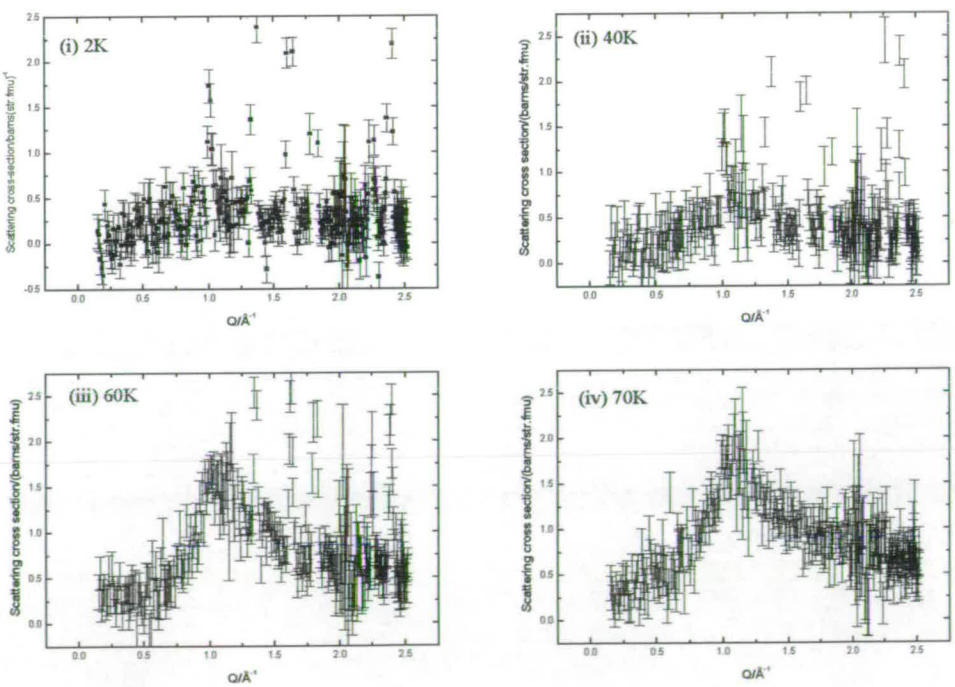

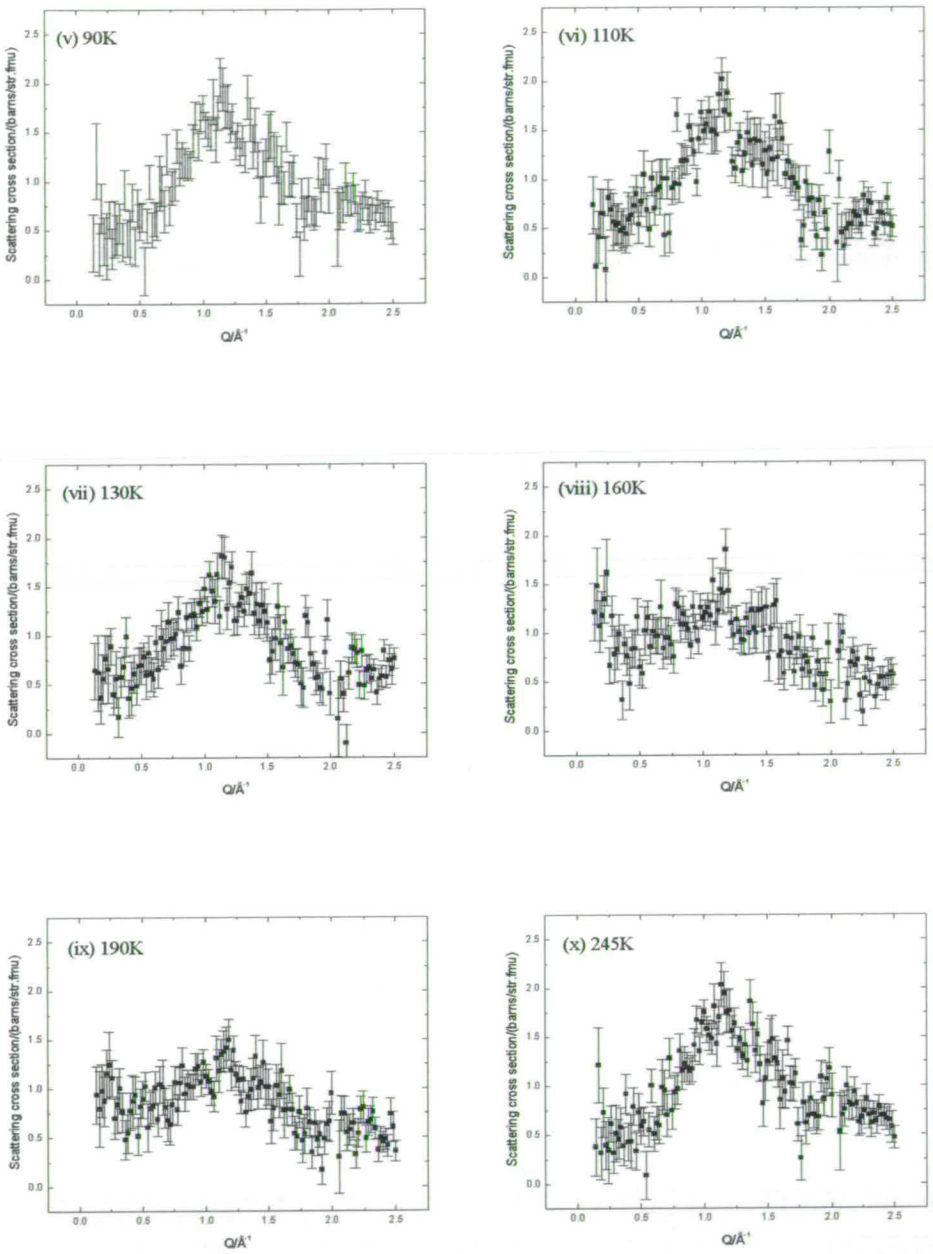

Figure 5.5 Magnetic scattering cross-section in the sample $KFe_3(SO_4)_2(OD)_6$ at temperatures of (i)2K (ii)40K (iii)60K (iv)70K (v)90K (vi)110K (vii)130K (viii)160K (ix)190K and (x)245K respectively

The data were treated as per the deuteronium salt, with least-squares fitting performed with a fixed peak centre of 1.13Å, determined in a similar fashion to that described above, and varying background, peak width and intensity. The results are given in the table below.

T/K	Background/ barns(str.fmu)$^{-1}$	Intensity/ barns(str.fmu)$^{-1}$	Correlation length ξ/Å	Reduced χ^2
2	0.13±0.05	0.32±0.06	9.33±1.12	2.18
40	0.24±0.03	0.40±0.04	11.44±1.01	1.60
60	0.30±0.03	0.92±0.04	11.39±0.45	1.22
70	0.41±0.04	0.99±0.06	10.67±0.64	1.39
90	0.49±0.06	0.97±0.07	10.31±0.51	1.04
110	0.57±0.06	0.81±0.07	10.16±0.60	1.38
130	0.62±0.05	0.68±0.06	11.10±0.78	1.01
160	0.89±0.05	0.25±0.06	10.86±2.08	1.31
190	0.82±0.05	0.28±0.06	11.05±1.87	0.92
245	0.49±0.06	0.97±0.07	10.31±0.51	1.04

Table 5.2 Results of fitting Warren function to data taken from $KFe_3(SO_4)_2(OD)_6$ as a function of temperature in the range 2 – 245K

The data obtained at the highest temperature of 245K was taken in half the time of all other measurements, and so will be ignored in the proceeding discussion. The temperature dependence of the spin correlation length ξ is very different from that of the deuteronium case. For the potassium salt there is a rise in correlation length on warming the sample through T_N and correlations persist all the way up to 245K with little change in size, if the error bars associated with the fitted values are taken into account. Thus even at high temperatures there are large regions of correlated spins of size comparable to that of an individual kagome 'star'. Such persistent correlated regions are of interest since this is in complete contrast to the behaviour expected of a conventional 2D magnet, where correlations should decrease on warming through T_N.

What is strange in this case is that the intensity of the diffuse feature falls on warming, and its breadth increases, consistent with a reduction in the number of correlated regions, and their size. Thus it may be that the values obtained are simply an artefact of the fitting routine. However if the fitted values are believed then it can be shown to be consistent with the work of Harris [8] which suggests that the higher temperature susceptibility behaviour is non Curie-Weiss in a temperature regime between 150 and 350K. It may therefore be the case that the temperature independence of the correlation length reflects the fact that correlated regions persist over a very wide temperature regime.

5.4 Neutron Spin Echo : Introduction

The neutron spin echo technique relies on the fact that a neutron which experiences an applied magnetic field will precess about that field with a frequency known as the *Larmor frequency*. If a field, H_0, is applied parallel to the z-axis, and an incident neutron beam initially polarised along this axis is then 'flipped' so as to be polarised along the x-axis, then Larmor precession will occur such that the angle of precession is described by

$$\phi = \frac{\gamma_L l H_0}{v} \tag{5.4}$$

where the Larmor frequency γ_L = 29.2 $MHzT^{-1}$, v is the neutron velocity, and l the distance travelled by the neutron. Though the neutron beam depolarises as a result of

this precession, if a reverse field, H_1, is applied then the neutrons will precess in the opposite direction, until at the point where

$$H_0 l_0 = H_1 l_1 \tag{5.5}$$

(l_0 being the distance neutrons travel in applied field H_0, l_1 the distance travelled in applied field H_1.) the beam will be fully polarised in the x direction once more. Such a recovery of polarisation is known as a *spin echo* [9]. Such spin echo signals give a measure of the function $I(\vec{\kappa},\tau)$ which is related to the neutron scattering function $S(\vec{\kappa},\omega)$ by the expression

$$I(\vec{\kappa},\tau) = \hbar \int S(\vec{\kappa},\omega)\cos[(\omega-\omega_0)\tau]d\omega \tag{5.6}$$

where $\hbar\omega_0$ is the mean energy transfer on scattering and τ is a time constant. Provided that the energy transfer $\hbar\omega_0$ is small compared with the energy, E, of the neutron then

$$\tau = \frac{\hbar\phi}{2E} \tag{5.7}$$

The range of values of τ is of the order of 10^{-9} – 10^{-11}s, achieved by varying the applied fields H_0 and H_1, giving correlation functions in reciprocal space on similar time scales. Thus the amplitude of the paramagnetic neutron spin echo (NSE) measured at a time t gives a direct measure of the real part of the intermediate scattering law $S_m(Q, t)$ for fluctuations of wavevector Q [10-13].

5.5 Experimental

5.5.1 Sample preparation

The sample prepared in the previous section for the work performed on the D7 instrument was also used for the experiment on IN11.

5.5.2 Spin echo experimental

The sample of $(D_3O)Fe_3(SO_4)(OD)_6$ (10g) was loaded into an annular aluminium sample can, placed in an *ILL* 'Orange' cryostat on the polarised neutron spectrometer IN11 at ILL and the wavelength set at 5.7Å. For all measurements, Q was fixed at 1.35 $Å^{-1}$, which is as close as possible to the maximum in S(Q) for the magnetic diffuse scattering, whilst avoiding any significant contribution from nuclear Bragg scattering. The normalised instrument resolution function was determined using a quartz sample as a calibrant and the NSE signal measured for values of t ranging from 9.7 to 870ps, and temperatures from the base experimental temperature of 1.5K to 60K.

5.5.3.Results

The results obtained are shown in figure 5.6, for temperatures spanning the freezing transition temperature T_f (as determined by dc susceptibility measurements). Data taken at temperatures above 20K have not been included since the experimental time available meant that only poor quality statistics were obtained.

Despite the poor signal to noise ratio the data suggests that the system is dynamic at 20K, on a time scale of the order of 100ps, and gradually freezes as it is cooled, until at 2K the value of $S_m(Q, t)$ tends to $S_m(Q, t=0)$ indicating that all moments are frozen on time scales up to 870ps. This freezing transition is present in a slightly different form in figure 5.7 below. In this case the NSE amplitude is displayed, for values of t equal to 87 and 870ps respectively, as the sample was cooled over a range of 60K down to 1.5K.

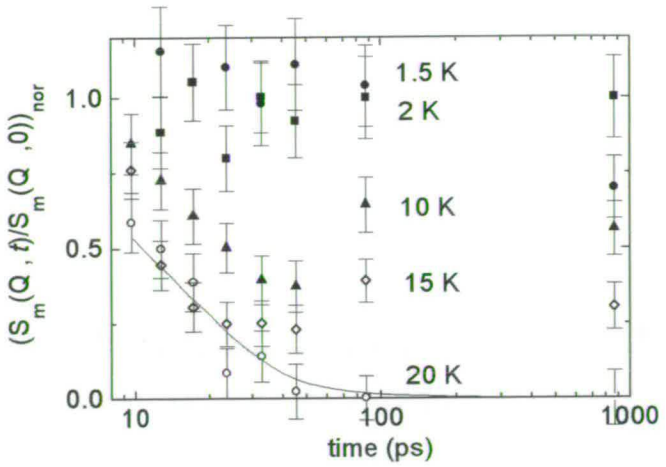

Figure 5.6 Time dependence of the NSE amplitude, normalised to the magnetic structure factor $S_m(Q,t=1)$ and corrected for the instrumental resolution, as the sample is cooled through the freezing transition. The various temperatures are denoted by filled circles (1.5K), filled squares (2K) filled triangles, (10K), open triangles (15K) and open circles (20K), and the line through the 20K data set shows the least-square fit of an exponential decay to the data.

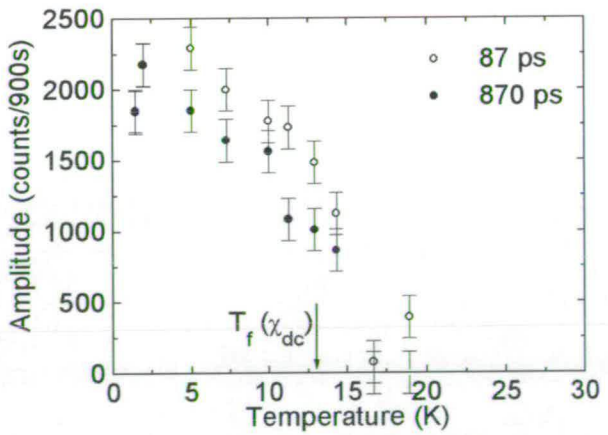

Figure 5.7 Temperature dependence of the NSE amplitude, corrected for the instrumental resolution measured with quartz, for delay times of 87 ps (open circles) and 870 ps (closed circles).

The gradual freezing transition suggested by these measurements is consistent with that seen in 'conventional' spin glass systems, where a broad distribution of relaxation times is seen spanning a temperature range from well below to well above T_f. For such glassy systems, the short-time component is generally found to adopt a Kohlrausch 'stretched' exponential form [10,11] as given by

$$S(Q,t)/S(Q,0) = \exp(-(t/\tau))^{\beta} \qquad (5.8)$$

where τ is the macroscopic relaxation time and β reflects the trajectory the system takes through phase space in its attempt to overcome a succession of energy barriers. Whilst the data obtained are not of sufficient quality to determine the values of both τ and β unambiguously in an unconstrained fit, the data obtained at 20K was fitted using a simple exponential (with $\beta = 1$), yielding a value of $\tau = 15 \pm 1$ps.

5.6 Summary

The diffuse scattering results obtained are in broad agreement with previous theoretical predictions [14]. Monte Carlo simulations show a broad feature centred at around 1.1Å, with further order scattering at larger Q. The data obtained show such a feature at 1.1 Å, but it is not possible to make a definitive statement about the higher Q data obtained due to the poor statistics. Whilst analysis using a Warren function allows a handle on the nature of correlations in these systems, it is clearly a simplification since there is, at least in principle, diffuse scattering associated with all the reflections pertinent to the kagome planes.

The results of both the diffuse scattering work on the D7 instrument and the spin echo work on the IN11 spectrometer allow a fuller description of the nature of the

hydro(deutero)nium salt to be made. The results from the work on D7 highlight the differences between the parent mineral potassium jarosite and its hydronium analogue. In the case of the latter, regions of correlated spins grow as the sample is cooled towards T = 0, with a spin correlation length corresponding to an individual kagome 'star' developing at T = 2K. This is consistent with the behaviour of other 2D layered systems. The spin echo results however show that the freezing of moments is much slower than would be expected in the case of conventional behaviour, with spin fluctuations persisting below T_f. It is only at 2K that all the spins appear frozen on a timescale of 870ps. This suggests that whilst there may be fluctuations at this temperature any such fluctuations do not involve large blocks of spins. It also fits in with the picture of a non-ergodic free energy landscape where the system becomes stuck in an energy 'valley' where there are insufficiently large spin fluctuations to allow the system to explore further in configurational space.

In the case of the potassium salt however there appears to be only a small temperature dependence in the spin correlation length, this increasing slightly as the sample is warmed through T_N. Thus even at warm temperatures there are regions of correlated spins and these remain down to low temperatures. Further measurements are needed in order to determine both the validity of the present results, and also whether such spin correlations will eventually fall away at higher temperatures. It is also of interest to monitor whether the reduction in the intensity of the diffuse scattering on cooling towards 2K is mirrored by the rise in the intensity of Bragg scattering, and thus how much spin disorder remains at low temperatures. It is still unclear why there are such differences between the potassium and hydronium salts.

References

[1] A.S.Wills, *PhD. Thesis*, University of Edinburgh (1996)

[2] A.S.Wills, A.Harrison, S.A.M. Mentink, T.E.Mason and Z.Tun, *EuroPhys. Lett.* **42** 325 (1998)

[3] B.E.Warren, *Phys. Rev.* **59** 693 (1941)

[4] O.Scharpf and H.Capelmann, *Phys. Stat. Sol. A* **135** 359 (1993)

[5] A.Harrison, A.S.Wills, D.Visser and J.S.Lord, *ISIS Annual Report* RB7838 (1996)

[6] Y.Uemura, B.D.Gaulin, M.Mekata, I.Mirebeau, J.L.Thoulence and S.Pouget, *J.Mag. Magn. Mats.* **177-181** 701 (1998)

[7] D.A.Garanin and B.Canals, Phys. Rev. B 59(1) 443 (1999)

[8] A.B.Harris, C.Kallin and A.J.Berlinsky, *Phys. Rev. B* **45**(6) 2899 (1992)

[9] F.Mezei, '*Neutron Spin Echo*', Lecture Notes in Physics Vol. 122 (Springer-Verlag, 1980)

[10] F.Mezei, A.P.Murani *J.Mag. Magn. Mats.* **14** 211 (1979)

[11] B.V.B.Sarkissan, *J.Phys.C:Cond.Mat.* **2** 7873 (1990)

[12] R.G.Palmer, D.L.Stein, E.Abrahams, P.W.Anderson, *Phys. Rev. Lett.* **53** 958 (1984)

[13] F.Mezei, W.Knaak, B.Farago, *Phys. Rev. Lett.* **58** 571 (1987)

[14] J.N.Reimers, *Phys. Rev. B* **46**(1) 193 (1992)

Chapter 6 Further jarosite systems

6.1 Neutron powder diffraction studies

The nature of the magnetic exchange exhibited in the family of jarosites has been shown to be very complex [1]. The different competing exchange pathways make it difficult to unravel exactly which interactions dominate the exchange Hamiltonian at any given point. Whilst the value and nature of J will dominate the Hamiltonian at high and low temperatures, that of J' and J'' may well become significant in the region of T_N. Clearly, substitution of the A cation can be seen to radically change the magnetic properties of a given material as evidenced by the vastly different behaviour of the K^+ and H_3O^+ iron salts [Chapters 4,5]. Whilst this '*order by disorder*' effect may be explained in terms of a reduction in the coverage of magnetic sites in the lattice appearing to lead to long-range order, it is also of importance to consider the very subtle balance between both nearest-neighbour and next-nearest neighbour exchange pathways. The figure below illustrates the various exchange pathways surrounding an individual iron atom. Within the kagome planes an iron atom (1) may interact with second (3) and third (4) nearest neighbours through hydrogen-bonded interactions *via* hydroxy and sulfate groups; superexchange with nearest neighbours (2) through a covalent bond [O(1)] is also possible. Exchange with an atom (5) in a neighbouring plane through hydrogen-bonded interactions involving the sulfate group is also possible.

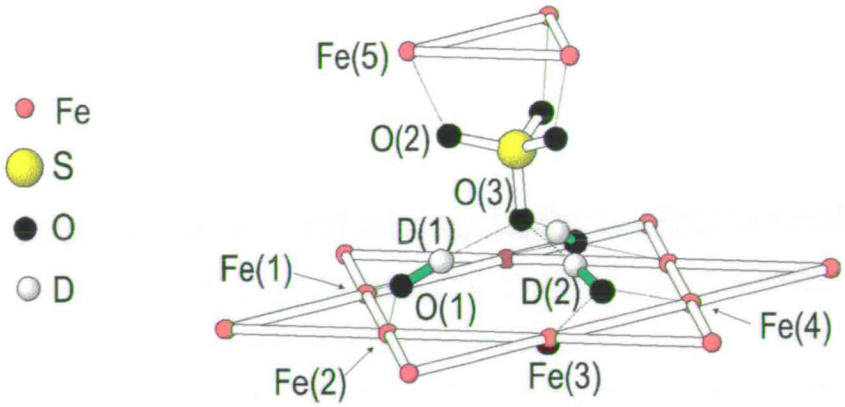

Figure 6.1 Local exchange pathways surrounding an individual iron atom in the jarosite structure.

It is clear that there is a very fine balance between the various exchange pathways, both in the kagome planes and between such planes. Interlayer exchange *via* the linking sulfate groups may proceed in three different ways which are illustrated below.

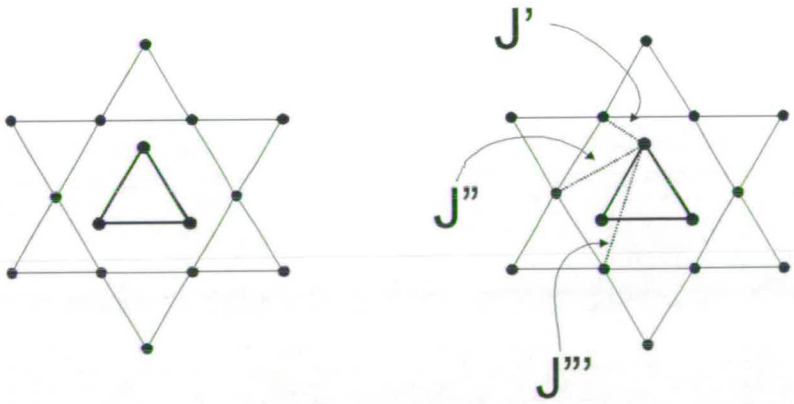

Figure 6.2 Illustration of the possible interlayer further neighbour exchange interactions

Thus J', J'' and J''' denote the first, second and third neighbour exchange interactions ranked according to the shortest through space distance between iron atoms. However it should be borne in mind that it is the nature of the *bonds* through which such interactions take place, rather than the through space distance, that is of importance. In an attempt to investigate the influence of interlayer exchange *via* the linking SO_4 groups, upon the magnetic properties of the system, samples of composition $KFe_3(SO_4)_2(OD)_6$, $KFe_3(CrO_4)_2(OH)_6$ and $KFe_3(SeO_4)_2(OH)_6$ were prepared for study on the D20 powder diffractometer at the ILL. The multidetector installed at the time allowed very high resolution, and optimised geometry meant a large flux, and thus short counting times for these samples.

6.2 Sample preparation

6.2.1 Synthesis of $KFe_3(CrO_4)_2(OH)_6$

K_2CrO_4 (3.88g) and $Fe(NO_3)_3.9H_2O$ (8.08g) were dissolved in 100ml of H_2O. The solution was stirred for 16 hours at 100°C. The resulting precipitate was filtered off, washed with distilled water and dried thoroughly at 120°C in a vacuum oven. The product (3.17g) was a fine orange powder.

6.2.2 Synthesis of $KFe_3(SeO_4)_2(OH)_6$

K_2SeO_4 (3.33g) and $Fe(NO_3)_3.9H_2O$ (30.3g) were dissolved in 100ml of D_2O. The solvent was then removed by rotary evaporation and the remaining solid redissolved in 100ml of D_2O. This solution was then transferred to a stainless steel bomb with PTFE lining and the bomb placed into a precision furnace at 140±0.5°C for 24 hours.

The resultant yellow precipitate was filtered off under nitrogen, washed with D_2O and dried thoroughly in a vacuum oven.

6.2.3 Synthesis of $KFe_3(SO_4)_2(OD)_6$

K_2SO_4 (2.88g) and $Fe_2(SO_4)_3.5H_2O$ (23.68g) were dissolved in 100ml of D_2O. The solvent was then removed by rotary evaporation and the remaining solid redissolved in 100ml of D_2O, with addition of 0.49g of D_2SO_4.This solution was then transferred to a stainless steel bomb with PTFE lining and the bomb placed into a precision furnace at 140±0.5°C for 24 hours. The resultant yellow-green precipitate was filtered off under nitrogen, washed with D_2O and dried thoroughly in a vacuum oven.

6.3 Sample Characterisation

Powder X-ray diffraction patterns of each sample were taken using a Philips PW1730 XRD (40mV,30mA Cu source [wavelength $K\alpha_1$ 1.541Å, $K\alpha_2$ 1.544Å]) details of which are given elsewhere [2]. Structural refinement of these data using the GSAS software package gave a good agreement with the $R\ \bar{3}\ m$ space group previously seen in other jarosite samples [2]. The refined lattice parameters and atom positions are summarised in Appendix B.

6.4 Magnetic susceptibility measurements

Susceptibility data were taken using a dc SQUID magnetometer (Quantum Design). In the case of the $KFe_3(SO_4)_2(OD)_6$ sample (93.6mg) data were taken over a temperature range of 6 – 350K in an applied field of 10000G. The resulting χ-T plot shows a distinct cusp at 65K with a broader maximum seen at 56K [2]. The sample of

$KFe_3(CrO_4)_2(OH)_6$ (15.1mg) was run in a similar fashion, the results of which are shown below in figure 6.3. The figure also contains plots of both the inverse susceptibility versus temperature and the effective moment versus temperature. In the case of the $KFe_3(SeO_4)_2(OH)_6$ (5.0mg) the data obtained is shown in figure 6.4 below. Similar plots are shown to those of the Cr sample. In the case of the sulfate and selenate salts measurements were performed on cooling both in zero field and in a field of 1000G, a difference between the two being indicative of some degree of spin glass behaviour.

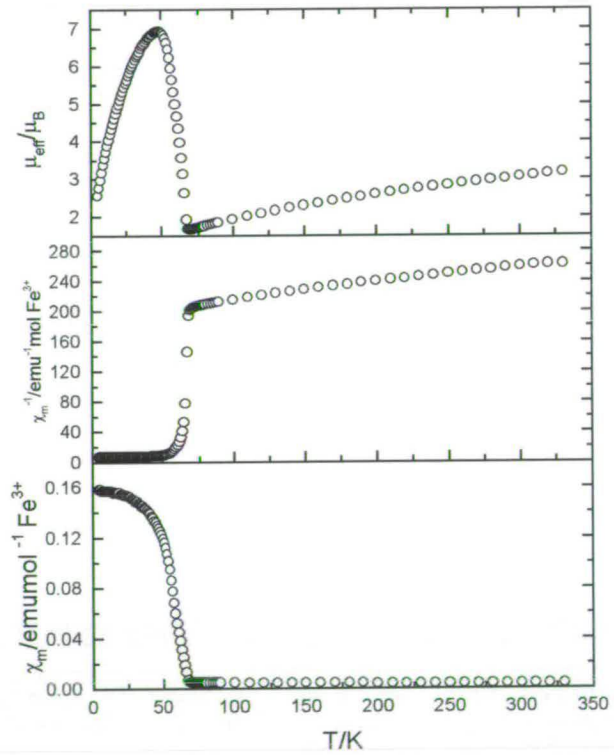

Figure 6.3 dc susceptibility data for the $KFe_3(CrO_4)_2(OH)_6$ sample. Plots of molar susceptibility versus temperature (lower graph), inverse susceptibility versus temperature (middle graph) and effective moment versus temperature (upper graph) are shown.

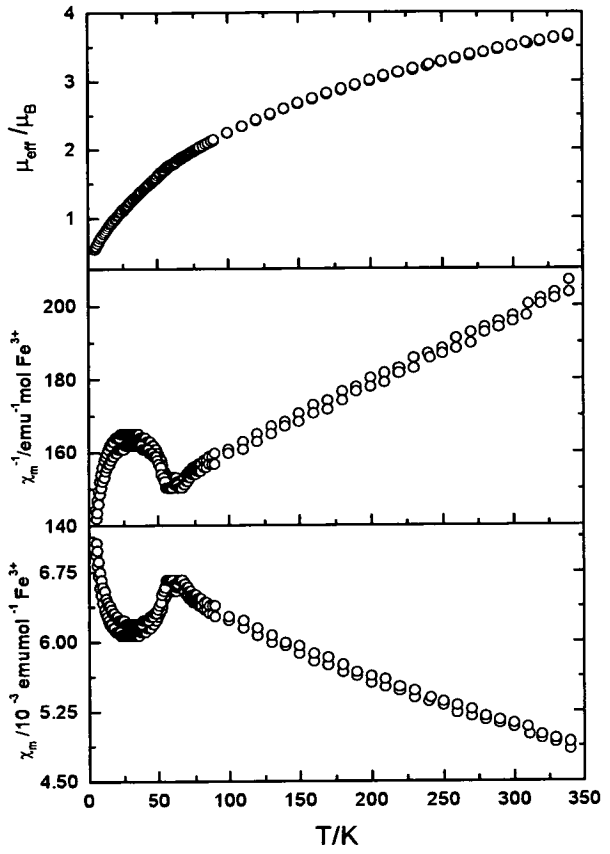

Figure 6.4 dc susceptibility data for the $KFe_3(SeO_4)_2(OH)_6$ sample. Plots of molar susceptibility versus temperature (lower graph), inverse susceptibility versus temperature (middle graph) and effective moment versus temperature (upper graph) are shown.

An estimate of the value of the Curie-Weiss theta θ_{CW} was obtained from the plot of inverse susceptibility versus temperature for each salt over a temperature range of 150-300K. These values, along with the values of the Curie constant C and the effective moment ($C = \mu_{eff}^2/9$), are summarised in the table below.

Sample	Curie Weiss constant θ_{CW} / K	Curie constant C/emu K mol^{-1}	Effective moment μ_{eff}/μ_B
$KFe_3(SO_4)_2(OH)_6$	-850±103	6.7±2.1	7.8±1.2
$KFe_3(CrO_4)_2(OH)_6$	-1000±354	5.0±2.9	6.7±1.3
$KFe_3(SeO_4)_2(OH)_6$	-805±251	5.6±2.7	7.1±1.5

Table 6.1 Values of Curie Weiss theta and effective moment for the samples $KFe_3(XO_4)_2(OH)_6$ *(X = S,Cr,Se)*

6.5 Neutron powder diffraction measurements

The samples of composition $KFe_3(XO_4)_2(OH)_6$ (where X = SO_4,SeO_4 and CrO_4) were taken to the ILL and mounted in vanadium sample cans on the D20 two-axis powder diffractometer. Variable temperature diffraction patterns were taken over a temperature range of 2-160K. In the case of $KFe_3(SO_4)_2(OH)_6$ new magnetic reflections are seen to develop at around 68K as the magnetic moments begin to freeze, with minima in the value of *dI/dT* corresponding to the transition temperatures seen in the susceptibility data at 56 and 65K. A plot of the integrated intensity of the magnetic Bragg peak at 40.8° 2θ against temperature, and the first derivative dI/dT against temperature is shown below in figure 6.5.

In the case of the $KFe_3(CrO_4)_2(OH)_6$ sample the onset of magnetic Bragg peaks is seen at around 70K with a minimum in *dI/dT* at 63K; a plot of integrated Bragg peak intensity versus temperature is shown in figure 6.6 below.

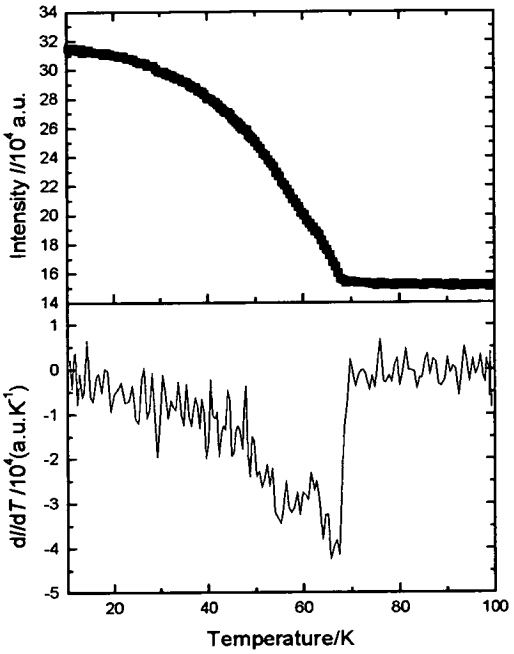

Figure 6.5 Plot of integrated intensity versus temperature for the magnetic Bragg peak seen in the diffraction pattern for $KFe_3(SO_4)_2(OH)_6$ at 40.3° two theta (upper) and first derivative dI/dT versus temperature (lower)

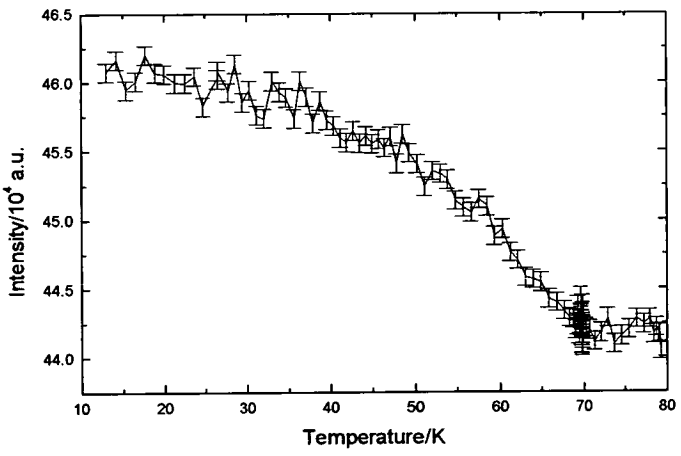

Figure 6.6 Plot of integrated intensity versus temperature for the magnetic Bragg peak at 38.0° two theta from the sample $KFe_3(CrO_4)_2(OH)_6$

In the case of the $KFe_3(SeO_4)_2(OH)_6$ sample similar features are seen to that of the susceptibility data, with minima in the first derivative of the integrated intensity corresponding to the two transition points seen at 58K and 65K. A plot of the integrated intensity versus temperature for the magnetic Bragg peak at 29.8° is shown below.

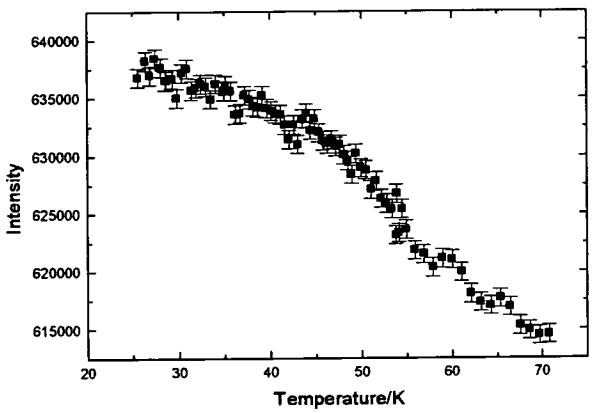

Figure 6.7 Plot of integrated intensity versus temperature for the magnetic Bragg peak at 29.8° two theta from the sample $KFe_3(SeO_4)_2(OH)_6$

6.5.1 Structure refinements

The least squares refined unit cell parameters for the three compounds at high temperature are shown in Appendix B. In all cases the diffraction patterns indexed as single phase samples with the space group $R\,\bar{3}\,m$ (*International Tables for Crystallography Volume A No.166*). In the case of the selenate, inclusion of H_3O^+ units resulted in an unstable refinement and so these were removed. Hence the refined atomic positions includes only the O-H groups present within the unit cell. The fractional occupancies of the potassium and H_3O^+ ions in the other two refinements

were manually varied until a best fit was achieved. In all cases the thermal occupancy parameters for all the oxygen ions in the unit cell were constrained so as to be of the same value. The parameters obtained are in agreement with expectation, based on the size of the XO_4 group. Thus the largest inter-planar distance is seen in the case of the selenate, which is followed by the chromate and finally the sulfate.

A summary of the lattice constants obtained, along with the estimated value of the Curie Weiss theta (as shown in table 6.1) are shown in the table below.

Sample	a /Å	c /Å	θ_{CW} / K
$KFe_3(SO_4)_2(OH)_6$	7.23832(29)	16.98603(89)	-850±103
$KFe_3(CrO_4)_2(OH)_6$	7.36018(24)	17.21445(10)	-1000±354
$KFe_3(SeO_4)_2(OH)_6$	7.32966(29)	17.33983(12)	-805±251

Table 6.2 Refined lattice parameters and estimated Curie Weiss theta values for the series $KFe_3(XO_4)_2(OH)_6$ (X = S,Cr,Se)

These values suggest that there is little correlation between the strength of exchange and the size of the unit cell, since there is very little difference in the magnitude of θ_{CW} on changing the linking group from sulfate to selenate. Furthermore the dc susceptibility behaviour is very similar with two transition temperatures at around 56K and 65K respectively, and zero field cooled field cooled divergence indicative of spin glass behaviour. This is an interesting result. It would suggest that in-plane exchange dominates the magnetic interactions at all temperatures other than very close to the freezing transition points where there is a crossover to 3D behaviour (as seen in the

single crystal results presented in Chapter 4). This does not really concur with the fact that the jarosites behave as Heisenberg magnetic systems, since by definition this requires a component of spin along all three principal axes and so the Hamiltonian should be influenced by the interlayer exchange. However the value of θ_{CW} is a very blunt tool in closely examining the balance of exchange pathways since it is directly proportional to $\sum_i J_i z_i S_i^2$ where z_i is the number of nearest neighbours for a given exchange J_i, hence it will always be dominated by the magnitude of J_i.

From the D7 measurements in the previous Chapter, in the case of the potassium salt very little temperature dependence in the size of the spin-spin correlation length was seen. If this behaviour is mirrored in the case of the selenate salt then it would suggest that spin-spin correlation exist even at high temperatures and that such planar correlations dominate the magnetism of the system, until close to T_N when interplanar correlations grow rapidly. Such correlations concur with previous work by Harris *et al* [3] which predict that the susceptibility behaviour will only obey Curie-Weiss behaviour in a temperature regime above 350K. Below this, there are significant correlations between ions and the inverse susceptibility will intercept with the temperature axis at $2JS(S+1)/k$ rather than the value of $-(4/3k)JS(S+1)$ as predicted by mean field theory.

In summary it is not easy to determine why there are such similarities between the two systems, without the aid of detailed spin wave dispersion measurements. Either in both systems the dominant exchange pathways lie in the kagome planes and interplanar exchange only becomes significant in the region of T_N, or it may be that

the balance of exchange forces in the two systems is such that they look identical with respect to their Curie-Weiss behavour.

The behaviour of the chromate salt is in stark contrast to that of the sulfate and selenate salts. While the estimated value of θ_{CW} indicates that the system is antiferromagnetic, a weak parasitic canting of moments leads to a ferromagnetic component to the dc susceptibility signal. Such behaviour has been seen before [4] and attributed to a Dzyaloshinsky-Moriya (DM) interaction. Such an exchange interaction arises when there is antisymmetric exchange between two spins such that the spins no longer lie anti-parallel to each other. Weak ferromagnetism will arise from antiferromagnetically aligned spins on two sublattices, which are equivalent in number but not exactly aligned anti-parallel. It is important to note that such an effect cannot occur if magnetic moments in a unit cell are related by a centre of symmetry. Thus the magnetic and nuclear unit cells must be of the same size. Whilst in the case of the chromate the variable temperature diffraction patterns obtained show that the nuclear and magnetic unit cells are identical in size, it is not clear why this should be the case, in contrast to the doubled *c*-axis magnetic cells seen in the case of the sulfate and selenate salts. Further high resolution diffraction studies are required to investigate the orientation of the XO_4 groups between layers, since it likely that the X-O bond lengths and bond angles may well influence the nature of the magnetic behaviour seen.

The low temperature refinements were also subject to Rietveld analysis. In the case of the sulfate and selenate salts refinements were attempted with a second phase containing the Fe moments defined within the space group $P\ \bar{3}$ with the length of the

c-axis doubled with respect to that of the nuclear unit cell. The positions of the Fe atoms and orientation of moments used in the refinements are shown below.

	atomic positions			*magnetic moments*		
Atom	*x*	*y*	*z*	m_x	m_y	m_z
Fe	0.5	0.5	0.75	-0.8333	0.5	0
Fe	0.6667	0.8333	0.4167	0.8333	0.5	0
Fe	0.8333	0.6667	0.0833	0	-1	0

Table 6.3 Atomic positions and orientation of magnetic moments in magnetic unit cell of space group $P\ \bar{3}$

In the case of the chromate salt refinement was attempted with a magnetic unit cell of the same size as the nuclear cell with the Fe moments defined within the space group *P3*. The position of the iron atoms in the cell and the orientation of magnetic moments are given in the table below.

	atomic positions			*magnetic moments*		
Atom	*x*	*y*	*z*	m_x	m_y	m_z
Fe	0.5	0.5	0.5	-0.8333	0.5	0
Fe	0.6667	0.8333	0.75	0.8333	-0.5	0
Fe	0.8333	0.6667	0.1667	0	1	0

Table 6.4 Atomic positions and magnetic moments defined within the space group P3 for the magnetic unit cell of $KFe_3(CrO_4)_2(OH)_6$

The results of these three refinements are shown in Appendix B.

6.6 $(D_3O)Cr_3(SO_4)_2(OD)_6$ Cr Jarosite

6.6.1 D1B Neutron Diffraction studies

Whilst it is possible to synthesise a wide range of jarosites with Fe^{3+} as the magnetic ion, the large size of the moment associated with this ion (S = 5/2) also carries with it a large exchange energy. Since frustration in these systems arises as a result of competition between a variety of exchange pathways, it is desirable to synthesise further jarosite analogues with magnetic ions of lower spin, thereby weakening exchange interactions and so gaining some insight into which exchange terms dominate in any particular system. A reduction in the classical spin also increases the likelihood of quantum fluctuations and so would also provide an experimental probe of theoretical models regarding the nature of such fluctuations on the kagome lattice [5]. With this in mind a sample of deuterated chromium jarosite was prepared with a view to performing neutron powder diffraction measurements.

6.6.1.2 Sample preparation

Batches of $(D_3O)Cr_3(SO_4)_2(OD)_6$ were prepared in a similar fashion to that described for the iron analogues in the previous Chapter. The starting material $Cr_2(SO_4)_3.xH_2O$ was dissolved in D_2O with gentle heating, the solvent then being removed by rotary evaporation. The resulting solid was then redissolved in D_2O and heated in a PTFE lined Parr bomb at 240°C in a muffle furnace for 48 hours. The resultant green powder was examined for phase purity by use of powder XRD and dc susceptibility measurements. The XRD measurements showed the samples to be single phase, and indexing of the pattern on a $R\ \bar{3}\ m$ unit cell proved successful. The dc susceptibility

measurements [6] show a broad feature in the inverse susceptibility at T ~ 40K, and a further point of inflexion at 2.2K in agreement with previous results [7].

6.6.1.3 D1B Neutron powder diffraction studies

Powder diffraction data were collected from 1.2g of sample using the D1B two axis diffractometer at the ILL, Grenoble. The sample was loaded into a thin walled copper sample can and inserted into an ILL dilution fridge, using a mixture of ^{3}He and ^{4}He and capable of temperatures down to around 10mK. A series of diffraction patterns were then taken at temperatures of 30mK, 600mK, 2K, 5K and 10K. The diffraction patterns obtained at 30mK and 10K are shown below, normalised to 100000 monitor counts.

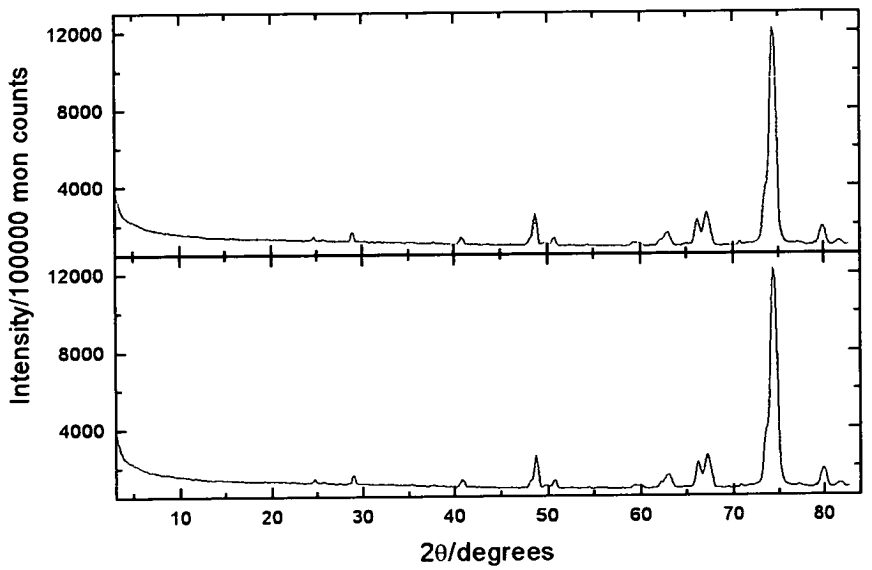

Figure 6.8 Diffraction patterns obtained at 2K (red pattern top) and 10K (black pattern bottom)

The full series of diffraction patterns is shown below.

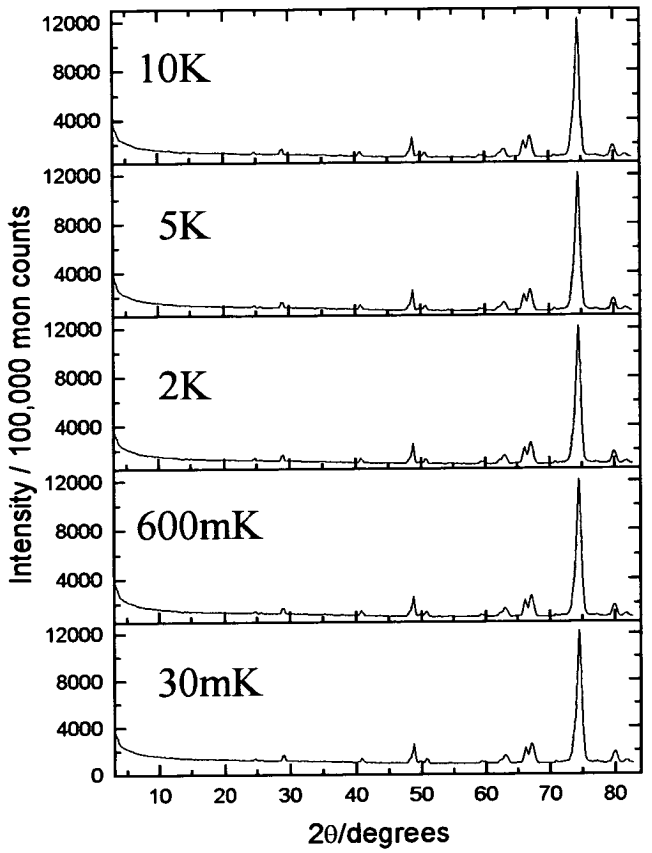

Figure 6.9 Full diffraction patterns obtained at (reading top to bottom) 10K,5K,2K,600mK and 30mK all normalised to 100000 monitor counts

Previous work [7] suggested the presence of a ferromagnetic transition at 2.2K, as evidenced by dc susceptibility data and neutron diffraction data showing additional weak magnetic Bragg reflections at 1.2K.

To examine the possibility of the presence of magnetic Bragg peaks difference plots between the low temperature and higher temperature datasets collected on D1B were created. These are shown below.

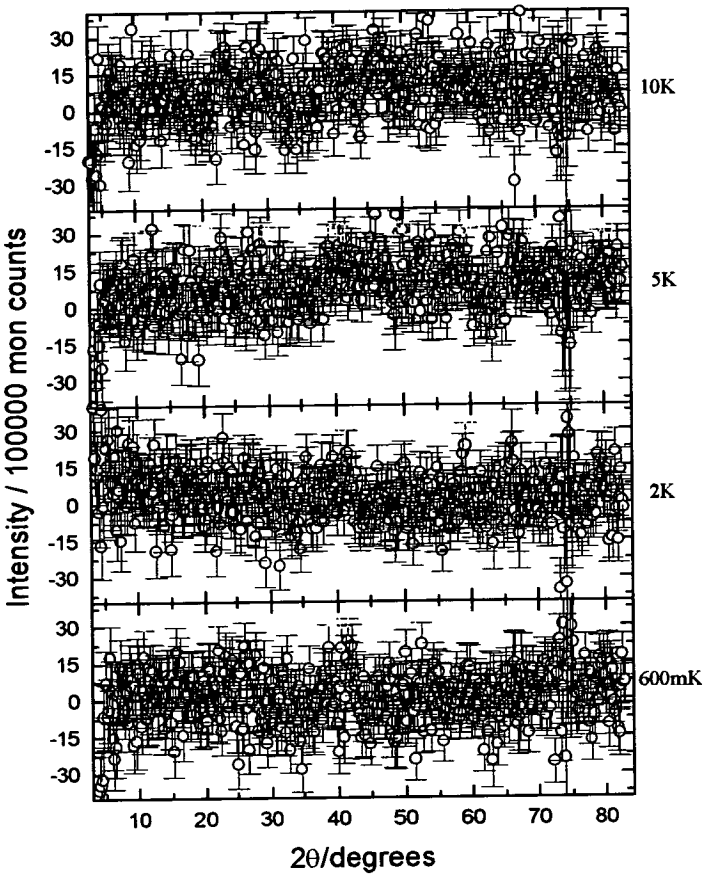

Figure 6.10 Difference plots created from the diffraction patterns taken. Plots shown (from top to bottom) are (30mK –10K), (30mK – 5K), (30mK –2K) and (30mK-600mK) subtracted datasets

As can be seen there is little evidence for the existence of additional magnetic Bragg peaks from any of the difference plots shown above. Further difference plots with the pattern obtained at 2K used as the baseline are shown below.

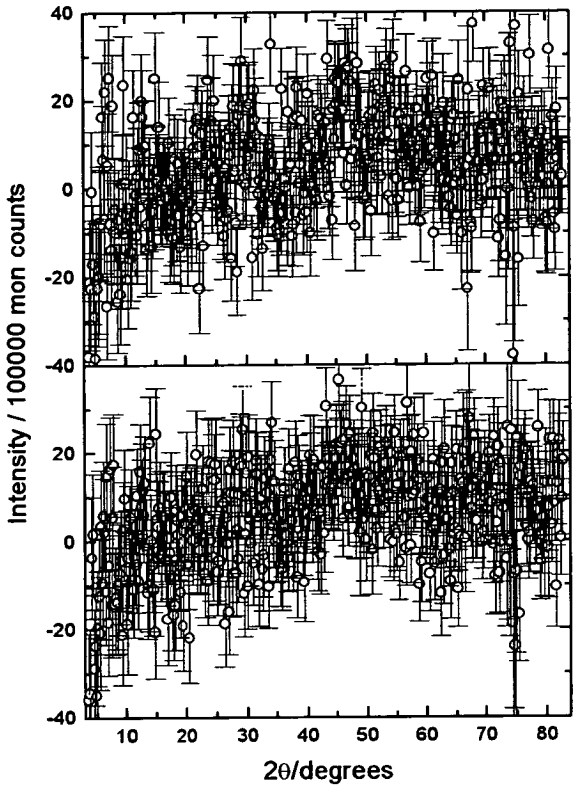

Figure 6.11 Difference plots of the (2K-5K) (lower) and (2K-10K) (upper) datasets normalised to 100,000 monitor counts

Similarly to those created using the 30mK dataset as a basis set there is no evidence to support the notion of additional magnetic reflections being present. However there would appear to be a degree of small angle scattering present in the difference plots in all cases other than those at 2K. Such a feature, at low angles, is indicative of the presence of short range ferromagnetic correlations, suggesting that there is a build up of such correlations at higher temperatures which fall away as T approaches 2K and then reappear at temperatures below 600mK. This is therefore indicative of a change in the nature of the magnetic unit cell, despite the absence of any observable long range order.

Previous powder neutron diffraction measurements [8] on the $KCr_3(SO_4)_2(OD)_6$ system showed evidence of magnetic Bragg peaks below 1.8K, though these were of weaker intensity than expected, suggesting that only a proportion of the moments were frozen into a long range ordered (q = 0) state. It would appear that the deuteronium salt shows an even greater degree of spin fluctuations than the potassium salt, since no evidence of long range order is seen in the diffraction data. However neither is there evidence of a large amount of diffuse scattering, indicative of in-plane spin-spin correlations, in contrast to the iron jarosites. Nonetheless, these results would seem to suggest that there is a similarity in the behaviour of the iron and chromium analogues, in that there is no evidence of long range order in either system. There should not be a significant difference in the concentration of chromium in this sample compared to the previous sample measured since, if the 'order by disorder' model is believed then a low concentration of chromium in the sample will lead to evidence of long range order and this is not seen in this case even at the lowest measured temperature of 100mK. It is clear that low temperature susceptibility measurements, in the range 10mK-1.8K, are required to fully assess the nature of any ordering, or indeed freezing transition.

6.6.2 D2B Neutron diffraction data

In order to study the crystallographic unit cell in more detail the same sample as run on D1B was loaded into a cylindrical vanadium can (2.2g). The can was then loaded into an ILL Orange cryostat and cooled to 1.5K where a diffraction pattern was obtained over a period of 10 hours. The sample was then warmed to 130K and a

pattern obtained over a similar length of time. The data obtained is shown in Appendix B, whilst the resulting lattice parameters and atomic positions as determined from Rietveld refinement of the data-sets performed using GSAS are shown below.

Atom	x	y	z	frac	uiso/Å^2	site symmetry
Cr	0.16667(0)	-0.16667(0)	-0.16667(0)	1.00(0)	0.00914(25)	2/M(110)
S	0(0)	0(0)	0.3063(10)	1.00(0)	0.00143(27)	3M(100)
O1	0(0)	0(0)	0.3918(4)	1.00(0)	0.00411(18)	3M(100)
O2	0.22093(32)	-0.22093(32)	-0.05760(22)	1.00(0)	0.00508(11)	M(110)
O3	0.12697(32)	-0.12697(32)	0.13706(28)	1.00(0)	0.00109(3)	M(110)
O4	0(0)	0(0)	0.0126(13)	0.50(0)	0.01061(4)	3M(100)
D1	-0.0637(16)	0.0637(16)	-0.0410(16)	0.50(0)	0.18907(13)	M(110)
D2	0.1973(7)	-0.1973(7)	0.1064(6)	1.00(0)	0.01126(4)	M(110)

a = b = 7.22604(12) Å c = 17.03497(45) Å $\alpha = \beta = 90°$ $\gamma = 120°$ Volume = 770.323(22) Å^3
$\chi^2 = 5.548$ $R_{wp} = 0.0541$

Table 6.5 Refined atomic positions and lattice parameters obtained from D2B data taken on the sample $(D_3O)Cr_3(SO_4)_2(OH)_6$ at 130K

This is in agreement with other jarosite samples, though the value of χ^2 could not be reduced below a value of 5.5. Previous refinements [7], encountered similar problems in indexing the unit cell on a $R\ \bar{3}\ m$ space group, and an extensive investigation of alternative space groups was performed concluding with the monoclinic space group *Cm*. However subsequent diffraction measurements taken at the ESRF synchrotron source [9] do not show any evidence for this distortion.

6.7 Muon spin relaxation measurements: $(H_3O)Cr_3(SO_4)_2(OH)_6$

From the neutron diffraction measurements performed above it is clearly of interest to study the nature of spin fluctuations in the chromium salts. However the deuteronium chromium salt is difficult to make in large yield, and so in order to prepare sufficient sample for muon measurements, the hydronium salt was prepared.

6.7.1 Sample preparation

Chromium (III) sulfate $Cr_2(SO_4)_3.xH_2O$ (Alfa, reagent grade) (9g) was dissolved up in 30ml of H_2O with gentle heating, and the solvent then removed with rotary evaporation. The resulting paste was redissolved in 30ml of H_2O and transferred to a PTFE-lined Parr bomb which was placed in a muffle furnace at 240°C for 48 hours The resultant pale green product $(H_3O)Cr_3(SO_4)_2(OH)_6$ (0.5g) was scraped off the walls of the liner and filtered under suction, with two washings of distilled water, before being dried overnight in a vacuum oven.

6.7.2 Sample characterisation

Phase purity was verified using a combination of powder X-ray diffraction and dc SQUID susceptibility measurements. The resultant diffraction pattern obtained is shown below. Indexing of the diffraction pattern on a $R\,{-}3\,m$ with starting parameters as given in previous work proved successful [7].

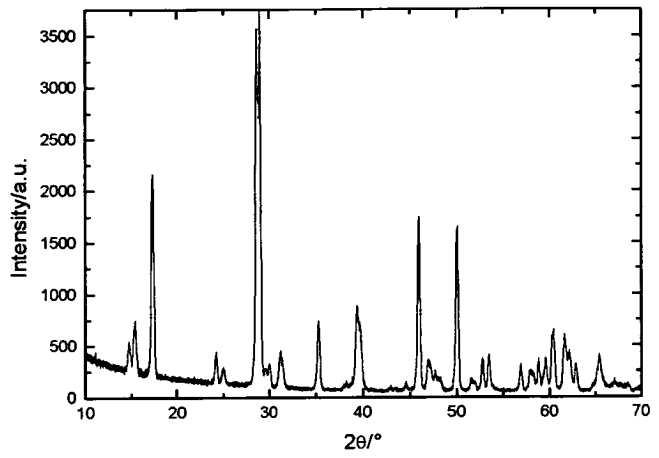

Figure 6.12 X-ray diffraction pattern obtained from the sample $(H_3O)Cr_3(SO_4)_2(OH)_6$

In the case of dc susceptibility measurements no evidence for the onset of a freezing transition was seen down to the lowest temperature of 1.7K achievable using the SQUID magnetometer. A plot of both dc susceptibility versus temperature and inverse susceptibility versus temperature are shown below, as well as the temperature dependence of the effective moment in Bohr magnetons. Fitting of the high temperature linear region of the molar susceptibility (150-300K) gives a value of C of 2.08±0.19 emu K mol^{-1} Cr^{-1} and θ_{CW} of −54.6±12.4 K.

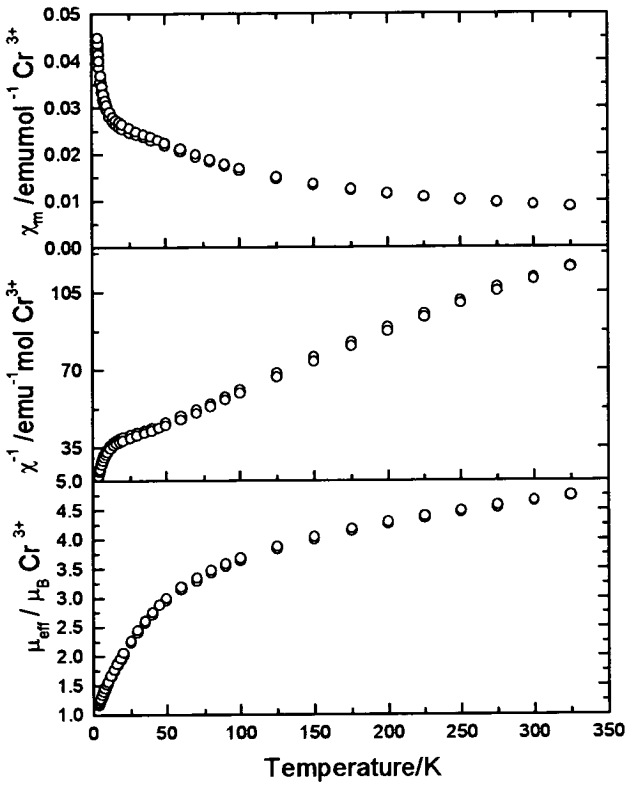

Figure 6.13 Plot of molar susceptibility versus temperature (top), inverse molar susceptibility versus temperature (middle) and effective moment versus temperature (bottom) obtained for the sample $(H_3O)Cr_3(SO_4)_2(OH)_6$

6.7.3 Muon spin relaxation studies

To further elucidate the nature of spin freezing in this system muon spin relaxation studies were performed at the LMU facility at PSI in Switzerland. The sample was made into a pellet using a Grasespec® pellet die of 13mm in diameter and mounted on a silver plate secured with some silver tape. This was then mounted into the $^3He/^4He$ dilution fridge on the LTF instrument and cooled to 100mK. A series of

scans were performed in the temperature range 100mK – 10K, i.e. both with the mixture in and out, with an applied longitudinal field of 100G. The field dependence of the muon depolarisation signal was further investigated by the application of a series of longitudinal fields of up to 25,000G and a plot of the muon signal vs. time on application of zero and 25000G is shown below.

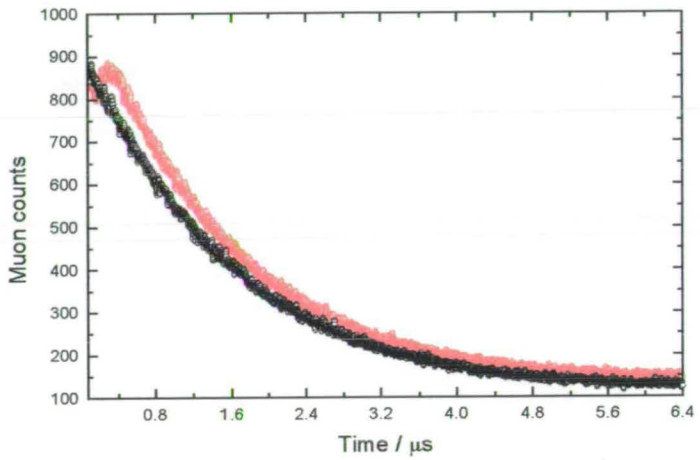

Figure 6.14 Polarisation signal $P_z(t)$ vs. time (μs) obtained in applied longitudinal field of 0G (red data) and 25000G (black data)

Fitting of the data obtained was performed using the Minfit software package [10]. Initially fitting was performed simultaneously to the forward and backward histograms, over the full data range, with a combination of Gaussian (6.1) and exponential (6.2) functions as given below.

$$G_z(t) = b + N\exp(-t/\tau)[1 + a_0\exp(-\sigma^2 t^2/2)] \quad (6.1)$$

$$G_z(t) = b + N\exp(-t/\tau)[1 + a_0\exp(-\lambda t)] \quad (6.2)$$

where b is a background term, N is the number of muon events, t is the time in μs, τ is the muon lifetime (2.19μs), a_0 is the muon asymmetry and σ and λ are the muon relaxation constants for the Gaussian and Lorentzian functions respectively. The

resulting values of sigma (the static Gaussian component) and lambda (the fluctuating lorentzian component) are shown below as a function of temperature.

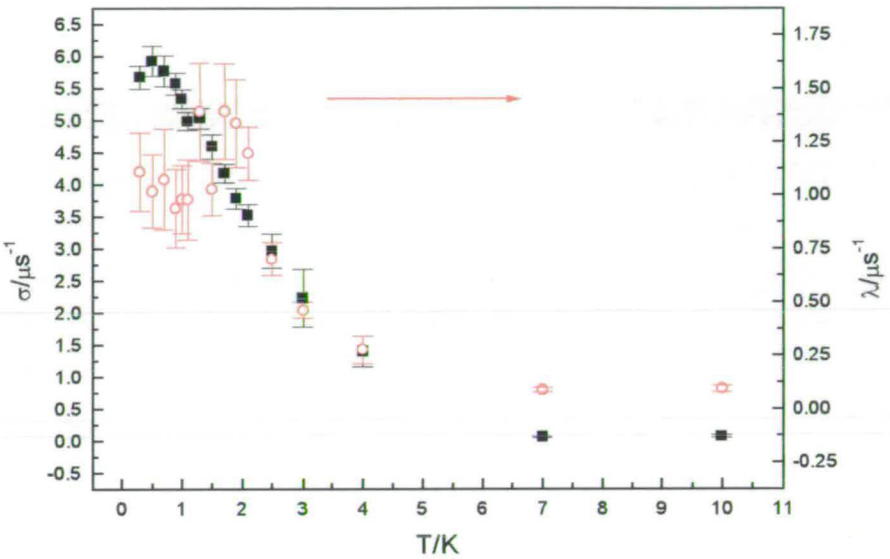

Figure 6.15 Plot of fitted parameters for the values of sigma/(μs^{-1})(black squares) and lambda/(μs^{-1}) (red circles) over temperature range of 100mK – 10K

From this plot it would seem that there is a magnetic ordering transition at around 1.5K, though it is not clear why there would be such a difference between the maximum in the values of both sigma and lambda. In order to try and verify this freezing temperature further fitting of the data was performed with a stretched exponential function with the exponent β allowed to vary from an initial value of 1. If the sample exhibits spin glass behaviour then the stretched exponential model should break down around T_f on cooling from above. Fitting to the forward histogram only showed a breakdown in the stretched exponential model around 1.5K suggesting that T_f is in the region 1.3-1.7K. In the work of Lee *et al* [8] on the potassium chromium

salt, diffraction measurements showed that only approximately 67% of the moments were frozen in the low temperature magnetic state. Thus the difference in the peak in the values of lambda and sigma may reflect the fact that a portion of the moments freeze at around 1.5K whilst there remain dynamic fluctuations even at very low temperatures.

Low temperature dc susceptibility measurements are planned in order to determine the existence or otherwise of a freezing transition.

6.8 Summary

This Chapter has considered the nature of a number of analogues of the parent mineral $KFe_3(SO_4)_2(OH)_6$. Substitution of the SO_4 group with a SeO_4 group sees an increase in the size of the unit cell, as determined by powder neutron diffraction measurements. However little variation in the magnetic behaviour of these systems is observed. It is not clear why these two systems should exhibit such similar behaviour. Substitution with CrO_4 leads to a 'parasitic' ferromagnetic component to the susceptibility signal, which can be explained in terms of a DM interaction arising due to spin canting. It is still a matter of debate as to what influence the CrO_4 group exerts on the nature of the exchange pathways in the system to cause such an effect.

Powder neutron diffraction measurements on a sample of $(D_3O)Cr_3(SO_4)_2(OD)_6$ show no evidence of long range order, in contrast to previous measurements, and further low temperature susceptibility and heat capacity measurements are required to verify the existence of any magnetic transition.

Muon spin relaxation measurements performed at the LMU facility in Switzerland on the compound $(H_3O)Cr_3(SO_4)_2(OH)_6$ show evidence for a degree of spin freezing at a

temperature of the order of 1.5K, though there appear to be spin fluctuations at temperatures as low as 300mK. Further measurements are required in order to fully understand the nature of the magnetic behaviour in this system.

References

[1] A.S.Wills, A.Harrison, C.Ritter and R.I.Smith, *Phys. Rev. B* **61**(9) 1 (2000)

[2] J.Frunske, *'Preparation and Investigation of New Magnetic Materials Based on the Jarosite Family of Minerals'* – Socrates Student Exchange Programme Report (1998)

[3] A.B.Harris, C.Kallin and A.J.Berlinsky, *Phys. Rev. B* **45**(6) 2899 (1992)

[4] M.G.Townshend, G.Longworth and E.Roudaut, *Phys. Rev. B* **33**(7) 965 (1986)

[5] *See for example* J.von Delft and C.L.Henley, *Phys. Rev. B* **48**(2) 965 (1993); A.Chubukov, *Phys. Rev. Letts.* **69**(5) 832 (1992)

[6] K.G.Pettigrew (*private communication*)

[7] A.S.Wills, *PhD. Thesis*, University of Edinburgh (1996)

[8] S.H.Lee, C.Broholm, M.F.Collins, L.Heller, A.P.Ramirez, C.Kloc, E.Bucher, R.W.Erwin and N.Lacevic, *Phys. Rev. B* **56**(13) 8091 (1997)

[9] D.Visser (*private communication*)

[10] I.Reid, *'The MINUIT-based μSR fitting programme MINFIT'*, PSI μSR facility (1999)

Chapter 7 Lanthanum Manganites

7.1 Introduction

The systems $Ln_{1-x}M_xMnO_3$ (where Ln is a rare earth ion - commonly La,Pr - and M is a divalent ion such as Ba^{2+}, Ca^{2+} or Sr^{2+}), were first investigated in the 1950's [1-7].The remarkable electronic and magnetic properties of such systems, in particular the large fall in resistance in moderate applied magnetic fields, has seen a resurgence in interest in recent years [8-15]. The parent compound $LaMnO_3$ is an antiferromagnetic insulator [5,16], however on doping with a divalent ion *M* the system rapidly becomes metallic and ferromagnet. What is even more remarkable is that these materials show large negative magnetoresistance, that is their resistance drops in the presence of an applied magnetic field. Interest from a technological viewpoint has centred on such ideas as exploitation of the rapid variation in resistivity in the region of T_C, through use as a bolometer [17]. The negative magnetoresistance has potential use in devices such as magnetic sensors, magnetoresistive read heads and magnetoresistive random access memory. From a more fundamental point of view such systems offer the chance to examine the merits of collective electron theories and to try and improve and enhance the understanding of such strongly correlated electronic systems.

7.2 Magnetoresistance

The magnetoresistance *MR* of a material can be defined using the expression

$$MR = \frac{R(H) - R(0)}{R(H)} \tag{7.1}$$

where *R(H)* is the resistance of the material in an applied field *H* and *R(0)* its resistance in zero field. Whilst in most materials this effect is negligible, in the case of $Ln_{1-x}M_xMnO_3$ compounds there is a huge drop in resistance on application of magnetic fields of the order of 5T. This effect is already utilised in computing disks through the use of permalloy, an iron nickel alloy, which shows a 20% fall in resistance on application of a field. Such a large fall has been dubbed *Giant Magnetoresistance* or GMR, and is seen in a variety of other metallic multilayered systems [18]. In the system $Ln_{1-x}M_xMnO_3$, and indeed $Ln_2Mn_2O_7$ type materials, the effect is even more pronounced, spanning several decades in resistance and has been dubbed '*C*olossal *M*agneto*R*esistance or CMR to distinguish it from that seen in magnetic multilayers. It should be noted that the underlying mechanism responsible for the magnetoresistance is different in the two series of compounds. In the case of metallic multilayers, layers of magnetic ions are stacked with non-magnetic layers between them, the electrical resistance of the resultant '*superlattice*' is then readily controlled by an applied magnetic field which causes alignment of the magnetic moments within these layers. In the CMR materials however, both bulk and film samples exhibit negative magnetoresistance, exchange interactions between manganese ions being created by hole doping with Mn^{4+} ions.

7.3 The Perovskite Structure

The cubic perovskite structure is a common one in solid state science and can be described generically as ABX_3, where A and B are cations and X an anion, the ideal structure being of space group $Pm3m$ as illustrated below.

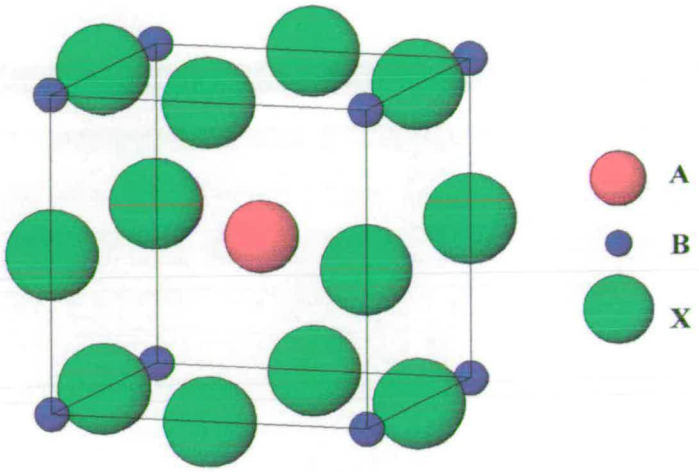

Figure 7.1 the cubic perovskite structure for composition ABX_3

This may also be viewed in terms of the B cations being surrounded by octahedra of X anions, with A cations filling in the holes as shown in figure 7.2.

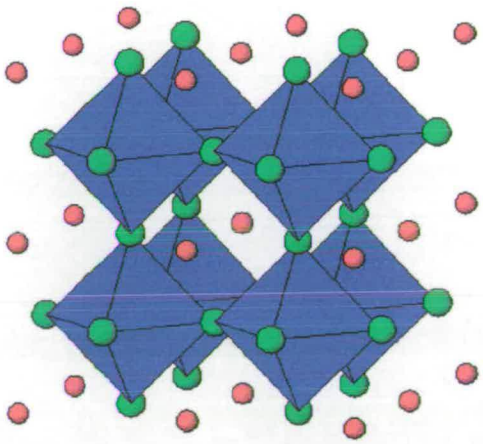

Figure 7.2 cubic perovskite structure showing BX_6 octahedra

The stability of the ideal ABX_3 structure, *i.e.* of the space group *Pm3m*, is linked to that of the BX_3 unit. If the radius of the *B* ion, r_B, is less than 0.51 Å, in the case of oxides, the *B* ion is no longer stable in an octahedral environment, and a tetrahedral site occupancy becomes more stable. A large *A* cation will generally stabilise a given BX_3 unit, since the BX_3 unit will be distorted so as to optimise the *A*-*X* bond length. However if the distortion of the BX_3 unit is too great then other space groups will become more competitive. The tolerance limits on such distortions are defined by the Goldschmidt ratio *t* given by

$$t = \frac{(r_A + r_X)}{\sqrt{2}(r_B + r_X)} \tag{7.2}$$

where r_A is the radius of the A cation, r_B the radius of the B ion and r_X the radius of the anion, all in Ångstroms.

In the case of a cubic structure, $t = 1$, and the perovskite structure is stable within the limits $0.75 < t < 1.00$. The other critical factor is the stability of the *A* and *B* ions in twelve-fold and six-fold co-ordination sites respectively. In the case of oxides, this means that the radius of the *A* ion must be greater than 0.90 Å, and the radius of the *B* ion greater than 0.51 Å. In the region $0.75 < t < 0.90$ co-operative buckling of octahedra will occur, resulting in an enlarged unit cell, whilst in the region $0.90 < t < 1.00$, no such buckling occurs but a small rhombohedral distortion is possible. In the former case an *O* - orthorhombic distortion occurs where the co-operative buckling of octahedra, relative to each other, leads to the so called $GdFeO_3$ structure with space group *Pbnm*: this is what occurs as the parent compound $LaMnO_3$ is progressively doped with Ca ions [14], and is shown in figure 7.3 below.

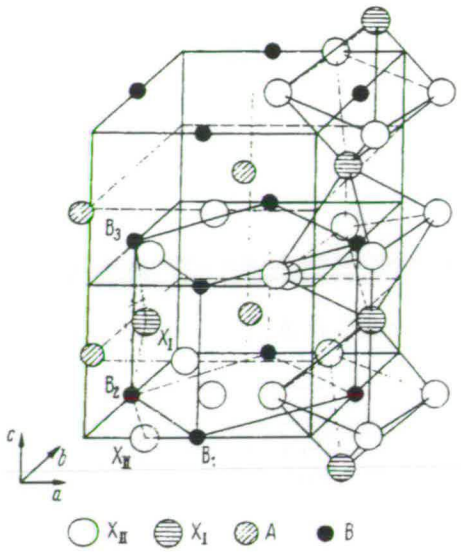

Figure 7.3 O-orthorhombic distortion illustrated for the case of $GdFeO_3$ [19]

This distortion, where $a < c/\sqrt{2} < b$ (a, b, c being the unit cell parameters), should not be confused with the so called *O'*-orthorhombic distortion, an alternative modification where $c/\sqrt{2} < a < b$, which arises as a result of a large Jahn-Teller effect. The Jahn-Teller theorem states that in the case of a polyatomic molecule with a degenerate electronic configuration, stability is achieved by a distortion of the local symmetry so as to lift such a degeneracy. The Mn^{3+} $3d^4$ ion, in an octahedral ligand field, has a ground state electronic configuration $t_{2g}^3 e_g^1$, with term symbol ^5E. It is this orbital degeneracy of the t_{2g} set which is lifted by localised distortions to tetragonal symmetry at the Mn^{3+} sites, in accordance with the Jahn-Teller theorem, as illustrated for $LaMnO_3$ in figure 7.4 below.

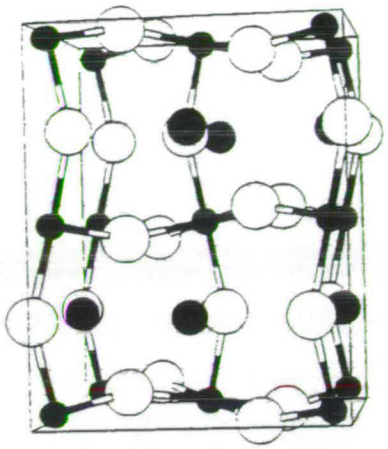

Figure 7.4 O'-orthorhombic distortion illustrated for the case of $LaMnO_3$. Small black spheres are Mn, grey spheres La and white spheres O [20]

If the energy involved in such distortions is large enough to override the thermal energy of lattice vibrations, then long-range order of the tetragonal distortions can occur, leading to ordering of the $d_{x^2-y^2}$ orbitals. Even when the energy associated with the Jahn-Teller distortion is insufficient to override lattice vibrations it will favour those vibrational modes of the O^{2-} ion that preserve tetragonal symmetry around each cation site. In general electrostatic forces maintain short-range correlation between Mn^{4+} ions, hence these ions are rarely nearest neighbours and only electronic order is involved in lattice distortions [20].

7.4 Metal-Insulator Transitions

The conducting properties of a particular material are dependent on several complex and often competing or inter-related factors. Conventional theory with regard to the

electronic structure of transition metal oxides states that the conduction bands created by atomic orbital overlap can be considered to be primarily metal-like in character. Thus if the metal ions have no d electrons then the conduction band is empty and separated by a substantial gap from the valence band, and the material is an insulator. However as the d band becomes partially filled with electrons the compound displays increasingly metallic properties. A simple count of d electrons can therefore give a qualitative picture of the likely conducting properties of a material. For example Ti (IV) has electron configuration $3d^0$ therefore has no electrons in the d band and hence TiO_2 is an insulator. However Ti_2O_3 and VO_2 have one electron per metal atom in the d band and so are metallic in nature, at room temperature. This is illustrated for the case of TiO_2 and VO_2 in Fig 3.5 below. In a similar fashion WO_3 has electronic configuration $5d^0$ and is insulating, whilst ReO_3 has electron configuration $5d^1$ and shows metallic behaviour.

The electronic properties of some ternary compounds can also be rationalised in this way, for example Na_xWO_3. Since the Na 3s orbitals are higher in energy than the W 5d orbitals only higher regions of the conduction levels will have any Na character. Additional valence electrons introduced by each Na atom will go into the W 5d band, and compositions with $x > 0.3$ show metallic behaviour. Ligand field splitting can also be considered in this simple approach. Where a transition metal occupies an octahedral site there will be a ligand field splitting of the free ion orbitals into the e_g and t_{2g} sets and these will broaden into bands. Thus if the bandwidth is less than the ligand field splitting then there will be a gap between the lower t_{2g} and e_g bands. For example, $LaCoO_3$ has Co (formally Co^{3+}) in a low spin d^6 configuration, with full t_{2g} band and empty e_g band, and so is non-metallic at lower temperatures. However the

gap between the t_{2g} band and e_g band is small and the compound undergoes a complex electronic transition at higher temperatures.

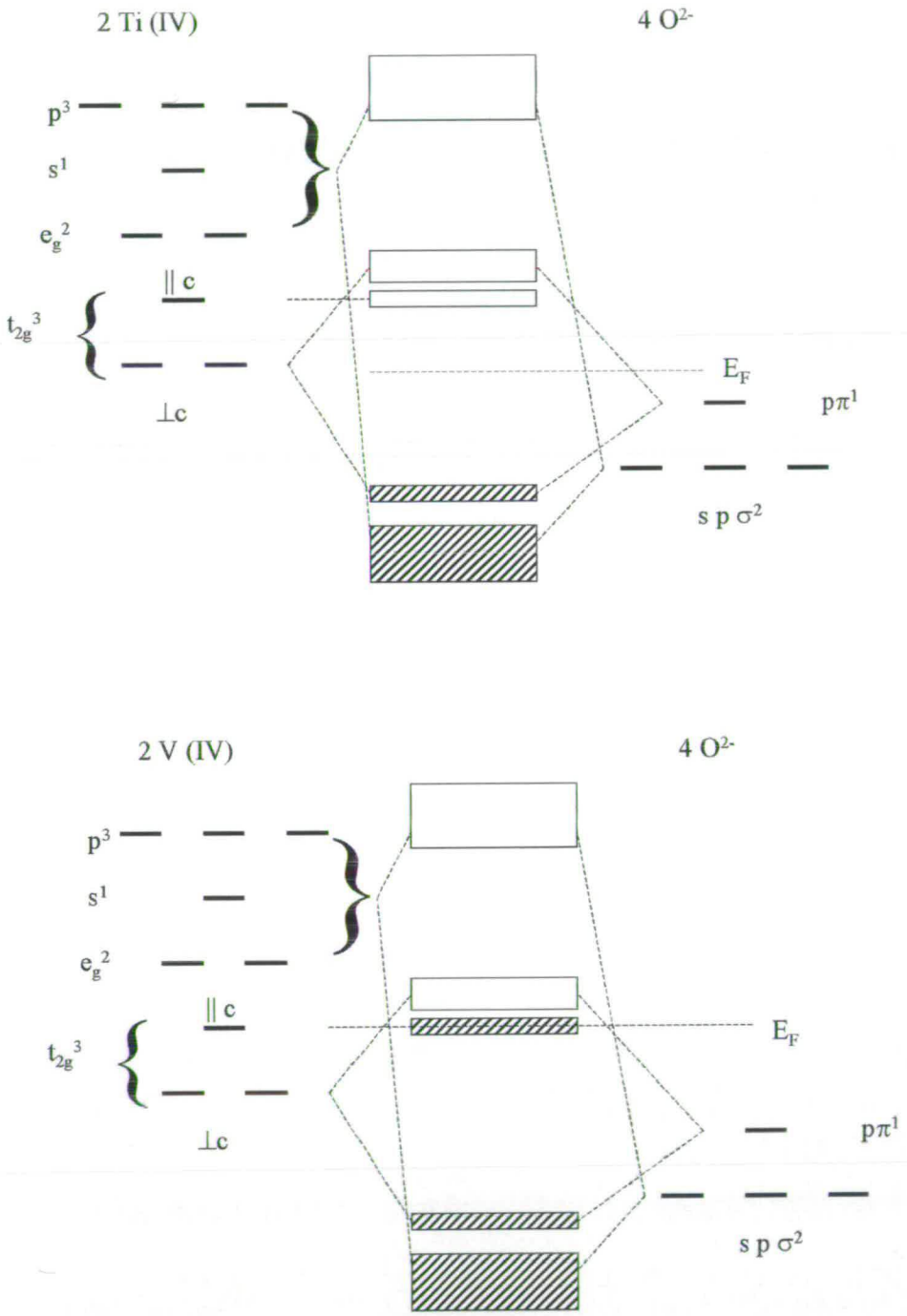

Figure 7.5 Band diagrams for TiO_2 (upper diagram) and VO_2 (lower diagram)

This rationale however, ignores the effects of electron-electron repulsion on the band structure of solids. To allow for this, the Hubbard model is introduced which assumes that the only important repulsion is a short range one between two electrons on the same atom. If orbital overlap is poor then the ground state of the solid will have electrons localised on each atom. In the case of a string of s orbitals the energy U required to move an electron on to another orbital, facilitating a spin 'flip' at the atomic site (and so allow pairing of electrons) is the difference between the ionisation energy of the atom (I) and the electron affinity of the neutral atom (A). This term U is a consequence of electron repulsion, and is called the Mott-Hubbard splitting energy. If there is one valence electron per atom then the band will be half-full and so band theory predicts that the solid should be metallic. However the influence of electron repulsion means that in practice such solids may be insulators. This can be illustrated in the diagram below.

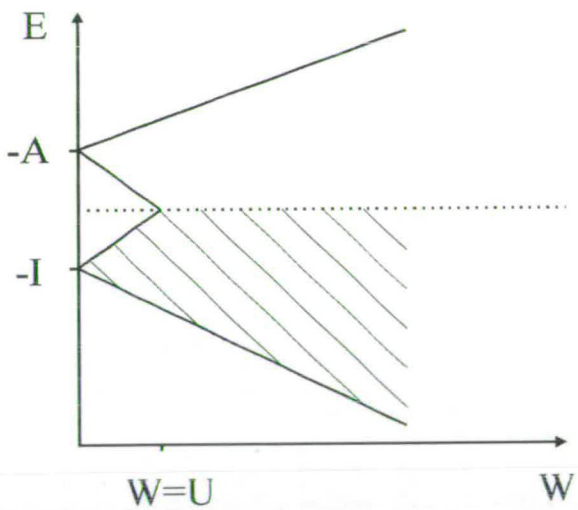

Figure 7.6 Energy diagram illustrating competition between repulsion energy U and bandwidth W

As the sub-bands broaden there is a point at which W, the bandwidth energy, is equal to the splitting energy U. Beyond this point (i.e. when $W > U$) there is no energy gap in the solid and it will exhibit metallic behaviour. As the value of W increases, the value of U tends to decrease since increasing orbital overlap will generally lead to a reduction in the polarisability of the solid. Ligand field effects are also important in this respect. As the d shell is filled moving across the transition series, orbitals are occupied in an order dependent upon the relative magnitude of the ligand field splitting, Δ, and of the intra-atomic exchange interaction which favours parallel electron spins. Low spin configurations will occur if Δ is sufficiently large.

In the majority of localised electronic configurations the exchange energy term is greater than Δ and the electrons are arranged so as to have as many as possible with parallel spins. For example in the case of MnO, Mn^{2+} ions are in O_h sites and the electronic configuration is $(t_{2g})^3$ $(e_g)^2$. This ligand field splitting is exhibited structurally as changes in bond lengths. It may be particularly marked when orbitals are filled asymmetrically (hence not full or half-full) and local co-ordination is distorted from perfect cubic (octahedral O_h or tetrahedral T_d) symmetry, a manifestation of the Jahn-Teller effect. This effect is more pronounced in the e_g than t_{2g} sets, since the former have stronger anti-bonding character, and normally results in a tetragonal elongation, with $a/c < 1$. Thus in the case of an octahedral co-ordination the Jahn-Teller distortion will result in a shortening of the four planar bonds, and a lengthening of the two axial bonds. In the case of the Mn^{3+} ion this results in a lowering in energy of the d_{z^2} orbital, and thus an increase in energy of the $d_{x^2-y^2}$

orbital. Within the lattice as a whole, co-operative Jahn-Teller effects are seen where the distortions created are orientated such that electrostatic repulsion between ions is minimised within the lattice. This is what is seen in the parent compound $LaMnO_3$.

Whilst Jahn-Teller effects are strictly applicable only to localised systems, there are analogous effects which can operate in the case of electrons in bands. Such electrons may cause a distortion which disrupts the simple periodicity of the lattice, and as a result perturbs the band structure. In the case of a string of orbitals in one dimension, Peierls' theorem [21] states that lattice distortions are an inevitable consequence of such an array, and this effect can be seen in the case of a three dimensional system. In this case distortions are such that there is a build up of electron density where the atoms are more closely spaced and thus the bonding between them is stronger. Such a build up of electron density is known as a charge density wave and can be responsible for the creation of a band gap in some materials. The gap produced by such periodic distortions can be thought of as the energy required to move an electron from a more strongly bound region to one where the atoms are less closely spaced. However such periodic distortions can also be incommensurate and thus do not correspond to integral multiples of normal lattice spacings. When a regular structure has a half-filled band the predicted periodic distortion is two lattice spacings and so there is expected to be a bond length alternation along a chain of atoms. For example in the case of VO_2 above 340 K, the material has a rutile structure and shows metallic behaviour. The closest approach of V atoms is along the c axis, and since there is one electron in the 3d (V) band the structure displays metallic conductivity at higher temperatures. Below 340 K however, the material becomes non-metallic and undergoes structural

distortions such that there are alternating V-V bond lengths along the chain. In terms of the band structure the pairing of V atoms gives rise to a splitting of the t_{2g} band into bonding and anti-bonding bands, composed of d orbitals that are directed between closely spaced pairs of metal atoms. Thus the band can now only accommodate 2 electrons per pair of V atoms and a band gap is created.

The distortions outlined so far result from collective electron effects in relation to the nature of the band structure in a particular system. However it is also possible for more localised distortions to occur as a result of electrostatic interaction between neighbouring ions and electrons (or holes). These distortions are then transported with the electron (or hole) and are known as polarons. If an electron is placed in an unfilled orbital on an atom in a solid, then there will be an overlap of orbitals on adjacent atoms giving rise to a band. The overlap effect will tend to delocalise the electron and its energy will fall by W/2, where W is the total bandwidth. However, if the electron is forced to stay on the one atom then the charge will polarise the surrounding atoms and lower the local energy. This polaron energy has two components; the first due to the interaction of electronic clouds with the surrounding ions, the second arising from the displacement of ions from their regular lattice positions. If electrons are able to move in a band formed by the orbital overlap, then only the electronic polarisation can follow it. Thus the behaviour of the electron depends on the balance between the lowering of energy if it remains localised on an atom (ΔE_i) or the stabilisation achieved by delocalisation, $W/2$. If $W/2 < |\Delta E_i|$ then the localised state is more stable, and the electron will be trapped by the local distortion it creates round a given lattice site, this being known as a small polaron. In

simple terms this can be rationalised by considering the idea that the introduction of an electron or hole changes the oxidation state of the atom in the solid, and so the ionic radius also changes, resulting in a local distortion which traps the charge. A small polaron is the most extreme case of electron-lattice interaction; some degree of polarisation will occur in ionic compounds even when the condition for complete trapping is not satisfied. Hence large polarons can also be formed, where the radius of the polaron is more than the lattice spacing.

In a transition metal oxide with one electron in the conduction band, and two atoms with an electron initially on one of them, the trapping of the electron is associated with an increase in the metal-oxygen bond distance. If the electron moves to the other site then the distortion will follow it. At some point the electron has the same energy on both atoms, and so the two potential energy curves cross, allowing overlap of orbitals on each atom giving rise to bonding and anti-bonding combinations, and a curve splitting. The trapping of charge does not occur if the bandwidth is sufficiently large. If the electronic interaction is small then the lowest energy states for the electron are either on one atom or the other. Thus there is an activation energy for the hopping of the electron between neighbouring atoms. This activated hopping is most characteristic of small polaron trapping. There *is* a small probability that the electron tunnels through the barrier but this involves motion of heavy ions and therefore this is normally very slow and only significant relevant to thermally activated hopping at low temperatures.

Metal-insulator transitions may also be driven by structural disorder, a phenomenon known as Anderson Localisation [22]. If it is assumed that the array of atoms in a solid have a disordered potential field, then the energy of atomic orbitals will vary randomly from site to site. Atoms with near-average energy are likely to have neighbours at similar energies, and so can form delocalised orbitals, whilst atoms at exceptionally high or low energies are unlikely to have similar neighbours, and so their orbitals will remain isolated *i.e.* as localised states. Thus there will be two orbital types created - those in the middle of the band extending through the solid as in a crystal, and those close to the top and bottom of the band which are localised on particular atoms. The region of localised states in the band will depend on the degree of disorder, and in the extreme case all the sites may be localised. The boundary between the delocalised and localised states is known as the mobility edge , and this can lead to a metal to insulator (*Anderson*) transition as the band is filled with electrons. When few electrons are present then the Fermi energy may be below the mobility edge, and so electrons at the Fermi energy are in localised states and cannot conduct current through the solid. At higher electron concentrations the Fermi energy may cross the mobility edge and so electrons are then in extended states thus enabling metallic conduction.

7.5 Charge Transport Mechanism For Doped Manganites

The mechanism of charge transfer and hence conduction in the $La_{1-x}Ca_xMnO_3$ system is based on Zener's double exchange mechanism which was first proposed in the 1950's [23]. Hund's rule of maximum multiplicity states that to attain the configuration of lowest energy all the spins of unpaired electrons must be aligned

parallel to each other. Since conduction electrons carry the polarisation of their spins unchanged from ion to ion, it is energetically more favourable to move to a neighbouring site with all d electron spins pointing in the same direction. Thus, electron transfer can be visualised as the transfer of an electron from the Mn^{3+} ion (electron configuration $3d^4$), to the O^{2-} ion simultaneously with the transfer of an electron from the central O^{2-} ion to the Mn^{4+} ion (electron configuration $3d^3$). Since all spins must be parallel to each other in order that such an exchange can occur it is therefore ferromagnetic in nature. This is illustrated in the figure below.

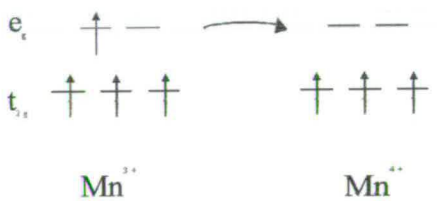

Figure 7.7 Illustration of double exchange. Electrons from the Mn(III) e_g set 'hop' into the e_g set of the Mn(IV) ions

This double exchange should not be confused with Kramer's superexchange [24] which involves electron transfer between excited ion states; in double exchange both Mn ions are in their ground states. This coupling between the Mn^{3+}-Mn^{4+} ions can be seen to be dependent upon the Mn-O-Mn bond angle. The efficiency of conduction will be greatest when the system is perfectly cubic and the bond angle (θ) is 180°, since the exchange is directly proportional to $\cos^2\theta$, and will decrease as distortions due to doping with M^{2+} ions become significant and the angle decreases. The optimum angle is 180° since this gives perfect ferromagnet spin alignments between the two

Mn sites. This dependency on the Mn-O-Mn angle is fundamental and underpins much of the work in this area. Almost all other factors such as doping levels, hydrostatic pressure and oxygen stoichiometry affect this angle directly and therefore also alter the conductivity of the material. For example, studies performed by Fontcuberta *et al* [25] found that the Curie temperature, designated T_M in their study, is linearly related to the size of the *A* cation, and that the bond angle Mn-O-Mn closes as the ionic radius $\langle r_A \rangle$ is reduced. Reduction of the Mn-O-Mn bond angle from 180° will cause an enhancement of the density of states, thus leading to a decrease in the bandwidth, relating directly to an increase of lattice distortion. The lowering of the onset of ferromagnetic order will lead to a narrower bandwidth *W* and with collapse of the bandwidth comes reduced mobility of charge carriers and hence an increase in resistivity at T_M. Mahendiran *et al* [26] concur with the idea of the Mn-O-Mn bond angle being a key parameter controlling the magnitude of the magnetoresistance seen. The bond angle plays a part in determining the activation energies of transport (E_A) since the extent of σ-bonding arising from the overlap of O(p) and Mn(d) orbitals increases as the Mn-O-Mn bond angle tends towards 180°. In addition their studies suggest that there is also a critical Mn-O bond distance (r_{Mn-O}) corresponding to ~1.97 Å below which CMR can occur. This suggests that there is a minimum strength of double exchange interaction required in order to stabilise the ferromagnetic state and give rise to the metallic-like electrical conduction observed. As with previous studies [25], it is stated that the Mn^{4+} content is also an important parameter in controlling the observed CMR. A minimum value of ~20% in Mn^{4+} is required to allow the doped system to become 'metallic' and hence for CMR to occur. The optimal compositions for a ferromagnetic state and large CMR effect have a Mn^{4+} content in the range 25-

40%. However it is not only the concentration but also the spatial distribution of the Mn^{4+} ions present in the sample which is of importance.

The idea of a critical value of $\langle r_A \rangle$, and hence Mn-O bond length, for the occurrence of CMR effects was also investigated by Barnabé and co-workers [27] for the system $Ln_{0.5}Ca_{0.5}Mn_{1-x}M_xO_3$ where Ln = La, Pr, Nd, Sm, Eu, Gd, Tb and M = Cr, Co, Ni, Fe, Mg, Al and Sn. Previous work [26,28-31] had shown that the magnitude of the transition temperatures T_C , was directly related to both the size of $\langle r_A \rangle$ and the cation size mismatch between the *A* and *B* sites. Consequently the extension of the range of $\langle r_A \rangle$, could be compensated for, with respect to the cation size mismatch, by doping on the *B* site. Recent studies had shown that the charge ordered state in the $Pr_{0.5}Ca_{0.5}MnO_3$ system could be destroyed by doping with Cr [32], and the use of a range of dopants on the *B* site was considered to help discover how far the CMR regime could be extended in these systems, with respect to the size of $\langle r_A \rangle$. What they observe is that as the level of dopant on the *B* site is increased then the ferromagnetic state is destroyed, since Mn-*M* interactions are generally antiferromagnetic and so double exchange is suppressed. In the case of Cr however the Mn-Cr interaction is ferromagnetic and so doping enhances the ferromagnetic state to the point where even 10% doping does not destroy the ferromagnetic state. In the case of the undoped $La_{0.5}Ca_{0.5}MnO_3$ the metal-insulator transition temperature, T_{MI}, falls smoothly with decreasing average radius at the A site $\langle r_A \rangle$. There is then a collapse at around $\langle r_A \rangle \sim 1.19$Å where charge ordering leads to a transition to antiferromagnetic insulating behaviour, and the compound remains insulating below this radius. In the case of Cr doping however the value of T_{MI} continues to fall

smoothly until $\langle r_A \rangle \sim 1.14$Å hence doping allows extension of the ferromagneitc metallic phase in the limits $1.14 \leq \langle r_A \rangle \leq 1.19$Å. Hence the new limit of metallic behaviour is seen to be $\langle r_A \rangle = 1.14$Å.

Whilst the above work has attempted to explain the conductive properties of these materials within the Double Exchange model, other workers believe that double exchange alone cannot explain the CMR effect [33-36], since if nothing else, it does not allow for such dramatic falls in resistance. The discovery of CMR in compounds such as $Tl_2Mn_2O_7$ which have a pyrochlore structure [35] means that double exchange cannot model the conduction since there is no mixed Mn valence state present in such systems. Following this logic, either the Double Exchange model is insufficient to explain the nature of CMR materials, since the magnitude of the effects seen are comparable to those seen in the perovskite systems, or it is simply not valid in the case of the pyrochlore compounds.

Coey *et al* [37] have investigated the nature of electronic interactions within these systems, with regard to rationalising the Double Exchange model. They state that the e_g electrons must be delocalised on a Mn-Mn distance scale, otherwise a static Jahn-Teller effect would operate, and an enlarged unit cell would be observed. Such an enlarged cell is not observed in their data obtained for samples with composition $x = 0.33$. Furthermore if delocalisation of electrons was not on a Mn-Mn scale, then the material would be antiferromagnetic, since double exchange would not be possible; the samples under study are all ferromagnetic in nature. Their work shows that whilst the electrons do appear to 'hop' between sites, there is still a significant density of

states at the Fermi surface. There are three possible explanations for this density of states. Firstly, that the electron wave packet is weakly localised by variations in the Coulombic potentials due to the mixture of La^{3+} and Ca^{2+}ions. However this would imply that the potential fluctuations in all compositions should be similar. There is no correlation found between ρ_0, the resistivity of the sample in the absence of an applied field, and electronegativity. Secondly electrons may be trapped by variations in the spin-dependent potential due to local deviations from ferromagnetic order. Resistivity data show a deviation from collinear ferromagnetism in all samples, the deviation being largest in compounds with higher resistivity and lower ordering temperatures (T_C). Thirdly, when the electron is already trapped the potential well is deepened by local deviations from collinearity on the edge of the wave packet, where there are fewer electrons and consequently weaker ferromagnetic interactions. The authors consider that there are other factors that influence electron localisation, notably lattice modes, which will play a role in triggering magnetic localisation, this being more probable with greater cation mass. Variation in the Mn-O-Mn angle will also be important, as proposed by other authors [28]. In terms of polaron activity in these samples, theory regards a small polaron to have a hopping frequency proportional to the term exp $(-2w/k\theta_D)$ where w is the energy of the intermediate state through which the polarons must pass to perform their hop, and θ_D the Debye Temperature. The barrier height should be greater than θ_D if the transport is to be impeded significantly. If the electronic wavepacket is seen as a large spin polaron, then it will be unlikely to diffuse as a whole. It is therefore more probable that the electrons will hop or tunnel across the surface barriers between wavepackets. A variation in ρ_0 should therefore reflect a barrier height variation rather than a change in the number of barriers to be

hopped over or tunnelled through. Such energy barriers must be of the order of the Hund's Rule splitting, U_H, of the e_g electrons (> 2eV) rather than that of the exchange energy (~ 0.05 eV). Thus the change of energy of an electron diffusing out of a large magnetic polaron and arriving in a region of reversed magnetisation is U_H. Experimentally, at temperatures greater than the Curie Temperature the resistivity of the less conducting compounds falls steadily as $\rho \sim \exp(T_0/T)^{\upsilon}$ where υ is *ca.* 0.25. This is in close agreement with Mott's expression for variable range hopping of electrons in a band of localised states in the absence of electron-electron interactions, where $\upsilon = 0.25$ [38]. In summary their work suggests that the spin-up e_g electrons are delocalised on an atomic scale in these compounds. Such electrons may be weakly delocalised in large wavepackets due to fluctuations in the potential experienced, on the scale of the e_g electron bandwidth, modified by lattice modes. The magnetoresistance (MR) seen at around T_C is therefore a consequence of self-consistent modification of the spin- dependent part of the potential fluctuations, and is equal to a fraction of the Hund's rule splitting U_H.

The nature of the samples being measured may also affect the magnitude of the MR seen. Ju *et al* [39] observe a difference between the resistivity of polycrystalline and single crystal samples. Polycrystalline samples show large MR at both T_C and at lower temperatures, in contrast to single crystal samples where MR is only seen around T_C. This suggests that grain boundaries play a significant role in the conduction properties of these samples. In work by Jia *et al* [40] a finite MR was seen in polycrystalline samples for $T << T_C$ as a result of grain boundary scattering - the thickness of the boundary being assumed to be greater than a few atomic spacings, as suggested in

previous work [41]. The low temperature MR behaviour of such polycrystalline samples exhibited significant changes both above and below the saturation field H_S. In the former case the resistivity drops slowly, but significantly, whilst in the latter case the resistivity drops rapidly. In the region where $T << T_C$ there is ferromagnetic ordering of Mn ions suggesting that intra-grain electron transfer between Mn^{3+} and Mn^{4+} sites is then facile. If, however, there is a large strain at the grain boundary then the spin direction of the respective sites may be more random, and consequently the grain boundary resistivity will be large. At the point where the applied field is equal to the saturation field, then the magnetic domains will be aligned with the field direction and so 'misaligned' spins at the grain boundary will be partially aligned leading to an easing of inter-grain electron transfer and a drop in resistivity. Above the level of the saturation field the spin canting angle will become smaller and thus electrons will move more easily between pairs of Mn^{3+} and Mn^{4+} ions. The authors attempted to assess the contribution of grain boundaries to the observed resistivity by using a so-called 'brick layer' model, considering grain boundaries of constant thickness δ surrounding cubic grains of size d. The expression for the total resistivity ρ_T is given by

$$\rho_T = \rho_b + 2(\delta / d)\rho_{gb} \tag{7.3}$$

where ρ_b and ρ_{gb} are the bulk resistivity and grain boundary resistivity respectively. This expression can be written as

$$\rho_{gb} = 2(\rho_b - \rho_T)d / \delta \tag{7.4}$$

In the case of $La_{0.67}Ba_{0.33}MnO_3$ a study found the average grain size to be *ca.* 5 μm, and so the grain size was taken as a cube of 5 μm with a grain boundary thickness of

100 nm. Using this model the grain boundary resistivity was calculated to be greater than the bulk grain resistivity, and the peak in this grain boundary resistivity occurred below T_C. Thus as the polycrystalline size is reduced, the intrinsic bulk resistivity contribution to the total resistivity becomes small.

Tokura *et al* [42] have attempted to investigate the nature of the bandwidth, and to tune it with respect to various parameters. In recent work the one electron bandwidth, W, was varied for the system $(Nd_{1-y}Sm_y)_{1/2}Sr_{1/2}MnO_3$, the compositions with $0.5 \leq y \leq 0.95$ showing a CMR effect in low field. Their study showed that the Mn - O - Mn bond angle deviated from 180° with a dependency on the tolerance ratio, f . This tolerance ratio is defined by the equation

$$f = (d_{Ln-O}) / \sqrt{2}(d_{Mn-O}) \tag{7.5}$$

A value for the tolerance ratio of $f = 1$ is the ideal case where the Mn-O-Mn bond angle is equal to 180°. A value of f less than 1 means a reduction in this bond angle, and thus $\theta < 180°$. Furthermore, the smaller the ionic radius $\langle r_A \rangle$ (or the smaller f is) then the smaller the bandwidth W. The system is poised on the brink of a ferro to antiferromagnetic transition and the magnitude of the transition temperature changes steeply as a function of the tolerance factor f. An increase in y will lead to a corresponding lowering in f, and hence the respective ferromagnetic transition shifts to lower temperature. This can be viewed as a decrease in the bandwidth W leading to an increase in the distortion of the Mn-O-Mn bond angle from 180°, and thus a weakening in the double exchange interaction with a corresponding lowering in T_C. In the case of compositions with $0 \leq y \leq 0.84$ a transition from a ferromagnetic metallic

state to an antiferromagnetic charge-ordered insulating state was seen at temperatures below T_C. At $y \geq 0.50$ and temperatures below 250 K a deviation from Curie - Weiss behaviour is seen. In terms of the resistivity this shows a large increase with y, at temperatures above the transition temperature, hence the fall in resistivity at T_C is enhanced. The electron-phonon coupling that is observed appears to arise from the charge order correlations and plays an important role in the small W (high y) region. Double exchange interactions overcome charge-order instability at lower temperature and this leads to a phase change to the ferromagnetic metallic state. The steep increase in resistivity and appearance of a first order transition at T_C implies that charge-order and/or antiferromagnetic correlations coexist at temperatures below 250 K. This suggests that there is a crossover from a second-order ferromagnetic transition to a first-order transition, which is strongly coupled to lattice degrees of freedom and observed by decreasing W (increasing y) near $x = ½$. Their data illustrate that W can be controlled both by application of a magnetic field as well as by chemical substitution (or variation in the tolerance factor f). The magnetoresistance data show a hysteresis reflecting a first-order phase transition for $y \geq 0.75$, but none for $y < 0.63$, this being consistent with the crossover described above. This suggests that there is coupling between charge and the lattice degrees of freedom, which increases due to the charge- ordered instability at temperatures above T_C.

In a review article, Roder and Bishop [43], consider the experimental data obtained so far, as well as the attempts by theorists to model these systems. They consider that the importance of the polaron role in charge transport is obvious, as seen in the activated conductivity behaviour in phases at temperatures above the Curie temperature, and

metal-insulator transition, temperatures. Work by Hundley *et al* [44] and Martinez *et al* [45] have developed expressions for the resistivity given by

$$\rho = \rho_m \exp[-M(H,T)/M_0] \tag{7.6}$$

where M is the magnetisation of the sample. This suggests that even in the ferromagnetic metal phase, transport is controlled by magnetic polarons. Martinez *et al* consider that the localisation of charge carriers above T_C is due to scattering of magnetic polarons on magnetic disorder above this temperature. Roder and Bishop disagree, and state that it is the lattice dynamics which affect the charge and spin dynamics rather than the other way round [43]. Jaimie *et al* [46] give thermopower measurements which fit well with polaronic behaviour. As the temperature tends to T_C the activation energy for the resistivity and thermopower has a magnetic field dependence which suggests that the polarons have magnetic character . Sharma *et al* [47] have conducted experiments directly probing the displacement of atoms (u) from their regular positions. Their work showed a correlation between the resistivity and the value of du/dT, suggesting that charge transport correlates with local lattice distortions. In summary they consider that magnetoelastic polarons dominate the charge transport at temperatures above T_C, and that as the temperature tends towards the ordering temperature from above, the magnetic component of such composite particles becomes spatially extended and leads to a delocalisation of charge and spin degrees of freedom in the ferromagnetic metal phase. Further evidence of polaron formation comes from EXAFS measurements by Tyson *et al* [48] which clearly demonstrate that Mn-O distances develop multiple length scales above the metal-insulator transition temperature, this being consistent with small polaron formation in

a homogeneous background matrix. Neutron PDF (Pair Density Function) measurements [49] lend weight to this argument.

In terms of theoretical approaches most of the initial work performed in this field has considered double exchange, with studies describing the ferromagnetic metallic phase as a simple ferromagnet, with its conductivity being that of a simple metal. However theorists have come to realise that it is not that straightforward, and that even if there is a ferromagnetic ground state there are other states close by in energy which may give rise to unconventional excitations. Millis *et al* have used a dynamic mean field theory, with double exchange coupling treated dynamically but using a 'frozen phonon' approach for the lattice [50]. Calculations imply that the metal-to-insulator transition is driven by the localisation of electrons on disorder, induced by lattice fluctuations which mimic the compositional dependence by variation in the strength of the Jahn-Teller coupling constant. This approach can therefore only operate in the extremes of x = 0 and x = 1. Roder *et al* [51] have used a standard mean-field theory for double exchange coupling. This assumes that electrons move in a static field created by spin, and the model allows for phonon dynamics.

It is clear from the short summary above that there are a large number of CMR active solid solution systems, all with complex phase diagrams. At the outset of the work in this thesis a lot of attention was given to the system $La_{1-x}Ca_xMnO_3$ and it was decided to focus on a particular compositional range, as outlined in the next section.

7.6 The $La_{1-x}Ca_xMnO_3$ system

Whilst the series of compounds $La_{1-x}Ca_xMnO_3$ had been studied previously [5] a revival in interest in such CMR active materials meant that attention was focussed again on the structural and magnetic changes exhibited upon progressively doping the parent compound $LaMnO_3$. Thus a temperature-composition phase diagram was published by Schiffer *et al* [52], which is reproduced below.

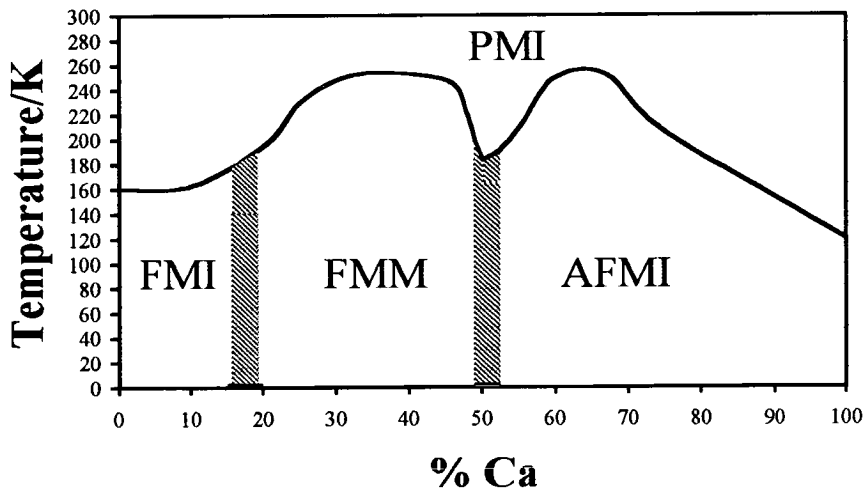

Figure 7.8 Temperature vs. composition (as percentage doping in calcium) phase diagram for the system $La_{1-x}Ca_xMnO_3$. The terms PMI, FMI, FMM and AFMI represent paramagnetic insulating, ferromagnetic insulating, ferromagnetic metallic and antiferromagnetic insulating phases respectively

From this diagram it is clear that there are two main areas of interest. These are the compositional regions 15-20% calcium doping, and around 50% calcium doping. In these regions it is unclear what happens to the structure as it moves firstly through a transition from antiferromagnetic to ferromagnetic spin ground state, and then from a

ferro to antiferromagnetic spin ground state, accompanied by a metal to insulating transition. Extensive work has also focussed on the x = 0.33 composition [53], since the largest magnitude of CMR and most pronounced ferromagnetism is found in this sample.

Porter *et al* [54] looked at the lower doping regime in work carried out at the Institut Laue-Langevin in Grenoble, collecting data on both the D1B and D2B diffractometers, with compositions spanning the region 10-20% in calcium concentration. Analysis of these data showed that the magnetic structure moves through a canted spin state to the ferromagnetic form, in direct contradiction to work by Maekawa *et al* [55] which suggested that a spiral spin state was energetically favoured at these doping levels. This was further elucidated by work performed by Kawano *et al* [56] on the Sr doped system which agreed with the canted spin state model observed by Porter and co-workers. However, despite recent publications [57], explanation of the evolution of the magnetic and crystallographic structures at the 50% doping level has proved extremely difficult, due in no small part to the extremely fine balance of the system, being on the brink of an electronic and magnetic transition. It was with the aim of unravelling the nature of the evolution of this system through this transition point that attention was focussed on the preparation of samples spanning the region close to the $La_{0.5}Ca_{0.5}MnO_3$ composition.

7.7 The composition $La_{0.5}Ca_{0.5}MnO_3$

As briefly outlined above the nature of the composition at x = 0.5 has proved intriguing and is still an area of active investigation. Initial work by Radaelli *et al*

[52,58] suggested the coexistence of both ferromagnetic and antiferromagnetic phases, with a ferromagnetic transition seen in the magnetisation at around 225K and an antiferromagnetic transition point seen as a drop in magnetisation at around 170K. Whilst Bragg reflections are sharp above and below these temperatures, in the intermediate region there is a dramatic broadening of these reflections, with a pronounced structure inconsistent either with a typical particle size or indeed strain effects. Such observations, the authors suggest, can only be explained either as a continuous distribution of lattice parameters with several maxima, or by a number of discrete phases each having a coherence length greater than that observable using X-rays (a few thousand Ångstroms). They utilise the latter model and use four phases to model the diffraction data obtained, two of which were magnetic phases. These 'phases' have very similar volumes, despite differing lattice parameters, suggesting that they may actually correspond to domains with different degrees of orientational order of MnO_6 octahedra. Simultaneous presence of domains of several metastable states, ranging from complete disorder of the Mn d_{z^2} orbitals to complete ordering in the *a-c* plane as proposed by Goodenough [59] for low temperatures, would account for the enhanced *a-c* strain observed in this intermediate region.

This work is supported by Chen *et al* [60] who obtained electron diffraction data for a sample of composition $La_{0.5}Ca_{0.5}MnO_3$. Low temperature images were indexed on a *Pbnm* orthorhombic cell, the observed superlattice spots having a modulation vector of $\vec{q} = (2\pi / a)(1/2 - \varepsilon, 0, 0)$ with incommensurability parameter ε = 0.013. Such superlattice spots provide direct evidence for charge ordering as alluded to by Radaelli by the observation of an inflection point in resistivity data obtained for a

sample of similar composition. Measurement of this charge ordering wavevector as a function of temperature, on cooling and warming, clearly shows that the first-order ferro-antiferromagnetic transition is associated with an incommensurate-commensurate charge order transition, and the authors contend that the peak broadening effects seen by Radaelli and co-workers is in fact linked to such a transition.

Magnetic specific heat measurements have been used as a probe of possible phase co-existence. Ramirez *et al* [61] found, in the case of a $La_{0.5}Ca_{0.5}MnO_3$ sample examined, clear evidence for two phase transitions, the first being ferromagnetic with the value of T_C showing no difference on warming/cooling. The second transition is a simultaneous antiferromagnetic and charge ordering transition which shows pronounced hysteresis. The combination of data from both specific heat and sound velocity measurements, acquired for a range of compositions, give results similar to those seen in $La_{0.67}Sr_{0.33}NiO_4$, the big difference between the systems being the Jahn-Teller distortions present in the manganite samples. This thus suggests that the large coupling of sound to the internal energy of the system, a hardening of the lattice, seen in the manganites, two orders of magnitude greater than that observed in the case of the nickelate, is due to large electron-phonon coupling *via* such Jahn-Teller distortions.

Ghivelder and co-workers [62] concur with the idea of lattice hardening, having performed specific heat measurements on a range of compositions with $x = 0.1$, 0.33 and 0.62. As the value of x is increased there is a corresponding increase in the Debye temperatures, thus a shift to higher lattice vibrations and hence a hardening of the lattice with increasing Ca content.

The co-existence of both ferromagnetic and antiferromagnetic phases at this composition is now widely accepted. For example in the work of Rhyne *et al* [63] diffraction data for a sample of nominal composition $La_{0.53}Ca_{0.47}MnO_3$ was indexed as *Pnma* with an additional monoclinic phase of space group *P21/m* at low temperature, amounting to around 40% of the volume fraction. Rietveld structure refinement analysis of neutron powder diffraction data confirmed the co-existence of ferro- and antiferromagnetic phases below T_N, persistent to 10K. A change in the lattice parameters of the monoclinic phase close to T_N, suggested the onset of charge ordering as previously described by Radaelli [58]. Work was then performed in order to compare this sample with previous work by Lynn and co-workers[64]. In this previous work the spin wave energy E_{sw} showed the following dispersion relation

$$E_{sw} = Dq^2 + \Delta \tag{7.7}$$

where $q = 2\pi/d$, d is the lattice spacing (Å) and the spin wave gap, Δ, was not measurable at $E_{sw} = 0$. The spin wave stiffness D showed only weak renormalisation with temperature, whilst no spin waves were seen above T_C. An anomalous central mode developed above about 80% of T_C, persisting well above this temperature, with a width varying as the square of q, suggesting the presence of spin diffusion.

Data on the $La_{0.53}Ca_{0.47}MnO_3$ sample were taken between 10 and 240K ($T_C \sim 237$K) and only within the first Brillouin zone at low scattering angles, hence only longer wavelength excitations were studied. At 10K negligible spin wave scattering is observed, whilst the spin wave energies are reduced as the temperature is increased. A quadratic dependence in the dispersion is seen, suggesting conventional Heisenberg

behaviour, whilst a spin gap of $\Delta \sim 0.1$meV is seen at $q = 0$ in contrast to the work of Lynn. What is also of note is the existence of FM spin waves in a compound also exhibiting antiferromagnetic spin order. The value of D shows significant renormalisation with temperature unlike in the case of the $La_{0.67}Ca_{0.33}MnO_3$, the value of $D/T_C = 0.57$ characteristic of an itinerant system. Furthermore, the intensity of the central peak is nothing like that seen in the previous work suggesting that its origin is in the formation of magnetic polarons.

The formation of such polarons is also considered by Garcia-Muñoz *et al* in recent work [65]. They investigate the nature of the dynamics of the system $La_{0.5}Ca_{0.5}MnO_3$ using muon spin relaxation measurements. In the small magnetic polaron picture, delocalised carriers in the form of electrons are 'dressed' in a co-operative lattice deformation extending over several cation sites, and such 'dressed' carriers then diffuse through the lattice. On warming from low temperatures a transition to short range order is observed with ferromagnetic clusters of *ca.* 18Å in size developing, as observed in high resolution neutron diffraction data. What is seen therefore is glassy like dynamics close to the Curie temperature T_C with a distribution of local moment correlation times which narrows with increasing temperature, to a unique relaxation time at room temperature.

In considering polaron dynamics Zhao [66] has looked at oxygen isotope effects on the nature of the magnetisation and resistivity of a sample of composition $La_{0.5}Ca_{0.5}MnO_3$. It is not clear why the charge-ordered state in such compounds can be destroyed by moderate applied magnetic fields ($H_{app} < 10$T), whilst photoemission and tunnelling experiments suggest the presence of a large energy gap. What is observed is a significant isotope effect, with $T_{CO}(^{18}O) > T_{CO}(^{16}O)$, where T_{CO} is the

temperature at which the onset of charge ordering is seen. A decrease in the value of T_{CO} as the magnitude of the applied magnetic field is increased is also observed, this decrease being greater in the case of the ^{16}O sample. Such a negative isotope effect on T_{CO} is in contrast to previous work where a positive isotope effect was reported for the magnitude of T_C [67]. Whilst the relative shift in T_C appeared independent of any applied field, in the case of T_{CO} the shift is heavily dependent on the magnitude of the applied magnetic field. If charge ordering arises as a consequence of long-range Coulombic repulsion between carriers, then no isotope effect should be observed. If charge ordering is related to small polaron ordering then the effective mass of the carrier is larger for the heavier isotope, which in turn will give the carrier a greater mass and so stabilise the charge ordered state. This would explain the higher value of T_{CO} seen for the ^{18}O isotope sample; however it still does not explain why such a charge ordered state is destroyed by applied fields. The authors speculate that there are possible parallels with the theory of bipolaron ordering in high temperature superconductors. The T_{CO} for bipolarons is a function of both a repulsive interaction v between bipolarons and a hopping integral t. Both of these terms could strongly depend on the isotope mass, in agreement with the shift seen in T_{CO}, whilst ordered/disordered bipolaron states could have a small energy gap associated with them explaining the ability to melt the charge ordered state by application of a field. The binding energy of these bipolarons is then equivalent to this energy gap.

7.8 Summary

This chapter has attempted to give an overview of the current understanding of the nature of the system $La_{1-x}M_xMnO_3$, and the temperature-composition phase diagram in the particular case where M = Ca. To investigate any changes in the crystallography of the system in the region of the phase diagram where $x \sim 0.50$, as well as the nature of spin fluctuations in the region of T_C, a combination of high resolution powder neutron diffraction studies and muon spin relaxation measurements were proposed, the results of which are presented in the next chapter.

Neutron powder diffraction data obtained for the series $La_{1-x}Pb_xMnO_3$ in the range $x = 0 - 0.5$ are also presented.

References

[1] G.H. Jonker and J.H. Van Santen, *Physica* **16** 337 (1950)

[2] J.H. Van Santen and G.H. Jonker, *Physica* **16** 599 (1950)

[3] J.B. Goodenough, *'Magnetism and the Chemical Bond'*, (Wiley & Sons,1963)

[4] J.B.Goodenough, *Phys Rev.* **100** (2) 564 (1955)

[5] E.O.Wollan and W.C.Koehler, *Phys. Rev.* **100** (2), 545 (1955)

[6] C.Zener, *Phys. Rev.* **81**(4) 440 (1951)

[7] C.Zener, *Phys. Rev.* **82**(3) 403 (1951)

[8] R.M. Kusters, J. Singleton, D.A. Keen, R. McGreevy, W. Hayes, *Phys. Rev. B* **155** 362 (1989)

[9] P.M. Levy, *Science* **256** 972 (1992)

[10] R.B. Dover, E.M. Gyorgy, R.J. Cava, J.J. Krajewski, R.J. Felder, W.F. Peck, *Phys. Rev. B* **47**(10) 6134 (1993)

[11] R. Von Helmholt, J. Wecker, B. Holzapfel, L. Schultz, K. Samwer, *Phys. Rev. Lett.* **71** 2331 (1993)

[12] K. Chahara, T. Ohno, M. Kasai, Y. Kozono, *Appl. Phys. Lett.* **63**(14) 1990 (1993)

[13] S. Jin, T.H. Tiefel, R. Ramesh, *J. Appl. Phys.* **76**(10) 6929 (1994)

[14] S.Jin, T.H. Tiefel, M. McCormack, R.A. Fastnacht, R. Ramesh, L.H. Chen, *Science* **264** 413 (1994)

[15] S. Jin, T.H. Tiefel, M. McCormack, H.M. O'Bryan, L.H. Chen, R. Ramesh, D. Schurig, *Appl. Phys. Lett.* **67**(4) 557 (1995)

[16] Q.Huang, A.Santoro, J.W.Lynn, R.W.Erwin, J.A.Borchers, J.L.Peng and R.L.Greene, *Phys. Rev. B* **55**(22) 14987 (1997)

[17] A.Goyal, M.Rajeswari, R.Shreekala, R.Lofland, S.M.Bhagat, T.Boettcher, C.Kwon, R.Ramesh, T.Venketesan, *Appl. Phys. Lett.* **71** 2535 (1997)

[18] See for example P.M.Levy, *Science* **256** 972 (1992); R.B.Dover, E.M.Gyorgy, R.J.Cava, J.J.Krajewski, R.J.Felder, W.F.Peck, *Phys. Rev. B* **47**(10) 6134 (1993)

[19] J.B. Goodenough and J.M. Longo, *Landolt-Börnstein Tabellen,* Springer-Verlag, Berlin, **III** 126 (1970)

[20] W.E. Pickett and D.J. Singh, *Phys. Rev. B* **53**(3) 1146-1159 (1996)

[21] *'Quantum Theory of Solids'*, R.E. Peierls (Clarendon Press, Oxford, 1955), 108

[22] P.W. Anderson, *Phys. Rev.* **109** 1492 (1958)

[23] C. Zener, *Phys. Rev.* **82**(3) 403 (1951); P.De Gennes, *Phys. Rev.* **118** 141 (1960)

[24] H.A. Kramers, *Physica* **I** 191 (1934)

[25] J. Fontcuberta, B. Martinez, A.Seffar, S. Pinol, J.L. Garcia - Munoz, X. Obradors, *Phys. Rev. Lett.* **76**(7) 1122 (1996)

[26] R. Mahendiran, S.K. Tiwary, A.K. Raychaudhuri, T.V. Ramakrishnan, R. Mahesh, N.Ragvittal, C.N.R. Rao, *Phys. Rev. B* **53**(6) 3348 (1996)

[27] A.Barnabé, A.Maignan, M.Hervieu, F.Damay, C.Martin and B.Raveau, *Appl. Phys. Lett.* **71**(26) 3907 (1997)

[28] H.Y.Hwang, S.W.Cheong, P.G.Radaelli, M.Marezio and B.Batlogg, *Phys. Rev. Lett.* **75** 914 (1995)

[29] A.Maignan, Ch.Simon, V.Caignaert and B.Raveau, *Solid St. Commun.* **94** 515 (1995)

[30] A.Maignan, Ch.Simon, V.Caignaert and B.Raveau, *Z.Phys. B* **99** 305 (1996)

[31] L.M.Rodriguez-Martinez and J.P.Attfield, *Phys. Rev. B* **54** 1 (1996)

[32] B.Raveau, A.Maignan and C.Martin, *J. Solid St. Chem.* **130** 162 (1997)

[33] A.J. Millis,.P.B. Littlewood, B.I. Shraiman, *Phys. Rev. Lett.*, **74**(25) 4488 (1995)

[34] P.D. Battle, S.J. Blundell, M.A. Green, W. Hayes, M. Honold, A.K. Klehe, N.S. Laskey, J.E. Millburn, L. Murphy, M.J. Rosseinsky, N.A Samarin , J. Singleton, N.E. Sluchanko, S.P. Sullivan and J.F. Vente, *J. Phys. Condens. Matter* **8** L427 (1996)

[35] M.A. Subramanian, B.H. Toby, A.P. Ramirez, W.J. Marshall, A.W. Sleight, G.H. Kwei, *Science* **273** 81 (1996)

[36] A.P. Ramirez, R.J. Cava and J. Krajewski, *Nature* **386** 156 (1997)

[37] J.M.D Coey, M. Viret, L. Ranno, K. Ounadjela, *Phys. Rev. Lett.* **75**(21), 3910 (1995)

[38] N.F. Mott, *J. Non-Cryst. Solids* **1** 1 (1968); N.F. Mott, *Phil. Mag.* **19** 835 (1969)

[39] H.L Ju and Hyunchul Sohn, *Solid St. Comm.* **102**(6) 463 (1997)

[40] Y.X. Jia, Li Lu, K. Khazeni, V.H Crespi, A. Zettl and M.L. Cohen, *Phys. Rev. B* **52** 9147 (1995)

[41] T.M Perekalina, T.A. Sivokon, S.A Cherkezyan and I.E. Lipinski, *Sov. Phys. - Solid State* **3** 1524 (1990)

[42] H. Kuwahara, Y. Moritomo, Y. Tomioka, A. Asamitsu, M. Kasai, Y. Tokura, *J. Appl. Phys.* **81**(8) 4954 (1997)

[43] A.R. Bishop and H. Röder, *Current Opinion in Solid St. and Mat. Sci.* **2** 244 (1997)

[44] M.F. Hundley, M. Hawley, R.H. Heffner, J. Qx, J.J Neumeier, J. Tesmer, J.D. Thompson, X.D Wu, *Appl. Phys. Lett.* **67** 860 (1995)

[45] B. Martinez, J. Fontcuberta, A. Seffar, J.L Garcia - Munoz, S. Pinol, X. Obradors, *Phys. Rev. B* **54** 10001 (1996)

[46] M. Jaime, M.B Salamon, M. Rubenstein, R.E Treece, J.S. Horwitz, D.B. Chrisey, *Phys. Rev. B* **54** 11914 (1996)

[47] R.P Sharma, G.C Xiong, C. Kwon, R. Ramesh, R.L. Greene, T. Venketesan, *Phys. Rev. B* **54** 10014 (1996)

[48] T.A Tyson, J. Mustre de Leon, S.D Conradson, A.R. Bishop, J.J. Neumeier, H. Röder, J. Zang, *Phys. Rev. B* **53** 13985 (1996)

[49] S.J.L Billinge, R.G. DiFrancesco, G.H Kwei, J.J. Neumeier, J.D Thomson, *Phys. Rev. Lett.* **77** 715 (1996)

[50] A.J. Millis, P.B. Littlewood, B.I. Shraiman, *Phys. Rev. Lett.* **77** 175 (1996); A.J. Millis, R. Mueller, B.I. Shraiman, *Phys. Rev. B* **54** 5405 (1996)

[51] H. Röder, J. Zang, A.R. Bishop, *Phys. Rev. Lett.* **76** 1356 (1996); J. Zang, A.R. Bishop, H. Röder, *Phys. Rev. B* **53** R8840 (1996)

[52] P. Schiffer, A.P. Ramirez, W. Bao and S.W. Cheong, *Phys. Rev. Lett.*, **75**(18), 3336 (1995)

[53] See for example M. McCormack, S. Jin, T.H. Tiefel, R,M, Fleming, Julia M. Phillips, *Appl. Phys. Lett.* **64** 3045 (1994); S. Jin, M. McCormack, T.H. Tiefel, R.

Ramesh, *J. Appl. Phys.* **76**(10) 6929 (1994); B. Chen, C. Uher, D.T. Morelli, J.V. Mantese, A.M. Mance, A.L. Micheli, *Phys. Rev. B* **53** 5094 (1996); J.M. De Teresa, M.R. Ibarra, J. Blasco, J. Garcia, C. Marquina, P.A. Algarabel, Z. Arnold, K. Kamenev, C. Ritter, R. von Helmholt, *Phys. Rev. B* **54**(2) 1187 (1996); R.H. Heffner, L.P. Le, M.F. Hundley, J.J. Neumeier, G.M. Luke, K. Kojima, B. Nachumi, Y.J. Uemura, D.E. MacLaughlin, S.W. Cheong, *Phys. Rev. Lett.* **77**(9) 1869 (1996)

[54] A. Harrison, D.A. Porter, A.V. Powell, Clemens Ritter, *ILL Annual Report,* 1996

[55] J. Inoue, S. Maekawa, *Phys. Rev. Lett.* **74**(17) 3407 (1995); J. Inoue, S. Maekawa, *Mat. Sci. Eng.* **B31** 193 (1995)

[56] H. Kawano, R. Kajimoto, M. Kubota, H. Yoshizawa, *Phys. Rev. B* **53**(5) 2202 (1996)

[57] G.Q. Gong, C.L. Canedy, G. Xiao, J.Z. Sun, A. Gupta, W.J. Gallacher, *J. Appl. Phys.* **79**(8) 4538 (1996); C.H. Chen, S.W. Cheong, *Phys. Rev. Lett.* **76**(21) 4042 (1996); P.G. Raedelli, D.E. Cox, M. Marezio, S.W. Cheong, *Phys. Rev. B* **55**(5) 3015 (1997); M.Roy, J.F.Mitchell, A.P.Ramirez and P.Schiffer, *Phys. Rev. B* **58**(9) 5185 (1998); M.Roy, J.F.Mitchell, A.P.Ramirez and P.Schiffer, *J. Phys. Condens. Matter* **11**(25) 4843 (1999)

[58] P.G. Raedelli, D.E. Cox, M. Marezio, S.W. Cheong P.E.Schiffer and A.P.Ramirez, *Phys. Rev. Lett.* **75**(24) 4488 (1995)

[59] J.B.Goodenough, *Phys. Rev.* **100** 564 (1955)

[60] C.H.Chen and S.W. Cheong, *Phys. Rev. Lett.* **76**(21) 4042 (1996)

[61] A.P.Ramirez, P.Schiffer, S.W. Cheong, C.H.Chen, W.Bao, T.T.M.Palstra, P.L.Gammel, D.J.Bishop and B.Zegarski, *Phys. Rev. Lett.* **76**(17) 3188 (1996)

[62] L.Ghivelder, I.Abrego-Castillo, N.McN.Alford, G.J.Tomka, P.C.Riedi, J.MacManus-Driscoll, A.K.M.Akther Hossain, L.F.Cohen, *J.Mag.Magn.Mat.* **189** 274 (1998)

[63] J.J.Rhyne, H.Kaiser, H.Luo, G.Xiao and M.L.Gardel, *J. Appl. Phys.* **83**(11) Pt.2 7339 (1998)

[64] J.W.Lynn, R.W.Erwin, J.A.Borchers, Q.Huang, A.Santoro, J-L.Peng and Z.Y.Li, *Phys. Rev. Lett.* **76**(21) 4046 (1996)

[65] J.L.Garcia-Muñoz, A.Llobet, C.Frontera, J.Fontcuberta, X.Obradors and C.Ritter, *J.Mag.Magn.Mat.* **197** 477 (1999)

[66] G.Zhao, K.Ghosh, H.Keller and R.L.Greene, *Phys. Rev. B* **59**(1) 81 (1999)

[67] G.Zhao, K.Conder, H.Keller and K.A.Muller, *Nature* **381**(6584) 676 (1996)

Chapter 8 Lanthanum Manganites: Experimental

8.1 Introduction

As outlined in the previous Chapter, the most complex region of the compositional phase diagram for the system $La_{1-x}Ca_xMnO_3$ is at the point where $x \sim 0.50$ since the system is finely balanced between both a ferro-antiferromagnetic and metal-insulator transition. Previous studies have underlined the key role of the Mn-O-Mn bond angle in promoting double exchange, and the direct consequence of this on the resistive properties exhibited by these materials below their respective Curie temperatures. There has also been a considerable amount of debate regarding the possibility of the co-existence of ferro and antiferromagnetic correlations at the $x = 0.50$ composition [1-3]. Therefore in an attempt to examine the nature of any crystallographic or magnetic changes in this region of the phase diagram, a series of samples with compositions close to the $x = 0.50$ boundary were prepared for an experiment performed on the HRPD powder neutron diffractometer at ISIS.

Whilst a lot of experimental attention has focussed on the $La_{1-x}Ca_xMnO_3$ system, other systems with different dopants at the Ln site have also proved interesting. In particular, the $La_{1-x}Pb_xMnO_3$ system has been studied [4] since samples with concentrations of lead of *ca.* 30% show values of T_C close to room temperature and so afford the possibility of exploiting the magnetoresistive properties of the system directly at room temperature. We therefore undertook a study of this system, also on the HRPD diffractometer, with samples spanning the compositional range $x = 0$ to $x = 0.5$.

Both sets of diffraction data provide a valuable insight into the nature of the evolution of the structure as it crosses through the complex phase boundary; however they cannot provide any information as to the spin dynamics of the system. A rigorous investigation of the spin dynamics would, in most cases, involve performing a number of single crystal neutron measurements, in order to probe both the strength of the exchange interaction *J*, and the nature of any spin wave dispersion. However extensive laboratory attempts to grow single crystals of a size suitable for such experiments, have proved unsuccessful at doping levels of calcium above x = 0.1. It is still possible to gain some insight into the nature of such dynamics in powdered samples through the use of muon spin relaxation measurements, and to this end, in the case of the $La_{1-x}Ca_xMnO_3$ system, measurements are presented on two samples of compositions x =0.46 and x =0.50, data having been collected both on the MuSR instrument at the ISIS facility and the DOLLY instrument at the Paul Scherrer Institute (PSI) in Villigen Switzerland.

8.2.1 Sample preparation

Samples of composition $La_{0.54}Ca_{0.46}MnO_3$, $La_{0.52}Ca_{0.48}MnO_3$ and $La_{0.50}Ca_{0.50}MnO_3$ were targeted for preparation *via* a traditional solid state reaction route. Stoichiometric amounts of La_2O_3 (Alpha, 99.999%), $MnCO_3$ (Aldrich, 99.999%) and $CaCO_3$ (Aldrich, 99%). were ground together using a pestle and mortar and then placed in alumina crucibles and heated at 950°C for 10 hours. The resulting dark purple sintered powder was then reground and pressed into pellets, under a load of 4.5 tons, using a Graseby Specac® 13mm die, and these pellets were refired three times at 1200°C for 10 hours with intermediate grindings.

To examine the phase purity of these samples X-ray powder diffraction patterns were taken using a Philips PW1730 Diffractometer using a Cu anode running at 40kV and 30mA. Each diffraction pattern was taken over a 2-theta interval of 10-70° at intervals of 0.02° and are shown below.

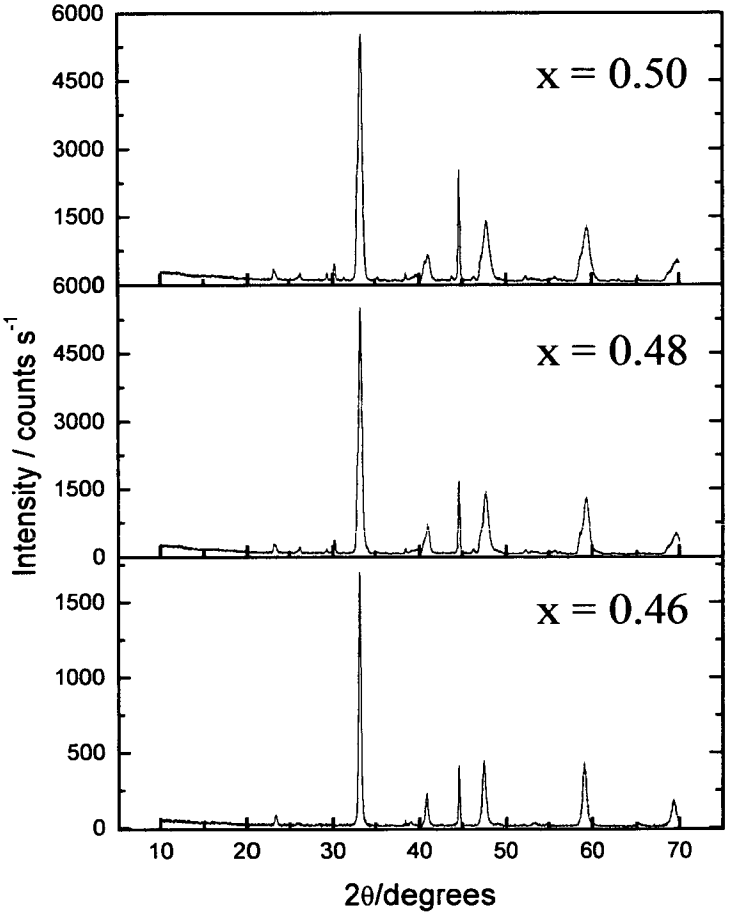

Figure 8.1 Powder X-ray diffraction patterns obtained for samples of $La_{1-x}Ca_xMnO_3$ with compositions x = 0.50 (top), x = 0.48 (middle) and x = 0.46 (bottom) respectively

Whilst the two samples of compositions x = 0.46 and x = 0.48 exhibit very similar diffraction patterns, there is significant peak broadening in the case of the x = 0.50 sample. This can be illustrated in the case of the (202) and (220) reflections as shown in the figure below.

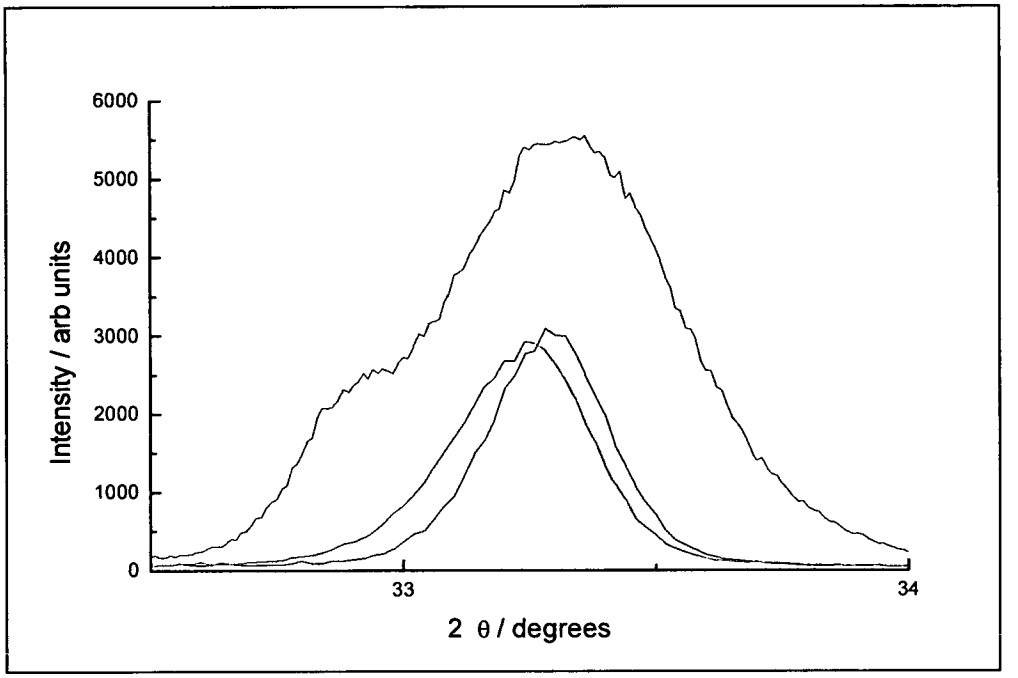

Figure 8.2 Section of diffraction patterns obtained for samples $La_{0.54}Ca_{0.46}MnO3$(black), $La_{0.52}Ca_{0.48}MnO_3$ (red) and $La_{0.50}Ca_{0.50}MnO_3$ (blue) illustrating significant peak broadening in the case of $La_{0.5}Ca_{0.5}MnO_3$ in comparison to the other two compositions

To verify the magnetic behaviour of the samples SQUID magnetometer measurements were also performed. Each sample was measured after cooling in first zero field and then a field of 100G, over a temperature range of 2-300K, in an applied field of 100G. The molar susceptibility of each sample is shown below.

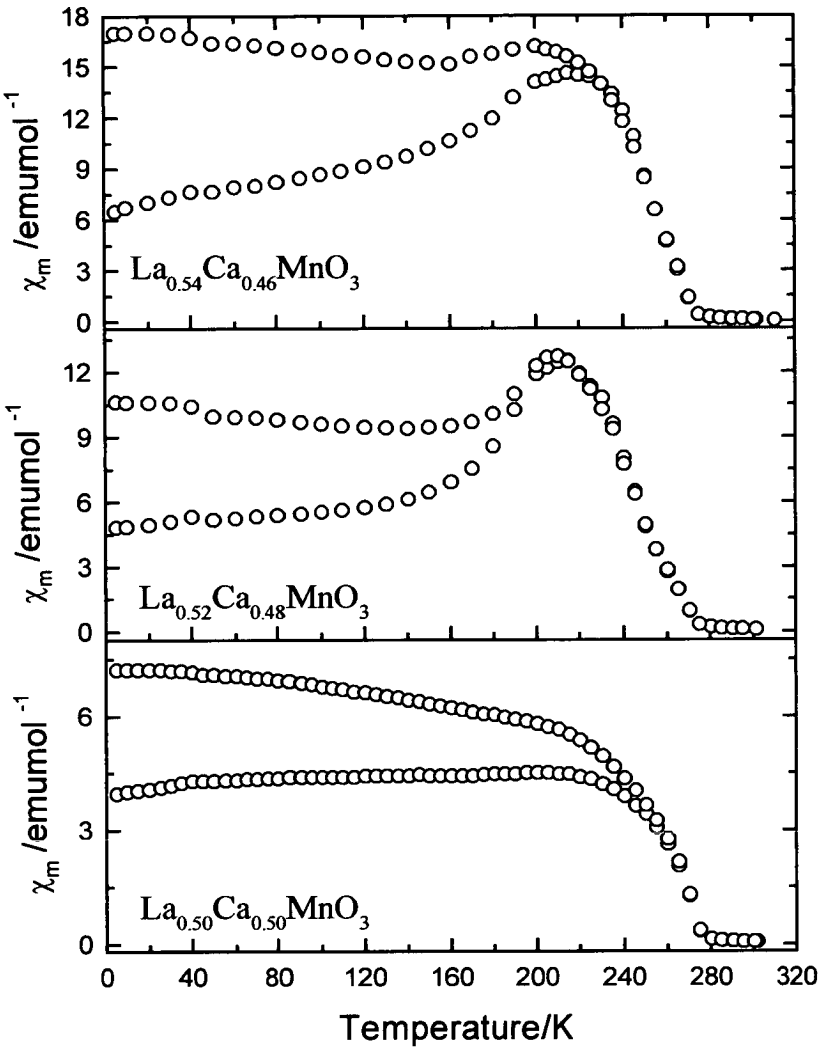

Figure 8.3 Plots of molar susceptibility χ_m versus temperature T for the samples $La_{0.54}Ca_{0.46}MnO_3$ (top), $La_{0.52}Ca_{0.48}MnO_3$ (middle) and $La_{0.50}Ca_{0.50}MnO_3$ (bottom)

The value of T_C for each material was determined from a plot of the derivative of the molar susceptibility $d\chi_m/dT$ against temperature T, in the case of the zero-field cooled data, as shown in the figure below.

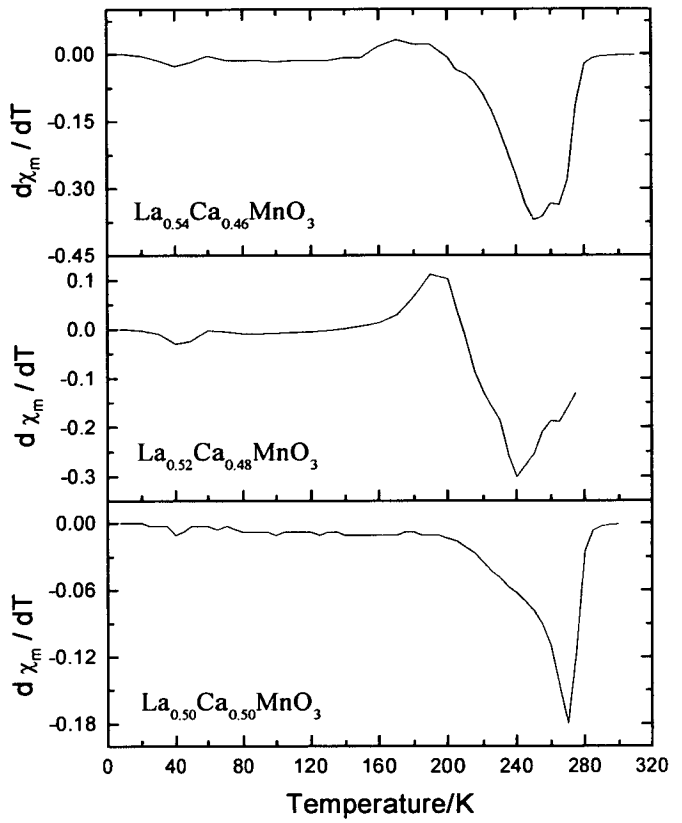

Figure 8.4 Plots of the first derivative of the molar susceptibility $d\chi_m/dT$ versus temperature T for the samples $La_{0.54}Ca_{0.46}MnO_3$ (top), $La_{0.52}Ca_{0.48}MnO_3$ (middle) and $La_{0.50}Ca_{0.50}MnO_3$ (bottom)

The minima in $d\chi_m/dT$ were found to be 250.1, 240.1 and 270.1K (in order of increasing calcium concentration).

Solutions of each composition were made up in concentrated hydrochloric acid, with nominal concentrations of 30 ppm in manganese and lanthanum, and 10 ppm in calcium. The exact concentrations of all three ions were then determined by ICP atomic emission spectroscopy, analysis for these metals being performed on single

solutions of each composition. Thermogravimetric analysis was also performed on each composition in order to determine the oxygen content. Each sample was heated under hydrogen gas over a temperature range of 15 - 1200°C, with a heating rate of 5°C min^{-1}. The combined results of the analyses are summarised below.

Nominal composition	Determined concentration Ca/ppm	Determined concentration Mn/ppm	Determined concentration La/ppm	Stoichiometric formula
$La_{0.54}Ca_{0.46}MnO_3$	9.48±0.08	32.63±0.23	38.81±0.21	$La_{0.50}Ca_{0.44}Mn_{0.99}O_{2.72}$
$La_{0.52}Ca_{0.48}MnO_3$	9.23±0.05	32.41±0.28	38.64±0.38	$La_{0.51}Ca_{0.45}Mn_{1.03}O_{2.77}$
$La_{0.50}Ca_{0.50}MnO_3$	9.77±0.04	29.30±0.24	39.13±0.24	$La_{0.51}Ca_{0.50}Mn_{0.97}O_{2.66}$

Table 8.1 Results of thermogravimetric and atomic emission analysis of $La_{1-x}Ca_xMnO_3$ samples respectively

8.2.2 HRPD Experimental work

The three samples of $La_{1-x}Ca_xMnO_3$ were then taken to the HRPD neutron diffractometer at the ISIS facility at the Rutherford Appleton Laboratory near Didcot. The sample of composition $La_{0.52}Ca_{0.48}MnO_3$ (1.05 g) was loaded into a flat vanandium sample can and data recorded at 300K before cooling to 150K where a further diffraction pattern was taken. The sample was then warmed to 200K and another pattern collected. The $La_{0.54}Ca_{0.46}MnO_3$ sample (3.054 g) was then loaded up in a larger flat vanadium can and similar measurements performed. Finally the $La_{0.50}Ca_{0.50}MnO_3$ sample was loaded up (1.356 g) and similar scans performed. The details are summarised in the following table.

Sample	Mass used / g	150K	200K	300K
$La_{0.52}Ca_{0.48}MnO_3$	1.050	x	x	x
$La_{0.54}Ca_{0.46}MnO_3$	3.054	x	x	x
$La_{0.5}Ca_{0.5}MnO_3$	1.356	x	x	x

Table 8.2 Compositions and temperatures at which measurements were taken during the experimental time on the HRPD instrument

Structure refinements of the data collected were carried out using the GSAS routine with starting cell parameters and atomic positions taken from previous work performed at the ILL [5]. The room temperature data indexed successfully using the space group *Pbnm* (*International Tables for Crystallography Volume A No.62*) and the refined lattice parameters are given below. Also shown are the bond lengths for the Mn-O bonds both in the *a-b* plane and along the *c*-axis (labelled Mn-O1 and Mn-O2 respectively), as depicted in the figure below. The associated bond angles are also shown, the bond angle Mn-O2-Mn being the double exchange angle.

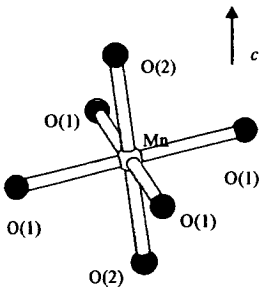

Figure 8.5 Definition of oxygen atoms in octahedral environment around the manganese atoms with direction of c-axis marked for clarity

Refined atomic positions and difference plots of the observed and calculated patterns are shown in Appendix C, along with the goodness of fit parameters χ^2 and R_{wp}.

The lower temperature data also indexed successfully using space group *Pbnm*: however the structure refinements also had to take into account additional intensity to existing reflections, as well as additional reflections resulting from magnetic Bragg scattering. Two phase refinements were attempted using a second magnetic phase with the requisite moments inserted manually into a cell of *P1* symmetry.

Parameters	300K	200K	150K
a/Å	5.43538(25)	5.42886(38)	5.423331(34)
b/Å	5.42500(26)	5.42137(39)	5.421154(36)
c/Å	7.65330(28)	7.65220(34)	7.655001(4)
Cell Volume/Å^3	225.673(6)	225.218(6)	225.061(74)
O1-Mn/Å	1.9420(8)	1.9350(10)	1.93688(25)
O2-Mn/Å	1.966(5), 1.926(5)	1.944(6), 1.951(6)	1.933(3), 1.958(3)
Mn-O1-Mn	160.28(27)	162.7(4)	162.272(4)
Mn-O2-Mn	161.31(16)	159.98(19)	160.393(2)
χ^2	2.503	6.826	20.28
R_{wp}	0.0425	0.0499	0.0509

Table 8.3 Refined lattice parameters and bond lengths obtained for $La_{0.54}Ca_{0.46}MnO_3$

Parameters	300K	200K	150K
a/Å	5.43034(62)	5.42706(49)	5.42525(35)
b/Å	5.42156(51)	5.41839(43)	5.41778(34)
c/Å	7.64583(34)	7.63962(31)	7.63929(33)
Cell Volume/Å^3	225.100(7)	224.650(8)	224.516(17)
O1-Mn/Å	1.9402(12)	1.92972(7)	1.92962(8)
O2-Mn/Å	1.954(9), 1.932(9)	1.93980(11), 1.95758(12)	1.95711(9), 1.93942(9)
Mn-O1-Mn	160.3(4)	163.566(2)	163.570(1)
Mn-O2-Mn	161.80(23)	159.379(1)	159.376(1)
χ^2	3.133	4.312	13.59
R_{wp}	0.0303	0.0367	0.0372

Table 8.4 Refined lattice parameters and bond lengths obtained for $La_{0.52}Ca_{0.48}MnO_3$

Parameters	300K
a/Å	5.42150(403)
b/Å	5.40699(319)
c/Å	7.60665(223)
Cell Volume/Å^3	222.981(46)
O1-Mn/Å	1.9293(29)
O2-Mn/Å	1.959(11), 1.920(11)
Mn-O1-Mn	160.3(10)
Mn-O2-Mn	161.6(4)
χ^2, R_{wp}	3.083, 0.0317

Table 8.5 Refined lattice parameters and bond lengths obtained for $La_{0.50}Ca_{0.50}MnO_3$

The cell parameters, position of the Mn moments and the orientation of these moments are summarised in the table below.

Atom	*x*	*y*	*z*	m_x	m_y	m_z
Mn	0.5	0	0	0	0	1
Mn	0.5	0	0.5	0	0	1
Mn	0	0.5	0	0	0	1
Mn	0	0.5	0.5	0	0	1

Table 8.6 Position of manganese moments in magnetic unit cell, with cell dimensions identical to that of the nuclear cell

In the case of the sample $La_{0.50}Ca_{0.50}MnO_3$ attempted refinements at lower temperature were not very successful. The multi-phasic nature of the sample, as shown by the analysis performed, made modelling of the broad reflections difficult.

The general trend in the lattice parameters obtained for the 300K data sets can be considered in terms of the degree of octahedral distortion and orbital ordering present in the sample. Woodward et al [6] state that, in space group *Pnma*, changes in the magnitude of the *c*-axis reflects the degree of octahedral tilting (and thus distortion from the ideal structure), whilst changes in the *a*-axis reflect the magnitude of the Jahn-Teller distortion present. This corresponds to changes in the *b* and *c* axes in the case of *Pbnm* settings. Thus the reduction in the length of the *b*-axis at 300K, on increasing the nominal doping of calcium, reflects an increase in the octahedral

distortion present. An increase in the *c* parameter when comparing the parameters obtained for the x = 0.46 and 0.48 samples respectively suggests a reduction in the degree of orbital ordering present. This is reinforced by the slight reduction in Mn-O2-Mn bond angle, which is the double exchange angle. A meaningful comparison with that of the x = 0.50 sample is not really possible due to the multi-phasic nature of the sample.

8.2.3 Neutron powder diffraction on the system $La_{1-x}Pb_xMnO_3$

8.2.3.1 Sample preparation and characterisation

In the case of the Pb doped system samples of composition x = 0.0, 0.1, 0.2, 0.3, 0.4, 0.45 and 0.50 were prepared by grinding together stoichiometric amounts of lead powder (Putratronic 99.999%), $MnCO_3$ (Aldrich 99.9%) and La_2O_3 (Alpha, 99.999%)and heating pressed pellets of the mixture at 900°C in alumina crucibles in a tube furnace. Each sample was heated for 3 months, with intermediate grindings to ensure homogeneous mixing. X-ray powder diffraction patterns were taken at intervals in order to monitor the concentration of lead in the compounds, since there was concern that the volatility of the lead might lead to a reduced concentration. Phase purity of the final products was verified by a combination of X-ray powder diffraction and SQUID dc susceptibility measurements. The manganese, lanthanum and lead concentrations in the samples were determined through the use of both ICP Atomic emission spectroscopy and thermogravimetric analysis, in a similar fashion to that described for the case of the $La_{1-x}Ca_xMnO_3$ series. All solutions for ICP-AES analysis were made up in concentrated hydrochloric acid. The combined results are shown below in Table 8.7.

Nominal Composition	Concentration of Pb/ppm	Concentration of Mn/ppm	Determined stoichiometry
$LaMnO_3$	0.00±0.00	31.48±0.04	$La_{0.94}Mn_{0.97}O_{2.84}$
$La_{0.9}Pb_{0.1}MnO_3$	12.92±0.06	30.62±0.23	$La_{0.88}Pb_{0.10}Mn_{0.97}O_{2.96}$
$La_{0.8}Pb_{0.2}MnO_3$	26.82±0.21	30.74±0.23	$La_{0.76}Pb_{0.21}Mn_{0.96}O_{2.98}$
$La_{0.7}Pb_{0.3}MnO_3$	38.76±0.14	30.38±0.15	$La_{0.66}Pb_{0.32}Mn_{0.97}O_{3.04}$
$La_{0.6}Pb_{0.4}MnO_3$	41.52±0.31	29.98±0.14	$La_{0.57}Pb_{0.35}Mn_{0.94}O_{2.93}$
$La_{0.5}Pb_{0.5}MnO_3$	49.94±0.15	36.53±0.16	$La_{0.52}Pb_{0.41}Mn_{1.13}O_3$

Table 8.7 Results from atomic emission and thermogravimetric analyses of the samples $La_{1-x}Pb_xMnO_3$ ($x = 0 - 0.5$)

Further measurements were also performed on the HRPD time of flight diffractometer at the ISIS facility, where samples of each composition were loaded into vanadium sample cans and diffraction patterns taken at 300K. Least squares structure refinements were then performed using the GSAS package.

8.2.4 Rietveld refinement of the data

In the case of the undoped sample of the parent compound $LaMnO_3$ refinements were initially attempted using a $R\ \bar{3}\ c$ space group with lattice parameters as per previous work and a rhombohedral angle of 60° (in rhombohedral settings) [7]. This proved unsatisfactory and so a second phase was introduced with a doubled unit cell, of similar space group, though possessing cubic symmetry with a rhombohedral angle of 90° (again in rhombohedral setting). This also proved unable to give a good agreement between the calculated and observed patterns and so a two phase

refinement was attempted with a rhombohedral phase with space group $R\ \bar{3}c$ and an orthorhombic phase with space group *Pnma*. Initial parameters were taken from the work of Huang *et al* [8] and refinement of the individual phase fractions showed the majority phase to be the orthorhombic one. The final refined parameters are listed in the Table below.

Phase 1 (Phase fraction 26.0(2)%)					$R\ \bar{3}c$
Atom	*x*	*y*	*z*	*frac*	*uiso/* Å^2
La	0	0	0.25	1	0.01026(68)
Mn	0	0	0	1	0.00328(11)
O	0.44572(32)	0	0.25	1	0.01214(49)
Lattice parameters		a = 5.53717(5) Å	c = 13.35327(12) Å		$\alpha = \beta = 90\ \gamma = 120°$
Phase 2 (74.0(1)%)					*P n m a*
La	-0.01589(316)	0.25	-0.00340(273)	1	0.01105(4)
Mn	0	0	0.5	1	0.00668(66)
O1	0.50635(462)	0.25	0.06469(380)	1	0.01260(57)
O2	0.2289(277)	0.03442(170)	-0.23149(286)	1	0.01369(41)
Lattice parameters		a = 5.49786(4)Å	b = 7.78481(8)Å	c = 5.53809(5)Å	$\alpha = \beta = \gamma = 90°$

Table 8.8 Refined lattice parameters for the compound $LaMnO_3$ with statistics of fit:

$$\chi^2 = 10.35\ R_{wp} = 0.0785$$

Consideration of data taken for the sample of nominal composition $La_{0.9}Pb_{0.1}MnO_3$ gave a single phase refinement with space group $R\ \bar{3}c$. Whilst the statistics of the fit

between observed and calculated was reasonably good, these were a little artificial thanks to the poor signal to noise ratio of the data obtained. Further refinement was not attempted.

Sample with compositions of x = 0.20, x = 0.30 and x = 0.40 all indexed as single phase materials with space group $R\ \bar{3}\ c$. The pertinent cell parameters are listed in the table below.

Parameter	Composition x in the series $La_{1-x}Pb_xMnO_3$				
	0.1	0.2	0.3	0.4	0.5
a/Å	5.48201(10)	5.48741(2)	5.48423(4)	5.48207(4)	5.48024(9)
α/°	60.6219(1)	60.4923(2)	60.3518(4)	60.2799(1)	60.1818(2)
O *x*	0.69792(0)	0.70333(0)	0.71043(18)	0.71454(19)	0.71958(27)
O *y*	0.80206(0)	0.79665(0)	0.78955(18)	0.78544(19)	0.78040(27)
Mn-O/Å	1.96858(4) 1.96842(4)	1.96440(1) 1.96425(1)	1.95639(11) 1.95625(11)	1.95216(11) 1.95201(11)	1.94748(13) 1.94733(13)
Mn-O-Mn/°	163.167(0)	164.909(0)	167.20(6)	168.52(6)	170.15(9)

Table 8.9 Least squares fitted unit cell parameters for the series of compounds $La_{1-x}Pb_xMnO_3$ with x=0.1 – 0.5

The full Rietveld refinement difference profiles are shown in Appendix C.

As can be seen from the above table several trends emerge from the least squares refinements. Firstly the lattice parameter *a* is reduced on progressive doping with lead,

as is the rhombohedral angle α. Furthermore the Mn-O-Mn bond angle becomes less distorted with increasing lead concentration *i.e.* this double exchange angle is increasingly optimised as the concentration of lead increases. This is in agreement with the progressive reduction in α, since such a reduction suggests the system is increasingly closer to cubic symmetry, the optimum bond angle for double exchange being 180°. There is little change in the Mn-O bond distances across the series reflecting the absence of a large Jahn-Teller effect since elongation along any particular axis is not seen.

The reduction in cell volume can be illustrated by consideration of the strongest reflections as shown in the figure below.

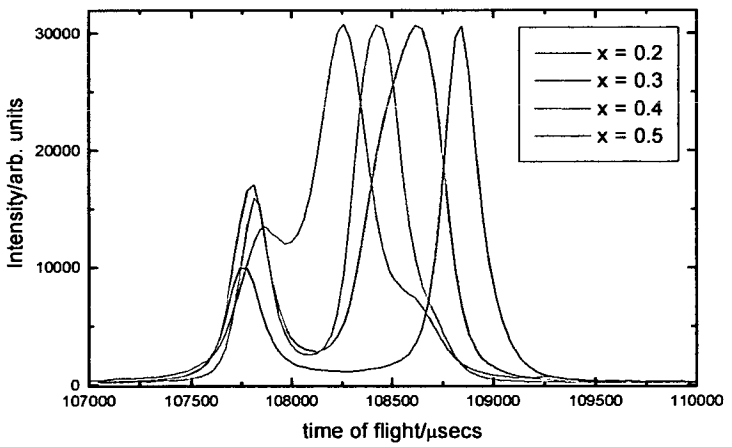

Figure 8.6 Section of diffraction patterns obtained for the samples with composition x = 0.2 (black), x =0.3 (red), x = 0.4 (green) and x = 0.5 (blue)

As can be seen the position of the reflections shifts to smaller time of flight (and hence d-spacing) as the concentration of lead increases. What can also be seen is a

narrowing of the splitting of these reflections. Indexing of the pattern on a $R\ \bar{3}\ c$ cell reveals that the reflections shown in the figure are the (2 2 2) (2 0 0) and (2 1 0) respectively. What is therefore illustrated is a reduction in the splitting of the (2 2 2)/(2 0 0) reflections and the (2 1 0) reflection as the system moves towards cubic symmetry where the (2 1 0) reflection becomes disallowed by symmetry constraints.

The $La_{0.5}Pb_{0.5}MnO_3$ composition proved difficult to index since, in common with the $La_{0.5}Ca_{0.5}MnO_3$ sample examined earlier, the reflections are considerably broader than in the case of the lower concentrations. Initial attempts at structural refinement centred around cells of space group $R\ \bar{3}\ c$ both as a rhombohedral cell *i.e.* with α = 60° and as a cubic cell with α = 90°. Neither gave satisfactory agreement between observed and calculated diffraction patterns. A mixture of two phases with lead concentrations of x = 0.2 and x = 0.3 with parameters as refined for these compositions failed to improve the goodness of fit between observed and calculated profiles. The presence of additional reflections which were un-indexable on rhombohedral cells suggested the presence of either magnetic ordering or an impurity phase. Hence Mn_3O_4 was introduced as an impurity phase, additional evidence for its presence in the sample being given by the observed upturn in the molar susceptibility at around 40K. Examination of the magnetic susceptibility data shows that the ordering transitions in the compounds with higher lead concentrations occur above room temperature and so the diffraction data collected on HRPD will also reveal the presence of magnetic ordering.

In summary the diffraction data obtained is in broad agreement with previous work [4]. The radii of La and Pb are similar and so the Goldschmidt tolerance ratio is close

to one suggesting that a rhombohedral crystal structure would be most stabilised in this case. In agreement with this prediction all the lower concentration samples can be indexed within a rhombohedral setting. $LaMnO_3$ is an exceptional case, as evidenced by the conflicting views in the literature [9]. As the lead doping level approaches x = 0.5 the system appears to enter a mixed phase of rhombohedral and cubic cells, though it is difficult to determine the exact nature of these phases. The presence of Mn_3O_4 suggests the likelihood of phase separation and possible limit on the concentration of lead in the system, since the ICP-AES results in the case of the x = 0.50 compound show the widest discrepancy between the target and actual concentrations. Further work is required to determine exactly how far the phase diagram can be extended in the Pb series.

8.3 Muon measurements on the MuSR instrument

8.3.1 Introduction

In order to follow the spin dynamics of the system, muon spin relaxation measurements were carried out using the MuSR spectrometer at the ISIS facility. A schematic view of the MuSR instrument is shown in the figure below. The two sets of 16 detectors (forward and backward) are shown, and rotation of these detectors allows the performance of both longitudinal and transverse field measurements, as outlined in Chapter 2. In the case of the MuSR instrument a longitudinal field of up to 2000G may be applied.

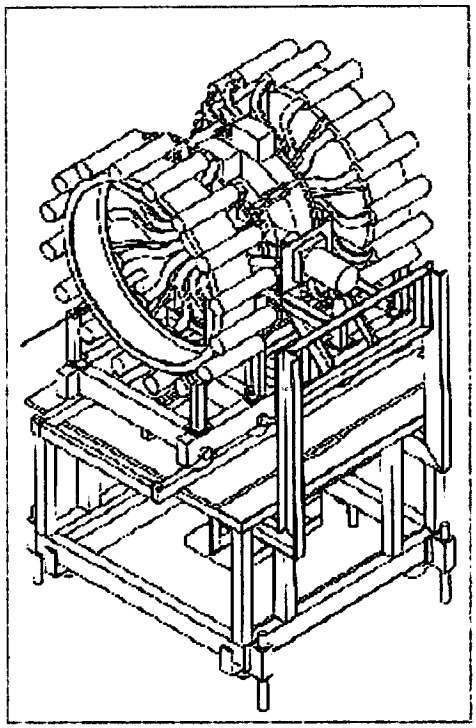

Figure 8.7 View of the MuSR instrument showing the two sets of detector banks each consisting of 16 detectors [10]

8.3.2 Sample Preparation

Samples of composition $La_{0.54}Ca_{0.46}MnO_3$ and $La_{0.5}Ca_{0.5}MnO_3$ were targeted for preparation. Stoichiometric amounts of La_2O_3 (Alpha, 99.999%), $MnCO_3$ (Aldrich, 99.999%) and $CaCO_3$ (Aldrich, 99%). were ground together using a pestle and mortar and then placed in alumina crucibles and heated at 950°C for 10 hours. The resulting dark purple sintered powder was then reground and pressed into pellets, under a load of 4.5 tons, using a Graseby Specac® 13mm die, and these pellets were refired three times at 1200°C for 10 hours with intermediate grindings. To assess the phase purity of the products powder X-ray diffraction patterns were taken over a range in degrees two theta of 10-70°. The resulting diffraction patterns are shown below.

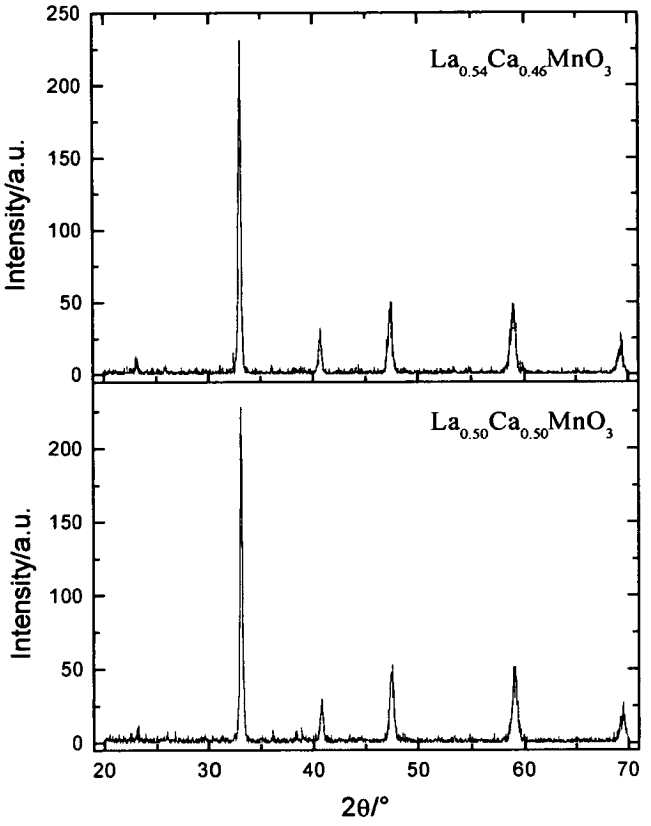

Figure 8.8 Powder X-ray diffraction patterns obtained for samples of $La_{1-x}Ca_xMnO_3$ with compositions x = 0.46 (top) and x = 0.50 (bottom) respectively

To verify the magnetic behaviour of the samples dc susceptibility measurements were performed using a SQUID magnetometer. Each sample was measured after cooling in first zero field and then a field of 100G, over a temperature range of 5-350K, in an applied field of 100G. The molar susceptibility of each sample is shown below. The additional feature in the susceptibility at around 40K can be attributed to a small percentage of Mn_3O_4 present in the samples.

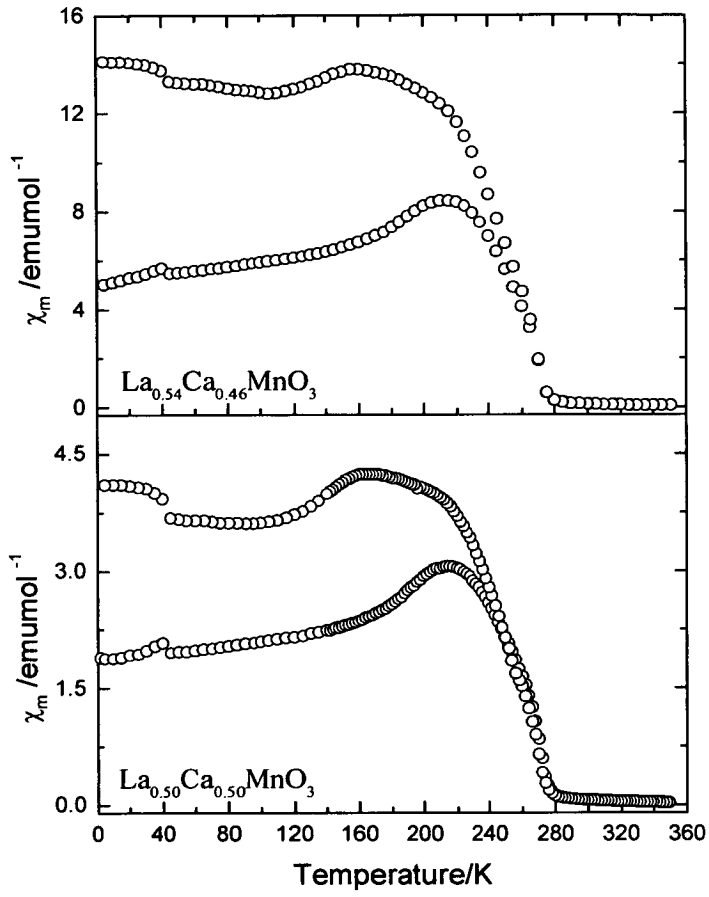

Figure 8.9 Plots of molar susceptibility χ_m versus temperature T for the samples $La_{0.54}Ca_{0.46}MnO_3$ (top) and $La_{0.50}Ca_{0.50}MnO_3$ (bottom)

The value of T_C was determined from a plot of the first derivative of the molar susceptibility $d\chi_m/dT$, in the case of the zero-field cooled data, as shown below.

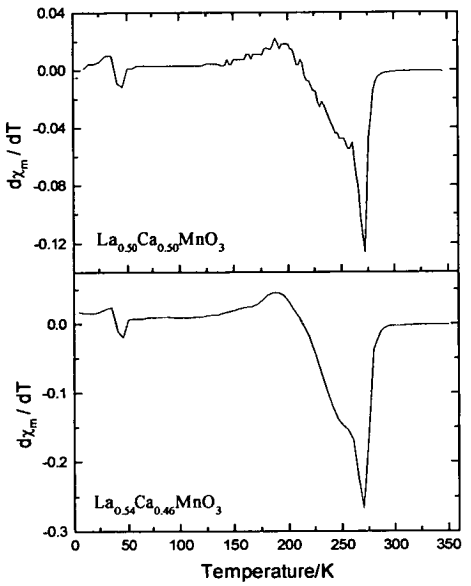

Figure 8.10 Plots of $d\chi_m/dT$ versus temperature T for the samples $La_{0.54}Ca_{0.46}MnO_3$ (lower) and $La_{0.50}Ca_{0.50}MnO_3$ (upper)

Chemical analysis was performed on both samples as described in the case of the HRPD samples in the previous section. The combined results of atomic emission spectroscopy and thermogravimetric analysis are shown in the table below.

Nominal Composition	Concentration of Ca/ppm	Concentration of Mn/ppm	Determined stoichiometry
$La_{0.54}Ca_{0.46}MnO_3$	8.876±0.019	27.95±0.05	$La_{0.48}Ca_{0.41}Mn_{0.95}O_{2.62}$
$La_{0.50}Ca_{0.50}MnO_3$	10.27±0.01	29.44±0.12	$La_{0.47}Ca_{0.47}Mn_{0.98}O_{2.58}$

Table 8.10 Chemical analysis results for $La_{1-x}Ca_xMnO_3$ samples of nominal composition $x = 0.46$ and $x = 0.50$

8.3.3 Experimental

Samples of composition x = 0.50 and 0.46 were loaded into silver holders with a mylar window glued on with araldite, and put into an Oxford Instruments 'Orange' cryostat. Following a calibration run at room temperature in a transverse field of 20G, a series of measurements were then performed observing the nature of the muon depolarisation on warming from a base temperature of 130K, in the absence of any applied longitudinal field.

Fitting of the data was performed using the UDA software on the VAX system at ISIS [11]. In the case of the x = 0.46 sample the depolarisation was described using a stretched exponential function of the form $G_z(t) = a_0 \exp(-(\lambda t)^{\beta})$ with a value for the exponent β which took the value 1 at high temperatures and was allowed to vary in the fit. Previous work [12,13] has suggested that materials which exhibit spin glass behaviour will show β values which fall, on the approach towards T_f, from a value of 1 in the paramagnetic phase, with a recovery in the value of β to a value of either 0.33 or 0.5 below T_f, this being indicative of a distribution of spin relaxation times. In the specific case of the $La_{1-x}Ca_xMnO_3$ case Heffner *et al* successfully modelled data collected on a sample of composition x = 0.33 with a stretched exponential with an exponent of 0.5 at low temperatures. This approach was therefore used as a starting point in the modelling, and the fitted values of λ and β are shown in figures 8.11 and 8.12. In figure 8.11 the results of a free fit of the value of β above T_C is shown, with the value then fixed at a value of 0.5 at lower temperature. Figure 8.12 shows the same data in the region close to T_C. If however there remains a dynamic component to the signal below T_C, either due to continued fluctuations in the magnet, or due to

muon hopping between implantation sites then there will be an exponential decay of the signal (*i.e.* with a value of $\beta = 1$) at lower temperatures. To examine this behaviour, further fitting of the data was performed with a value of β allowed to freely vary on cooling towards T_C, and then constrained to equal 1 at lower temperatures, the results of which are shown in figure 8.13. The region close to T_C is shown in figure 8.14. The peak in the value of λ is close to the value of T_C determined from the dc susceptibility measurements (270K).

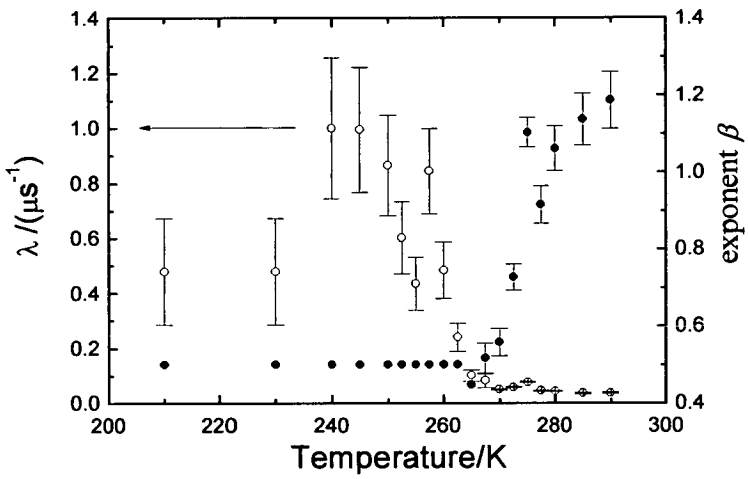

Figure 8.11 Plot of λ (open circles) and β (filled circles) versus temperature obtained from fitting to data taken from the $La_{0.54}Ca_{0.46}MnO_3$ sample with $\beta = 0.5$ at low temperatures

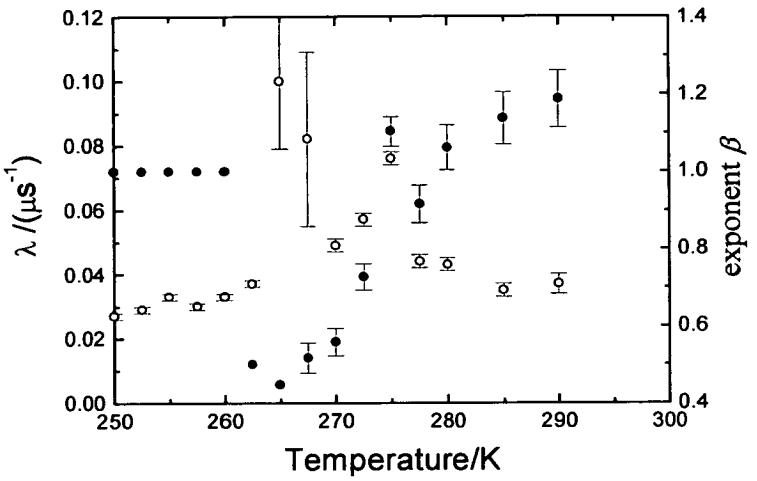

Figure 8.12 Plot of λ (open circles) and β (filled circles) versus temperature obtained from fitting to data taken from the $La_{0.54}Ca_{0.46}MnO_3$ sample showing the region close to T_C

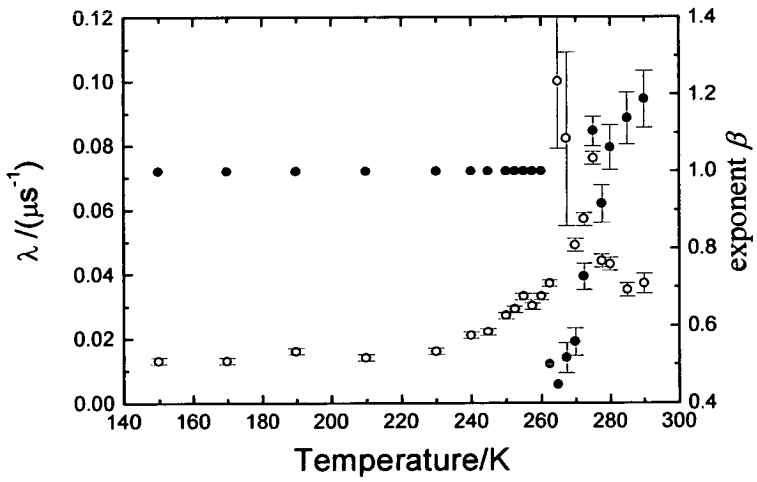

Figure 8.13 Plot of λ (open circles) and β (filled circles) versus temperature obtained from fitting to data taken from the $La_{0.54}Ca_{0.46}MnO_3$ sample with a value of $\beta = 1$ at low temperatures

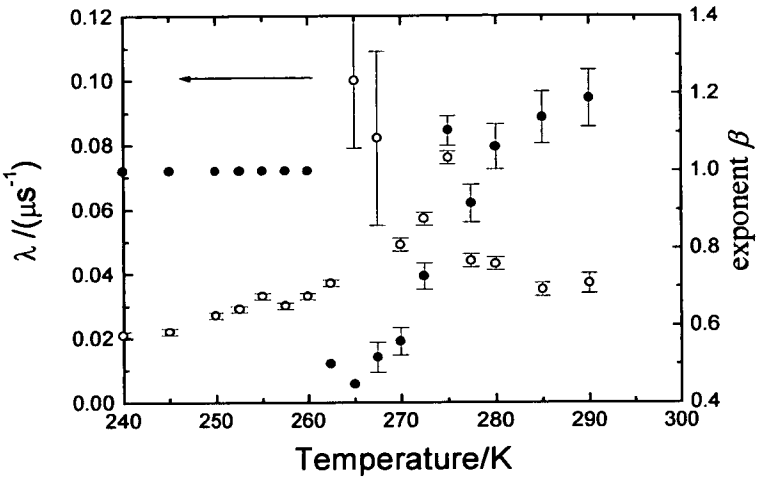

Figure 8.14 Plot of λ (open circles) and β(filled circles) versus temperature obtained from fitting to data taken from the $La_{0.54}Ca_{0.46}MnO_3$ sample showing the region close to T_C

In the case of the x = 0.50 sample fitting of the observed data was performed in a similar fashion to that described above. A stretched exponential function was used to model the data, with the value of β allowed to vary from an initial value of 1. A 'best' fit was achieved with a value of β which fell from a value of around 1 above T_C to a value of 0.5 at lower temperatures, in agreement with the work of Heffner *et al.* The values obtained for λ, show a peak coincident with the value of T_C and a peak at 150K suggesting a further change in the charge ordering in the system. The fitted values for the values of the relaxation factor λ and the exponent β are shown in figure 8.15 below, with the region close to T_C shown in figure 8.16.

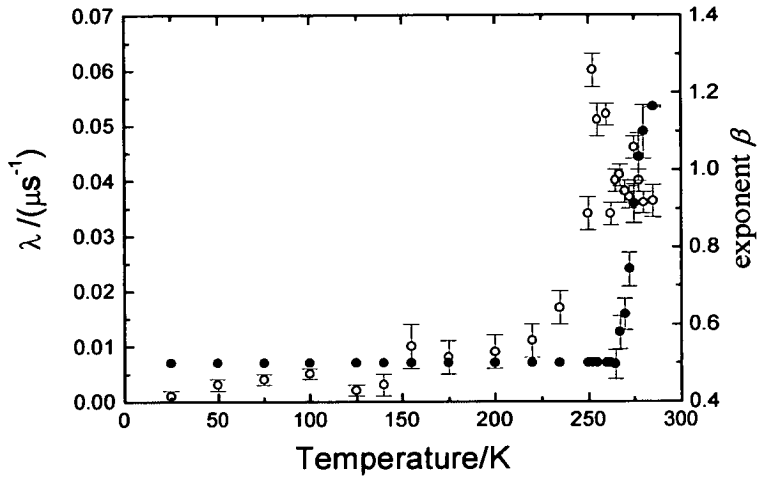

Figure 8.15 Plot of λ (open circles) and β (filled circles) versus temperature obtained from fitting to data taken from the $La_{0.50}Ca_{0.50}MnO_3$ sample with a value of β = 0.5 at low temperatures and β free to vary above T_C

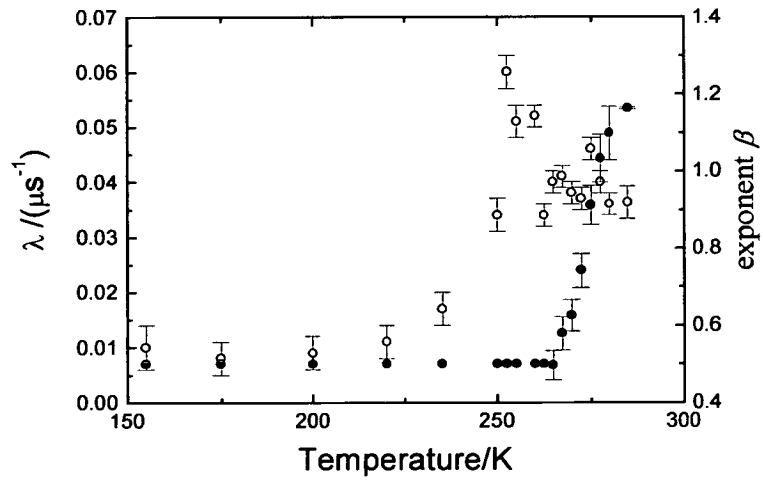

Figure 8.16 Plot of λ (open circles) and β (filled circles) versus temperature from fitting to data taken from the $La_{0.50}Ca_{0.50}MnO_3$ sample in the region of T_C

In summary the data seem to be broadly consistent with previous measurements. In the case of the x = 0.46 sample fitting of the data with a stretched exponential function shows a value of the exponent β which falls on cooling towards T_C from an initial value of 1, to a value approaching 0.5. At lower temperatures, well below T_C, there appears to be a dynamic component to the signal as evidenced by fitting of the data with a Lorentzian function, however it is not possible to model this accurately within the timescale of the measurements performed at ISIS. In the case of the x = 0.50 sample the behaviour seen is in agreement with the work of Heffner *et al.* There appears to be an additional feature in the data around 150K, possibly relating to charge ordering. It is still unclear what physical significance the exponent 0.5 has, in relation to the behaviour of the manganite system, since there are no other comparable systems where such analysis has been applied.

8.4 Muon measurements at PSI

8.4.1 Introduction

Due to the pulsed nature of the muon beam at the ISIS facility, there is an inherent 'dead time' which limits the timescale on which measurements can be performed, as outlined in Chapter 2. In order to probe faster relaxation times a direct current source has to be used, and to this end measurements were performed using the DOLLY instrument at the LMU at the Paul Scherrer Institute in Villigen Switzerland. A photograph of the instrument is shown in figure 8.17 below. The muon beam enters the target area *via* the guide tube seen on the right hand side of the photograph. The sample itself is loaded into the cryostat, which lies perpendicular to the incident beam;

the top of the sample rod is being adjusted by the experimenter pictured in the foreground.

A diagram of the detector arrangement is shown in Figure 8.18. The incoming muons pass through the detector *M* and positron emission can then be monitored through the use of the *B* (backward), *F* (forward), *U* (up) and *D* (down) detectors. The *R* detector is not used in the measurements performed here, whilst the *B_veto* and *F_veto* components allow for collimation of the incident muon beam and rejection of muons not stopped by the sample respectively.

8.4.2 Experimental

A pellet of sample with composition $x = 0.50$ (13mm diameter) was attached to a silver plate with silver tape, inserted into the spectrometer and cooled to 75K. A series of zero longitudinal field measurements were then performed, on warming, to determine the temperature dependence of the corrected asymmetry signal.

A sample with composition $x = 0.46$ was also run on the DOLLY instrument in a similar manner to that described above. A powdered sample (*ca.*1g) was pressed into a pellet of 13mm diameter using a Graspec® pellet press and die. The sample was then mounted on a silver plate and secured with silver tape before being loaded into the 'Mango' cryostat on the DOLLY instrument. A series of scans were then performed from a base temperature of 75K warming up through T_C to room temperature.

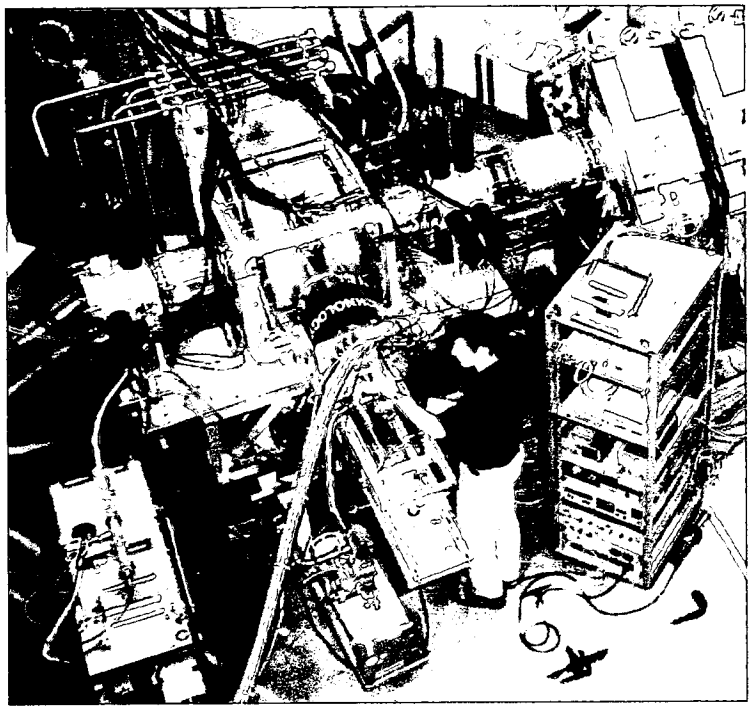

Figure 8.17 Picture of the DOLLY instrument. The muon beam is incident upon the sample from the right hand side of the photograph, with the cryostat perpendicular to it

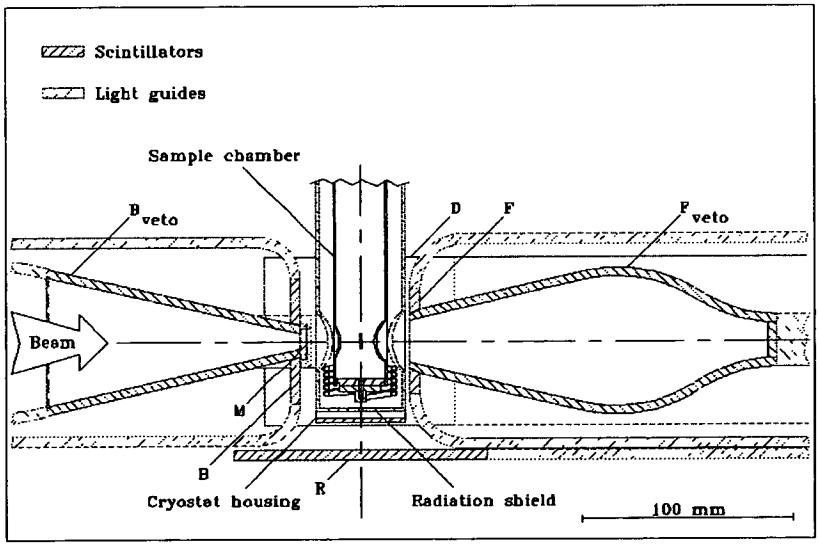

Figure 8.18 Horizontal cut of the detector arrangement on the DOLLY instrument.

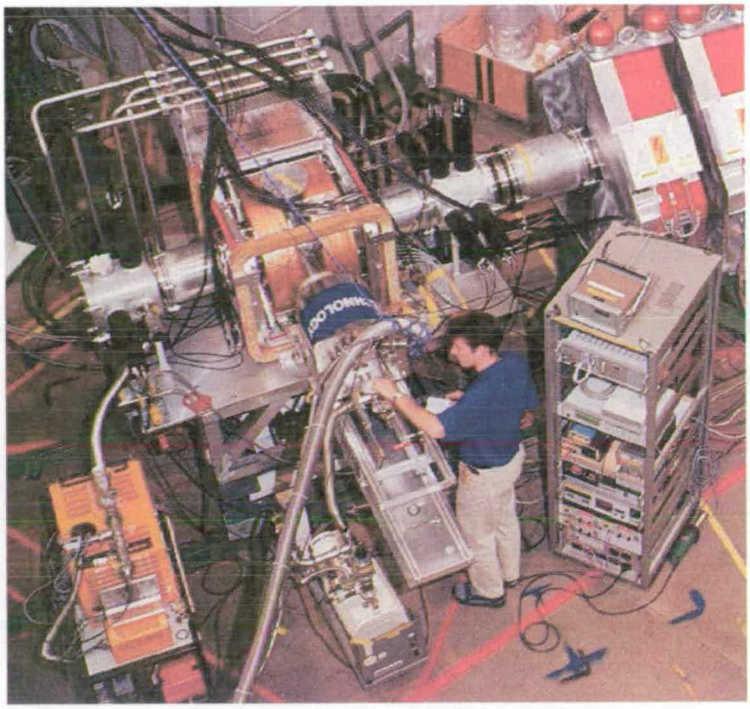

Figure 8.17 Picture of the DOLLY instrument. The muon beam is incident upon the sample from the right hand side of the photograph, with the cryostat perpendicular to it

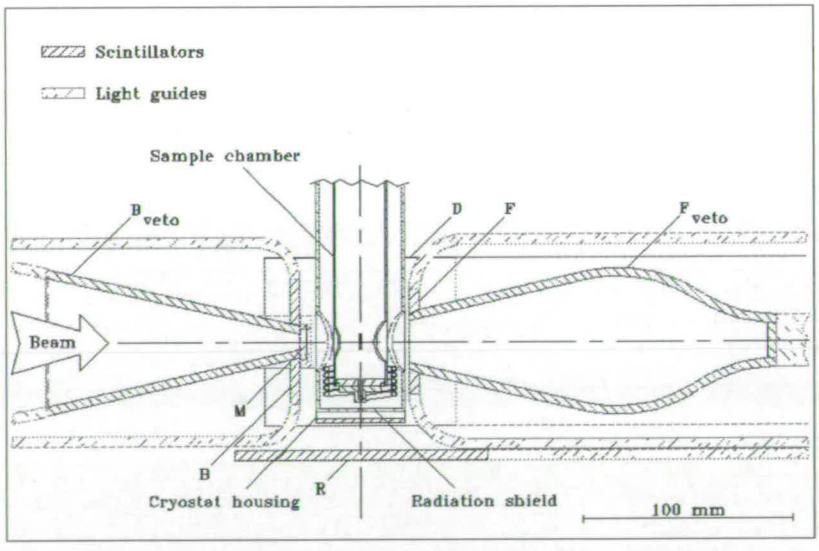

Figure 8.18 Horizontal cut of the detector arrangement on the DOLLY instrument.

8.4.3 Data analysis

In the case of the x = 0.46 sample, the data were fitted initially to a stretched exponential function of the form $G(t) = b + Nexp(-(t/\tau))[1+A_0exp(-(\lambda t))^{\beta}cos(F\omega t+\phi)]$. Fitting was performed using data from the forward detector only, within the Minfit package [14]. Fitting involved using the routine Norm to determine the value of the background and number of counts, and the least-squares minimisation routine Migrad to determine the value of the variables A_0, λ and β. The values obtained for the asymmetry and relaxation factor are shown below in figures 8.19 and 8.20.

The results obtained are in broad agreement with those obtained from the MuSR experiment. In this case the nature of the exponent β falls from an initial value of 1 (*i.e.* a Lorentzian function) to a value approaching 0.5 in the region of T_C. At lower temperatures there then appears to be a recovery in the value of β indicative of a dynamic component to the relaxation signal. Since, as can be seen in figure 8.19, at these temperatures the value of the asymmetry is very small, it would appear possible that such a dynamic component to the signal, reflects fluctuations within only a small fraction of the total moment. In the case of the temperature dependence of the asymmetry, this seems to fall on cooling through T_C , though there is a scatter in its value in the region of T_C.

If, as suggested in the MuSR data, there remains a dynamic component to the signal below T_C, then the relaxation signal can be approximated by a combination of a Gaussian (static) component, and a Lorentzian (fluctuating) component. The results of such a fit are shown below.

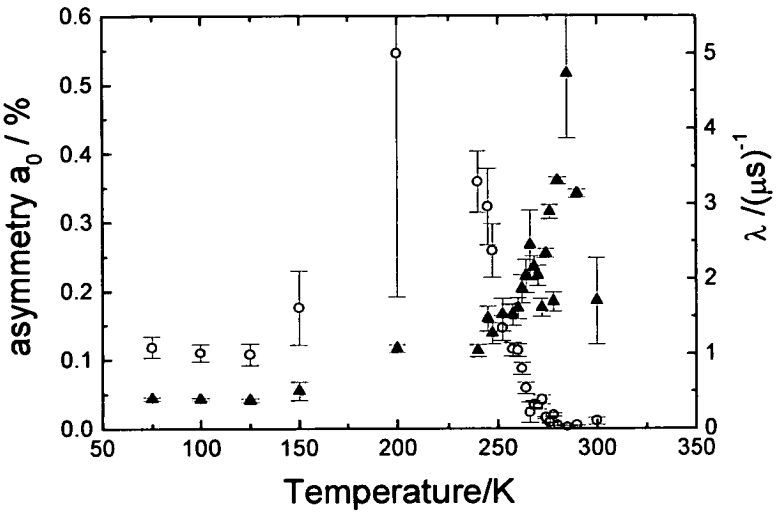

Figure 8.19 Plot of asymmetry (filled triangles) and λ (open circles) versus temperature as determined from least-squares fitting using Migrad, to data obtained from the sample $La_{0.54}Ca_{0.46}MnO_3$

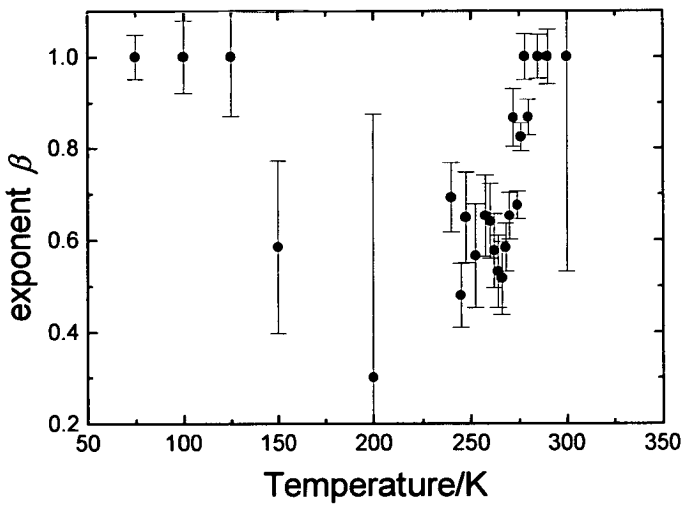

Figure 8.20 Plot of stretched exponential exponent β versus temperature in the case of the sample of composition $La_{0.54}Ca_{0.46}MnO_3$

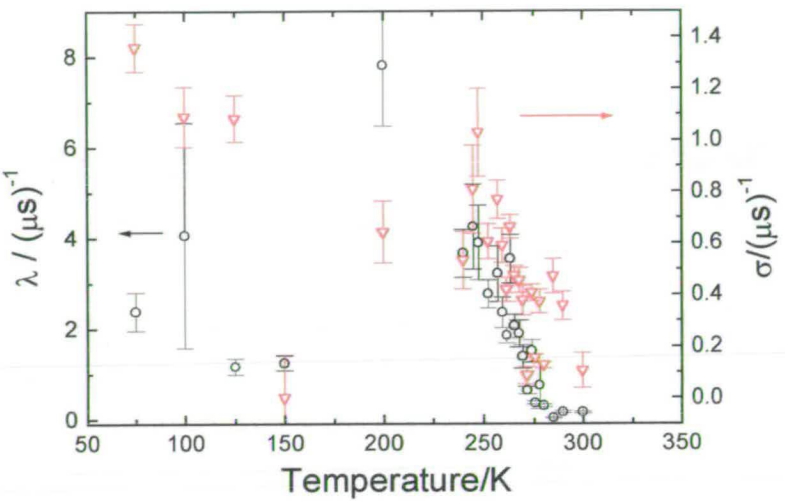

Figure 8.21 Plot of relaxation coefficients λ (open circles) and σ (open triangles) versus temperature obtained in the case of fitting to the $La_{0.54}Ca_{0.46}MnO_3$ data sets

The results obtained, though noisy, are in broad agreement with expectation. The value of σ shows a maximum in the region of T_C and then rises slowly on cooling, whilst the value of λ peaks in the region of 220 – 240K and then falls away on cooling as a larger proportion of the moments become frozen. Such a peak in λ is consistent with the strong divergence in the zero-field cooled and field cooled behaviour seen in the dc susceptibility measurements.

In the case of the x = 0.50 sample analysis was performed in a similar fashion. Fitting of the data acquired using the forward detector, using a stretched exponential

function, gave values of λ and asymmetry as shown below in figure 8.22. The associated values of the exponent β are shown in figure 8.23.

The data obtained here appears to be more complex than that obtained at ISIS. What is observed is a fall in the value of β on cooling through T_C, followed by a recovery of Lorentzian behaviour (*i.e.* $\beta = 1$) on further cooling. Whilst the behaviour of β above T_C is consistent with spin glass like behaviour, there appears to be a fraction of the moments which remain dynamic below T_C, this fraction being more significant than in the case of the x = 0.46 sample. Such fluctuations must be very fast in nature, since there was no evidence for them in the ISIS data. What is also of interest is the behaviour of λ which shows a large maximum at around 190K and a secondary feature at around 140K. This may well indicate the onset of charge ordering as suggested by previous susceptibility and muon measurements [3,14].

To further investigate the behaviour of the system fitting of the data sets was performed using a combination of a Gaussian and Lorentzian component to the total signal with starting values taken from those obtained in the case of the x = 0.46 sample. Fitting of the data beginning with the lower temperature data, generated values of the relaxation coefficients σ (associated with the Gaussian function) and λ (associated with the lorentzian function) as shown in figure 8.24.

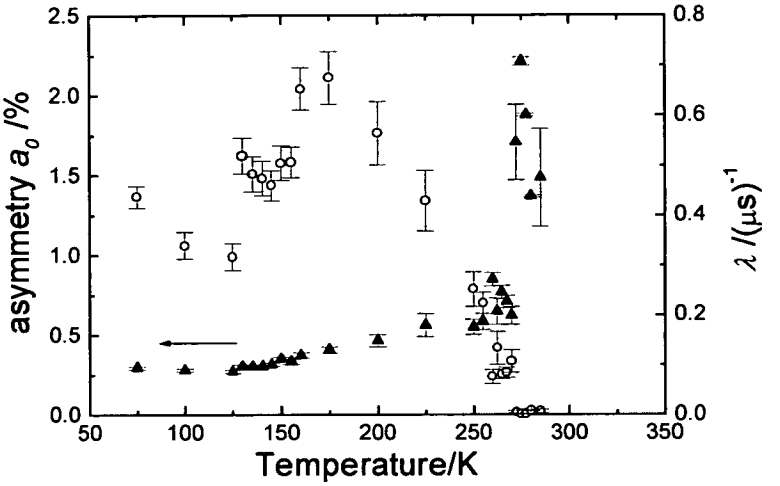

Figure 8.22 Plot of λ (open circles) and asymmetry (filled triangles) versus temperature obtained for the sample of composition $La_{0.50}Ca_{0.50}MnO_3$

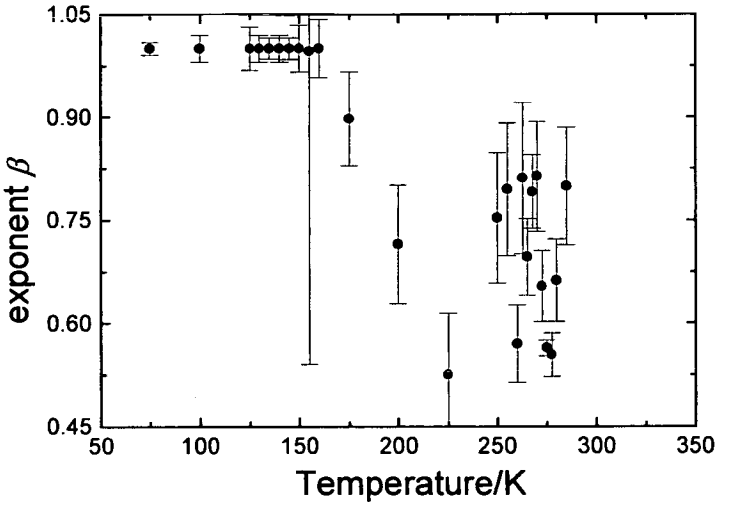

Figure 8.23 Plot of exponent β versus temperature obtained for the sample of composition $La_{0.50}Ca_{0.50}MnO_3$

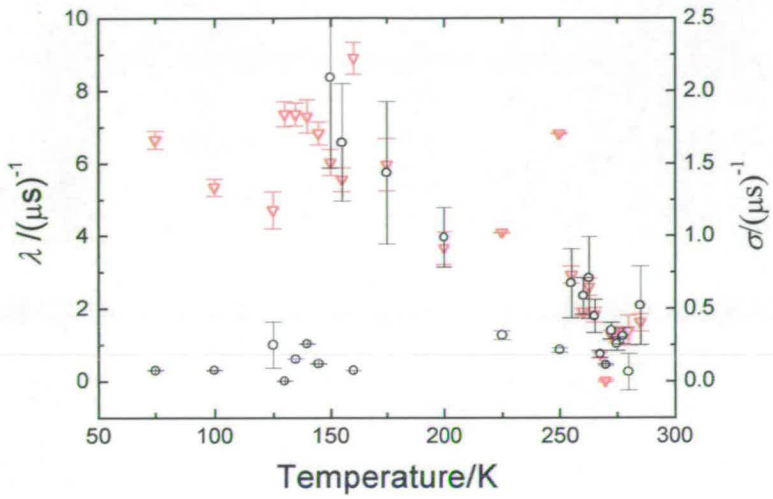

Figure 8.24 Plot of relaxation coefficients λ (open circles) and σ (open triangles) versus temperature obtained in the case of fitting to the $La_{0.50}Ca_{0.50}MnO_3$ data sets

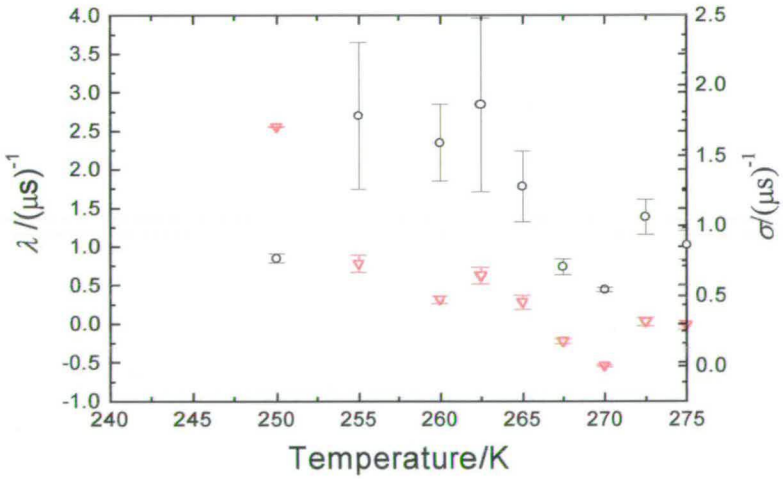

Figure 8.25 Plot of relaxation coefficients λ (open circles) and σ (open triangles) versus temperature obtained for the $La_{0.50}Ca_{0.50}MnO_3$ data in the region of T_C

The results obtained do not allow a clear picture of the behaviour of the system to be determined. The value of σ shows a general rise on cooling below T_C, in line with expectation of an increased frozen component, though the values of λ show a far less distinct trend. Whilst there is a peak in λ in the region of T_C as illustrated in the expanded scale of figure 8.25, there then appears to be a secondary maximum in the region of 150K. The stability of the fit is poor in this region, as suggested by the size of the error bars associated with these values, with strong correlations between the parameters allowed to vary in the fitting routine. This suggests that a single dynamic component to the signal is not sufficient in this region. In a further attempt to model the data in this region a signal composed of a Gaussian and two Lorentzian components was used. However the error associated with both λ values remained significant, and no clear trend in their values was observed.

8.4.4 Summary

Data were acquired using both the MuSR and DOLLY instruments. In the case of the MuSR data obtained for the composition x = 0.46, there is broad agreement with the dc susceptibility measurements performed, and suggest spin glass behaviour in the region above T_C. A small degree of spin fluctuation below T_C was evidenced by use of a Lorentzian fitting function. The subsequent measurements at PSI also show spin glass behaviour above T_C, whilst fluctuations below T_C have been modelled through the use of a combined Gaussian and Lorentzian relaxation function.

The case of the x = 0.50 sample is more complex. The measurements performed on the MuSR spectrometer suggest behaviour in agreement with previous measurements [13], with the value of the exponent β falling to a value of 0.5 in the region of T_C. A

maximum in the value of λ is seen in the region of T_C and there is a suggestion of a further local maximum at around 150K which may point to the onset of charge ordering as seen in recent measurements [15].

The data obtained using the DOLLY instrument does not fully agree with that obtained at ISIS. A breakdown in modelling of the data using a stretched exponential function is seen, consistent with continued fluctuations below T_C. This would suggest that the Heffner model is not valid within the time window afforded by the work at the LMU facility. However modelling of the data using a combined Gaussian and Lorentzian signal, in an attempt to model such fluctuations (as performed successfully in other spin glass systems), was inconclusive. Whilst there is a maximum in λ in the region of T_C there also appears to be a maximum in the region of 150K, which cannot be successfully modelled, either with the above combined signal, or indeed through the introduction of a further Lorentzian component. It remains an open question as to the physical origin of this behaviour, though the lack of evidence for such fluctuations in the ISIS data suggests that they may be very rapid and possibly even out with the time window afforded by DOLLY.

8.5 Magnetic correlations: D7 Spectrometer

Previous diffraction data [3] suggested the presence of both antiferro- and ferromagnetic correlations in the system when x = 0.50. In an effort to probe these correlations a sample of composition $La_{0.5}Ca_{0.5}MnO_3$ was prepared by reaction of the La_2O_3, $CaCO_3$ and MnO_2. The reactants were ground together and fired at 1400°C for two days with intermittent grindings. X-ray diffraction data for the sample showed a crystalline majority phase, with a small level of impurity. This impurity was shown to

be Mn_3O_4 as evidenced by a maximum in the dc susceptibility at around 40K [16]. The sample (*ca.* 40g) was loaded into a double walled aluminium can, with an *id* of 25mm with inner wall of *od* 20mm, on the D7 spectrometer at the ILL in Grenoble. The machine was configured such as to allow full XYZ 3-directional polarisation analysis at an incident wavelength of 4.8Å, operating as a multi-detector diffractometer, rather than with energy analysis and hence as a time of flight spectrometer. On cooling, in an 'Orange' cryostat, a rapid loss of the flipping ratio (N_{sf}/N_{nsf}) was seen indicative of rapid depolarisation of the incident beam. The reduction in flipping ratio was so pronounced that it was not possible to measure the magnetic contribution to scattering at any temperatures below the Curie point (270K). The sample was then removed and a sample of composition $La_{0.46}Ca_{0.54}MnO_3$ (*ca.* 40g) was loaded into the same double walled aluminium can and cooled to 10K. The powder X-ray diffraction pattern obtained for this sample is shown below.

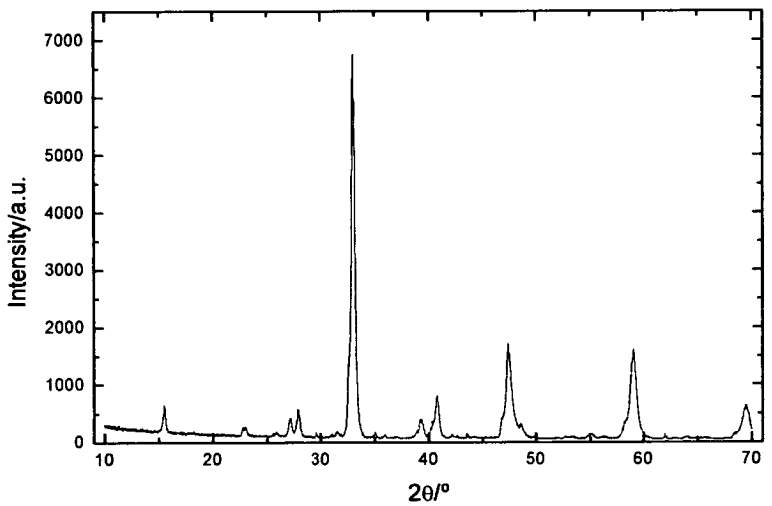

Figure 8.26 X-ray powder diffraction pattern obtained from the sample of composition $La_{0.46}Ca_{0.54}MnO_3$

Evidence for the presence of Mn_3O_4 was seen in dc susceptibility measurements, as per the previous sample, whilst the results of chemical analysis, performed as described above for the other manganite samples, showed the stoichiometry of the sample to be $La_{0.44}Ca_{0.48}Mn_{0.93}O_{2.55}$. A similarly low spin flip ratio was seen to that observed in the case of the $La_{0.5}Ca_{0.5}MnO_3$ sample. A measurement of flipping ratio as a function of temperature was then performed to see whether the ratio recovered either in the region around T_N or at higher temperatures around T_C. The recovery in flipping ratio is shown below.

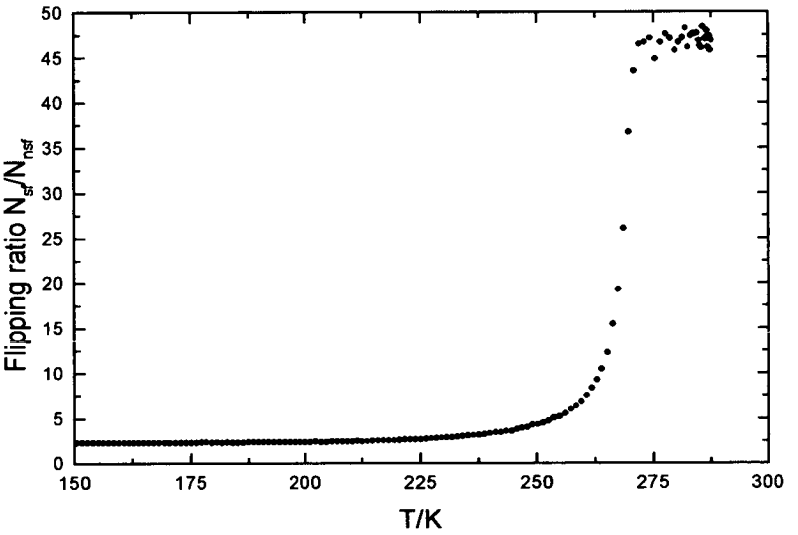

Figure 8.27 Plot of spin-flip ratio vs. temperature for sample of composition $La_{0.46}Ca_{0.54}MnO_3$ on warming from 10K

A further series of scans were performed at 254,260,270 and 300K allowing full deconvolution of the components of scattering, in particular the determination of the

magnetic component of scattering. The magnetic scattering cross section at 254K and 270K respectively is shown in the figure below.

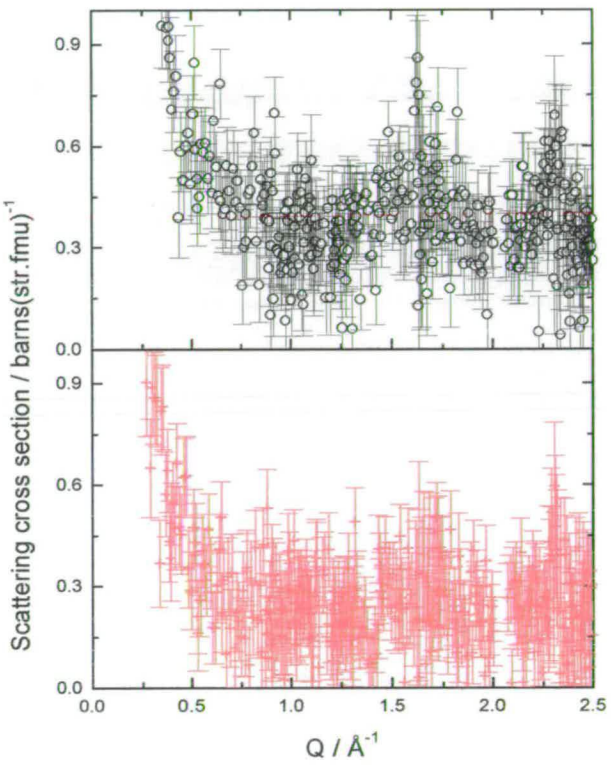

Figure 8.28 Plot of magnetic scattering cross section versus Q at T = 270K (black circles) and T = 254K (red circles) obtained for the sample $La_{0.46}Ca_{0.54}MnO_3$

The figure shows that the scattering cross sections are very similar at both temperatures. The rise in intensity at low values of Q is indicative of short range ferromagnetic correlations, the rise being steeper in the case of the data obtained at the higher temperature. It is clear that ferromagnetic interactions dominate the signal in these compounds, and further studies at higher temperatures would allow a determination of the strength of such correlations well above the ordering transition.

However as can be evidenced in this case the ferromagnetic correlations will swamp any contribution to the magnetic scattering cross section from antiferromagnetic correlations and so prevent any meaningful determination of the influence of such correlations on the magnetic behaviour of the system.

In summary the measurements performed on D7 show that strong ferromagnetic correlations dominate the magnetic scattering over a wide temperature range.

References

[1] J. Fontcuberta, B. Martinez, A.Seffar, S. Pinol, J.L. Garcia - Munoz, X. Obradors, *Phys. Rev. Lett.* **76**(7) 1122 (1996)

[2] R. Mahendiran, S.K. Tiwary, A.K. Raychaudhuri, T.V. Ramakrishnan, R. Mahesh, N.Ragvittal, C.N.R. Rao, *Phys. Rev. B* **53**(6) 3348 (1996)

[3] P.G. Raedelli, D.E. Cox, M. Marezio, S.W. Cheong P.E.Schiffer and A.P.Ramirez, *Phys. Rev. Lett.* **75**(24) 4488 (1995)

[4] *See for example* S.Sundar Manoharan, N.Y.Vasanthacharya, M.S.Hegde, K.M.Satyalakshmi, V.Prasad and S.V.Subramanyam, *J. Appl. Phys.* **76**(6) 3923 (1994); R.Mahendiran, R.Mahesh, A.K.Raychaudhuri and C.N.R.Rao, J.Phys.D:Appl.Phys. **28** 1743 (1995); A.V.Powell, C.Herwig, D.C.Colgan and A.G.Whittaker, *J.Mater.Chem.* **8**(1) 119 (1998)

[5] A. Harrison, D.A. Porter, A.V. Powell, C. Ritter, *ILL Annual Report,* 1996

[6] P.M.Woodward, T.Vogt, D.E.Cox, A.Arulraj, C.N.R.Rao, P.Karen and A.K.Cheetham, *Chem. Mater.* **10** 3652 (1998)

[7] C.Herwig, *'Structural, electronic and magnetic properties of compounds in the* $La_{1-x}Pb_xMnO_3$ *and* $Nd_{1-x}Pb_xMnO_3$ *systems'*, Honours Project Report (Heriot-Watt University, 1996)

[8] Q.Huang, A.Santoro, J.W.Lynn, R.W.Erwin, J.A.Borchers, J.L.Peng and R.L.Greene, *Phys. Rev. B* **55**(22) 14987 (1997)

[9] E.O.Wollen and W.C.Koehler, *Phys. Rev.* **100** 564 (1955); J.B.A.A.Elemans, B.Van Laar, K.R.Van der Veen and B.O.Loopstra, *J.Solid State Chem.* **3** 238 (1971); B.C.Tofield and W.R.Scott, *J.Solid State Chem.* **10** 183 (1974)

[10] More details regarding the MuSR instrument are available at the ISIS facility website http://www.isis.rl.ac.uk/muons/musr.htm

[11] *The Musr User Guide,* P.J.King, S.P.Cottrell, J.S.Lord, C.A.Scott and S.H.Kilcoyne, ISIS Facility, CCLRC Rutherford Appleton Laboratory (1999)

[12] Y.J.Uemura, A.Keren, L.P.Le, G.M.Luke, B.J.Sternlieb and W.D.Wu, *Hyperfine Interact.* **85** 133 (1994)

[13] R.H. Heffner, L.P. Le, M.F. Hundley, J.J. Neumeier, G.M. Luke, K. Kojima, B. Nachumi, Y.J. Uemura, D.E. MacLaughlin, S.W. Cheong, *Phys. Rev. Lett.* **77**(9) 1869 (1996)

[14] *'The MINUIT-based μSR fitting programme MINFIT'*, I.Reid (1999)

[15] J.L.Garcia-Muñoz, A.Llobet, C.Frontera, J.Fontcuberta, X.Obradors and C.Ritter, *J.Mag.Magn.Mat.* **197** 477 (1999)

[16] D.Visser (*private communication*)

Chapter 9 Conclusions

The work in this thesis has considered the nature of the systems $AM_3(SO_4)_2(OH)_6$ (where A = K, $H(D)_3O$; M = Fe,Cr) and $La_{1-x}M_xMnO_3$ (where M = Ca,Pb).

In the case of the $KFe_3(SO_4)_2(OH)_6$ system single crystal neutron studies have been performed in order to determine the magnetic structure and nature of magnetic excitations in the system. Diffraction studies using the D10 instrument at the ILL have confirmed the nuclear structure of this material in agreement with previous powder diffraction studies, and allowed determination of the critical exponent β close to T_N(62.2K). A clear crossover from 2D to 3D behaviour is seen in the region of 55K, whilst the values of the critical exponents obtained are in agreement with theoretical predictions for a 3D Heisenberg system.

Use of the CRYOPAD unit has allowed the first unambiguous determination of the magnetic structure at 10K, showing it to be the q = 0 structure, a coplanar structure in agreement with previous theoretical predictions. No evidence of multi-domain behaviour, is seen in the CRYOPAD measurement. Attempts to determine the nature of the spin wave dispersion in the system proved unsuccessful due to the poor signal to noise ratio resulting from the small hydrogenated sample used.

Further studies are required to try and map out the spin wave dispersion, though such work requires a larger single crystal than that used in the experiments presented in this thesis. Present laboratory preparative routes to jarosites seem unlikely to yield a suitable crystal, so use of a further natural sample may well prove more profitable.

Measurements performed on a powdered sample of $KFe_3(SO_4)_2(OD)_6$ using the D7 spectrometer at the ILL, show that there is a considerable amount of diffuse scattering in the region of T_N, which condenses into the Bragg peaks as the sample is cooled below T_N. It would appear that the fall in intensity of the diffuse scattering corresponds exactly to the increase in intensity of Bragg scattering, though further more detailed analysis of the present data is required to determine the relationship between the two. It should be noted in passing however that use of the data obtained is somewhat of an approximation since integration will be performed over only a small range in Q-space. The nature of the diffuse scattering seen is in agreement with the dc susceptibility data obtained from the single crystal sample, which shows a broad feature at around 40K; the studies on D7 show that there is still significant short-range order at this point, and thus such a broad feature may well correspond to spin fluctuations within the kagome planes.

In the case of the hydronium salt work has been performed on both the IN11 and D7 spectrometers at the ILL. The former spin echo experiment showed that all the moments were frozen on a timescale down to 870ps, at a temperature of 1.5K. This is in agreement with μSR studies, performed both with pulsed and direct current muon sources, which suggest that there is spin freezing below T_f. The experiment performed on D7 shows evidence for considerable diffuse scattering at low temperatures which becomes less significant as the sample is warmed through T_f. The spin-spin correlation length can be modelled using a Warren function, and the results from such fitting show a decrease in spin-spin correlation length on warming from 2K, from a value of the order of 11Å, to a value of the order of 7Å. These values can be rationalised in

terms of the geometry of individual kagome 'stars' in the lattice. The inverse relation between temperature and correlation length is in agreement with recent theoretical predictions, though its exact functional form cannot be determined from these measurements. This is in stark contrast to the results obtained for the potassium salt which show two-spin correlation lengths of the order of 10Å over all temperatures. It is still unclear how the competing further neighbour in plane exchange and interplanar exchange terms are balanced in the two cases, and thus what influences the exhibition of long range order seen in the case of the potassium salt.

To investigate the role of the SO_4 group in the interplanar exchange process, neutron powder diffraction studies were performed on the three compounds $KFe_3(SO_4)_2(OH)_6$, $KFe_3(CrO_4)_2(OH)_6$ and $KFe_3(SeO_4)_2(OH)_6$. All the samples indexed on the $R\ \bar{3}\ m$ space group generic to the jarosite family. In the case of the sulfate and selenate salts, low temperature diffraction data can be modelled using a magnetic phase with space group $P\ \bar{3}$, as has been used in previous refinements. The case of the chromate salt differs in that it shows a ferromagnetic transition at around 50K, in agreement with previous studies. The similarity in the behaviour of the sulfate and selenate salts suggest that in plane exchange terms dominate the Hamiltonian. This is surprising however since Se-O bonds will have greater covalent character than that of S-O bonds and so might well be expected to promote exchange more strongly. This would therefore add weight to the interplanar exchange terms J', J'' and J''' and so different behaviour would be expected. The fact that the transition temperatures in all three cases are very close in magnitude adds further weight to the hypothesis

regarding the greater influence of further neighbour interplanar exchange in the case of potassium jarosites.

The difference in behaviour of the chromate salt is also perplexing. The diffraction patterns obtained suggest that the magnetic structure is different to those seen in the other members of the series, and hence that the size of the nuclear and magnetic unit cells are identical. The ferromagnetic component to the dc susceptibility signal seen can therefore be rationalised in terms of a canting of the spins in each layer as a result of a D-M interaction. The underlying influence on the spin structure is still not clear.

Neutron powder diffraction studies have also been performed on the $(D_3O)Cr_3(SO_4)_2(OD)_6$ system to investigate its lower temperature behaviour. Contrary to previous work no evidence was seen for the onset of ferromagnetic order at 2.2K, though this may well simply reflect differences in composition between the two samples. However a rise in the small angle component of scattering may well be indicative of short range ferromagnetic correlations. Further studies are planned in the near future in order to investigate the nature of the diffuse scattering in this system more carefully, through polarised neutron scattering studies on the D7 spectrometer at the ILL. Low temperature dc susceptibility measurements are also required to verify the exact nature of any freezing transition, since the SQUID magnetometer currently available can reach temperatures no lower than 1.7K. Muon experiments have been performed at the LMU facility in Switzerland on a sample of $(H_3O)Cr_3(SO_4)_2(OH)_6$ using a dilution fridge capable of temperatures down to 10mK. Modelling of the data through the use of both a Gaussian and Lorentzian component to the signal function, shows evidence for spin freezing at around 1.5K, though a

large fraction of the moments remain dynamic down to temperatures of the order of 200mK. This behaviour is similar to that previously observed in the case of the sample $KCr_3(SO_4)_2(OH)_6$. Contrary to the deuterated analogue there is no evidence for a cusp in the dc susceptibility at around 1.7K, and further studies are required to understand why this difference may exist.

High resolution neutron diffraction studies have been conducted on the system $La_{1-x}Ca_xMnO_3$ in the region close to where x = 0.50, using the HRPD diffractometer at the ISIS facility. All samples index successfully on the *Pbnm* space group, whilst lower temperature magnetic phases have been modelled successfully through manual refinement of the moments within a *P1* space group. The changes in lattice parameters on increasing the calcium concentration in the samples has been rationalised in terms of the degree of distortion of the MnO_6 octahedra and orbital ordering present in such systems on cooling from room temperature. Such parameters can be linked to the efficiency of double exchange between Mn(III) and Mn(IV) sites in the lattice which is of direct relevance to the magnitude of the CMR effect seen in such systems. μSR studies on nominal compositions with x = 0.46 and x = 0.50 have been performed not only at the ISIS pulsed muon facility but also at the LMU direct current source. The ISIS data for both compounds has been modelled successfully through the use of a stretched exponential function of the form $G_z(t) = a_0 exp(-\lambda t)^{\beta}$, with the exponent β. falling from 1 at high temperatures to 0.5 in the region of T_C, consistent with spin glass behaviour. Evidence for a dynamic component to the signal below T_C is seen in the case of the x = 0.46 sample. The LMU studies in the case of the x = 0.46 sample are consistent with those results obtained at ISIS, the use of a combination of

Gaussian and Lorentzian functions to model the low temperature data providing further evidence of a small fraction of spin fluctuations below T_C. The data obtained in the case of the x = 0.50 sample is very complex, and whilst the modelling of the high temperature data is consistent with spin glass behaviour, modelling of the low temperature data has proved difficult. There appears to be a larger dynamic component to the signal below T_C in comparison with that seen in the case of the x = 0.46 sample.

High resolution neutron powder diffraction studies have also been carried out on the system $La_{1-x}Pb_xMnO_3$ with compositions spanning x = 0 – 0.5, using the HPRD diffractometer. The parent compound $LaMnO_3$ has been indexed using a combination of a rhombohedral $R\ \bar{3}\ c$ space group and an orthorhombic *Pnma* space group. All other compositions index successfully on the rhombohedral $R\ \bar{3}\ c$ space group. A transition to cubic symmetry can be seen on increasing the concentration of lead. Clean synthesis of high concentration lead compounds is shown to be difficult due to problems with the formation of Mn_3O_4. Further work is necessary in order to investigate other potential synthetic routes to the higher concentration lead compounds.

Appendix A Spin Glass Models

1. Edwards-Anderson (EA) Model

In this model [1] the focus is on temporal order, since there is an absence of long range spatial order. Each spin S_i becomes locked into a preferred direction whose orientation is random over a distribution of sites i. It is possible to define an 'order parameter, q thus

$$q=\lim_{t\to 0}<< S_i(0).S_t(t) >_T >_C \tag{A.1}$$

where q =1 at $T = 0$, $q \to 0$ as $T \to T_f$, the subscript T denotes thermal averaging and the subscript C configurational averaging over all spins. The model thus attempts to 'sample' the system at different times, using q as the order parameter, commonly called the Edwards-Anderson (EA) order parameter.

The model is based on the Hamiltonian

$$H=\sum_{ij} J_{ij}S_i.S_j - \sum_i H_i.S_i \tag{A.2}$$

for a random bond 3 D square lattice. i.e. classical spins on sites i and j interact via J_{ij} exchange coupling which is randomly chosen via a Gaussian distribution

$$P(J_{ij}) = \frac{1}{(2\pi\Delta^2)^{1/2}} \exp\left(\frac{-J_{ij}^2}{2\Delta^2}\right) \tag{A.3}$$

where Δ is the variance in J_{ij}. The free energy of the system is then given by

$$F = -k_B T \ln z = -k_B T Tr(\exp\{-H/k_B T\}) \tag{A.4}$$

where z is the partition function.

Therefore only variation in spin orientations is considered, the structural disorder within the system being frozen in. The problem is that averaging lnz over the distribution $P(J_{ij})$ is non-trivial. Instead the partition function is averaged to some integer power n, in order to give an expression for $F(q)$ in a mean field approximation. This in turn can be used to calculate $q(T)$ and hence expressions for the internal energy U and the specific heat $C_m(T)$ $(=\partial U/\partial T)$. The model thus predicts an asymmetric cusp in the ac susceptibility at T_f whilst the susceptibility should approach a constant value at very low temperatures. This is in good agreement with measured ac susceptibilities, though agreement with specific heat data is poor, suggesting a problem with the use of a mean field approximation.

2. Sherrington – Kirkpatrick (SK) Model

This approach [2] modifies the EA Model by proposing that the true mean field theory (mft) of spin glasses should actually be the exact solution of an infinite range EA model where every spin (of N in number) couples equally with every other spin. Thus the probability distribution $P(J_{ij})$ is assumed to be the same for *all i-j* pairs of spins *independent* of their distance apart.

Consider an Ising spin glass with a Gaussian distribution of J_{ij} given by

$$P(J_{ij}) = \frac{1}{\sqrt{2\pi\Delta^2}} \exp[-(J_{ij} - J_0')^2 / 2\Delta^2 \tag{A.5}$$

where a mean J_0' has been included to allow for the possibility of ferromagnetism. Such a Gaussian function requires that $\Delta' = \Delta/N^{1/2}$ and $J_0' = J_0 / N$. Thus

$$P(J_{ij}) = \left(\frac{N}{2\pi}\right)^{1/2} \frac{1}{\Delta} \exp[-N(J_{ij} - J_0 / N)^2 / 2\Delta^2] \tag{A.6}$$

Use of the '*replica trick*' *i.e.* calculating $\langle z^n \rangle_C$ rather than $\langle \ln z \rangle_C$, allows calculation of $F(q,m)$ and thus, for given ratios of J_0/N expressions for $q(T)$ and $M(T)$. From these expressions the SK model predicts both a cusp in the ac susceptibility ($\chi_{AC} = \frac{[1-q(T)]}{k_B T - J_0[1-q(T)]}$) *and* in the specific heat. However the expression for the entropy of the system falls to a negative limit (- $Nk_B/2\pi$) at T = 0, a non physical value which shows the SK model to be unstable at low temperatures.

3. Thouless – Anderson – Palmer (TAP) Model

This model [3] attempts to combine both the EA and SK models in order to model the region close to T_f, where $(1\text{-}q) \leq T/T_f$, and the behaviour of the system at low temperature in the limit $T \rightarrow 0$. In this case

$$\langle S_i \rangle = \tanh\left\{\frac{1}{k_B T}\sum_j \langle S_j \rangle_T - \left(\frac{1}{k_B T}\right)^2 \sum_j J_{ij}^2 \left[1 - \langle S_j \rangle_T^2\right] \langle S_i \rangle_T\right\} \tag{A.7}$$

where i = 1,2,3.....N and the local applied field H_i is neglected, and the set of N coupled equations negates the use of the replica method, a source of instability in the SK model. The EA order parameter q is now defined as

$$q = \frac{1}{N}\sum_i \langle S_i \rangle_T^2 \tag{A.8}$$

The expression for the free energy F_{TAP} thus has three terms. Firstly the energy of the frozen spin glass, secondly the correlation energy of fluctuations (reduced from the paramagnetic result by $[1-\langle S_i \rangle_T^2]$ for each spin) and thirdly the entropy of N Ising spins possessing the mean value $\langle S_i \rangle_T$. In the region where $T \ll T_f$ the order parameter

behaves as $q(T) = 1 - \alpha_1(T/\Delta)^2$ in contrast to the SK model where $q = 1 - \alpha_2 T/\Delta$, whilst at $T \sim T_f$ there is a saddle point behaviour defining the accessible region $q_0 \geq q = 1 - T/T_f$, below which divergences in the value of F_{TAP} are seen.

Calculation of the entropy S of the system, shows $S_{TAP} \rightarrow 0$ as $T \rightarrow 0$ in contrast to the SK model, and the TAP ground state vanishes at $T=0$. However the TAP model offers *many* physical and stable solutions which can be seen as locally stable thermodynamic states, whose free energy does not necessarily correspond to a global minimum. How do these thermodynamic states relate to *real* spin glass systems? In freezing multi degenerate ground state configurations are created, those with *lower* free energy corresponding to pure equilibrium states, and those with *higher* free energies corresponding to metastable states. To characterise the ensemble of equilibrium states a weighting probability is used

$$\omega_\alpha \propto \exp\left(\frac{1}{k_B T} F_\alpha\right) \tag{A.9}$$

where F_α is the free energy of equilibrium state α.

To distinguish between one equilibrium state α and another β one can define a 'distance' $d^2_{\alpha\beta}$ between the two states as given by

$$d^2_{\alpha\beta} = \frac{1}{N}\sum_i \left(< S_i >_\alpha - < S_i >_\beta\right)^2 \tag{A.10}$$

Similarly an overlap between two states α and β is given by

$$q_{\alpha\beta} = \frac{1}{N}\sum_i < S_i >_\alpha < S_i >_\beta \tag{A.11}$$

Here the EA order parameter q_{EA} represents states which have the same overlap themselves i.e. $q_{\alpha\alpha} = q_{\beta\beta} = q_{EA}$. This then allows the definition of a relationship between the distance between states and the degree of overlap between them as given by

$$d_{\alpha\beta}^2 = 2(q_{EA} - q_{\alpha\beta}) \tag{A.12}$$

The probability distribution $P(q)$ of the various overlaps amongst the pure equilibrium states is given by

$$P(q) = \overline{P_J(q)} = \overline{\sum_{\alpha\beta} \omega_\alpha \omega_\beta \delta(q_{\alpha\beta} - q)} \tag{A.13}$$

where bar averaging is over different values of the couplings J.

$P(q)$ is therefore the probability of finding two states with overlap q after weighting each state with their ensemble probabilities $\omega_{\alpha,\beta}$. In terms of configurational space the nature of the free energy can be represented as shown in figure A.1.

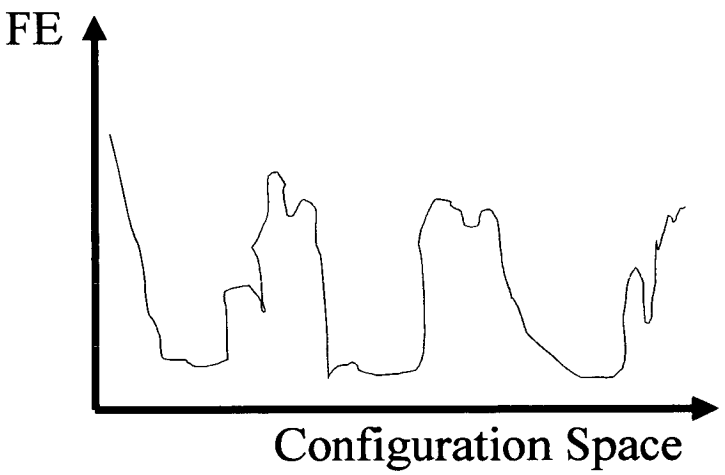

Figure A.1 Plot of free energy (FE) vs. configurational space showing the 'multi-valley' energy landscape of possible thermodynamic states

Thus the lowest lying minima represent pure equilibrium states, with metastable states at higher energies; on cooling the spin glass may become stuck in one of these metastable states and become *non-ergodic*, that is to say unable to explore all of configurational space. The height of energy barriers is directly proportional to the number of spins N in the system, and hence any attempt to pass from one solution to another by flipping of spins, requires spin flips which increase the energy of the system by amounts of order N. This explains the depth of the 'valleys' in configurational space, and since the time taken to pass from one 'valley' to another is the exponential of the height of the lowest saddle point between the two valleys, it is unsurprising that there are many different spin relaxation times present in the system. It also explains some of the problems encountered in computer modelling of such systems, since routines can easily get anchored in a particular solution 'valley' and be unable to explore any further regions of configurational space.

4. Droplet Model

This is a phenomenological scaling theory of droplet excitations in short range Ising spin glasses [4]. A droplet in its ground state is defined as the lowest energy excitation of length state L around a particular point x_j. Such a droplet has all its spins placed in *opposite* directions with respect to those in the ground state Γ.i.e. $\overline{\Gamma}$ is a global reversal of spins inside length scale L, and is illustrated below.

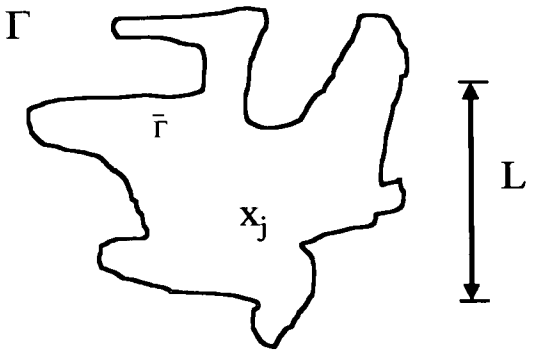

Figure A.2 Schematic diagram of the droplet model. Spin reversal of all spins within length scale L generates a ground state $\bar{\Gamma}$. Outside the droplet all the spins are aligned with ground state Γ

Thus it is assumed that a phase transition occurs below T_f where a global spin reversal leads to a breaking of symmetry and only two pure equilibrium states are related by this global symmetry.

A distribution of free energies is present as described by the expression

$$F_L \propto \gamma(T) L^{\theta} \tag{A.14}$$

where γ is a stiffness constant.

At $\theta < 0$ the magnitude of the free energy, F, is directly proportional to $L^{|\theta|}$, thus low lying excitations can develop over increasing length scales eventually leading to the destruction of the frozen spin glass state. Calculation of the correlations between droplet free energies suggests that a true phase transition is expected. Annihilation and creation of droplet excitations determines the equilibrium low frequency dynamics of the ordered phase and the free energy is assumed to be low such that

$$F_L \sim k_B T << \gamma L^{\theta} \tag{A.15}$$

Typical free energy barriers are $B \sim L^{\psi}$ where $\theta \leq \psi \leq d\text{-}1$

Thus a droplet of scale L will last for a time τ given by

$$\tau = \tau_0 \exp\left(\frac{B}{k_B T}\right) \quad \text{or} \quad \ln\left(\frac{\tau}{\tau_0}\right) \sim \frac{L^{\psi}}{k_B T} \tag{A.16}$$

This also gives

$$\chi'(\omega) \sim |\ln \omega|^{-\theta/\psi} \qquad \chi''(\omega) \sim |\ln \omega|^{-1+(\theta/\psi)} \tag{A.17}$$

In the case of 3D spin glasses the droplet model assumes conventional dynamic scaling is operative.

References

[1] S.F.Edwards and P.W.Anderson, *J.Phys. F* **5** 965 (1975); S.F.Edwards and P.W.Anderson, *J.Phys. F* **6** 1927 (1975)

[2] D.Sherrington and S.Kirkpatrick, *Phys. Rev. Lett.* **35** 1792 (1975); D.Sherrington and S.Kirkpatrick, *Phys. Rev. B* **17** 4384 (1978)

[3] D.J.Thouless, P.W.Anderson and R.G.Palmer *Phil. Mag.* **35** 593 (1977)

[4] D.S.Fisher and D.A.Huse, *Phys. Rev. Lett.* **56** 1601 (1988); *Phys. Rev. B* **38** 386 (1988)

Appendix B Rietveld refinement results from data obtained on the system $KFe_3(XO_4)_2(OH)_6$ (where X = S, Cr and Se) and the system $(D_3O)Cr_3(SO_4)_2(OD)_6$

Atom	x	y	z	site symmetry
Fe	0.1667	-0.1667	-0.1667	2/M(110)
S	0	0	0.3085	3M(100)
O1	0	0	0.3943	3M(100)
O2	0.2208	-0.2208	-0.0511	M(110)
O3	0.1333	-0.1333	0.1332	M(110)
K	0	0	0	-3M(110)
Space group R $\bar{3}$ *m*		*lattice parameters a = 7.31Å c = 17.21Å*		

Table B.1 Atom positions for the sample $KFe_3(SO_4)_2(OD)_6$ obtained from refinement of powder X-ray diffraction data

Atom	x	y	z	site symmetry
Fe	0.1667	-0.1667	-0.1667	2/M(110)
Cr	0	0	0.3134	3M(100)
O1	0	0	0.4055	3M(100)
O2	0.2119	-0.2119	-0.0519	M(110)
O3	0.1303	-0.1303	0.1379	M(110)
K	0	0	0	-3M(110)
Space group R $\bar{3}$ m		*lattice parameters a = 7.44Å c = 17.48Å*		

Table B.2 Atom positions for the sample $KFe_3(CrO_4)_2(OH)_6$ obtained from refinement of powder X-ray diffraction data

Atom	x	y	z	site symmetry
Fe	0.1667	-0.1667	-0.1667	2/M(110)
Se	0	0	0.3115	3M(100)
O1	0	0	0.4040	3M(100)
O2	0.2139	-0.2139	-0.0537	M(110)
O3	0.1286	-0.1286	0.1380	M(110)
K	0	0	0	-3M(110)
Space group R –3 m		*lattice parameters a = 7.40Å c = 17.57Å*		

Table B.3 Atom positions for the sample $KFe_3(SeO_4)_2(OH)_6$ obtained from refinement of powder X-ray diffraction data

Atom	x	y	z	frac	uiso/Å^2	site symmetry
Fe	0.16667(0)	-0.16667(0)	-0.16667(0)	1.00(0)	0.00339(14)	2/M(110)
S	0(0)	0(0)	0.30062(15)	1.00(0)	0.03193(6)	3M(100)
O1	0(0)	0(0)	0.391851(5)	1.00(0)	0.00604(13)	3M(100)
O2	0.22218(3)	-0.22218(3)	-0.05435(3)	1.00(0)	0.00604(13)	M(110)
O3	.123211(4)	-.123211(4)	.136162(3)	1.00(0)	0.00604(13)	M(110)
O4	0.22218(3)	-0.22218(3)	-0.05435(28)	1.00(0)	0.00604(13)	
O5	0.12321(4)	-0.12321(4)	0.13616(3)	1.00(0)	0.00604(13)	
K	0(0)	0(0)	0(0)	0.60(0)	0.10656(19)	-3M(100)
O7	0(0)	0(0)	-0.0601(0)	0.15(0)	0.10656(19)	
D1	-0.06457(0)	0.06457(0)	-0.03889(0)	0.15(0)	0.02339(3)	M(110)
D2	0.19269(35)	-0.19269(35)	0.11174(27)	1.00(0)	0.02339(3)	M(110)

a = b = 7.23832(29)Å c = 16.98603(89)Å $\alpha = \beta = 90°$ $\gamma = 120°$ Volume =770.724(56)Å^3
$\chi^2 = 580.7$ $R_{wp} = 0.0559$

Table B.4 Rietveld refinement results for D20 data obtained from $KFe_3(SO_4)_2(OD)_6$ at 80K

Atom	x	y	z	frac	uiso/Å^2	site symmetry
Fe	0.16667(0)	-0.16667(0)	-0.16667(0)	1.00(0)	0.00110(17)	2/M(110)
S	0(0)	0(0)	0.31875(15)	1.00(0)	0.06589(9)	3M(100)
O1	0(0)	0(0)	0.40077(5)	1.00(0)	0.00811(15)	3M(100)
O2	0.21951(3)	-0.21951(3)	-0.05354(3)	1.00(0)	0.00811(15)	M(110)
O3	0.12549(4)	-0.12549(4)	0.13496(3)	1.00(0)	0.00811(15)	M(110)
O4	0.22218(3)	-0.22218(3)	-0.05435(28)	1.00(0)	0.00811(15)	3M(100)
O5	0.12321(4)	-0.12321(4)	0.13616(3)	1.00(0)	0.00811(15)	3M(100)
K	0(0)	0(0)	0(0)	0.60(0)	0.08000(19)	-3M(100)
O7	0(0)	0(0)	-0.0601(0)	0.21(0)	0.00811(15)	3M(100)
D1	-0.06457(0)	0.06457(0)	-0.03889(0)	0.21(0)	0.04537(3)	M(110)
D2	0.19109(35)	-0.19109(35)	0.11382(27)	1.00(0)	0.04537(3)	M(110)

a = b = 7.23660(11)Å c = 16.98231(3)Å $\alpha = \beta = 90°$ $\gamma = 120°$ Volume =770.724(56)Å^3
$\chi^2 = 11.00$ $R_{wp} = 0.0775$

Table B.5 Rietveld refinement results for D20 data obtained from $KFe_3(SO_4)_2(OD)_6$ at 62K

Atom	x	y	z	frac	uiso/Å^2	site symmetry
Fe	0.16667(0)	-0.16667(0)	-0.16667(0)	1.00(0)	0.00562(18)	2/M(110)
Cr	0(0)	0(0)	0.3124(6)	1.00(0)	0.00102(5)	3M(100)
O1	0(0)	0(0)	0.4086(4)	1.00(0)	0.00520(0)	3M(100)
O2	0.21378(26)	-0.21378(26)	-0.05482(29)	1.00(0)	0.00520(0)	M(110)
O3	0.12586(27)	-0.12586(27)	0.13950(23)	1.00(0)	0.00520(0)	M(110)
K	0(0)	0(0)	0(0)	1.00(0)	0.00963(6)	-3M(100)
H2	0.1937(5)	-0.1937(5)	0.1155(4)	1.00(0)	0.00287(0)	M(110)

$a = b = 7.36018(24)$Å $c = 17.21445(103)$Å
$\alpha = \beta = 90°$ $\gamma = 120°$ Volume = 807.608(59) Å^3
$\chi^2 = 68.33$ $R_{wp} = 0.0121$

Table B.6 Rietveld refinement results for D20 data obtained from the sample

$KFe_3(CrO4)_2(OH)_6$ at 80K

Atom	x	y	z	frac	uiso/Å^2	site symmetry
Fe	0.16667(0)	-0.16667(0)	-0.16667(0)	1.00(0)	0.01268(2)	2/M(110)
Cr	0(0)	0(0)	0.31263(2)	1.00(0)	0.02249(7)	3M(100)
O1	0(0)	0(0)	0.41345(11)	1.00(0)	0.02395(5)	3M(100)
O2	0.21378(8)	-0.21378(8)	-0.05482(8)	1.00(0)	0.02214(27)	M(110)
O3	0.12521(9)	-0.12521(9)	0.13943(6)	1.00(0)	0.00318(2)	M(110)
K	0(0)	0(0)	0(0)	1.00(0)	0.00377(12)	-3M(100)
H1	0.03282(3)	-0.03282(3)	-0.088173(9)	0.50(0)	0.08000(11)	M(110)
H2	0.19593(19)	-0.19593(19)	0.11595(12)	1.00(0)	0.03726(4)	M(110)
O4	0(0)	0(0)	-0.04006(13)	0.50(0)	0.08000(15)	3M(100)

$a = b = 7.35133(12)$Å $c = 17.22077(2)$Å
$\alpha = \beta = 90°$ $\gamma = 120°$ Volume = 805.964(12)Å^3
$\chi^2 = 68.33$ $R_{wp} = 0.0121$

Table B.7 Rietveld refinement results for D20 data obtained from the sample

$KFe_3(CrO4)_2(OH)_6$ at 12K

Atom	x	y	z	frac	uiso/Å^2	site symmetry
Fe	0.16667(0)	-0.16667(0)	-0.16667(0)	1.00(0)	0.01731(25)	2/M(110)
Se	0(0)	0(0)	0.3098(4)	1.00(0)	0.00167(3)	3M(100)
O1	0(0)	0(0)	0.4030(5)	1.00(0)	0.00941(14)	3M(100)
O2	0.21302(35)	-0.21302(35)	-.0543(4)	1.00(0)	0.00941(14)	M(110)
O3	0.1254(4)	-0.1254(4)	0.13957(33)	1.00(0)	0.00941(14)	M(110)
K	0(0)	0(0)	0(0)	1.00(0)	0.025(0)	-3M(100)
H2	0.1935(6)	-0.1935(6)	0.1164(5)	1.00(0)	0.01708(29)	M(110)

a = b =7.32966 (29)Å c = 17.33983(12)Å $\alpha = \beta = 90°$ $\gamma = 120°$ Volume = 806.759(62)Å^3
$\chi^2 = 140.1$ $R_{wp} = 0.0201$

Table B.8 Rietveld refinement results for D20 data obtained from the sample $KFe_3(SeO4)_2(OH)_6$ at 161K

Atom	x	y	z	frac	uiso/Å^2	site symmetry
Fe	0.16667(0)	-0.16667(0)	-0.16667(0)	1.00(0)	0.00323(4)	2/M(110)
S	0(0)	0(0)	0.31020(4)	1.00(0)	0.00167(0)	3M(100)
O1	0(0)	0(0)	0.40660(5)	1.00(0)	0.00941(0)	3M(100)
O2	0.213(35)	-0.21300(35)	0.0505(4)	1.00(0)	0.00941(0)	M(110)
O3	0.1308(4)	-0.13080(4)	0.1391(33)	1.00(0)	0.00941(0)	M(110)
K	0(0)	0(0)	0(0)	1.00(0)	0.02500(0)	-3M(100)
H2	0.1984(8)	-0.1984(8)	0.1114(5)	1.00(0)	0.01708(0)	M(110)

a = b =7.323397(4)Å c = 17.23025(12)Å $\alpha = \beta = 90°$ $\gamma = 120°$ Volume = 805.659(6)Å^3
$\chi^2 = 10.43$ $R_{wp} = 0.0549$

Table B.9 Rietveld refinement results for D20 data obtained from the sample $KFe_3(SO4)_2(OH)_6$ at 5K

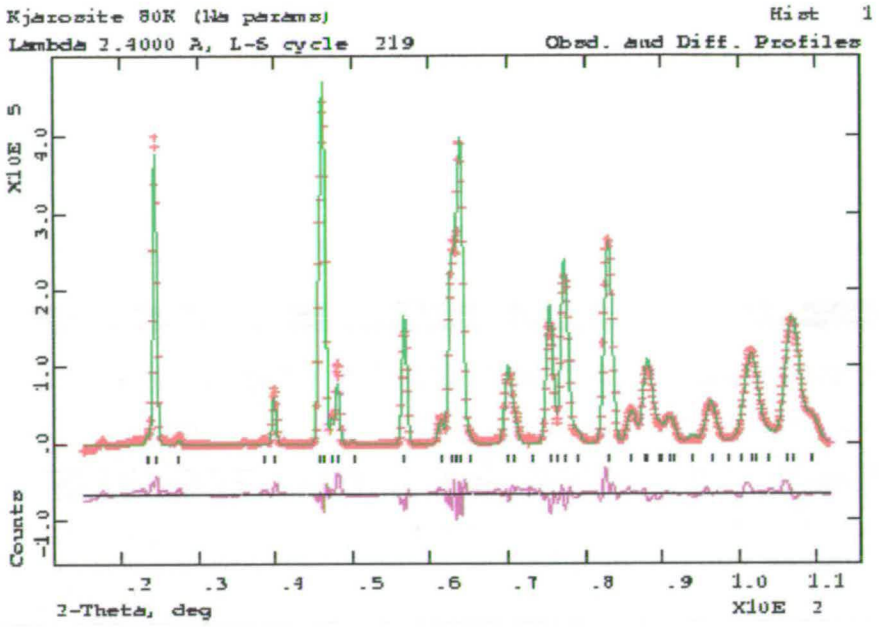

Figure B.1 Rietveld refinement of D20 data obtained for $KFe_3(SO4)_2(OH)_6$ at 80K

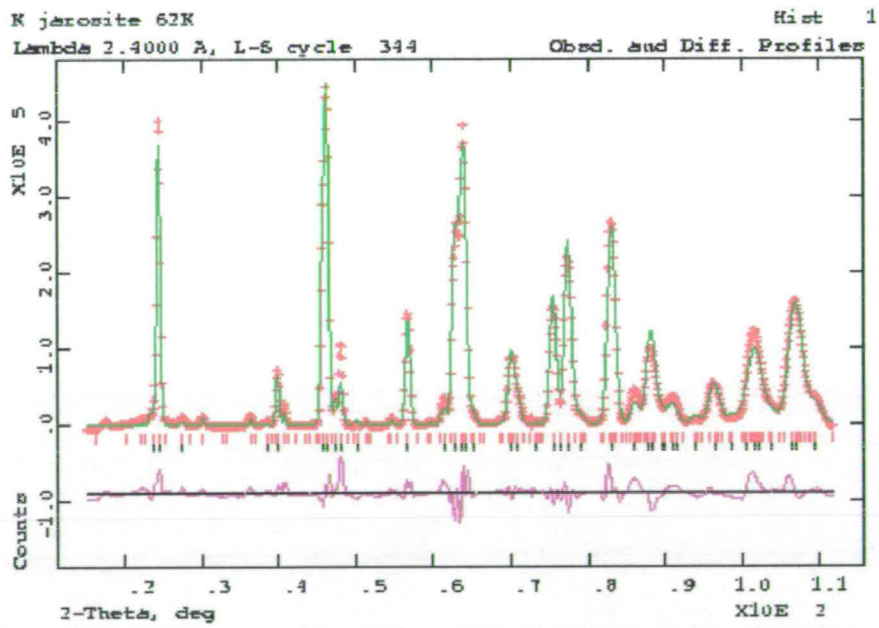

Figure B.2 Rietveld refinement of D20 data obtained for $KFe_3(SO4)_2(OH)_6$ at 62K

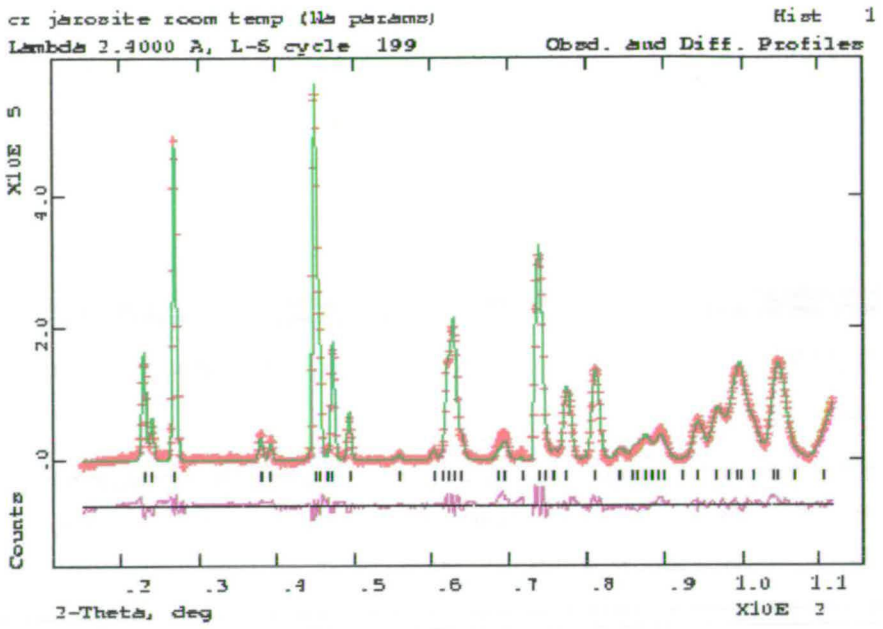

Figure B.3 Rietveld refinement of D20 data obtained for $KFe_3(CrO4)_2(OH)_6$ at 80K

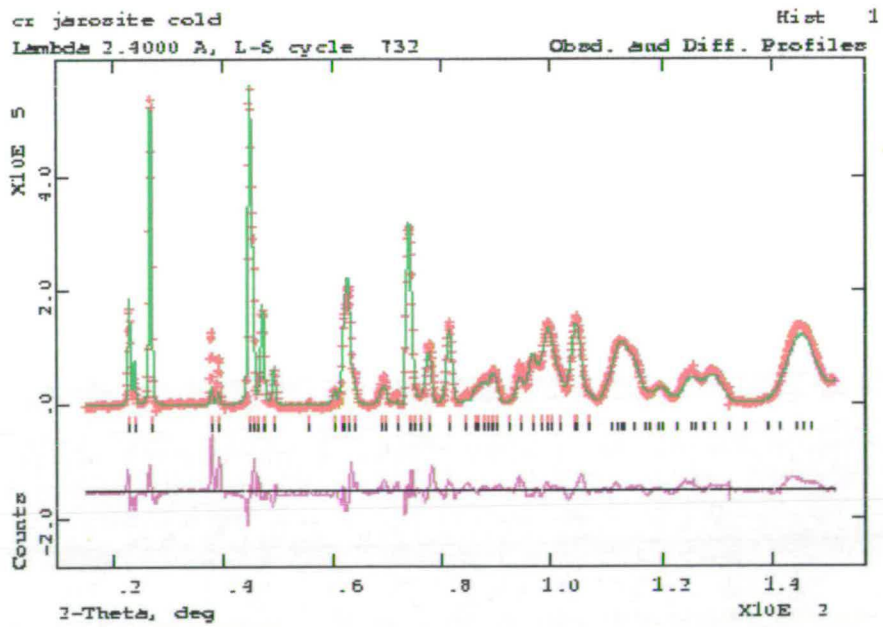

Figure B.4 Rietveld refinement of D20 data obtained for $KFe_3(CrO4)_2(OH)_6$ at 12K

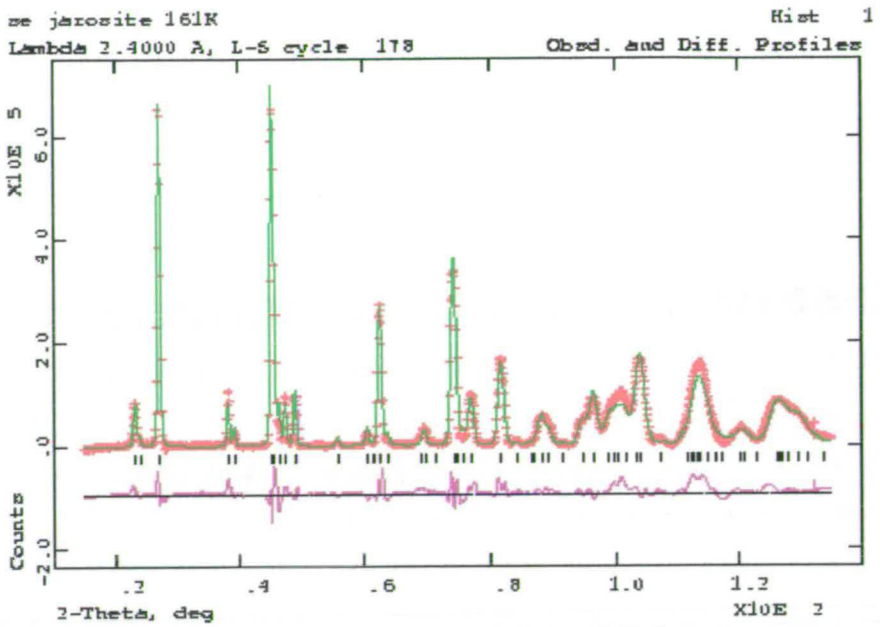

Figure B.5 Neutron Diffraction pattern obtained for $KFe_3(SeO4)_2(OH)_6$ at 161K

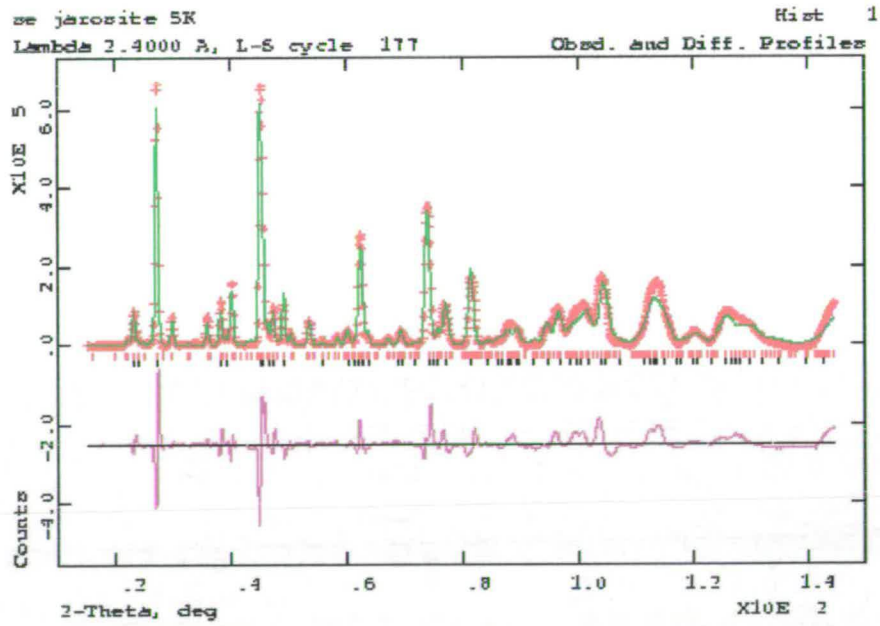

Figure B.6 Neutron Diffraction pattern obtained for $KFe_3(SeO4)_2(OH)_6$ at 5K

Atom	x	y	z	frac	uiso/Å^2	site symmetry
Cr	0.16667(0)	-0.16667(0)	-0.16667(0)	1.00(0)	0.00914(25)	2/M(110)
S	0(0)	0(0)	0.3063(10)	1.00(0)	0.00143(27)	3M(100)
O1	0(0)	0(0)	0.3918(4)	1.00(0)	0.00411(18)	3M(100)
O2	0.22093(32)	-0.22093(32)	-0.05760(22)	1.00(0)	0.00508(11)	M(110)
O3	0.12697(32)	-0.12697(32)	0.13706(28)	1.00(0)	0.00109(3)	M(110)
O4	0(0)	0(0)	0.0126(13)	0.50(0)	0.01061(4)	3M(100)
D1	-0.0637(16)	0.0637(16)	-0.0410(16)	0.50(0)	0.18907(13)	M(110)
D2	0.1973(7)	-0.1973(7)	0.1064(6)	1.00(0)	0.01126(4)	M(110)

a = b = 7.22604(12) Å c = 17.03497(45) Å $\alpha = \beta = 90°$ $\gamma = 120°$ Volume = 770.323(22) Å^3
$\chi^2 = 5.548$ $R_{wp} = 0.0541$

Table B.10 Rietveld refinement results for D2B data obtained from the sample $(D_3O)Cr_3(SO4)_2(OD)_6$ at 130K

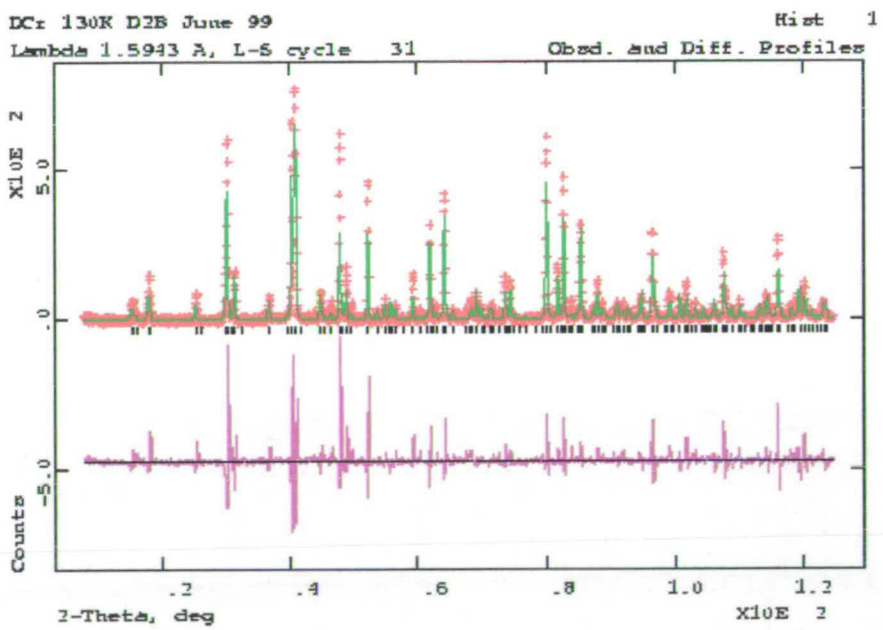

Figure B.7 Neutron Diffraction pattern obtained for the sample $(D_3O)Cr_3(SO4)_2(OD)_6$ at 130K

Appendix C Refined parameters from HRPD work on the system $La_{1-x}Ca_xMnO_3$

Atom	x	y	z	frac	uiso/Å^2	site symmetry
La	-0.00264(12)	0.01543(26)	0.25(0)	0.54(0)	0.01326(1)	M(001)
Ca	-0.00264(12)	0.02156(41)	0.25(0)	0.46(0)	0.01326(1)	M(001)
Mn	0.5(0)	0(0)	0(0)	1.00(0)	0.00299(11)	-1
O1	0.06033(8)	0.48981(12)	0.25(0)	1.00(0)	0.01104(4)	M(001)
O2	-0.27379(8)	0.27920(7)	0.03158(67)	1.000	0.01104(4)	1

a = 5.43538(25)Å b = 5.42500(26)Å c = 7.65330(28)Å
$\alpha = \beta = \gamma = 90.00(0)^\circ$ Volume = 225.673(6)Å^3
$\chi^2 = 2.503$ $R_{wp} = 0.0425$

Table C.1 Results from Rietveld refinement of HRPD data obtained for the sample $La_{0.54}Ca_{0.46}MnO_3$ at 300K

Atom	x	y	z	frac	uiso/Å^2	site symmetry
La	-0.00260(11)	0.01540(1)	0.25(0)	0.54(0)	0.01300(0)	M(001)
Ca	-0.00260(11)	0.01540(1)	0.25(0)	0.46(0)	0.01300(0)	M(001)
Mn	0.5(0)	0(0)	0(0)	1.00(0)	0.01266(61)	-1
O1	0.05238 (11)	0.48866(13)	0.25(0)	1.00(0)	0.00874(37)	M(001)
O2	-0.27796(9)	.27709(8)	0.03459(5)	1.00(0)	0.00874(37)	1

a = 5.42886(38)Å b = 5.42137(39)Å c = 7.65220(34)Å
$\alpha = \beta = \gamma = 90.00(0)^\circ$ Volume = 225.218(6)Å^3
$\chi^2 = 6.826$ $R_{wp} = 0.0499$

Table C.2 Results from Rietveld refinement of HRPD data obtained for the sample $La_{0.54}Ca_{0.46}MnO_3$ at 200K

Atom	x	y	z	frac	uiso/Å^2	site symmetry
La	-0.01780(11)	0.01830(2)	0.25(0)	0.54(0)	0.00792(12)	M(001)
Ca	-0.01780(11)	0.01830(2)	0.25(0)	0.46(0)	0.00792(12)	M(001)
Mn	0.5(0)	0(0)	0(0)	1.00(0)	0.00178(6)	-1
O1	0.0544(14)	0.4915(16)	0.25(0)	1.00(0)	0.01218(36)	M(001)
O2	-0.2789(11)	0.27560(12)	0.03360(6)	1.00(0)	0.01218(36)	1

a = 5.42333(34)Å b = 5.42115(36)Å c = 7.65500(42)Å
$\alpha = \beta = \gamma = 90.00(0)°$ Volume =225.061(74)Å^3
$\chi^2 = 20.28$ $R_{wp} = 0.0509$

Table C.3 Results from Rietveld refinement of HRPD data obtained for the sample $La_{0.54}Ca_{0.46}MnO_3$ at 150K

Atom	x	y	z	frac	uiso/Å^2	site symmetry
La	-0.00461(16)	0.01256(13)	0.25(0)	0.52(0)	0.01349(2)	M(001)
Ca	-0.00461(16)	0.01256(13)	0.25(0)	0.48(0)	0.01349(2)	M(001)
Mn	0.5(0)	0(0)	0(0)	1.00(0)	0.00643(1)	-1
O1	0.06025(12)	0.48902(2)	0.25(0)	1.00(0)	0.01338(5)	M(001)
O2	-0.27455(5)	0.27759(11)	0.03051(13)	1.00(0)	0.01338(5)	1

a = 5.43034(62)Å b = 5.42156(51)Å c = 7.64583(34)Å
$\alpha = \beta = \gamma = 90.00(0)°$ Volume = 225.100(7)Å^3
$\chi^2 = 3.133$ $R_{wp} = 0.0303$

Table C.4 Results from Rietveld refinement of HRPD data obtained for the sample $La_{0.54}Ca_{0.48}MnO_3$ at 300K

Atom	x	y	z	frac	uiso/Å^2	site symmetry
La	-0.00461(2)	0.01256(21)	0.25(0)	0.52	0.01564(1)	M(001)
Ca	-0.00461(2)	0.01256(21)	0.25(0)	0.48	0.01564(1)	M(001)
Mn	0.5(0)	0(0)	0(0)	1	1.26100(9)	-1
O1	0.04975(11)	0.48959(21)	0.25(0)	1	0.01203(5)	M(001)
O2	-0.27851(11)	0.27624(11)	0.03646(4)	1	0.01203(5)	1

a = 5.42706(49)Å b = 5.41839(43)Å c = 7.63962(31)Å
$\alpha = \beta = \gamma = 90.00(0)^\circ$ Volume = 224.650(8)Å^3
$\chi^2 = 4.312$ $R_{wp} = 0.0367$

Table C.5 Results from Rietveld refinement of HRPD data obtained for the sample $La_{0.54}Ca_{0.48}MnO_3$ at 200K

Atom	x	y	z	frac	uiso/Å^2	site symmetry
La	-0.00461(0)	0.01257(2)	0.25(0)	0.52(0)	0.01335(14)	M(001)
Ca	-0.00461(0)	0.01257(2)	0.25(0)	0.48(0)	0.01335(14)	M(001)
Mn	0.5(0)	0(0)	0(0)	1.00(0)	0.01195(13)	-1
O1	0.04975(6)	0.48959(9)	0.2500	1.00(0)	0.01275(6)	M(001)
O2	-0.27851(7)	0.27624(7)	0.03635(3)	1.00(0)	0.01275(6)	1

a = 5.42525(35)Å b = 5.41778(34)Å c = 7.63929(33)Å
$\alpha = \beta = \gamma = 90.00(0)^\circ$ Volume = 224.516(17)Å^3
$\chi^2 = 13.59$ $R_{wp} = 0.0372$

Table C.6 Results from Rietveld refinement of HRPD data obtained for the sample $La_{0.54}Ca_{0.48}MnO_3$ at 150K

Atom	x	y	z	frac	uiso/Å^2	site symmetry
La	-0.02143(17)	0.13737(3)	0.25(0)	0.50(0)	0.17465(26)	M(001)
Ca	-0.02143(17)	0.13737(3)	0.25(0)	0.50(0)	0.17465(26)	M(001)
Mn	0.5(0)	0(0)	0(0)	1.00(0)	0.01802(5)	-1
O1	0.22122(13)	0.52525(14)	0.25(0)	1.00(0)	0.10008(2)	M(001)
O2	-0.28080(5)	0.29115(10)	-0.00836(6)	1.00(0)	0.10634(13)	1

a = 5.43978(32)Å b = 5.38126(27)Å c = 7.65534(45)Å
$\alpha = \beta = \gamma = 90.00(0)°$ Volume = 224.094(14)Å^3
Phase fraction 32.0%

Atom	x	y	z	frac	uiso/Å^2	site symmetry
La	-0.00211(4)	0.00691(4)	0.25(0)	0.50(0)	0.00117(5)	M(001)
Ca	-0.00211(4)	0.00691(4)	0.25(0)	0.50(0)	0.00117(5)	M(001)
Mn	0.5(0)	0(0)	0(0)	1.00(0)	0.00760(21)	-1
O1	0.05453(3)	0.47833(3)	0.2500	1.00(0)	0.01328(3)	M(001)
O2	-0.27341(2)	0.27738(17)	0.03299(9)	1.00(0)	0.0099(17)	1

a = 5.42150(4)Å b = 5.40699(32)Å c = 7.60665(2)Å
$\alpha = \beta = \gamma = 90.00(0)°$ Volume = 222.981(46)Å^3
Phase fraction 43.7%

Atom	x	y	z	frac	uiso/Å^2	site symmetry
La	0.25(0)	0.25(0)	0.25(0)	0.50(0)	0.02401(6)	M(001)
Ca	0.25(0)	0.25(0)	0.25(0)	0.50(0)	0.02401(6)	M(001)
Mn	0(0)	0(0)	0	1.00(0)	0.00266(6)	-1
O1	0.68749(19)	0.81249(19)	0.2500	1.00(0)	0.02933(28)	M(001)

a = b = c = 5.47168(13)Å
$\alpha = \beta = \gamma = 60.09(2)°$ Volume = 116.067(18)Å^3
Phase fraction 24.3%

Table C.7 Results from Rietveld refinement of HRPD data obtained for the sample $La_{0.50}Ca_{0.50}MnO_3$ at 300K. Final statistics of fit $\chi^2 = 3.083$ $R_{wp} = 0.0317$

Rietveld refinement profiles obtained for samples of composition $La_{1-x}Ca_xMnO_3$ and $La_{1-x}Pb_xMnO_3$

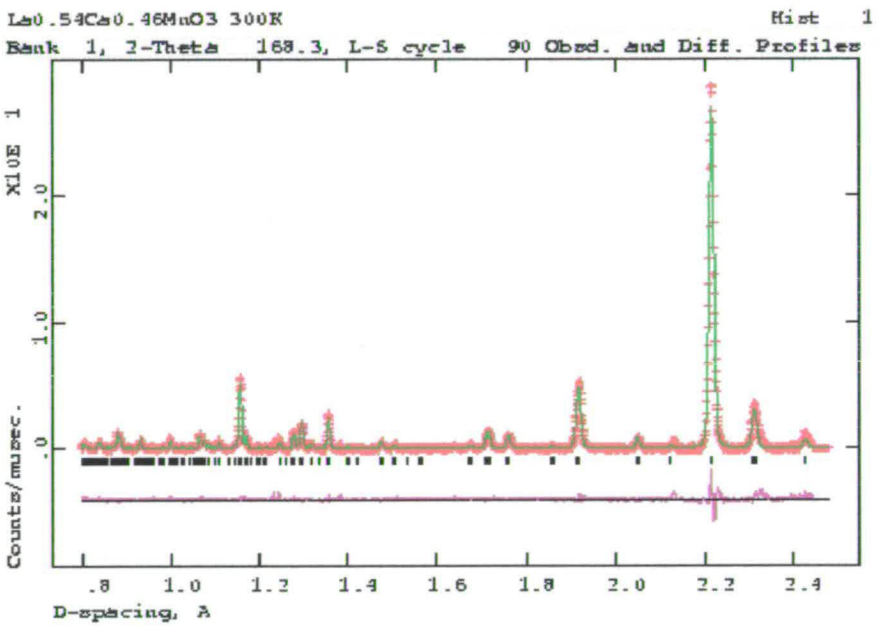

Figure C.1 Rietveld refinement of HRPD data from $La_{0.54}Ca_{0.46}MnO_3$ at 300K

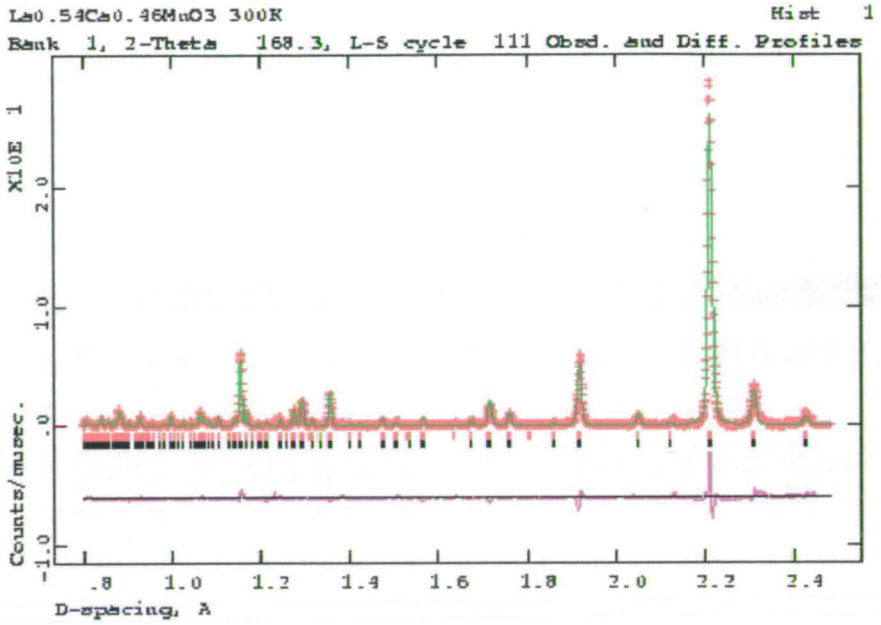

Figure C.2 Rietveld refinement of HRPD data taken from $La_{0.54}Ca_{0.46}MnO_3$ at 200K

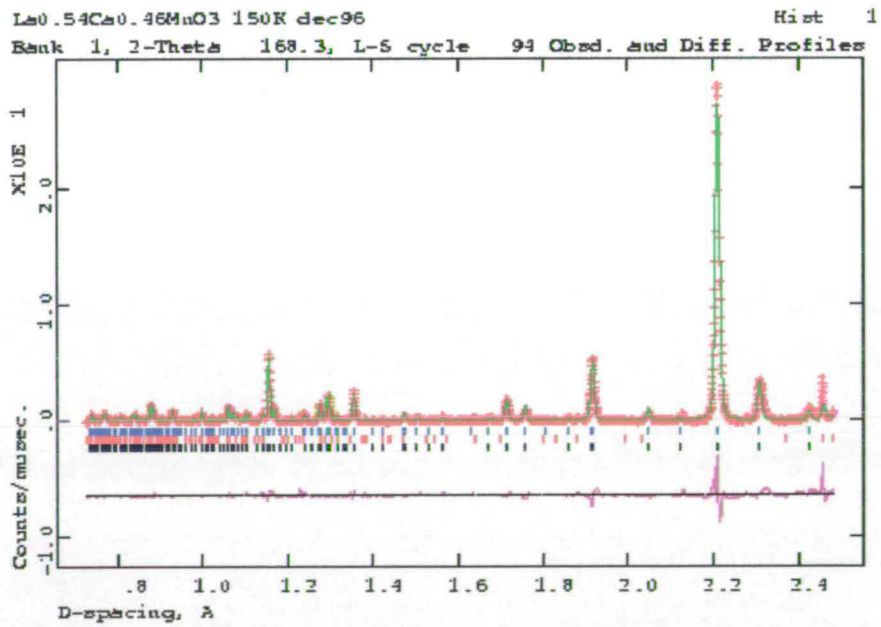

Figure C.3 Rietveld refinement of HRPD data taken from $La_{0.54}Ca_{0.46}MnO_3$ at 150K

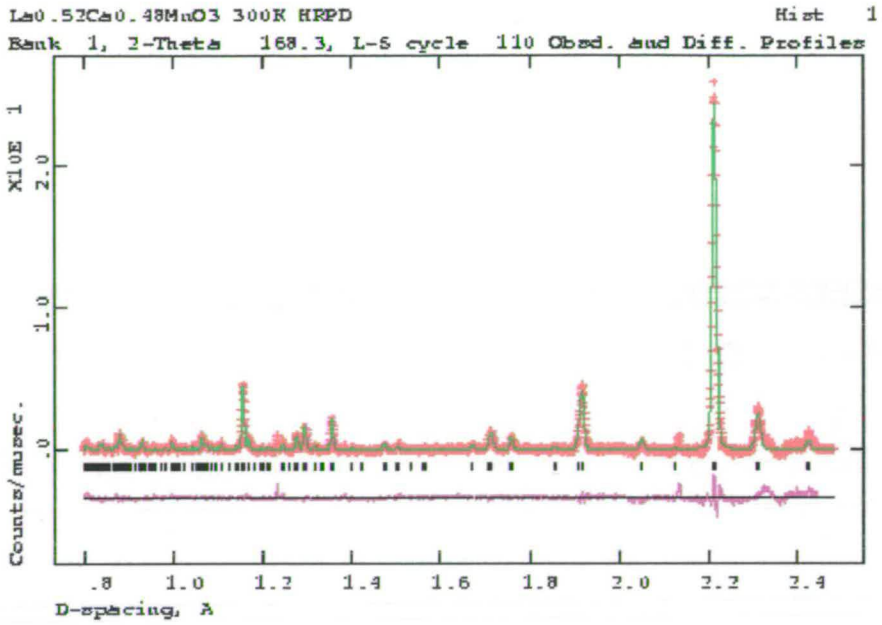

Figure C.4 Rietveld refinement of HRPD data taken from $La_{0.52}Ca_{0.48}MnO_3$ at 300K

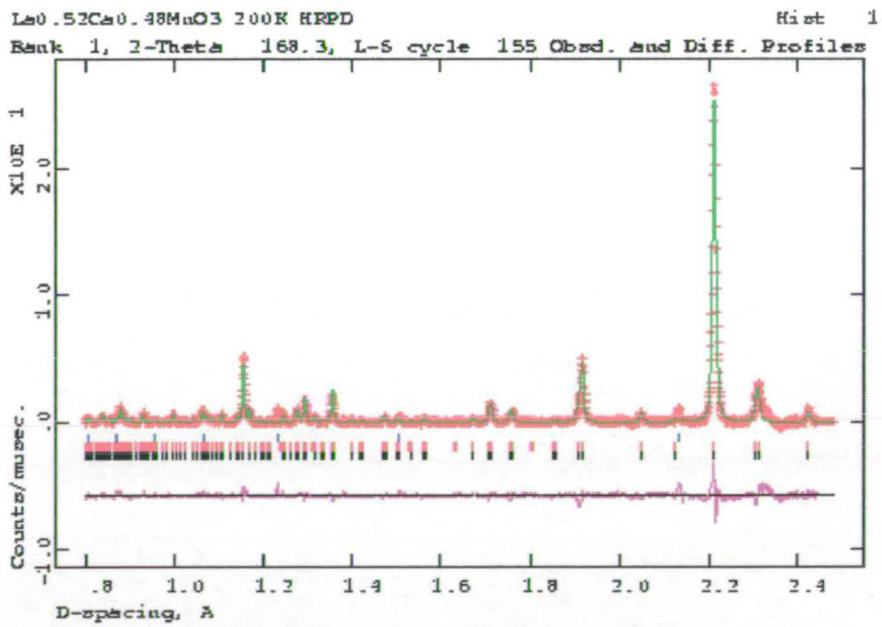

Figure C.5 Rietveld refinement of HRPD data taken from $La_{0.52}Ca_{0.48}MnO_3$ at 200K

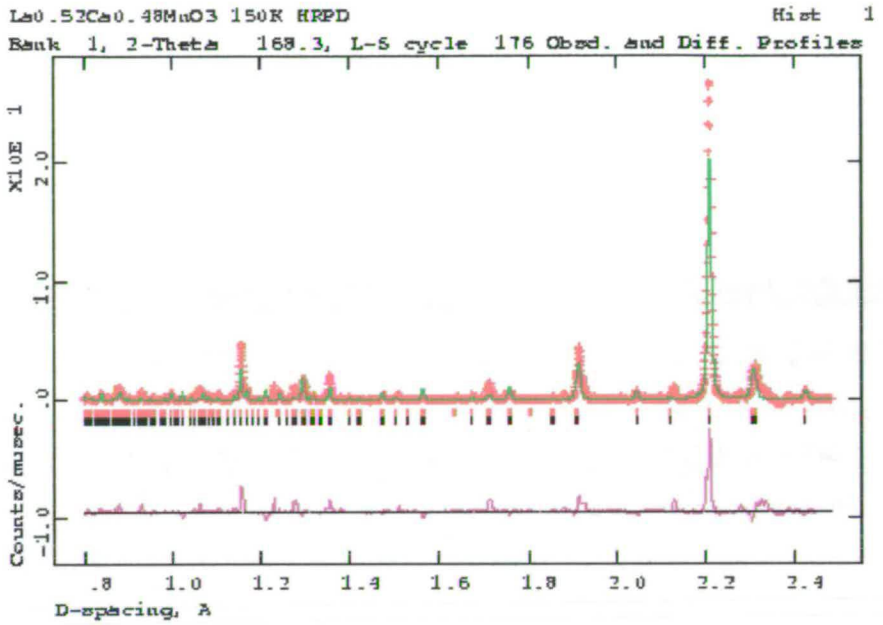

Figure C.6 Rietveld refinement of HRPD data taken from $La_{0.52}Ca_{0.48}MnO_3$ at 150K

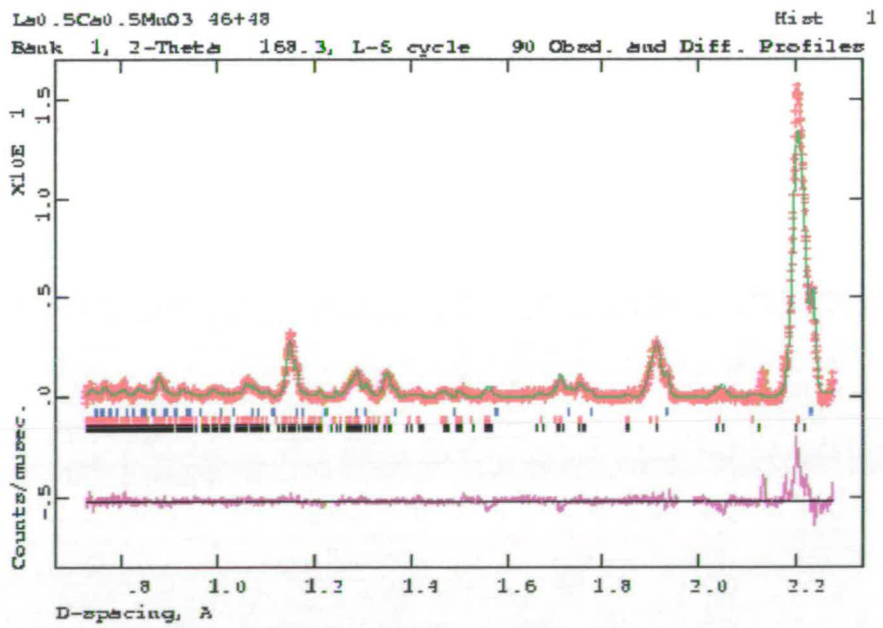

Figure C.7 Rietveld refinement of HRPD data taken from $La_{0.50}Ca_{0.50}MnO_3$ at 300K

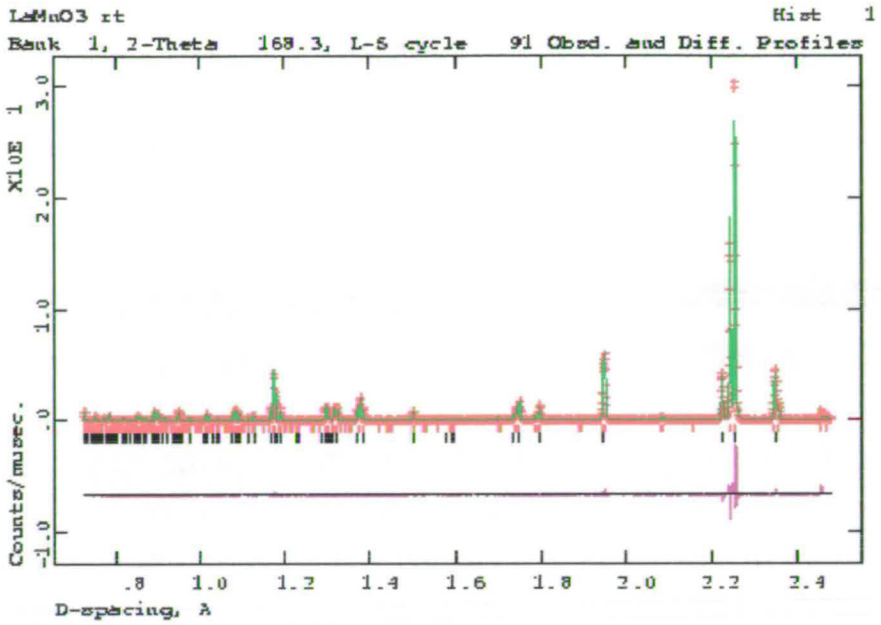

Figure C.8 Rietveld refinement of HRPD data taken from $LaMnO_3$ at 300K

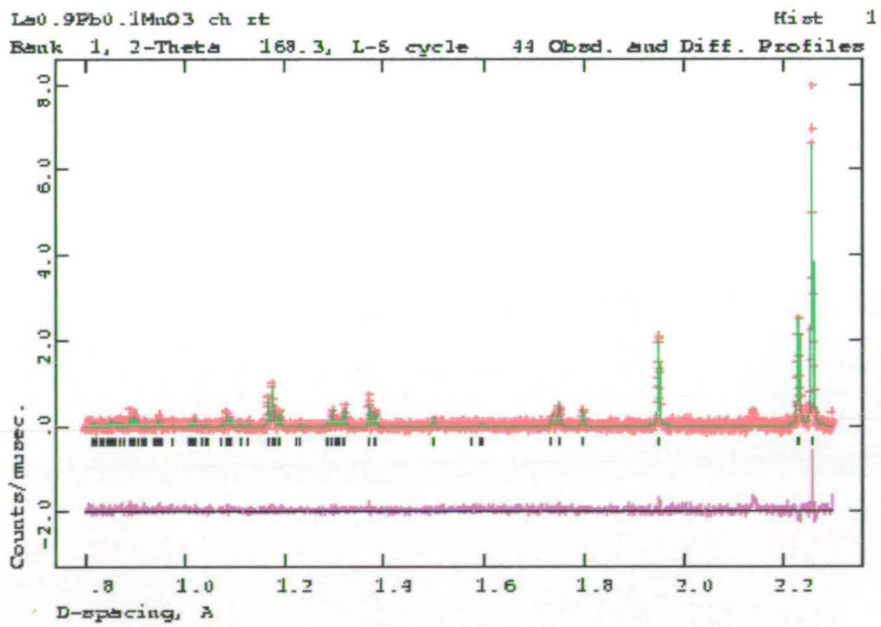

Figure C.9 Rietveld refinement of HRPD data taken from $La_{0.9}Pb_{0.1}MnO_3$ at 300K

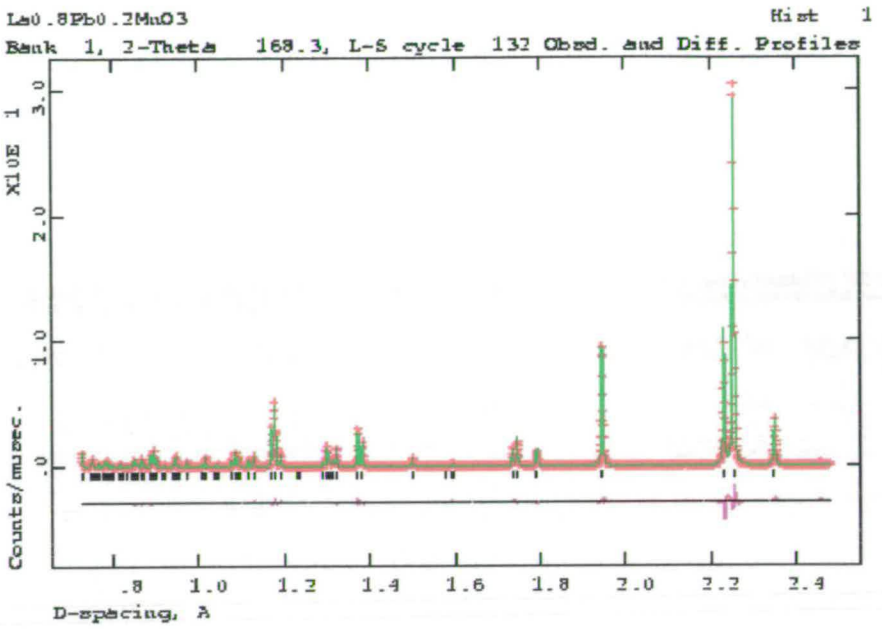

Figure C.10 Rietveld refinement of HRPD data taken from $La_{0.80}Pb_{0.20}MnO_3$ at 300K

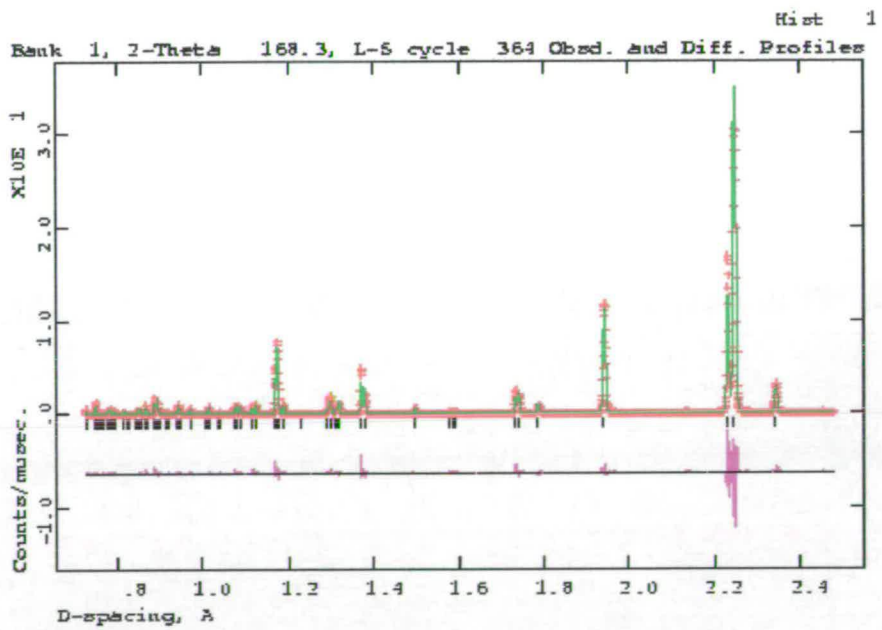

Figure C.11 Rietveld refinement of HRPD data taken from $La_{0.70}Pb_{0.30}MnO_3$ at 300K

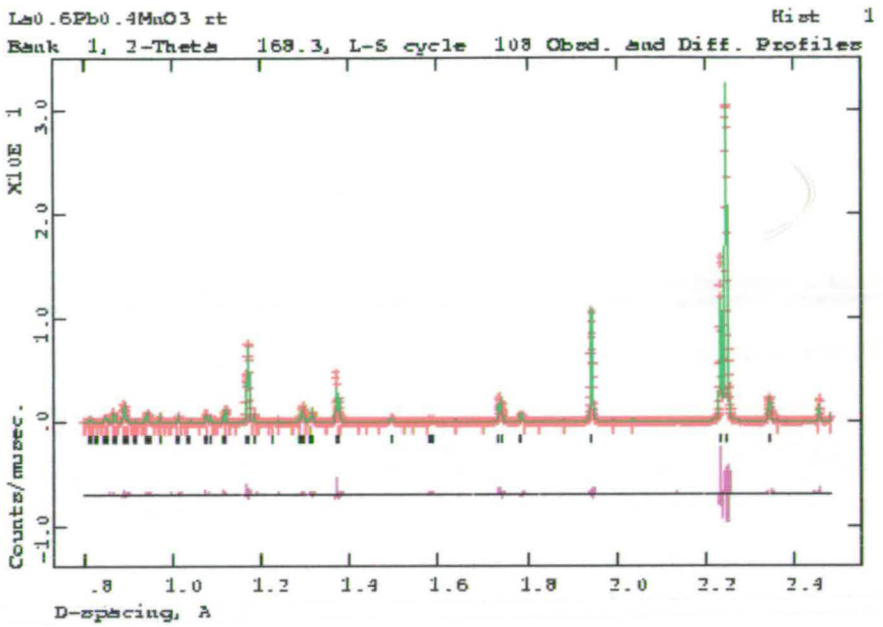

Figure C.12 Rietveld refinement of HRPD data taken from $La_{0.60}Pb_{0.40}MnO_3$ at 300K

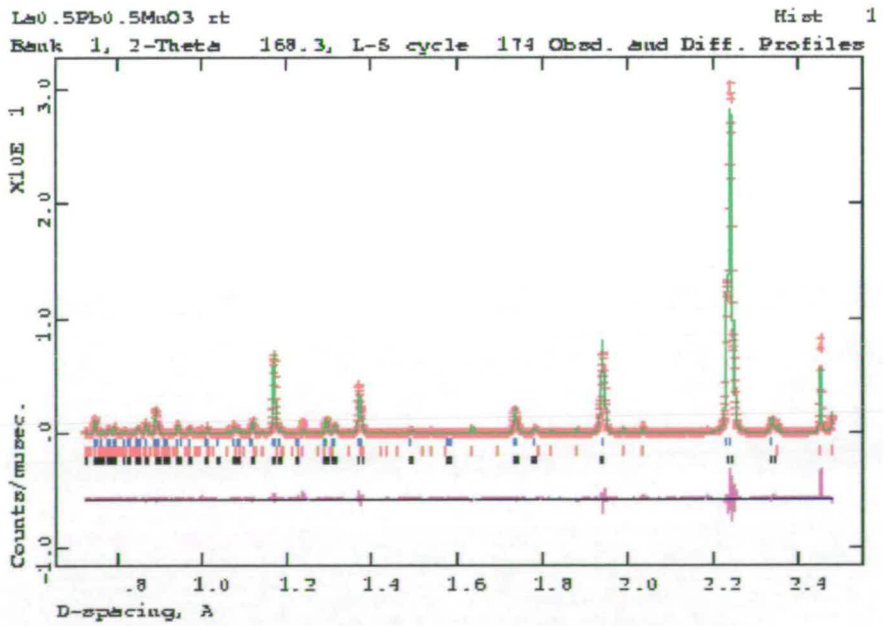

Figure C.13 Rietveld refinement of HRPD data taken from $La_{0.50}Pb_{0.50}MnO_3$ at 300K

Neutron spin echo study of magnetic fluctuations in the kagome antiferromagnet $(D_3O)Fe_3(SO_4)_2(OD)_6$

G.S. Oakley[a], S. Pouget[b] , A. Harrison[a*], J.V. Frunzke[a!], and D. Visser[c]

[a] *Department of Chemistry, The University of Edinburgh,Edinburgh, EH9 3JJ, UK*
[b] *Institut Laue Langevin, BP 156, 38042 Grenoble cedex 9, France*
[c] *Department of Physics, The University of Warwick,Coventry, CV4 7AL, UK*

Abstract

The kagome lattice with antiferromagnetic nearest-neighbour exchange provides a simple example of a geometrically frustrated magnet with a highly degenerate ground state. Theoretical work indicates that the static and dynamic correlations of this magnet are unconventional, with strong fluctuations down to very low temperatures. Deuteronium Jarosite ($(D_3O)Fe_3(SO_4)_2(OD)_6$) provides a rare example of a suitable model material to test such theory. dc susceptibility studies show strong antiferromagnetic exchange between the S=5/2 moments ($\theta_{CW} \cong$ -700K), and a spin-glass transition at $T_f \cong$ 13K. We report neutron spin echo measurements on this compound using the polarised neutron spectrometer IN11 at ILL taken with momentum transfer Q = 1.35Å^{-1} for times ranging from 9.7 to 870 ps. The magnetic fluctuations were observed to slow down gradually on cooling through T_f, until they appear to be static at the shortest experimental timescale at 1.5K.

Corresponding author. FAX +131 650 4743; email a.harrison@ed.ac.uk

! Current address: Universität Kaiserslautern, Fachbereich Chemie, 67663 Kaiserslautern, Germany

Introduction

Kagome Heisenberg antiferromagnets have been the focus of considerable experimental and theoretical activity over the past few years on account of the unusual ground state and excitations shown by this highly frustrated magnet[1-4]. The topology of nearest-neighbour exchange on this lattice leads to a highly degenerate ground state. The consensus of theoretical work is that as the temperature of the system is reduced, the spins condense to a strongly fluctuating coplanar array[3,4], but it is still not clear whether there is any long-range order as $T \rightarrow 0$. There are relatively few suitable model materials to test such theory, and the most-studied compound in this field, the layered garnet $SrCr_{8-x}Ga_{4+x}O_{19}$ (SCGO(x)) [5-7], has a crystal structure that deviates significantly from the simple kagome lattice [5-7].

An alternative model material is provided by the Jarosite family of minerals [8], $AFe_3(SO_4)_2(OH)_6$ (where A is a univalent cation, most commonly K^+), and isomorphs in which Fe^{3+} is exchanged for another trivalent cation such as Al^{3+}, Cr^{3+} [9], Ga^{3+} [10] or V^{3+}[11]. For the iron compounds, Fe^{3+} ions sit at the vertices of a kagome lattice, acting as S = 5/2 Heisenberg moments coupled through strong antiferromagnetic exchange ($\theta_{CW} \cong -700K$) and in almost all cases, magnetic long-range order is observed below $T_N \cong 55K$. The exception is the hydronium salt[10] ($A^+ = H_3O^+$) for which dc susceptibility measurements reveal a spin-glass-like transition at $T_f \cong 15K$, and powder neutron diffraction from a deuterated sample reveals diffuse scattering at low temperatures, indicative of short-range magnetic correlations whose length $\xi \cong 19$ Å at 2K. Muon spin relaxation data taken on this sample on spectrometer EMU at ISIS revealed that the

moments slow down as this material is cooled to T_f and do so in a fashion characteristic of a spin-glass[12]. Unfortunately, the time-window provided by this instrument does not extend to sufficiently small values to allow us to observe spin freezing, so we studied faster magnetic fluctuations by neutron spin echo (NSE) measurements using the polarised neutron spectrometer IN11 at the Institut Laue-Langevin (ILL).

Experimental

10g of $(D_3O)Fe_3(SO_4)_2(OD)_6$ was made in four batches by a modification of an established hydrothermal route[10]. Hydronium jarosite is commonly prepared by hydrolysis of a solution of ferric sulphate, in turn prepared by dissolving $Fe_2(SO_4)_3.x(H_2O)$ in water. In order to minimise the level of hydrogen in the sample, anhydrous $Fe_2(SO_4)_3$ was prepared in a fine, crystalline form and hydrolysed in a PTFE-lined steel bomb in D_2O for 39 hours at 155°C. Exchange of D with H from atmospheric water is very rapid for all stages in the synthesis and also for the product, so care was taken to perform manipulations either under an inert atmosphere, or as quickly as possible if it was necessary to handle the sample in air. The ratio H/D in the final product was estimated as 1/20 by polarised neutron scattering on diffractometer D7 at ILL. The magnetic freezing transition T_f was determined as 13.0±0.1K for every batch in the preparation.

The sample was loaded into an annular aluminium sample can, placed in an ILL 'Orange' cryostat on the polarised neutron spectrometer IN11 at ILL and the wavelength was set at 5.7Å.

The amplitude of the paramagnetic NSE measured at a time t gives a direct measure of the real part of the intermediate scattering law $S_m(Q, t)$ for fluctuations of wavevector Q[13]. For all our measurements, Q was fixed at 1.35 $Å^{-1}$, which is as close as possible to the maximum in S(Q) for the magnetic diffuse scattering, whilst avoiding any significant contribution from nuclear Bragg scattering. The NSE signal was measured for values of t ranging from 9.7 to 870ps, and temperatures from the base experimental temperature of 1.5K to 60K. Each t scan was normalised to the magnetic structure factor, $S_m(Q, t = 0)$, which was determined using three-dimensional magnetic polarisation analysis, and the data were finally divided by the normalised spectrometer resolution function, which had been determined with a quartz sample for the same values of t. The results of these measurements are displayed in **Figure 1** for temperatures spanning the magnetic freezing temperature as determined by dc susceptibility. Data taken above 20K have not been included because the signal was too weak to be measured in the time available with meaningful statistics.

Although the data are noisy, it is quite clear that the system is dynamic at time-scales of the order of 100 ps at 20K, and gradually freezes as it is cooled through T_f until at 2.0K, $S_m(Q, t)$ tends to $S_m(Q, t = 0)$, indicating that all moments are frozen on time-scales up to 870 ps. The freezing transition is illustrated in a different fashion in **Figure 2** which displays the NSE amplitude, corrected for the resolution measured with quartz, for t = 870 or 87 ps as the sample was cooled from 60K to the experimental base temperature of 1.5K.

This type of gradual freezing transition is similar to that seen in 'conventional' spin glasses[13] where a broad spectrum of relaxation times is observed over a wide range of temperature from very low values to significantly above T_f. For such glassy systems, the short-time component is generally found to adopt a Kohlrausch 'stretched' exponential form[13, 14]:

$$S(Q,t) / S(Q,0) = \exp(-(t / \tau)^{\beta}) \qquad [1]$$

where τ is the macroscopic relaxation time and the exponent β reflects the type of trajectory the system takes through phase space as it attempts to overcome a succession of energy barriers [15,16]. Our data are not sufficiently good to determine τ and β simultaneously in an unconstrained fashion with great confidence, so we fitted the data for the 20K measurement to a simple exponential (β =1 in [1]) to obtain an optimised value of τ = 15±1 ps; the outcome of this procedure is included in **Figure 1**.

Discussion and Conclusions

The observation of glassy spin dynamics in a magnet that is quite homogenous in terms of exchange interactions and occupancy of the magnetic lattice is quite remarkable, though paralleled by the behaviour of certain other frustrated antiferromagnets: similar glassy dynamics are observed by muon spin relaxation measurements in SCGO(x) [5] and $(D_3O)Fe_3(SO_4)_2(OD)_6$ [12] as well as by NSE in SCGO(x) [7]. A simple model exists to rationalise glassy behaviour in a homogenous kagome antiferromagnet, based on creation

of topological defects, as blocks of spins rotate cooperatively at no or little energy cost[17]. Weak interactions between such inhomogeneities, arising from minor perturbations to the simple nearest-neighbour Hamiltonian such as further-neighbour exchange, lead to a freezing transition, but the temperature of this process and its detailed dynamics have not been modeled in any detail. An estimate for the magnitude of the energy barriers produced by interactions between such defects may be provided by further measurements of the NSE signal for a wider range of temperatures above T_f, applying an Arrhenius analysis to a set of value of τ as a function of temperature.

Acknowledgements

We wish to thank A.S. Wills for advice for the sample preparations, B. Ferago for help in preparing for the NSE measurements, ILL for technical support and neutron scattering facilities, and EPSRC for a studentship.

References

[1] C. Broholm, G.Aeppli, G.P. Espinosa and A.S. Cooper, Phys. Rev. Lett. 65 (1990) 3173

[2] S.-H. Lee, C. Broholm, G. Aeppli, T. G. Perring, B. Hessen and A. Taylor, Phys. Rev. Lett. 76 (1996) 4424

[3] J.T. Chalker, P.C.W. Holdsworth and E.F. Shender, Phys. Rev. Lett. 68 (1992) 855

[4] E.F. Shender, V.B. Cherepanov, P.C.W. Holdsworth and A.J. Berlinsky, Phys. Rev. Lett. 70 (1993) 3812

[5] Y.J. Uemura, A. Keren, K. Kojima, L.P. le, G.M. Luke, W.D. Wu, Y. Ajiro, T. Asano, Y. Kuriyama, M. Mekata, H. Kikuchi and K.Kakurai, Phys. Rev. Lett. 73 (1994) 3306

[6] S.-H. Lee, C. Broholm, G. Aeppli, A.P. Ramirez, T.G. Perring, C.J. Carlile, M. Adams, T.J. L. Jones and B. Hessen, Europhys. Lett., 35 (1996) 127

[7] Y.J. Uemura, B.D. Gaulin, M. Mekata, I. Mirebeau, J.L. Tholence and S. Pouget, J. Magn. Magn. Mat. 177-181 (1998) 701

[8] M.G. Townsend, G. Longworth and E. Roudaut, Phys. Rev. B. 33 (986) 4919

[9] S.-H. Lee, C. Broholm, M.F. Collins, L. Heller, A.P. Ramirez, C. Kloc, E. Bucher, R.W. Erwin and N. Lacevic, Phys. Rev. B. 56 (1997) 2161

[10] A.S. Wills, A. Harrison, S.A.M.Mentink, T.E. Mason and Z. Tun, Europhys. Lett. 42 (1998) 325

[11] A. S. Wills, Ph.D. Thesis, The University of Edinburgh (1997)

[12] A. Harrison, A.S.Wills, D. Visser and J.S. Lord, ILL Annual Report for 1996, RB7838

[13] F. Mezei and A.P. Murani, J.Magn.Magn.Mat. 14 (1979) 211

[14] B.V.B. Sarkissian, J. Phys.C.:Condens. Matt. 2 (1990) 7873

[15] R.G. Palmer, D.L. Stein, E. Abrahams and P.W.Anderson, Phys. Rev. Lett. 53 (1984) 958

[16] F. Mezei, W. Knaak and B. Farago, Phys. Rev. Lett. 58 (1987) 571

[17] I. Ritchey, P. Chandra and P. Coleman, Phys. Rev. B 47 (1993) 1534

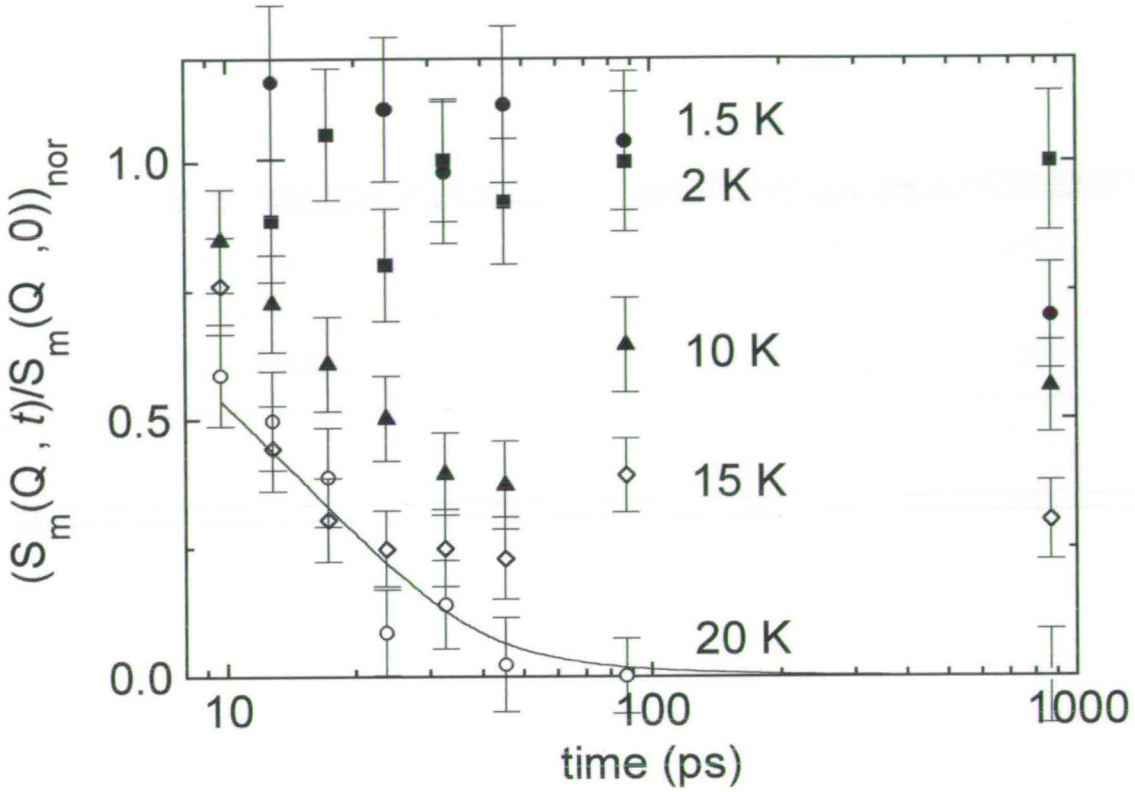

Figure 1. Time dependence of the NSE amplitude, normalised to the magnetic structure factor $S_m(Q,t=1)$ and corrected for the instrumental resolution, as the sample is cooled through the freezing transition. The various temperatures are denoted by filled circles (1.5K), filled squares (2 K) filled triangles, (10K), open triangles (15K) and open circles (20K), and the line through the 20K data set shows the least-square fit of an exponential decay to the data.

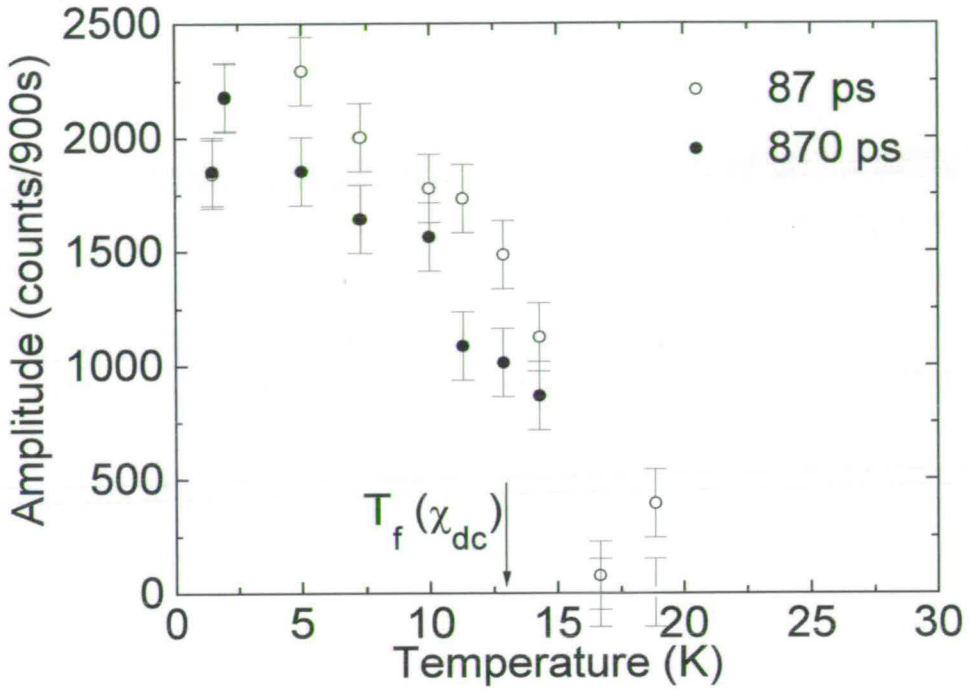

Figure 2. Temperature dependence of the NSE amplitude, corrected for the instrumental resolution measured with quartz, for delay times of 87 ps (open circles) and 870 ps (closed circles).

A Polarised Neutron Scattering Study of the Magnetic Correlations in the Kagome Antiferromagnet $AFe_3(SO_4)_2(OD)_6$ (A = D_3O, K)

G.S.Oakley[a], D.Visser[b*] , J. Frunske[a§], K.H.Andersen[c], A.S.Wills[d] and A.Harrison[a]

[a] Department of Chemistry, The University of Edinburgh, Edinburgh EH9 3JJ, UK

[b] Department of Physics, The University of Warwick, Coventry CV4 7AL, UK

[c] Institut Laue Langevin, BP 156, F 38042 Grenoble Cedex 9, France

[d] Brockhouse Institute for Materials Research, McMaster University, Hamilton, Ontario

L8S 4M1 Canada

[§] present address: Universität Kaiserslautern, Fachbereich Chemie, D-67663, Kaiserslautern, Germany

[*]corresponding author: fax +44 1203 692016, e-mail: phsdc@csv.warwick.ac.uk

Abstract:

This paper reports a full 3-directional (XYZ) polarisation analysis study of the short and long range order in $D_3OFe_3(SO_4)_2(OD)_6$ and $KFe_3(SO_4)_2(OD)_6$ performed on the D7 Diffractometer at the ILL. Both compounds belong to the jarosite family of minerals. The Fe^{3+} ion in these materials are arranged in a two dimensional kagome lattice which exhibits, in the case of antiferromagnetic superexchange, a strong geometric frustration. Only short range magnetic correlations down to 1.5K have been observed in the D_3O salt, in contrast to the successive long range magnetic ordering transitions seen in the K salt at $T_{N1} \approx 65K$ and $T_{N2} \approx 50K$ respectively. The diffuse scattering observed in the deuteronium salt is compared with the theoretical

predictions for the magnetic structure factor for a kagome lattice with nearest - neighbour antiferromagnetic exchange.

Introduction

The jarosite family of minerals $AFe_3(SO_4)_2(OD)_6$, where A is a monovalent cation, provides magnetic materials of a model kagome lattice type [1]. The kagome lattice can be viewed as a two-dimensional network of corner-sharing triangles resulting in four superexchange pathways per magnetic ion. Isotropic magnetic superexchange and/or XY anisotropy introduce in such a system geometric frustration resulting in a 120° type magnetic spin ordering per triangle. However, the topology of the superexchange within the lattice induces a highly degenerate ground state. Theoretical predictions indicate that the magnetic moments condense in strongly fluctuating 'a $\sqrt{3}$ x a $\sqrt{3}$' coplanar spin configurations as $T \rightarrow 0$ K [2,3].

Presently only $D_3OFe_3(SO_4)_2(OD)_6$ [4] seems to show the characteristics of a fully frustrated groundstate with spin freezing observed at T_{sf} = 13.8 K. DC susceptibility measurements show, below this temperature, divergence between the zero field cooled (ZFC) and field cooled (FC) behaviour, whilst AC magnetic susceptibility measurements have a frequency dependence below T_{sf}. The dynamics of this spin glassy state were determined by muon spin relaxation and neutron spin echo studies. The results show that the moments are frozen at T = 1.5 K (see present proceedings)[10].

All other Fe-jarosites show a transition to the so called 'q = 0' magnetic structure at $T_N \approx 65$ K [5]. This long range magnetic order is attributed to a partial occupancy of the magnetic Fe^{3+} lattice (~90%), an 'order by disorder' effect which is well demonstrated in $D_3OFe_3(SO_4)_2(OD)_6$ (with an Fe^{3+} occupancy of > 97%) when doped with Al^{3+} [6]. A neutron powder diffraction study of $D_3OFe_3(SO_4)_2(OD)_6$ showed the presence of only weak magnetic scattering contribution around $Q \approx 1.05$ Å^{-1}. Unfortunately the weakness of the magnetic scattering did not allow either the form of the diffuse scattering to be determined over an extended Q range, nor an accurate determination of the magnetic moment.

In this paper we present the first results of a full neutron polarisation study of $D_3OFe_3(SO_4)_2(OD)_6$, A = K, D_3O, which was carried out on the D7 diffractometer at the Institut Laue Langevin, Grenoble. The XYZ method [7] allows the separation of the magnetic scattering from the nuclear scattering and the spin incoherent scattering, as well as a determination of the ratio of the diffuse and Bragg component of this magnetic scattering. The compound K $Fe_3(SO_4)_2(OD)_6$ has an Fe^{3+} site occupation level of 90(2)% and shows magnetic long range order at $T_N = 65$ K. In Fig. 1(a) the powder diffraction pattern taken at 1.5K is shown. Both nuclear and magnetic reflections are present. In Fig. 1(b) only the magnetic part of the scattering process, determined using full neutron spin polarisation analysis, is displayed. The magnetic Bragg scattering corresponds to the 'q = 0' spin structure. At 1.5K there is still a considerable amount of diffuse scattering. Integrating the magnetic intensity over the Q range $0.25 \leq Q \leq 2.5$ Å^{-1} covers an average 76% of the magnetic form factor squared, corresponding to a differential coherent magnetic cross section ($d\sigma/d\Omega$) of 2.19 barns/sr.formula unit (fmu). For the total magnetic cross section / fmu (3 Fe^{3+}

ions) one should expect to find a cross section of 3.8 barns/sr.fmu. Therefore ≈ 43% of the cross section is not observed.

The observed magnetic cross section at T = 1.5K can be divided into 1.56 barns/sr.fmu for the magnetic Bragg scattering, with 0.62 barns/sr.fmu distributed over the whole Q range as diffuse magnetic scattering as shown in Fig. 1(c). The missing part of the magnetic scattering will have inelastic character. Fig. 1(c) also shows the magnetic scattering profile above T_N = 70K. All the magnetic scattering is now diffuse and the cross section obtained is 2.14 barns/fmu.

In Fig. 2(a) the diffraction pattern of $D_3OFe_3(SO_4)_2(OD)_6$ at 2K is shown. No magnetic Bragg scattering is observed whilst the diffuse magnetic scattering is hardly visible. Full polarisation analysis allows an unambiguous determination of the magnetic scattering component as shown in Fig. 2(b). The magnetic cross section at 2 K, corresponds to 2.34 barns/sr.fmu when integrated over the same Q range as for $KFe_3(SO_4)_2(OD)_6$.

The diffuse magnetic scattering in $D_3OFe_3(SO_4)_2(OD)_6$ measured with an incident wavelength of 1.99 Å [4] peaks at Q = 1.1 $Å^{-1}$ and was fitted to a Warren type function [8], giving an in plane two spin correlation length of ξ = 19(2) Å. The diffuse magnetic scattering profile as obtained from the present polarisation study (λ = 4.58 Å) shows a strong similarity in its profile. However it is clear that additional scattering due to higher order components is present for Q > 1.3 $Å^{-1}$. A determination of the scattering cross section S(Q) for an antiferromagnetic kagome lattice with nearest neighbour superexchange using Monte Carlo (MC) techniques [9] shows that S(Q) peaks at Q = 1.1 $Å^{-1}$. The MC calculations show a further structure at Q = 2.4 and Q = 3.5 $Å^{-1}$. Such features are clearly not present in our data which

may indicate that the in plane next nearest neighbour and inter-planar superexchange pathways play a substantial role in shaping the form of S(Q).

The similarity of the diffuse magnetic scattering profile in $D_3OFe_3(SO_4)_2(OD)_6$ at T = 1.5K (Fig. 2(b)) and $KFe_3(SO_4)_2(OD)_6$ measured 5K above T_N, Fig. 1(c), shows that the correlation lengths in both compounds correspond to the diameter of an individual kagomé star.

Although the shape of S(Q) is similar in both cases, it represents different types of states. In the case of the K^+ salt the system is entirely dynamic, whilst the profile at 2K in the D_3O case reflects the Q dependence of the frozen moment. A previous neutron spin echo study suggests that the magnetic moments in the latter case are dynamic at time scales of the order of 100 ps at 20K and gradually freeze as the material is cooled through T_f until at 2K, all moments are frozen on the timescale up to 870 μs [10].

The temperature dependence of S(Q) of $D_3OFe_3(SO_4)_2(OD)_6$ shows that the scattering profile changes very little between 2 and 20K. Diffuse magnetic scattering has been observed up to $T > 5T_f$. It has to be noted that in both cases a contribution to S(Q) may be present due to the dynamic (inelastic) response integrated in by the two-axis diffraction condition on D7. The energy transfer window on D7 for the given wavelength of 4.58 Å is typically $-3.5 \leq \omega \leq 10$ meV. This inelastic response may cause an overestimation of the cross-section value of the elastic magnetic signal. This effect has been clearly observed in the extended Q range data (2 - 4 $Å^{-1}$) for $D_3OFe_3(SO_4)_2(OD)_6$, at the wavelength of 3.5 Å, whilst similar observations have been seen for the closely related system SCGO(x) [11].

References

[1] A.S.Wills and A.Harrison *Faraday Trans.* **92** (1996) 2161

[2] J.T.Chalker, P.C.W.Holdsworth and E.F.Shender, *Phys. Rev. Lett.* **68** (1992) 855

[3] A.B.Harris, C.Kallin and A.J.Berlinsky, *Phys. Rev.* **B45** (1992) 2899

[4] A.S.Wills, A.Harrison, S.A.M.Mentink, T.E.Mason and Z.Tun, *Europhys. Lett.* **42** (1998) 325

[5] M.G.Townshend, G.Longworth and E.Roudant, *Phys. Rev.* **B33** (1986) 4919

[6] A.Harrison, A.S.Wills and C.Ritter, *Physica* **B241-243** (1998) 359

[7] O.Scharpf and H.Capelmann, *Phys. Stat. Sol. (A)* **135** (1993) 359

[8] J.E.Greedan, M.Bieringer, J.Britten, D.M.Giaquinta, H.C. zur Loye, *J. Solid State Chem.* **116** (1995) 118

[9] J.N.Reimers *Phys. Rev.* **B46** (1992) 193

[10] G.S.Oakley, S.Pouget, A.Harrison, J.Frunske and D.Visser, *Physica B* (in press)

[11] C.Mondelli, H.Mutka, B.Frick and C.Payen, *Physica B* (in press)

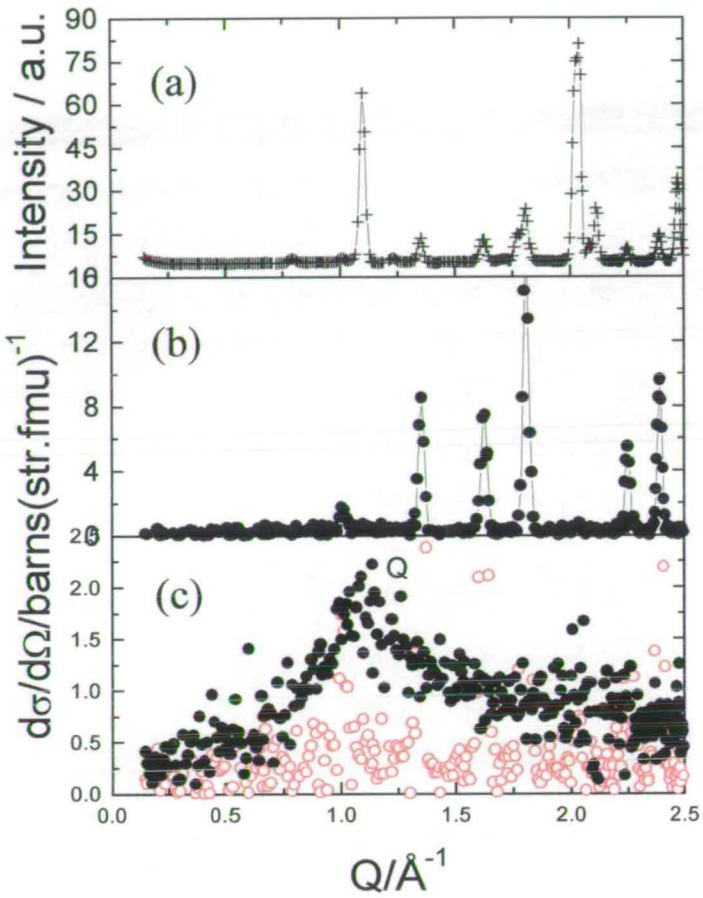

Fig.1 (a) Diffraction pattern of $KFe_3(SO_4)_2(OD)_6$ at T = 1.5K; (b) magnetic scattering contribution to (a) at T = 1.5K; (c) diffuse scattering contribution to (a) at T = 1.5K (open circles) and at T = 70K (filled circles)

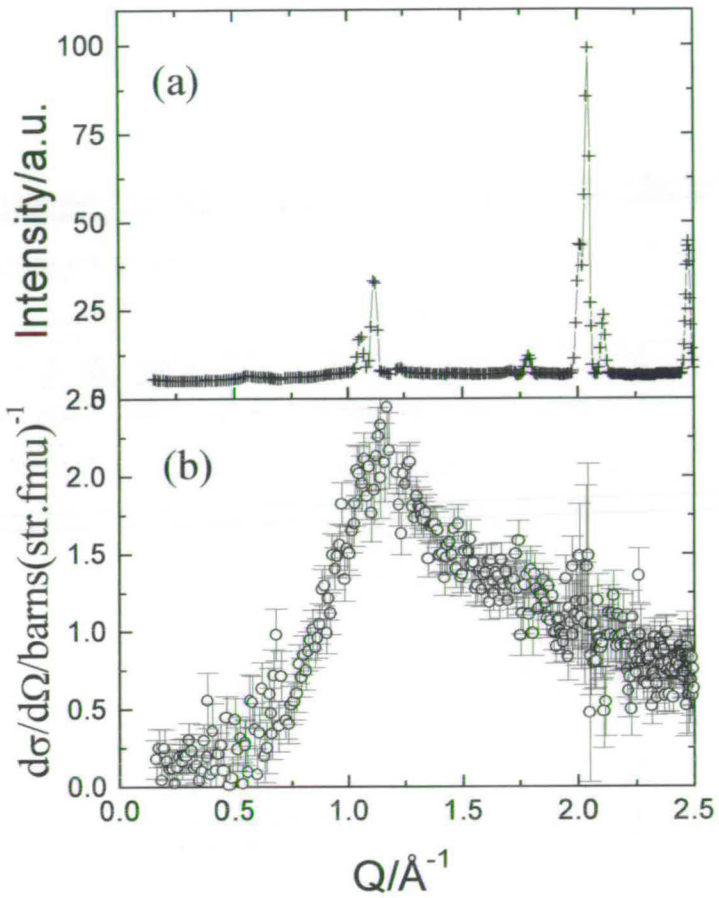

Fig.2 (a) Diffraction pattern of $D_3OFe_3(SO_4)_2(OD)_6$ at T = 2.0K; (b) magnetic scattering contribution to (a) at T = 2.0K